SYNTHESIS AND COORDINATION CHEMISTRY OF LIGANDS CAPABLE OF SIMULTANEOUSLY COORDINATING METAL IONS AND BINDING ANIONS

CHRISTOPHER HAYDN LEWIS SLATER

A thesis submitted to the University of Huddersfield in partial fulfilment of the requirements for the degree of Doctor of Philosophy

The University of Huddersfield

30 / 8 / 2018

Copyright statement

i. The author of this thesis (including any appendices and/or schedules to this thesis) owns any copyright in it (the "Copyright") and s/he has given The University of Huddersfield the right to use such copyright for any administrative, promotional, educational and/or teaching purposes.

ii. Copies of this thesis, either in full or in extracts, may be made only in accordance with the regulations of the University Library. Details of these regulations may be obtained from the Librarian. This page must form part of any such copies made.

iii. The ownership of any patents, designs, trademarks and any and all other intellectual property rights except for the Copyright (the "Intellectual Property Rights") and any reproductions of copyright works, for example graphs and tables ("Reproductions"), which may be described in this thesis, may not be owned by the author and may be owned by third parties. Such Intellectual Property Rights and Reproductions cannot and must not be made available for use without the prior written permission of the owner(s) of the relevant Intellectual Property Rights and/or Reproductions

Acknowledgements

Firstly, I would like to thank Prof. Craig Rice for his continuous support and friendship during my PhD without whom I wouldn't have been able to do this. Thank you to Dr Robert Faulkner for being there through the good days and the bad.

Thank you to my bike for getting me to university with a smile. Thank you to my family and friends for their constant support and understanding as I've completed this PhD. A special thank you to my mum, Peggy, for funding, supporting and pushing me to succeed even when I didn't want to. Finally, a deepest thank you to my beautiful partner Frankie Davidson, you made doing this PhD worth every minute.

Table of Contents

List of Figures

Figure 1.1.11. *Crystal structure of the dinuclear double helicate fragment {($\mathbf{L}^{1.18}$)$_2$(μ-OMe)$_4$ZnTi} a) wireframe view, b) space filling view.*[45]

Figure 1.2.1. *a) Wu et. al. trisurea based anion receptor ligand where $\mathbf{L}^{1.21}$ X = Y = O, $\mathbf{L}^{1.22}$ X = S, Y = O and $\mathbf{L}^{1.23}$ X = Y = S b) crystal structure of the [($\mathbf{L}^{1.21}$)$_2$PO$_4$]$^{3-}$ complex c) crystal structure of the [($\mathbf{L}^{1.22}$)$_2$(HPO$_4$)(H$_2$PO$_4$]$^{3-}$ complex.*[55]

Figure 1.2.2. *Structural representation of Lehn and co-workers O-bistren halide complexes.*[50]

Figure 1.2.3. *Three binging modes of the dimethylene thiourea bridged 2, 2'-bipyridine ligand. a) [$\mathbf{L}^{1.24}$(O$_2$CMe]$^-$, b) [$\mathbf{L}^{1.24}$(H$_2$PO$_4$)$_2$]$^{2-}$, c) [$\mathbf{L}^{1.24}$Re$_2$(CO)$_6$Br$_2$(H$_2$PO$_4$)$_2$]$^{2-}$.*[60]

Figure 1.3.1. I*llustration of four different helicate type assemblies and their internal central cavity.*[61]

Figure 1.3.2. *Two crystal structures from the mentioned work of Cronin et. al. Where, a) the addition of spherical or trigonal anions to the system yields a dinuclear triple helicate and b) the addition of lager tetrahedral anions to the system yields a dinuclear triple mesocate.*[62]

Figure 1.3.3. *Seriies of Fe(II) assembled halide host molecules a) Solomon Linked catenane, b) Pentafoil knot, c) Star of David catenane.*[63]

Figure 1.3.4. *a) Schematic of the reaction of $\mathbf{L}^{1.320}$ to form the {*L$_6$M$_4$*(EO$_4$)} cage assembly where R = H, tBu; M = Zn, Ni; E = S, Se, Mo, W, Cr (n = 2) and P (n = 3).*[65]

Figure 1.3.5. *a) Crystal structure of the {L$_6$M$_4$(EO$_4$)} cage assembly (selected atoms omitted for clarity) and c) b) view of the anion/urea interactions of the {L$_6$M$_4$(EO$_4$)} cage assembly (selected atoms omitted for clarity).*[65]

Figure 1.3.6. *Schematic of the reaction of $\mathbf{L}^{1.321}$ to form the [($\mathbf{L}^{1.321}$)$_2$(SO$_4$)Ag$_2$] anion capsule assembly.*[67]

Figure 1.3.7. *a) Crystal structure of the [($\mathbf{L}^{1.321}$)$_2$(SO$_4$)Ag$_2$] anion capsule assembly (dashed lines showing the twelve anion/urea hydrogen bonding interactions), b) Crystal structure of the [($\mathbf{L}^{1.321}$)$_2$(SO$_4$)Ag$_2$] anion*

capsule assembly where each of the two ligands are individually highlighted and the disorder of the encapsulated SO_4^{2-} molecule is shown, c) Crystal structure of the $[(\mathbf{L}^{1.321})_2(SO_4)Ag_2]_n$ anion capsule 1D coordination polymer assembly with respective CN···Ag coordination bonds. Selected atoms omitted for clarity.[67]

Figure 1.3.8. *Diagram illustrating the solid-state crystallisation products of the Custelcean et. al. TREN based SO_4^{2-} capsule with a) $[Mg(H_2O)_6]^{2+}$, $[Ca(H_2O)_6]^{2+}$, $[Cd(H_2O)_6]^{2+}$ b) $Na_2(H_2O)_4]^{2+}$ c) $K_2(H_2O)_4]^{2+}$.*[68]

Figure 1.3.9. *Bis-pyrazolyl-pyridine ligands $\mathbf{L}^{1.330}$, $\mathbf{L}^{1.331}$, and $\mathbf{L}^{1.332}$ synthesised by Ward et. al.*[64]

Figure 1.3.10. *Crystal structures of Ward et. al $\{L_6M_4\}$ cages, a) $\mathbf{L}^{1.330}$ and BF_4^-, b) $\mathbf{L}^{1.331}$ and SiF_6^{2-}, c) $\mathbf{L}^{1.332}$ and PF_6^-.*[64]

Figure 1.3.11. *Schematic of the reaction of ligand $\mathbf{L}^{1.340}$ (where R = S CONHCH(CH(CH$_3$)$_2$)CO$_2$Me) with Co(II) perchlorate to give the dinuclear triple helicate showing the binding of perchlorate anions.*[81]

Figure 1.3.12. *Crystal structure of the NO_3^- containing dinuclear triple helicate assembly $[(\mathbf{L}^{1.340})_3Co_2(NO_3)_2]^{2+}$. Selected atoms omitted for clarity.*[81]

Figure 1.3.13. *Schematic of the reaction of $\mathbf{L}^{1.341}$ (where R = CONHCH(CH(CH$_3$)$_2$)CO$_2$Me) with Co(II) and NO_3^- to give the NO_3^- encapsulated HHH dinuclear triple helicate assembly.*[82]

Figure 1.3.14. Ligand $\mathbf{L}^{1.342}$

Figure 1.3.15. *Solid state structure of a) $[(\mathbf{L}^{1.342})_2Cu_2](BF_4)^{3+}$. Thermal ellipsoids shown at the 50% probability level and the remaining anions omitted for clarity.*[83]

Figure 1.3.16. *Solid state structure of $[(\mathbf{L}^{1.342})_2Cu_2(OPO_3H_2)]^{3+}$. Thermal ellipsoids shown at the 50% probability level and the remaining anions omitted for clarity.*[83]

Figure 1.3.17. *Crystal structure of* $[(\mathbf{L}^{1.342})_3Cu_3(OPO_3H_2)_3]^{3+}$. *a) top view of the trinuclear circular helicate. b) view of the three dihydrogen phosphate anions. c) view of the six dihydrogen phosphate anions involved in both inter and intra-molecular hydrogen bonding.*[83]

Figure 1.3.18. *Crystal structure of* $([(\mathbf{L}^{1.342})_3Cu_3(OPO_3H_2)_3])_2^{6+}$. ***a)*** *side view of the dimeric structure.* ***b)*** *space-filling view of the dimer.* ***c)*** *top view of the circular helicate dimer showing the intra-molecular hydrogen bonding.*[83]

Figure 2.1.1. *^{1}H NMR of benzoylated thiourea product (**1**) a = water impurity and b =* $(CD_3)(CHD_2)SO$.

Figure 2.1.2. *^{1}H NMR of the bis-thiourea product (2) a = water impurity and b =* $(CD_3)(CHD_2)SO$.

Figure 2.1.3. *^{1}H NMR of ligand* $\mathbf{L}^{2.1}$ *a = water impurity and b =* $(CD_3)(CHD_2)SO$.

Figure 2.2.1. *X-ray structure of three different views of the X-ray structure of the major component of* $[(\mathbf{L}^{2.1})_2Cu_2(trif)_2]^{2+}$ *showing the coordination and hydrogen bonding of the triflate anion. Thermal ellipsoids shown at the 50% probability level. Selected hydrogen atoms and anions omitted for clarity.*

Figure 2.2.2. *Three different views of the X-ray structure of* $[(\mathbf{L}^{2.1})_2Cu_2(H_2O)_2(NO_3)_4]$ *showing the coordination and hydrogen bonding of the nitrate anion. Thermal ellipsoids shown at the 50% probability level. Selected anions omitted for clarity.*

Figure 2.2.3. *Three different views of the X-ray structure of* $[(\mathbf{L}^{2.1})_2Cu_2]^{2+}$ *showing the Cu(II) coordination. Thermal ellipsoids shown at the 50% probability level. Selected anions omitted for clarity.*

Figure 2.2.4. *Three different views of the X-ray structure of* $[(\mathbf{L}^{2.1})_2Cu_2(O_2SeOMe)]^{2+}$ *showing the coordination and hydrogen bonding of both the phosphate and triflate anions. Thermal ellipsoids shown at the 50% probability level. Selected anions and atoms omitted for clarity.*

Figure 2.2.5. *Three different views of the X-ray structure of* $[(\mathbf{L}^{2.1})_2Cu_2(H_2PO_4)(trif)]^{2+}$ *showing the coordination and hydrogen bonding of both the phosphate and triflate anions. Thermal ellipsoids shown at the 50% probability level. Selected anions and atoms omitted for clarity.*

Figure 2.2.6. *Four different views of the X-ray structure of* $[(\mathbf{L}^{2.1})_3Cu_3(PO_4BF_3)]^{3+}$ *showing the coordination and hydrogen bonding of the anion. Thermal ellipsoids shown at the 50% probability level. Selected anions and atoms omitted for clarity (a-b). Partial view of the X-ray structure showing the* O_3POBF_3 *unit (d) and its bonding interactions (c).*

Figure 2.3.1. *Ligand* $\mathbf{L}^{2.2}$

Figure 2.3.2. ^1H *NMR of ligand* $\mathbf{L}^{2.2}$ *a = water impurity and b =* $(CD_3)(CHD_2)SO$.

Figure 2.3.3. *Three different views of the X-ray structure of* $[(\mathbf{L}^{2.2})_2Cu_2(H_2PO_4)(trif)_2]^{2+}$ *showing the coordination and hydrogen bonding of both the phosphate and triflate anions. Thermal ellipsoids shown at the 50% probability level. Selected anions and atoms omitted for clarity*

Figure 2.3.4. *X-ray structure of* $[(\mathbf{L}^{2.2})_2Cu_2(PO_4(BF_3)_2)]^+$ *showing the coordination and hydrogen bonding of the anion. Thermal ellipsoids shown at the 50% probability level. Selected anions and atoms omitted for clarity.*

Figure 2.3.5. *Three different views of the X-ray structure of* $[(\mathbf{L}^{2.2})_2Cu_2(PO_4(BF_3)_2)]^+$ *showing the coordination and hydrogen bonding of the anion. Thermal ellipsoids shown at the 50% probability level. Selected anions and atoms omitted for clarity (a). Partial view of the X-ray structure showing the* $\{PO_4(BF_3)_2\}$ *unit (c) and its bonding interactions (b).*

Figure 2.4.1. *Ligand* $\mathbf{L}^{2.3}$

Figure 2.4.2. ^1H *NMR of ligand* $\mathbf{L}^{2.3}$ *a = water impurity and b =* $(CD_3)(CHD_2)SO$.

Figure 3.2.8. *ESI-MS of the reaction of Cu(triflate)$_2$ and* $\boldsymbol{L^{3.1}}$ *(sample time 48 hrs) showing the isotope pattern for the ion at m/z 1665 corresponding to both the singly charged* $\{[(\boldsymbol{L^{3.2}})_2Cu_2](trif)_3\}^+$ *ion and the doubly charged* $\{[(\boldsymbol{L^{3.2}})_4Cu_4](trif)_6\}^{2+}$ *ion.*

Figure 4.1.1 ^{1}*H NMR of benzoylated thiourea product (**1**) a = water impurity and b =* $(CD_3)(CHD_2)SO$.

Figure 4.1.2 ^{1}*H NMR of the tris-thiourea product (**2**)*

Figure 4.1.3. *Two different views of the X-ray structure of the tris-thiourea product (**2**) showing the (a) intermolecular and (b) intramolecular hydrogen bonding of the compounds thiourea groups. Thermal ellipsoids shown at the 50% probability level. Selected atoms and anions omitted for clarity.*

Figure 4.1.4. ^{1}*H NMR of ligand* $\boldsymbol{L^{4.1}}$

Figure 4.2.1. *a) Three different views of the X-ray structure of the major component of* $[(\boldsymbol{L^{4.1}})_2Cu_3(BF_4)_{0.66}(Cl)_{0.34}]^{5+}$ *showing the coordination and hydrogen bonding of the tetrafluoroborate anion b) Thermal ellipsoids shown at the 50% probability level. Selected hydrogen atoms and anions omitted for clarity.*

Figure 4.2.2. *The single-crystal X-ray structure of the minor* Cl^- *guest of the disordered* $[(\boldsymbol{L^{4.1}})_2Cu_3(BF_4)_{0.66}(Cl)_{0.34}]^{5+}$ *molecule.*

Figure 4.2.3. *Three different views of the X-ray structure of* $[(\boldsymbol{L^{4.1}})_2Cu_3(Br)]^{5+}$ *showing the coordination and hydrogen bonding of the anion. Thermal ellipsoids shown at the 50% probability level. Selected hydrogen atoms and anions omitted for clarity.*

Figure 4.2.4. *Three different views of the X-ray structure of* $[(\boldsymbol{L^{4.1}})_2Cu_3(SiF_6)]^{4+}$ *showing the coordination and hydrogen bonding of the anion. Thermal ellipsoids shown at the 50% probability level. Selected hydrogen atoms and anions omitted for clarity.*

Figure 4.3.1. *Aqueous solutions of the* $[(\mathbf{L^{4.1}})_2Cu_3]^{6+}$ *species with a variety of different anions displaying the variety of colours (a). A solution of* $[(\mathbf{L^{4.1}})_2Cu_3]^{6+}$ *which was reacted with (b)* HSO_4^- *and (c)* $H_2PO_4^-$ *and deposits brown and green crystals respectively*

Figure 4.3.2. *Three different views of the X-ray structure of* $[\mathbf{L^{4.1}}_2Cu_3(PO_4)]^{3+}$ *showing the coordination and hydrogen bonding of the anion. Thermal ellipsoids shown at the 50% probability level. Selected hydrogen atoms and anions omitted for clarity.*

Figure 4.3.3. *Two different views of the X-ray structure of* $[(\mathbf{L^{4.1}})_2Cu_3(VO_4)]^{3+}$. *Thermal ellipsoids shown at the 50% probability level. Selected hydrogen atoms and anions omitted for clarity.*

Figure 4.3.4. *X-ray structure of* $[(\mathbf{L^{4.1}})_2Cu_3(WO_4)]^{4+}$. *Thermal ellipsoids shown at the 50% probability level. Selected hydrogen atoms and anions omitted for clarity.*

Figure 4.3.5. *Two different views of the X-ray structure of* $[(\mathbf{L^{4.1}})_2Cu_3(CrO_4)]^{4+}$. *Thermal ellipsoids shown at the 50% probability level. Selected hydrogen atoms and anions omitted for clarity.*

Figure 4.3.6. *Two different views of the X-ray structure of* $[(\mathbf{L^{4.1}})_2Cu_3(SO_4)]^{4+}$. *Thermal ellipsoids shown at the 50% probability level. Selected hydrogen atoms and anions omitted for clarity.*

Figure 4.3.7. *Two different views of the X-ray structure of* $[(\mathbf{L^{4.1}})_2Cu_3(AsO_4)]^{3+}$. *Thermal ellipsoids shown at the 50% probability level. Selected hydrogen atoms and anions omitted for clarity.*

Figure 4.3.8. *Three different views of the X-ray structure of* $[(\mathbf{L^{4.1}})_2Cu_4(IO_6)(H_20)_2]^{4+}$ *showing the coordination and hydrogen bonding of the anion. Thermal ellipsoids shown at the 50% probability level. Selected hydrogen atoms and anions omitted for clarity.*

Figure 4.3.9. *Three different views of the X-ray structure of* $[\mathbf{L^{4.1}}_2Cu_3I]^{5+}$ *showing the coordination and hydrogen bonding of the anion. Thermal ellipsoids shown at the 50% probability level. Selected hydrogen atoms and anions omitted for clarity.*

Figure 4.3.10. *Three different views of the X-ray structure of* $[(\mathbf{L}^{4.1})_2Cu_3CO_3]^{4+}$ *showing the coordination and hydrogen bonding of the anion. Thermal ellipsoids shown at the 50% probability level. Selected hydrogen atoms and anions omitted for clarity.*

Figure 4.3.11. *Three different views of the X-ray structure of* $[(\mathbf{L}^{4.1})_2Cu_3(S_2O_3)]^{4+}$ *showing the coordination and hydrogen bonding of the anion. Thermal ellipsoids shown at the 50% probability level. Selected hydrogen atoms and anions omitted for clarity.*

Figure 4.4.1. *ESI-MS of* $[(\mathbf{L}^{4.1})_2Cu_3(SO_4)](ClO_4)_4$.

Figure 4.4.2. *ESI-MS of* $[(\mathbf{L}^{4.1})_2Cu_3(WO_4)](ClO_4)_3$.

Figure 4.4.3. *ESI-MS of* $[(\mathbf{L}^{4.1})_2Cu_3(CO_3)](trif)_3$.

Figure 4.4.4. *ESI-MS of* $[(\mathbf{L}^{4.1})_2Cu_3(I)](trif)_5$.

Figure 4.4.5. *UV-Vis absorption spectra of* $[(\mathbf{L}^{4.1})_2Cu_3]^{6+}$; $[(\mathbf{L}^{4.1})_2Cu_3]^{6+}$ *plus one equivalent of phosphate.* $[(\mathbf{L}^{4.1})_2Cu_3]^{6+}$ *1.33 x* 10^{-3} *M.*

Figure 4.4.6. *UV-Vis absorption spectra of* $[(\mathbf{L}^{4.1})_2Cu_3]^{6+}$; $[(\mathbf{L}^{4.1})_2Cu_3]^{6+}$ *plus one equivalent of iodide;* $[(\mathbf{L}^{4.1})_2Cu_3(I)]^{6+}$ *plus one equivalent of hydrogen phosphate.* $[(\mathbf{L}^{4.1})_2Cu_3]^{6+}$ *1.33 x* 10^{-3} *M.*

Figure 4.4.7. *UV-Vis absorption spectra of* $[(\mathbf{L}^{4.1})_2Cu_3]^{6+}$; $[(\mathbf{L}^{4.1})_2Cu_3]^{6+}$ *plus one equivalent of nitrate;* $[(\mathbf{L}^{4.1})_2Cu_3]^{6+}$ *plus one equivalent of nitrate and then one equivalent of hydrogen phosphate.* $[(\mathbf{L}^{4.1})_2Cu_3]^{6+}$ *1.33 x* 10^{-3} *M. Notice that there is no change in the UV-Vis spectrum upon addition of nitrate 1.33 x* 10^{-3} *M.*

Figure 4.4.8. *UV-Vis absorption spectra* $[(\mathbf{L}^{4.1})_2Cu_3](trif)_6$ *plus one equivalent of* Cl^-, Br^-, I^-, VO_4^{3-}, WO_4^{2-}, CrO_4^{2-}, HSO_4^- *and* $H_2PO_4^-$. *All experiments were carried out in MeCN/*H_2O *(1:1 v/v to avoid precipitation) with the concentration of* $[(\mathbf{L}^{4.1})_2Cu_3](trif)_6$ *= 1.33 mM.*

Figure 4.4.9. *UV-Vis absorption spectra of $[(\mathbf{L}^{4.1})_2Cu_3](trif)_6$ plus one equivalent of HSO_4^- and then $H_2PO_4^-$.*

Figure 4.4.10. *UV-Vis absorption spectra of $[(\mathbf{L}^{4.1})_2Cu_3](trif)_6$ plus one equivalent of Na_2SO_4 and then Na_2HPO_4.*

Figure 4.4.11. *UV-Vis absorption spectra of $[(\mathbf{L}^{4.1})_2Cu_3](NO_3)_6$; $[(\mathbf{L}^{4.1})_2Cu_3](NO_3)_6$ plus one equivalent of $Bu_4NH_2PO_4$; giving $[(\mathbf{L}^{4.1})_2Cu_3(PO_4)](NO_3)_3$. $[(\mathbf{L}^{4.1})_2Cu_3]^{6+}$ 1.33 x 10^{-3} M.*

Figure 4.4.12. *UV-Vis absorption spectra of $[(\mathbf{L}^{4.1})_2Cu_3](OAc)_6$; $[(\mathbf{L}^{4.1})_2Cu_3](OAc)_6$ plus one equivalent of $Bu_4NH_2PO_4$; giving $[(\mathbf{L}^{4.1})_2Cu_3(PO_4)](OAc)_3$. $[(\mathbf{L}^{4.1})_2Cu_3]^{6+}$ 1.33 x 10^{-3} M.*

Figure 4.4.13. *UV-Vis absorption spectra of $[(\mathbf{L}^{4.1})_2Cu_3](Cl)_6$; $[(\mathbf{L}^{4.1})_2Cu_3](Cl)_6$ plus one equivalent of $Bu_4NH_2PO_4$; giving $[(\mathbf{L}^{4.1})_2Cu_3(PO_4)](Cl)_3$. $[(\mathbf{L}^{4.1})_2Cu_3]^{6+}$ 1.33 x 10^{-3} M.*

Figure 4.4.14. *IC experimental data a) 50 ppm solution of each of chloride, nitrate, phosphate and sulfate exposed to $[(\mathbf{L}^{4.1})_2Cu_3](trif)_6$ and b) 50 ppm standard.*

Figure 4.6.1. *Four different views of the X-ray structure of $[(\mathbf{L}^{4.1})_4Cu_8(SeO_3)_4]^{8+}$(a - b) showing the coordination and hydrogen bonding of the anion (c – d). Thermal ellipsoids shown at the 50% probability level. Selected hydrogen atoms and anions omitted for clarity*

Figure 4.6.2. *Three different views of the X-ray structure of $[(\mathbf{L}^{4.1})_2Cu_3(SeO_3)]^{4+}$ showing the coordination and hydrogen bonding of the anion. Thermal ellipsoids shown at the 50% probability level. Selected hydrogen atoms and anions omitted for clarity.*

Figure 5.1.1. *^1H NMR of benzoylated thiourea product (**1**) a = water impurity and b = $(CD_3)(CHD_2)SO$.*

Figure 5.1.2. *^1H NMR of the bis-thiourea product (**2**) a = water impurity and b = $(CD_3)(CHD_2)SO$. The expansion shows the absence of a amide peaks at ~ 11 ppm.*

Figure 5.1.3. *^1H NMR of ligand $\mathbf{L}^{2.1}$ a = water impurity and b = $(CD_3)(CHD_2)SO$.*

Figure 5.1.4. *ESI-MS of $[(\mathbf{L}^{2.1})_2Cu_2(trif)](trif)_2$ with the obtained isotope pattern (inset top) and calculated (inset bottom) for m/z 1335 $\{[(\mathbf{L}^{2.1})_2Cu_2](trif)_3\}^+$.*

Figure 5.1.5. *ESI-MS of $[(\mathbf{L}^{2.1})_2Cu_2(H_2PO_4)](trif)_3$ with the obtained isotope pattern (inset top) and calculated (inset bottom) for m/z 1282 $\{[(\mathbf{L}^{2.1})_2Cu_2(H_2PO_4)](trif)_2\}^+$*

Figure 5.1.6. *ESI-MS of $[(\mathbf{L}^{2.1})_3Cu_3(O_3POBF_3)](BF_4)_3$ with the obtained isotope pattern (inset top) and calculated (inset bottom) for m/z 1668 $\{[(\mathbf{L}^{2.1})_3Cu_3(O_3POBF_3)](BF_3)_2\}^+$.*

Figure 5.1.7. *^{1}H NMR of benzoylated thiourea product (**1**) a = water impurity and b = $(CD_3)(CHD_2)SO$.*

Figure 5.1.8. *^{1}H NMR of the bis-thiourea product (**2**) a = water impurity and b = $(CD_3)(CHD_2)SO$. The expansion shows the absence of amide peaks at ~ 11 ppm.*

Figure 5.1.9. *^{1}H NMR of ligand $\mathbf{L}^{2.2}$ a = water impurity and b = $(CD_3)(CHD_2)SO$.*

Figure 5.1.10. *ESI-MS of $[(\mathbf{L}^{2.2})_2Cu_2](trif)_4$ with the obtained isotope pattern (inset top) and calculated (inset bottom) for m/z 1391 $\{[(\mathbf{L}^{2.2})_2Cu_2](trif)_3\}^+$.*

Figure 5.1.11. *ESI-MS of $[(\mathbf{L}^{2.2})_2Cu_2(HPO_4)](trif)_2$ with the obtained isotope pattern (inset top) and calculated (inset bottom) for m/z 1339 $\{[(\mathbf{L}^{2.2})_2Cu_2(H_2PO_4)](trif)_2\}^+$.*

Figure 5.1.12. *ESI-MS of $[(\mathbf{L}^{2.2})_2Cu_2(O_3POBF_3)](trif)_2$ with the b) obtained isotope pattern and a) calculated for m/z 1107 $\{[(\mathbf{L}^{2.2})_2Cu_2(O_3POBF_3)]\}^+$.*

Figure 5.1.13. *^{1}H NMR of bis-benzoylated thiourea product (**1**) a = water impurity and b = $(CD_3)(CHD_2)SO$.*

Figure 5.1.14. *^{1}H NMR of the bis-thiourea product (**2**) a = water impurity and b = $(CD_3)(CHD_2)SO$.*

Figure 5.1.15. *^{1}H NMR of ligand $\mathbf{L}^{2.3}$ a = water impurity and b = $(CD_3)(CHD_2)SO$.*

Figure 5.1.16. *ESI-MS of $[(\mathbf{L^{2.3}})_2Cu_2](trif)_4$ with the obtained isotope pattern (inset top) and calculated (inset bottom) for m/z 1389 $\{[(\mathbf{L^{2.3}})_2Cu_2](trif)_3\}^+$.*

Figure 5.3.1. *^{1}H NMR of the benzoylated urea derivative (**1**)*

Figure 5.3.2. *^{1}H NMR of the trithiourea compound (**2**)*

Figure 5.3.3. *^{1}H NMR of ligand $\mathbf{L^{4.1}}$.*

Figure 5.4.1. *UV-Vis absorption spectra of $[(\mathbf{L^{4.1}})_2Cu_3](trif)_6$; $[(\mathbf{L^{4.1}})_2Cu_3](trif)_6$ after 1 and 3 hrs giving $[(\mathbf{L^{4.1}})_2Cu_3(CO_3)](trif)_4$; $[(\mathbf{L^{4.1}})_2Cu_3(CO_3)](trif)_4$ plus one equivalent of $Bu_4NH_2PO_4$ giving $[(\mathbf{L^{4.1}})_2Cu_3(PO_4)](trif)_3$. $[(\mathbf{L^{4.1}})_2Cu_3]^{6+}$ 1.33 x 10^{-3} M.*

Figure 5.4.2. *UV-Vis absorption spectra of $[(\mathbf{L^{4.1}})_2Cu_3](trif)_6$; $[(\mathbf{L^{4.1}})_2Cu_3](trif)_6$ plus 1 equiv. $NaReO_4$; $[(\mathbf{L^{4.1}})_2Cu_3](trif)_6$ plus 1 equiv. $NaReO_4$ after 3 hrs giving $[(\mathbf{L^{4.1}})_2Cu_3(CO_3)](trif)_4$; $[(\mathbf{L^{4.1}})_2Cu_3]^{6+}$ 1.33 x 10^{-3} M.*

Figure 5.5.1. *IC calibration cure of 10 - 200 ppm solutions of $Bu_4NH_2PO_4$.*

Figure 5.5.2 *Blank Solution.*

Figure 5.5.3 *10 ppm Phosphate Standard.*

Figure 5.5.4 *Sample Solution.*

Figure 5.5.5 *Expanded Sample Solution.*

Figure 5.5.6 *Spiked Sample Solution.*

Figure 5.5.7 *Expanded Spiked Sample Solution.*

List of Schemes

List of Tables

Abbreviations

A – anion

Ar – aryl

Bu – butyl

$CDCl_3$ – *d*-chloroform

DMSO – d^6-dimethyl sulfoxide

E – element

ESI-MS – electrospray ionisation mass spectrometry

Et – ethyl

Et_2O – diethyl ether

EtOH – ethanol

IC – ion chromatography

M – metal

Me – methyl

MeCN – acetonitrile

$MeNO_2$ – nitromethane

MeOH – methanol

NMR – Nuclear magnetic resonance

L – ligand

Ph – phenyl

Py – pyridyl

tren – tris(2-aminoethyl)amine

trif – trifluromethyl sulphonate ($CF_3SO_3^-$)

Tz – thiazoyl

Crystal structure atom colours

Standard atom colours unless stated (*i.e*. different coloured ligands for clarity)

White = hydrogen

Grey = carbon

Yellow = sulphur

Blue = nitrogen

Red = oxygen

Cream = boron

Lime = florine

Green = chlorine

Brown = bromine

Purple = iodine

Orange = copper

Silver = vanadium

Light blue = tungsten

Pale blue = chromium

Pale pink = arsenic

Dark yellow = selenium

Abstract

This thesis is concerned with the synthesis of ditopic ligands than can both coordinate transition metal ions and interact with anions. All the ligands contained two or more bidentate thiazole-pyridyl *N*-donor coordination domains and two or more secondary amine units which have shown to interact well with anions.

In Chapter 2 the bidentate thiazole-pyridyl ligands (**L**$^{2.1}$, **L**$^{2.2}$ and **L**$^{2.3}$) were synthesised in moderate yields via diamine starting materials following a simple three step procedure. This involved, benzoyl-isothiocyanation, base hydrolysis and finally a Hantzsch thiazole ring closure reaction. Each of the three ligands have the same basic functionality with two thiazole-pyridyl domains separated by a spacer unit. **L**$^{2.1}$ contains a diamino 1,2-ethyl central spacer unit, **L**$^{2.2}$ a diamino 1,4-butyl central spacer unit and **L**$^{2.3}$ a diamino *cis*-1,4-but-2-ene central spacer unit. The coordination chemistry of **L**$^{2.1}$, **L**$^{2.2}$ and **L**$^{2.3}$ with Cu(II) metal salts (usually as the ClO_4^-, BF_4^- and triflate salts) was examined, as well as other selected counter anions. For **L**$^{2.1}$ six different helicate architectures were determined by single crystal X-ray diffraction as well as being confirmed in the gas phase by ESI-MS for the systems concerning. These included the dinuclear double helicates; $[(\mathbf{L}^{2.1})_2Cu_2(trif)_2]^{2+}$, $[(\mathbf{L}^{2.1})_2Cu_2(H_2O)_2(NO_3)_4]$, $[(\mathbf{L}^{2.1})_2Cu_2]^{2+}$, $[(\mathbf{L}^{2.1})_2Cu_2(OSe(OMe)_2)]^{2+}$ and $[(\mathbf{L}^{2.1})_2Cu_2(H_2PO_4)(trif)]^{2+}$. In addition to this the trinuclear helicate $[(\mathbf{L}^{2.1})_3Cu_3(PO_4BF_3)]^{3+}$ was also isolated, where the coordinated dihydrogen phosphate underwent reaction with the tetrafluoroborate anion. For ligand **L**$^{2.2}$ two different dinuclear double helicate structures were formed which included $[(\mathbf{L}^{2.2})_2Cu_2(H_2PO_4)(trif)_2]^{2+}$ and $[(\mathbf{L}^{2.2})_2Cu_2(PO_4(BF_3)_2)]^{+}$ with the latter species arising from reaction of dihydrogen phosphate with the tetrafluoroborate anion. For the alkene-containing ligand **L**$^{2.3}$ two isomeric helicate structures were obtained with $Cu(trif)_2$ that differ in the coordination of the triflate anion.

A similar synthesis route was used to produce the *bis*-bidentate ligand **L**$^{3.1}$ which comprised of a 2,2'-phenylene central spacer unit linking the two thiazole-pyridyl domains. Again, **L**$^{3.1}$ was reacted with a series

of Cu(II) metal salts and the resulting structures determined by single crystal X-ray diffraction as well as being confirmed in the gas phase by ESI-MS. Two different structures were observed for this system, the mono-nuclear $[(\mathbf{L}^{3.1})Cu](ClO_4)_2$ and the tetranuclear circular head-to-tail helicate $[(\mathbf{L}^{3.2})_4Cu_4](trif)_8$. In the latter the ligand was observed to undergo a reaction at one of the two amine units with a molecule of the acetonitrile solvent to give a new amidine-containing $R_2N\text{-}C{=}NH(CH)_3$ unit. This resulted in the ligand system re-programming itself to give the unsymmetrical bidentate/tridentate ligand $\mathbf{L}^{3.2}$ and consequently forming the tetranuclear head-to-tail circular helicate $[(\mathbf{L}^{3.2})_4Cu_4]^{8+}$.

The final chapter is concerned with the tripoidal ligand $\mathbf{L}^{4.1}$ which was synthesised in a similar fashion to the previous ligands. However, the ligand contained three bidentate thiazole-pyridyl domains linked by a tris-(aminoethyl)amine (tren) central spacer unit. $\mathbf{L}^{4.1}$ was reacted with a series of Cu(II) metal salts (ClO_4^-, BF_4^- and triflate) and the resulting structures were determined by single crystal X-ray diffraction as well as being confirmed in the gas phase by ESI-MS. Sixteen different anion containing crystal structures were obtained for this system, where 13 of which adopted the $[(\mathbf{L}^{4.1})_2Cu_3A]^{n+}$ trinuclear capsule type motif (*i.e.* BF_4^-, Br^-, I^-, CO_3^{2-}, SiF_6^{2-}, VO_4^{3-}, WO_4^{2-}, CrO_4^{2-}, SO_4^{2-}, AsO_4^{3-}, SeO_4^{2-}, SeO_3^{2-} and PO_4^{3-}). The larger octahedral iodate anion gave the expanded tetranuclear species $[(\mathbf{L}^{4.1})_2Cu_4(IO_6)(H_2O)_2]^{4+}$ and dependant on stoichiometry the third row chalcogenide selenite gave the remarkably different $[(\mathbf{L}^{4.1})_4Cu_8(SeO_3)_4]^{8+}$ cage type assembly. UV-Vis experiments showed that the self-assembled host ($[(\mathbf{L}^{4.1})_2Cu_3]^{6+}$) displayed a high degree of selectivity to shape, size and charge of the guest anion, with the highly charged phosphate anion encapsulated in preference to most common anions. Importantly, gravimetric and ion chromatography experiments showed that the $[(\mathbf{L}^{4.1})_2Cu_3]^{6+}$ host system is capable of both forming and encapsulating phosphate anions in a competitive aqueous solvent (*i.e.* water) and removing them in a virtually stoichiometric manner resulting in concentrations < 0.1 ppm.

1. Introduction

1.1 Supramolecular Chemistry

Conventional synthesis is the formation of molecules via making and breaking covalent bonds usually using chemical reagents (e.g. catalyst, reductant, oxidant, base, acid). The production of compounds is usually achieved by an iterative process with each step involving breaking bonds or producing a new bond (or handful of bonds). Clearly this methodology has been extensively studied and used to produce almost all of the important and useful synthetic compounds in use today. However, the processes associated with this methodology are limited as it can often be time consuming and require multiple steps even to make relatively small molecules. These difficulties make the preparation of large and complex molecules almost inaccessible as the potential synthetic routes can be laborious and even inaccessible. An alternative to this process is the use of self-assembly. Self-assembly is a chemical process in which a system of smaller components spontaneously forms an organized molecular structure as a consequence of chemical programming among the individual components, without external direction.[1–6]

Self-assembly is a sub-field of supramolecular chemistry itself a subject that does not rely on the traditional formation of chemical bonds but programmed information contained within chemical sub-units whose information can be chemically expressed. Since the important early discoveries throughout the late 20th century by the likes of Pedersen, Lehn and Cram, supramolecular chemistry has since been recognised to have huge relevance to modern day science.[7] Applications of this field include biological, environmental and materials science as well as newly emerging field of nanotechnology.[8–16] Indeed, in recognition of the importance of this field the 2016 Nobel prize was awarded to Sauvage, Stoddart and Feringa, for their ground-breaking research into molecular machines (Fig 1.1.1).[17]

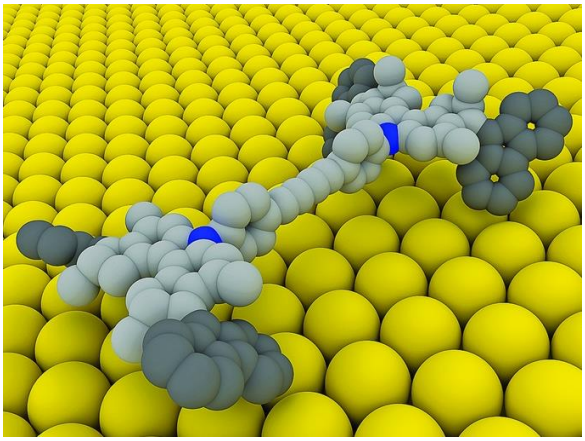

Figure 1.1.1. *Computationally derived view of a nano car derived from the work of Feringa et. al.* [18]

Supramolecular chemistry is a vast, multidisciplinary field, which considers both the design and formation of large structural assemblies from what are, relatively small and simple pre-programmed sub-units. Such covalently bonded sub-units are held together in the assembly by a combination of various bonds/interaction such electrostatic interactions, metal coordination, hydrogen bonding, anion coordination, charge transfer, π-π stacking, induction/dispersion forces (van der Waals forces) and hydrophobic effects.[19] Importantly these interactions are reversible which allows for self-correction in the assembly process allowing the production of the most thermodynamically stable species.[1,20,21] With careful consideration of all these principles, the modern-day chemist can gain access to molecules that can self-recognise, and self-organise to form a vast array of architectures, that would otherwise not be possible or viable by using conventional organic synthesis techniques.

One sub-area of supramolecular chemistry is metallo-supramolecular chemistry which is the self-assembly of structurally complex architectures from the coordination of suitably instructed ligand strands and metal ions. This field has given rise to many interesting and novel self-assembled species such as cages, racks, ladder, grids, helicates (both linear and circular) as well as other elaborate molecular architectures. [22–27]

One of the simplest and most widely studied metallo-supramolecular assembly is the linear helicate. These systems involve suitably programmed ligand chains that contain two or more distinct binding domains that react with suitable metals ions to form assemblies of the type $[L_xM_x]^{n+}$ (where $x \geq 2$).[3] The assembly is

controlled by the use of an instructed ligand strand which contains two potential binding domains separated in some fashion by a spacer/bridge that prevents the domains coordinating a single metal ion producing the entropically favoured mononuclear species. As a result the two domains coordinate two *different* metal ions and this is the supplemented by coordination of a different ligand strand such that the assembly contains two or more ligands and metal ions to give the $[M_{\geq 2}L_{\geq 2}]^{n+}$ type motif.

Whilst mononuclear helicates are acknowledged, the process in which they are formed is generally not recognised to be self-assembly – a process which generally requires two or more ligands and metal ions. Polynuclear linear helicate systems are diverse and to date many examples are known. Furthermore, helicate systems have been sufficiently instructed within the base unit design so that heterometallic (mixed metal), heteroleptic (mixed ligand), head-to-tail (directional), mesocate (non-chiral) can be formed.[28–33] Also, the binding domains along the ligand strand can be different in nature so that transition metal helicates can incorporate anions and s-block metal ions.[23,34–37]

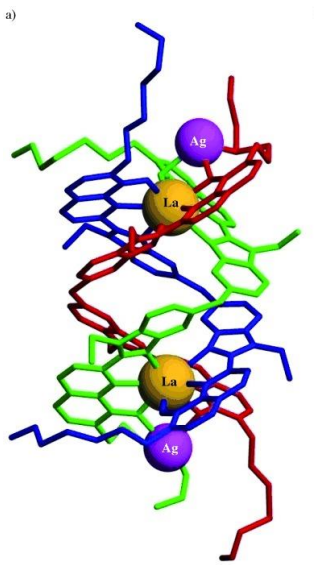

Figure 1.1.2. *Mixed lanthanum and siliver metal triple helicate* $[(\boldsymbol{L}^{1.10})_3(La)_2(Ag)_2]^{8+}$. [29]

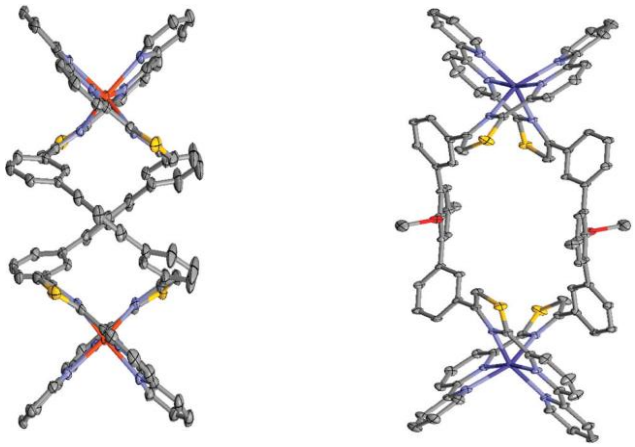

Figure 1.1.3. *Crystal structures of a) dinuclear double helicate complex* $[(\mathbf{L}^{1.11})_2Fe_2]^{4+}$ *and b) dinuclear double mesocate complex* $[(\mathbf{L}^{1.12})_2Fe_2]^{4+}$.[38]

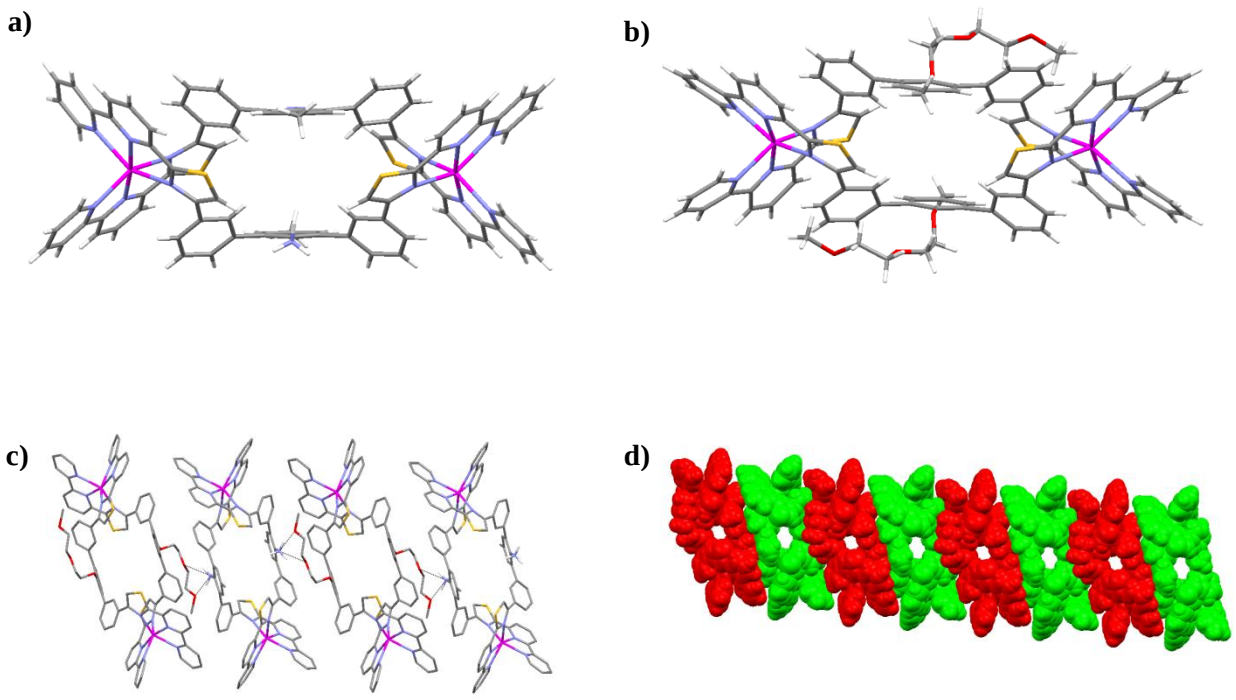

Figure 1.1.4. *a) Dinuclear double mesocate* $[(\mathbf{L}^{1.13})_2Fe_2]^{6+}$, *b) dinuclear double mesocate* $[(\mathbf{L}^{1.14})_2Fe_2]^{6+}$, *c) solid-state 1-dimentional polymer chain of dinuclear double mesocates* $[(\mathbf{L}^{1.13})_2Fe_2(\mathbf{L}^{1.14})_2Fe_2]_n^{12+}$ *d) space filling view of the solid-state 1-dimentional polymer chain of dinuclear double mesocates* $[(\mathbf{L}^{1.13})_2Fe_2(\mathbf{L}^{1.14})_2Fe_2]_n^{12+}$. [39]

One example of a "mixed species" helicate system is the self-assembly of 1-dimensional chain containing different dinuclear mesocates. In this example a mesocate is formed with a bis-tridentate ligand which contains a protonated ammonium unit (**L**$^{1.13}$, Fig. 1.1.4a) and the same assembly is observed when an ethylene glycol is included within the mesocate assembly (**L**$^{1.14}$, Fig. 1.1.4b). Mixing these two species shows that in the solid-state the ammonium unit and the glycol unit form hydrogen bonds between one another (Fig. 1.1.4c) so that a 1-dimensional chain of alternating mesocates is produced (Fig. 1.1.4d).[39]

It is possible for dinuclear double helicate polymer assemblies to display higher order levels of self-assembly. An interesting example of this has been described in a 2012 publication by Ward and Stephenson.[40] In this report a dinuclear double helicate complex was produced by reaction of a bis-bidentate dimethylene benzophenone bridged pyrazolyl-pyridine ligand (**L**$^{1.15}$**)** with Ag(I) perchlorate. The resulting $[(\mathbf{L}^{1.15})_2Ag_2]^{2+}$ complex (Fig 1.1.5) was observed to then form further argentophilic coordination bonds to further dinuclear double helicate fragments to form an infinite one-dimensional polymer chain of the type $[(\mathbf{L}^{1.15})_2Ag_2]_n^{n+}$ (Fig 1.1.6). Most interestingly, three of these polymer chain units were then observed to form weak ligand-ligand and ligand-perchlorate interactions whereby each of the three dinuclear double helicate polymer strands twists around one another to produce (in the solid state) a triple helical array (Fig 1.1.7). Each of the interactions involved in the formation of this architecture (*i.e* ligand-metal, Ag–Ag, ligand-ligand and ligand-anion) are well known and documented in past literature. However, what is most unique is the combination of all these interactions being displayed in one system which yields the formation of this higher order architecture.

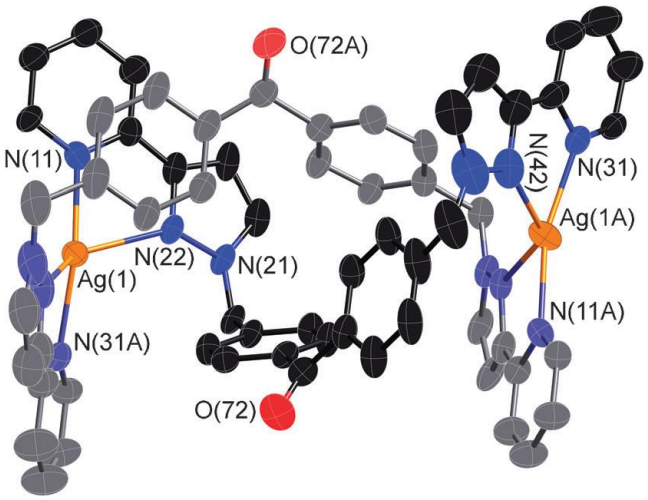

Figure 1.1.5. *Crystal structure of the single dinuclear double helicate unit* $[(\mathbf{L}^{1.15})_2Ag_2]^{2+}$.[40]

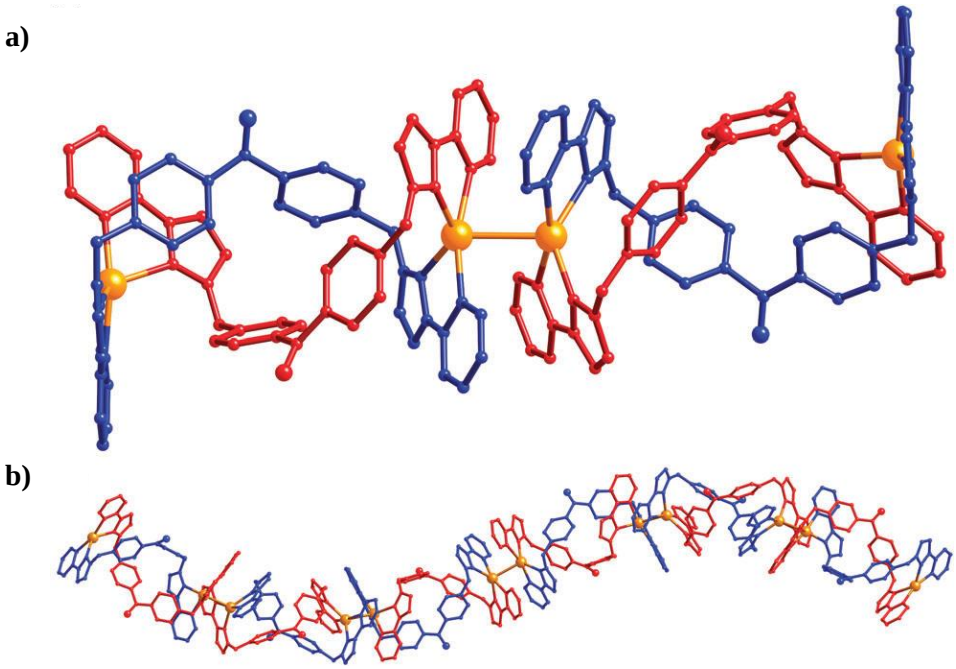

Figure 1.1.6. *Two different wire-frame views of the dinuclear double helicate polymer chain where each chain is coloured red or blue for clarity. a)* $[(\mathbf{L}^{1.15})_2Ag_2]_2^{4+}$ *b)* $[(\mathbf{L}^{1.15})_2Ag_2]_6^{12+}$.[40]

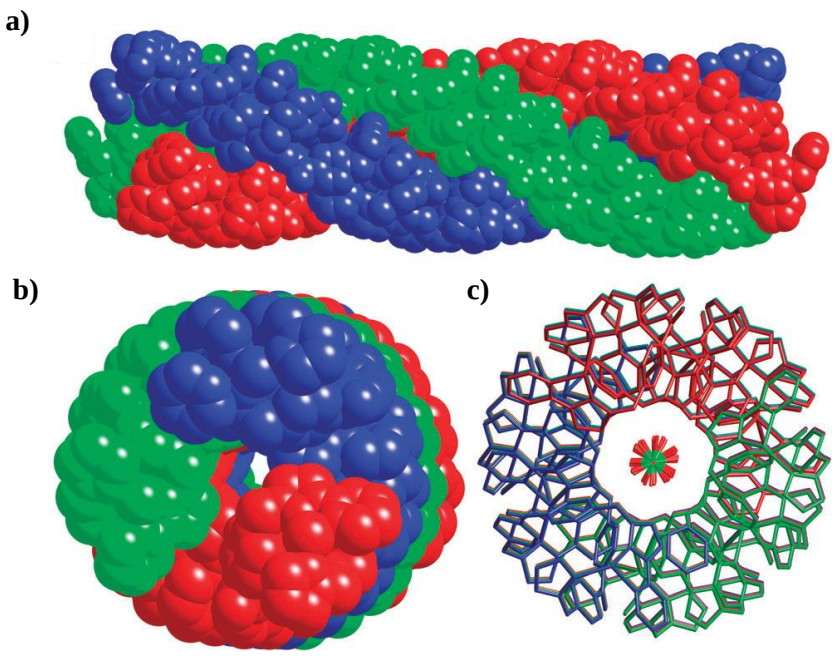

Figure 1.1.7. *Three different views of the triple helical array where each of dinuclear double helicate polymer strands are coloured differently for clarity a), b) Space-filling view, c) Wire-frame end-on view displaying the molecules central ClO_4^- containing channel.*[40]

Another well-known type of metallosupramolecular assembly is the circular helicate. This is similar to the structure of a linear helicate in that a ligand is used that contains two remote binding sites each of which coordinated a different metal ion. However, whist retaining the "over-and-under" ligand geometry these are cyclic oligomers of the formula $[M_n(L)_n]^{x+}$ (n > 2). However, the formation of the cyclic helicate, is less well understood than the linear counterpart. One of the issues in the formation of cyclic helicates is that the self-assembly rules that apply to helicate formation, i.e. using a ligand that contains two distinct binding domains that coordinate different metal ions, applies to the formation of cyclic helicates. One problem with cyclic helicate formation is that the linear form is entropically favoured and to stop this forming some form of interaction (either attractive or repulsive) has to be employed. This can take the form of templating by anions or by attractive/favourable intramolecular interactions which forms of the cyclic species relative to its linear alternative.[24,35,41,42]

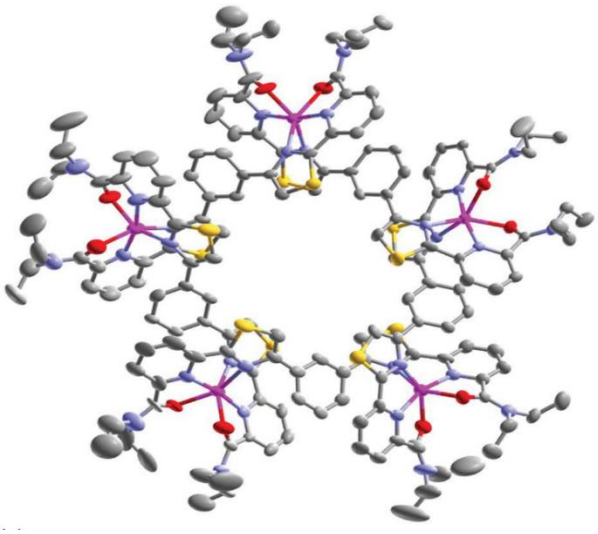

Figure 1.1.8. *Pentanuclear circular helicate* $[(\mathbf{L}^{1.16})_5Zn_5]^{10+}$.[43]

The research laboratory of Rice and co-workers has reported several different examples of the formation of circular helicate assemblies. A 2010 study by this group demonstrated how a collection of three different 1, 3-disubstituted phenyl centred ligand strands could be reacted with Cu(II) ions to produce a series of different pentanuclear circular helicates. The ligand strands themselves compromised of one *bis*-tridentate thiazole-bipyridene strand $\mathbf{L}^{1.170}$, one *bis*-bidentate thiazole-pyridyl strand $\mathbf{L}^{1.171}$ and one unsymmetrical multidentate ligand which comprised of one tridentate thiazole-bipyridyl domain as well as one bidentate thiazole-pyridyl domain $\mathbf{L}^{1.172}$. Firstly, it was observed that when $\mathbf{L}^{1.172}$ was reacted with Cu(II) in a 1:1 ratio a *head-to-tail* pentanuclear circular helicate was produced. In this structure each of the metal centres formed five N-donor coordination bonds from the ligand strands (1.936(9) – 2.327(9) Å). This binding configuration arose from a tridentate thiazole-bipyridyl unit from one ligand strand and a bidentate thiazole-pyridyl unit from a different ligand to yield the *head-to-tail* motif (Fig. 1.1.9.) a). Secondly, a 1:1 mixture of $\mathbf{L}^{1.170}$ and $\mathbf{L}^{1.171}$ was reacted with Cu(II) ions (1:1). Interestingly, this gave a pentanuclear heteroleptic circular helicate complex (Fig. 1.1.9. b, c). In this structure the metal centres retained the five-coordinate geometry as seen in the previous example but it was formed from coordination of different bidentate and a tridentate ligands, forming a homoleptic assembly.[44]

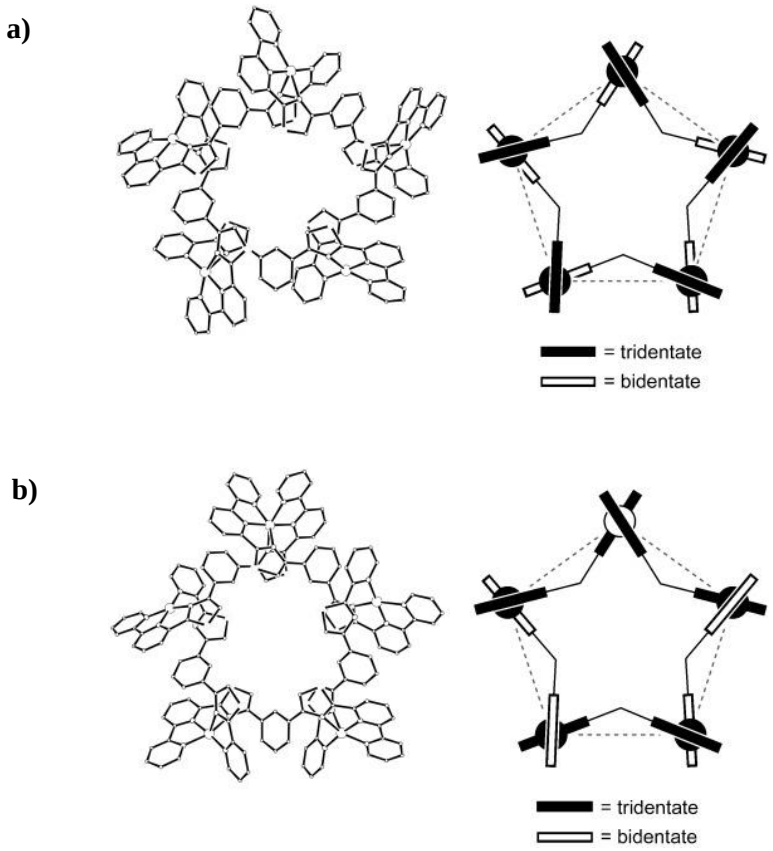

Figure 1.1.9. *a) Head-to-tail pentanuclear circular helicate* $[(\mathbf{L}^{1.172})_5Cu_5]^{10+}$ *b) Heteroleptic mixed ligand pentanuclear circular helicate.* $[(\mathbf{L}^{1.170})_3(\mathbf{L}^{1.171})_2Cu_5]^{10+}$*, c) Space filling view of the crystal structure of the heteroleptic mixed ligand pentanuclear circular helicate* $[(\mathbf{L}^{1.170})_3(\mathbf{L}^{1.171})_2Cu_5]^{10+}$*.*[44]

In recent work (2013) from Ward *et al*, a highly unusual example of a heterometallic cyclic helicate architecture has been produced.[45] Described by this study was the synthesis of an unsymmetrical heteroleptic catecholate pyrazolyl-pyridine based ligand ($\mathbf{L}^{\mathbf{1.18}}$) which was then reacted with a mixture of Zn(II) and Ti(IV) salts in a methanol/triethylamine solvent mixture. This resulted in the formation of the octanuclear circular helicate assembly $[(\mathbf{L}^{\mathbf{1.18}})_8(\mu\text{-OMe})_8Zn_4Ti_4]$ (Fig. 1.1.10.). The resulting mixed metal structure can be broken down into a collection of four separate dinuclear double helicates of the form $\{(\mathbf{L}^{\mathbf{1.18}})_2(\mu\text{-OMe})_4ZnTi\}$. Each of these two ligands adopt a head-to-tail arrangement whereby the catecholate domains fully deprotonate and coordinate a single Ti(IV) metal ion (1.924(6) – 2.031(6) Å) while the pyrazolyl-pyridine domain coordinate a single Zn(II) metal ion (2.094(6) – 2.207(5) Å) (Fig. 1.1.11.). This coordination geometry is further supplemented by the interaction of each metal centre with a pair of methoxide bridging molecules. This assembly is controlled via the hardness of the two binding domains; with the Ti(IV) coordinated via the hard ArO^- domains and the Zn(II) coordinated buy the relatively softer *N*-donor domains. This combination of interactions leads to four of these dinuclear fragments being held together in the resulting square cyclic array.

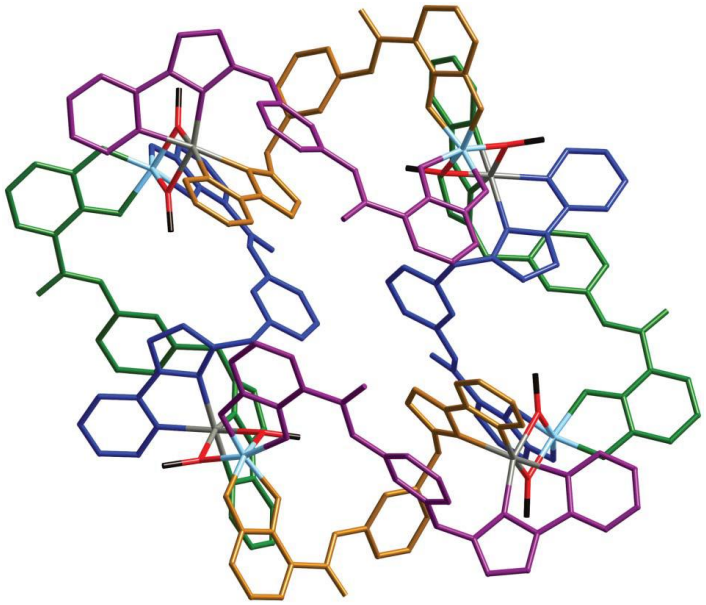

Figure 1.1.10. *Crystal structure wire frame view of the mixed metal octanuclear circular helicate* $[(\boldsymbol{L}^{\boldsymbol{1.18}})_8(\mu\text{-}OMe)_8Zn_4Ti_4]$.[45]

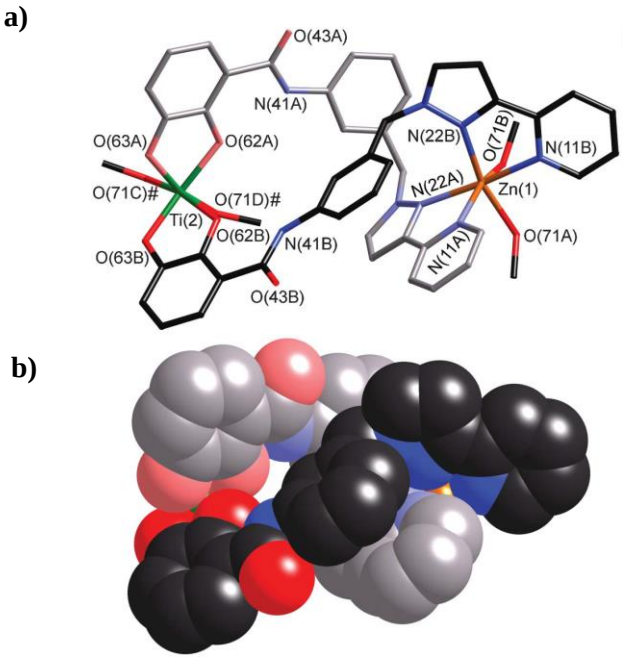

Figure 1.1.11. *Crystal structure of the dinuclear double helicate fragment {($L^{1.18}$)$_2$(μ-OMe)$_4$ZnTi} a) wireframe view, b) space filling view.*[45]

1.2 Anion binding

Due to their vital role in both biological and ecological systems, the sensing of anions and selectively sequestering them is a highly important area of chemical research. As a result, the interests concerning the ability of a system to interact and bind anionic guest molecules has become a vast area of research for chemists over recent decades. For example, by careful considerations in both the molecular design and structure of a host molecule, systems can be functionalised to undergo processes such as sensing and/or the sequestering of anionic species, anion transportation (lipid layers), catalytic processes as well as aiding the formation of interesting molecular assemblies.[46–50] There have been many reported examples of organic molecules that have been synthesised that can act as anion hosts. These compounds generally contain one or more hydrogen bond donor groups (amines, amides, phenols and carboxylic acids amongst others) which are arranged in a convergent manner so that they act as a host to anionic guests.[46,51–54]

One such example, by Wu and co-workers, illustrates how phosphate anions can be encapsulated using a series of ortho-phenylene linked tris-urea based ligands $\mathbf{L}^{1.21}$ (Fig. 1.2.1). It was observed that these ligands had a high affinity for both sulphate and phosphate anions, with phosphate been the greatest of the two. Examination of the $\mathbf{L}^{1.21}$ phosphate containing crystal structure confirmed the inclusion of the fully deprotonated PO_4^{3-} anion within the 2:1 $[(\mathbf{L}^{1.21})_2\ PO_4]^{3-}$ complex, where the central guest anion received a total of 12 hydrogen bonding interactions from the ligand's urea hydrogen atoms (N···O 2.871(6) - 2.986(6) Å). Further investigation and structural analysis were performed on a similar system which incorporated a mixed urea/thiourea based ligand ($\mathbf{L}^{1.22}$) together with phosphate. However, in this example the assembly was observed to adopt a different 2:2 $[(\mathbf{L}^{1.22})_2(HPO_4)(H_2PO_4)]^{3-}$ complex (N···O 2.916 Å, (O···O 2.469(6) – 2.579(5) Å)). Interestingly, ligand $\mathbf{L}^{1.23}$ (thiourea only) was not seen to produce an anion containing complex with basic anions and the addition of phosphate to this system only resulted in deprotonation of the ligand thiourea units.[55]

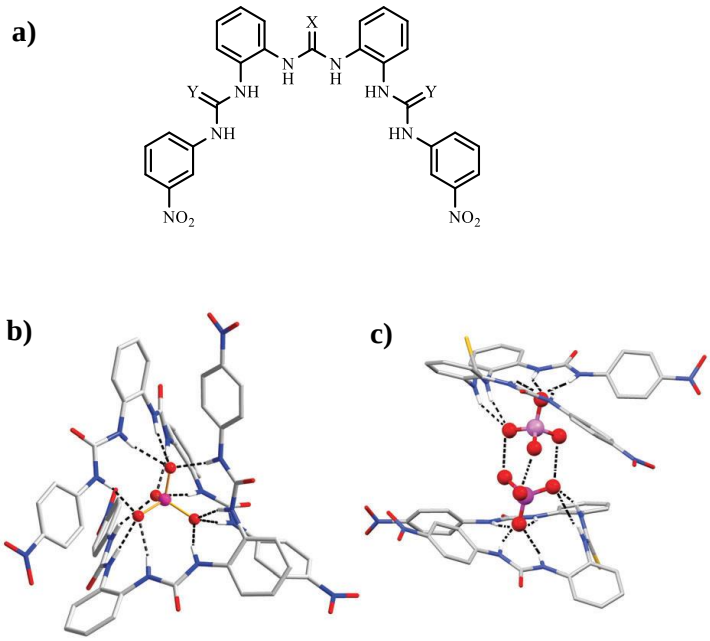

Figure 1.2.1. *a) Wu et. al. trisurea based anion receptor ligand where* $\boldsymbol{L}^{1.21}$ *X = Y = O,* $\boldsymbol{L}^{1.22}$ *X = S, Y = O and* $\boldsymbol{L}^{1.23}$ *X = Y = S b) crystal structure of the* $[(\boldsymbol{L}^{1.21})_2PO_4]^{3-}$ *complex c) crystal structure of the* $[(\boldsymbol{L}^{1.22})_2(HPO_4)(H_2PO_4)]^{3-}$ *complex.*[55]

Cryptand type molecules have historically been employed as anion binding hosts.[50] From the early work of Park and Simmons[56,57] in their development of halide binding diazobicyclic kanapinand system as well as that of Lehn and co-worker's[58,59] development of polyether and polyaza cryptands (known as 0-bistren) in binding studies with halides as well as poly-atomic anions such as azide.

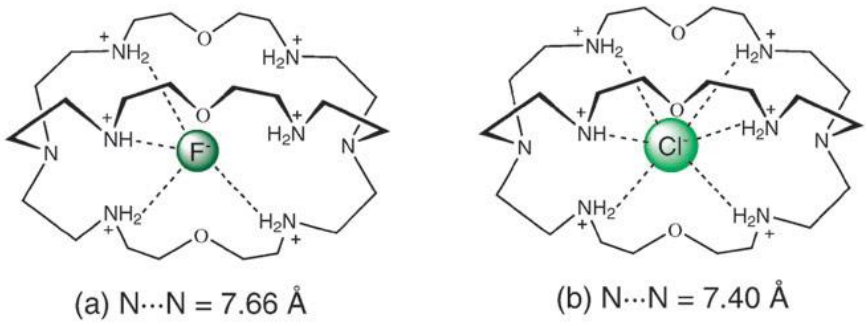

Figure 1.2.2. *Structural representation of Lehn and co-workers O-bistren halide complexes.*[50]

Displaying strong similarities to their cationic metal binding counterparts, this type of anion host molecule has an internally sited binding cavity. The guest anions are held within the cavity mostly via multiple -NH_2^+···anion hydrogen bonding interactions and the selectivity of these systems is dependent on how well the guest species shape/size fits the hosts internal cavity. The main drawback with this type of system is that they are generally very sensitive to pH changes and the initial synthesis required to produce the host molecule can be challenging.

Work undertaken by Fletcher *et. al.* investigated the strength of anion binding towards inert dirhenium(I) complexes.[60] In this study a series of thiourea containing bis-2,2'-bypyridine ligands were synthesised, namely ligand **L**$^{1.24}$, and reacted to give the bis(*fac*-tricarbonylrhenium(I)) complexes (Fig. 1.2.3.). ^{1}H NMR studies confirmed that the complexes underwent binding of both acetate and dihydrogen phosphate anions. Further investigations via UV-Vis and emission spectra showed that the simple single thiourea bridged bis-2,2'-bypyridine ligand showed a high level of selectivity towards the dihydrogen phosphate anion. In fact, it was concluded that this complex had an affinity to bind two dihydrogen phosphate anions via O···HO

hydrogen bonding interactions between the anions themselves as well as the carbonyl groups on the rhenium metal centres. Interestingly, it was proposed that the binding of this second dihydrogen phosphate anion increased the binding strength of the first adduct.

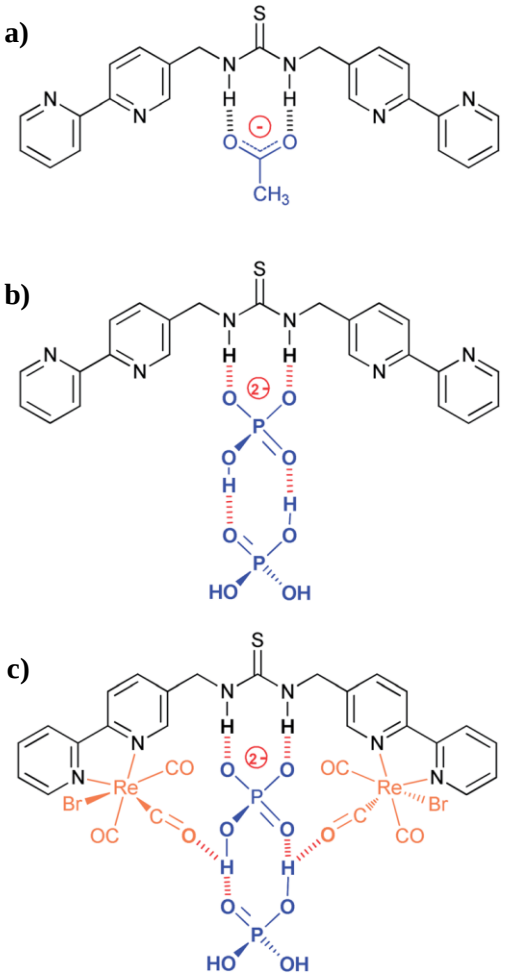

Figure 1.2.3. *Three binging modes of the dimethylene thiourea bridged 2, 2'-bipyridine ligand. a) [**L**$^{1.24}$(O$_2$CMe)$^-$, b) [**L**$^{1.24}$(H$_2$PO$_4$)$_2$]$^{2-}$, c) [**L**$^{1.24}$Re$_2$(CO)$_6$Br$_2$(H$_2$PO$_4$)$_2$]$^{2-}$.*[60]

1.3 Self-assembled metal complexes as anion receptors

The use of self-assembled metallic complexes as anion binding hosts has become a major area of interest for the supramolecular chemist.

Metallo-helicate assemblies offer good potential to act as anion host molecules. In many examples, the nature in which these architectures are formed is that a central cavity develops within the molecules structure that can accommodate an anion guest molecule (Fig 1.3.1.).

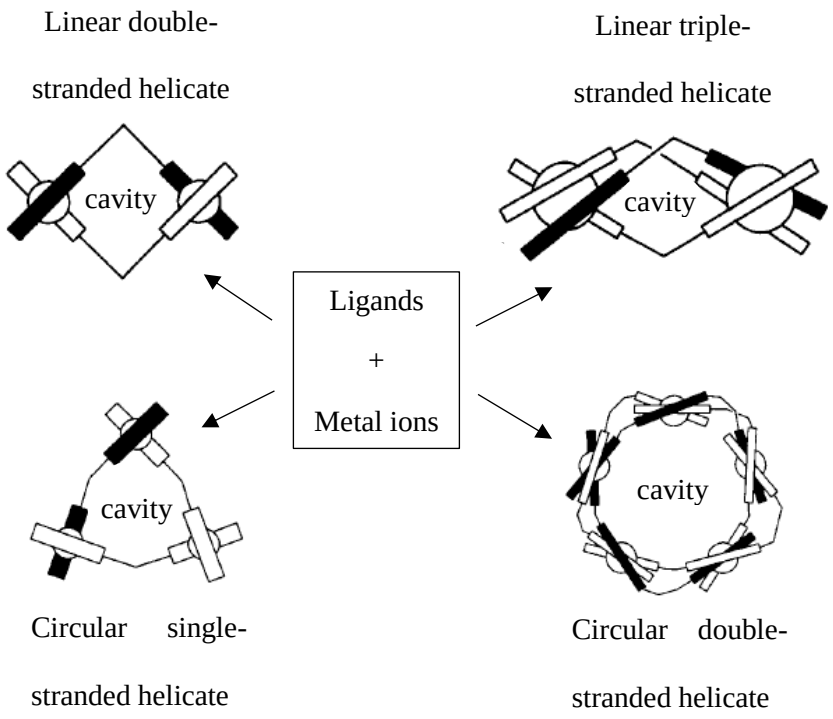

Figure 1.3.1. I*llustration of four different helicate type assemblies and their internal central cavity.*[61]

In a study by Cronin *et. al.* a bis bipyridine ligand bridged by a dimethyl imidazole spacer unit (**L**$^{1.31}$) was synthesised and reacted with Fe(II) metal ions to produce a dinuclear triple helicate complex. This dinuclear complex featured a central cavity that was capable of the encapsulation of anions. In this study it was found that the resulting $\{L_3M_2\}$ type architecture could interchange between a traditional *S*-type helicate and a *C*-

type mesocate motif. This rearrangement was a result of the interaction between the ligand's imidazole spacer unit and the guest anion that was included within the complexes central cavity. It was found that spherical and trigonal planar anionic species yielded the formation of the helicate and larger tetrahedral anions influenced an expansion of the central cavity to yield the formation of the mesocate.[62]

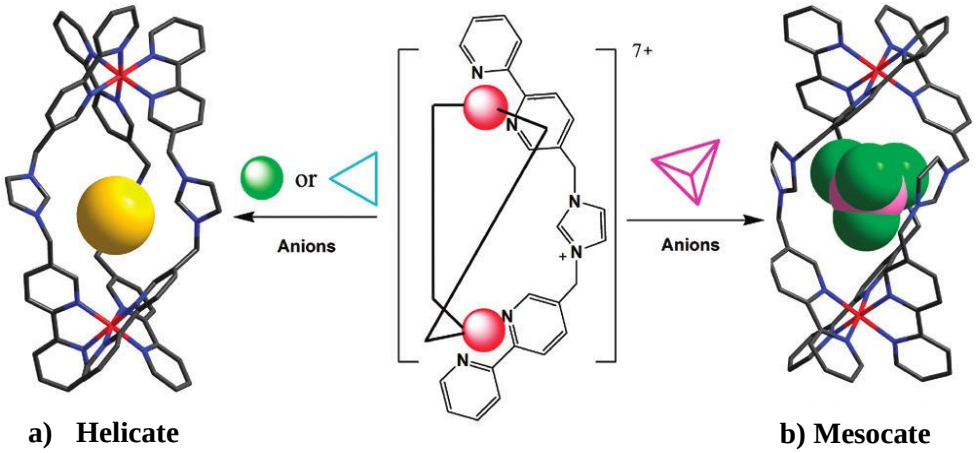

Figure 1.3.2. *Two crystal structures from the mentioned work of Cronin et. al. Where, a) the addition of spherical or trigonal anions to the system yields a dinuclear triple helicate and b)the addition of lager tetrahedral anions to the system yields a dinuclear triple mesocate.*[62]

An interesting report by Leigh *et. al.* which used ^{1}H NMR titration experiments to probe the affinity of previously reported multinuclear Fe(II) architectures to bind halide anions.[63] These included double (Solomon Link) and triple (Star of David) catenanes as well as a pentafoil knot (Fig 1.3.3). All the three host structures produced different sized central cavities that were observed to bind a single halide anion via a combination of -CH···A^{-} hydrogen bonding interactions and long-range Fe···A^{-} electrostatic interactions. Halide anions included chloride, bromide and iodide, where the Solomon linked catenane (Fig 1.3.3a) was found to bind all three anions with both chloride and bromide being the most preferred (Cl^{-}, K_1 = (3.0 ± 2.5) × 10^{8} M^{-1}; Br^{-}, K_1 = (1.0 ± 0.5) × 10^{7} M^{-1}). Whilst this is a strong interaction it is several orders of

magnitude weaker than that seen for the smaller cavity of the pentafoil knot (Fig 1.3.3b) (Cl^-, K_1 = (3.6 ± 0.2) × 10^{10} M^{-1}; Br^-, K_1 = (1.7 ± 0.5) × 10^{10} M^{-1}). The larger cavity of the Star of David catenane (Fig 1.3.3c) was only found to show a preference for the larger iodide anion (I^-, K_1 = (1.2 ± 0.1) × 10^4 M^{-1}) but this was comparably weaker than that seen in the previous Solomon linked catenane anion (I^-, K_1 = (2.1 ± 0.2) × 10^5 M^{-1}) and the pentafoil knot (I^-, K_1 = (5.8 ± 1.3) × 10^5 M^{-1}). This work successfully illustrates that complex linked and knotted structures, produced from circular metal double helicates can bind anions. Interestingly, examples such as the pentafoil knot showed the strongest reported affinity towards the chloride anion, being comparable to that of silver salts.

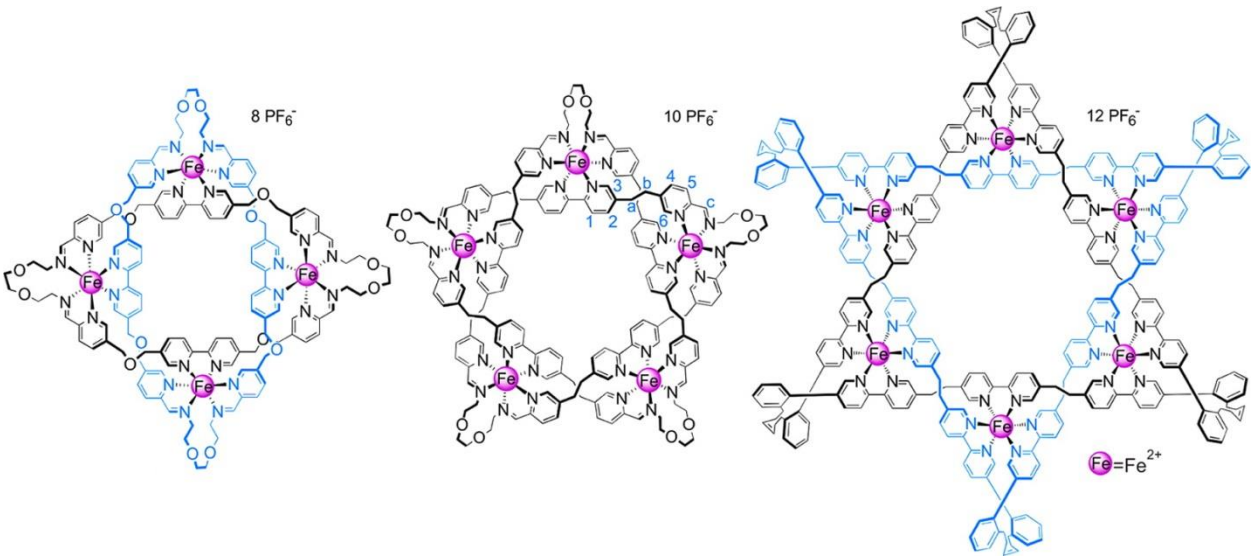

a) **b)** **c)**

Figure 1.3.3. *Series of Fe(II) assembled halide host molecules a) Solomon Linked catenane, b) Pentafoil knot, c) Star of David catenane.*[63]

Whilst some excellent examples of anion host/sensors have been produced in the last 10 years, and the chemist's ability to recognise anions has significantly advanced. However, there are some limitations in this field of chemistry as many receptors are complex to prepare, require multi-step synthesis and are generally limited to non-aqueous environments, Furthermore, most anion receptors only work in non-aqueous environemts and there are only a limited number of reported examples of receptors that recognize

anions in water. Clearly this limits the ability of these systems to be practically useful as in the vast majority of scenarios such as anion recognition/sensing/sequestering will involve aqueous systems. One method to circumvent complex synthetic procedures is to generate anion receptors from self-assembly, where the receptor is not synthesized in the conventional sense but is rather assembled in solution, generating a complex architecture from smaller pre-programmed chemical fragments.[5,6] Using this functionality large and complex systems that contain a multitude of species (e.g. –NH, -CONH, -OH, M^{n+} etc) capable of interaction with anions can be included within a small molecule which upon self-assembly generates a large complex molecule negating the need for complex synthetic procedures. As a consequence, the possibilities of anion encapsulation by self-assembled cationic cage type assemblies has become a rapidly growing area of interest for the supramolecular chemist.

A good example of this type of behaviour has been demonstrated by a recent review by Custelcean highlighting the effectiveness of these assemblies in capturing anionic molecules.[64] In one such study, Custelcean *et. al.* synthesised a urea functionalised bis-bipyridine ligand (**L**$^{1.320}$) that was capable of encapsulating high charge density oxo-anions from aqueous methanol solvent systems. When this ligand was reacted with Ni^{2+} or Zn^{2+} in the presence of a tetrahedral anion EO_4^{n-} (where E = P, Cr, S, Se, Mo and W) a M_4L_6 tetranuclear cage was observed to have formed (Fig. 1.3.4, Fig. 1.3.5).

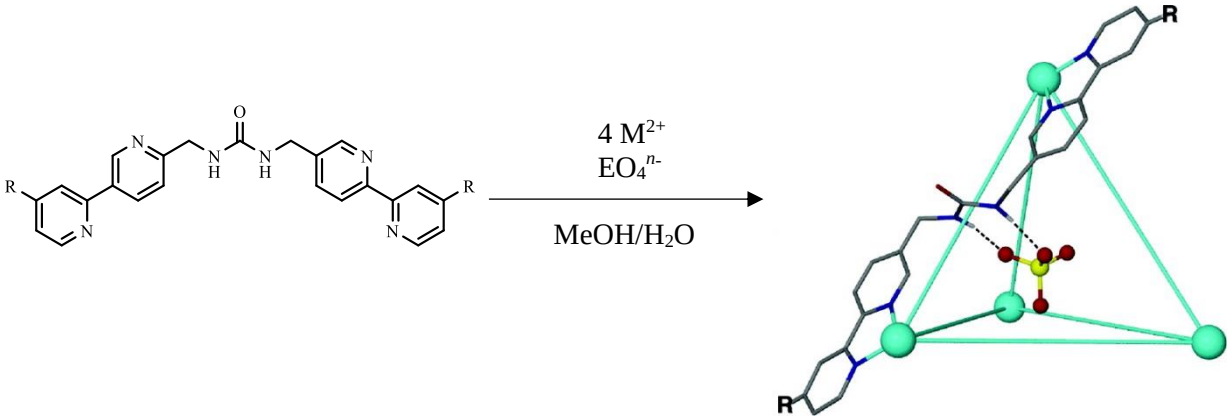

Figure 1.3.4. *a) Schematic of the reaction of* ***L***$^{1.320}$ *to form the {L₆M₄(EO₄)} cage assembly where R = H, tBu; M = Zn, Ni; E = S, Se, Mo, W, Cr (n = 2) and P (n = 3).*[65]

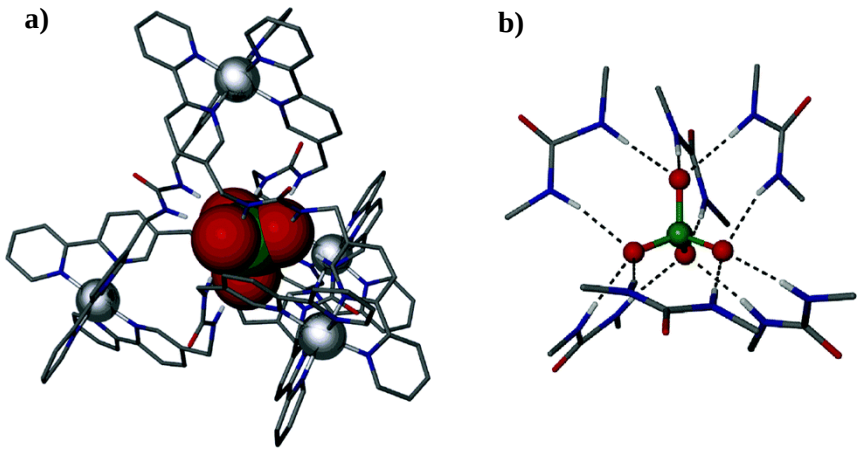

Figure 1.3.5. *a) Crystal structure of the {$L_6M_4(EO_4)$} cage assembly (selected atoms omitted for clarity) and c) b) view of the anion/urea interactions of the {$L_6M_4(EO_4)$} cage assembly(selected atoms omitted for clarity)*[65]

The self-assembled M_4L_6 tetranuclear cage contains a total of six urea functional groups that can point inwards to a central cavity and contained within this is an oxo-anion. The anion is held within the structure by a total of twelve –NH···A hydrogen bonding interaction from the ligands inward facing urea units (NH···O 2.04 – 2.08 Å). ^{77}Se NMR spectroscopy was used to access the selectivity trend of the complex towards these anions, this showed it to be PO_4^{3-} >> CrO_4^{2-} > SO_4^{2-} > SeO_4^{2-} > MoO_4^{2-} > WO_4^{2-}. This selectivity profile was attributed to a combination of the charge, size, basicity, hydration and hydrogen bond acceptor characteristics of the anion. It is worth noting that in this example, the formation of the M_4L_6 motif was dependant on the templating effects of the shape of the anion and the self-assembly is a result of the anion rather than self-assembly of an anion binding species.[65]

In a different study, Custelcean *et. al.* employed a different method of encapsulating oxo-anions from aqueous solutions using a potentially tripodal tris(2-aminoethyl)amine (tren) based ligand (Fig. 1.3.6). This tripodal motif featured three separate amide urea groups which are well known to interact strongly with oxo-anions such as phosphate or sulfate.[66] It was observed that upon reaction of this ligand (**L**$^{1.321}$) with Ag_2SO_4 in aqueous acetone, the SO_4^{2-} anion became encapsulated by two separate ligand strands. In the solid state, each ligand was seen to donate six hydrogen bonding interactions via there three urea amide protons to give a total of twelve interactions

to the encapsulated SO_4^{2-} molecule (NH···O 2.14 – 2.23 Å). Whilst the Ag(I) metal ions were observed to form coordination bonds to the ligand's amide oxygen atom as well as the nitrogen atom of the ligands Ar-CN substituents. This facilitated the capsule to assemble into a one-dimensional coordination polymer of the type $[(\mathbf{L}^{1.321})_2(SO_4)Ag_2]_n$ in the solid state (Fig 1.3.7 c).[67]

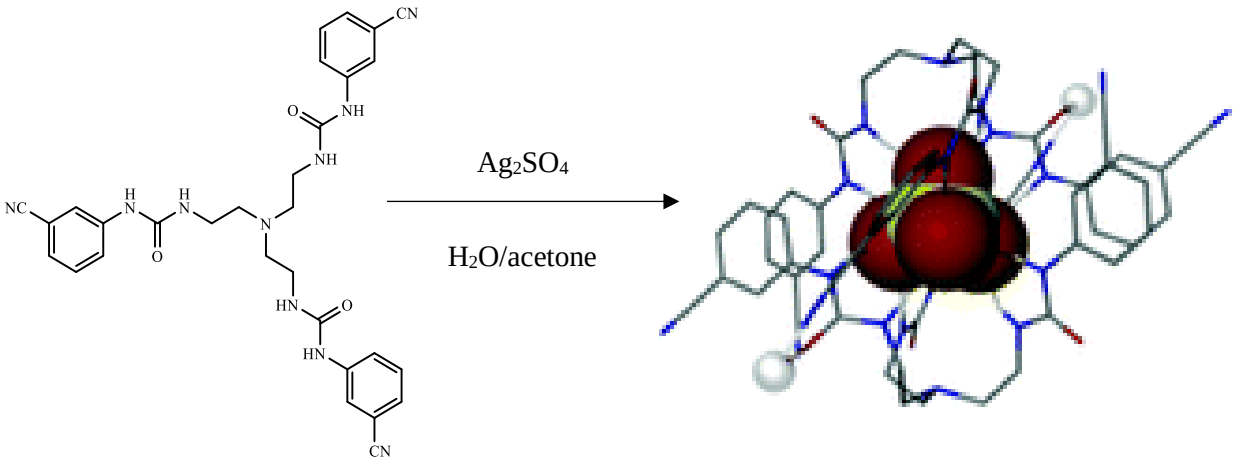

Figure 1.3.6. *Schematic of the reaction of* $\boldsymbol{L}^{1.321}$ *to form the* $[(\boldsymbol{L}^{1.321})_2(SO_4)Ag_2]$ *anion capsule assembly.*[67]

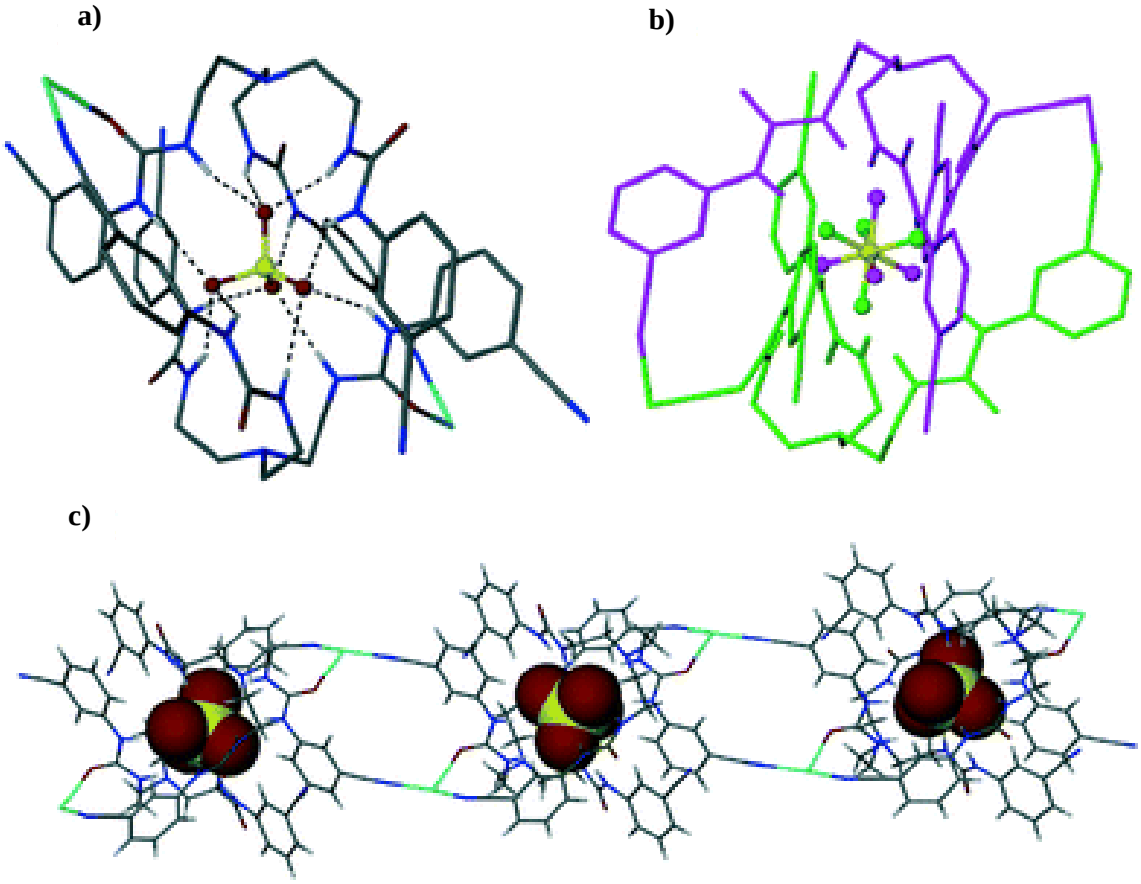

Figure 1.3.7. *a) Crystal structure of the [(**L**$^{1.321}$)$_2$(SO$_4$)Ag$_2$] anion capsule assembly (dashed lines showing the twelve anion/urea hydrogen bonding interactions), b) Crystal structure of the [(**L**$^{1.321}$)$_2$(SO$_4$)Ag$_2$] anion capsule assembly where each of the two ligands are individually highlighted and the disorder of the encapsulated SO_4^{2-} molecule is shown, c) Crystal structure of the [(**L**$^{1.321}$)$_2$(SO$_4$)Ag$_2$]$_n$ anion capsule 1D coordination polymer assembly with respective CN···Ag coordination bonds. Selected atoms omitted for clarity.*[67]

A different study using a second tripoidal ligand of very similar structure to that described above but containing a pyridyl rather than phenyl substituent was employed (**L**$^{1.322}$). This system was used to investigate the potential of removal of SO_4^{2-} anions in the remediation processes associated with contaminated water from nuclear waste (Fig. 1.3.8). In this study, no additional metal ions were used (e.g. Ag(I)), instead this system was selectively precipitated from the solution using only the available metal ions that were present e.g. $M_2SO_4 \cdot XH_2O$ (where M^+ = Na, K) and $MSO_4 \cdot XH_2O$ (M^{2+} = Ca, Mg). It was observed that in the solid state the anions form hydrogen bonding interaction to the urea functional groups on the

ligand chain. This interaction is supplemented by hydrogen bonding interaction between the pyridyl nitrogen atom and the coordinated water molecules on the hydrated metal cation. All these interactions (e.g. urea···anion and -C_5H_4N···H_2O-M^{n+}) resulted in a polymeric array and resulted in precipitation of the $M_2SO_4 \cdot XH_2O$ (where M = Na, K) and $MSO_4 \cdot XH_2O$ (M = Ca, Mg, Cd) salts upon addition of the ditopic host. The conclusions gained from this work were such that the system performed exceptionally under the harsh, basic (~ pH 14) and high ionic strength conditions that are common to this type of application.[68]

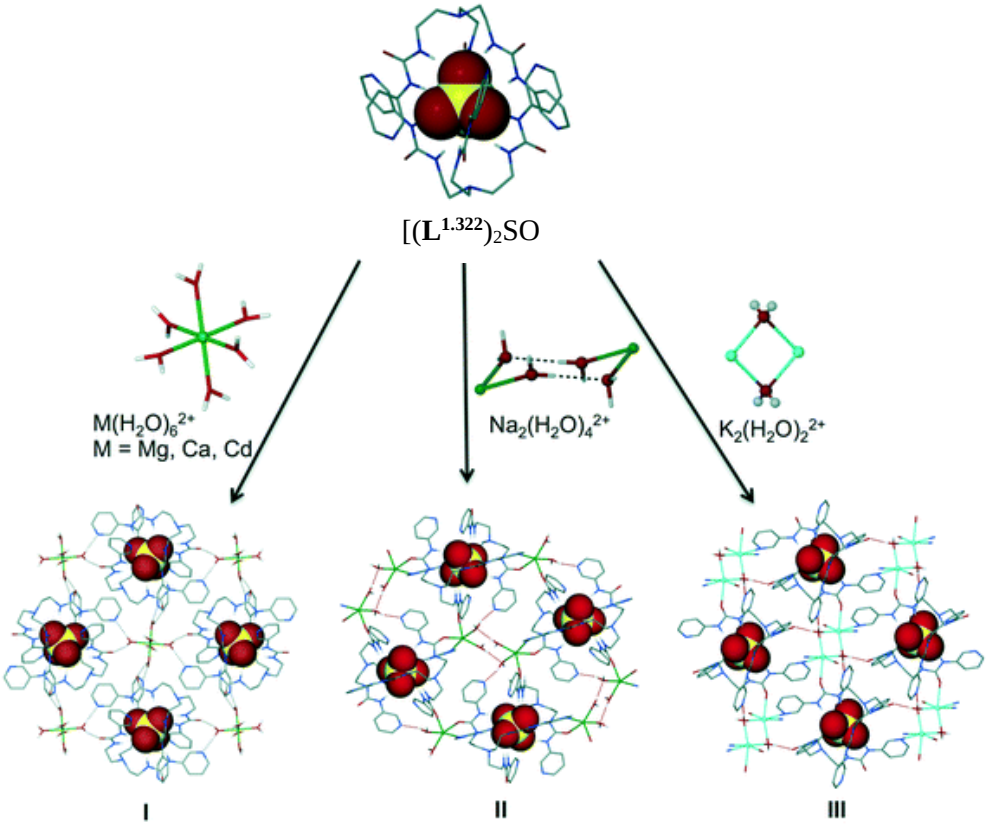

Figure 1.3.8. *Diagram illustrating the solid-state crystallisation products of the Custelcean et. al. TREN based SO_4^{2-} capsule with a) $[Mg(H_2O)_6]^{2+}$, $[Ca(H_2O)_6]^{2+}$, $[Cd(H_2O)_6]^{2+}$ b) $Na_2(H_2O)_4]^{2+}$ c) $K_2(H_2O)_4]^{2+}$.*[68]

The group of Ward and co-workers have produced various examples which feature the formation of self-assembled anion encapsulating cages of the type $[M_4L_6]^{n+}$. In the most part these studies involved the synthesis of different bis-pyrazolyl-pyridine ligands with various methylene linked aromatic spacer units (Fig. 1.3.9.). It was found that when this type of ligand species was reacted with metal salts (e.g. Co(II), Zn (II), Cd(II)) a $[M_4L_6]^{n+}$ tetragonal type cage was formed that featured an internal central cavity which was in turn occupied by an anion guest. In all these examples the encapsulate anion species was bound within the complex's central cavity via multiple hydrogen bonding interaction between the anion and the ligands inward facing methylene ($-CH_2-$) protons. In this work it was demonstrated that the formation of the cage was independent of the anion and therefore did not rely on formation mechanisms that involved guest species templating effects. Each of the ligands that were produced formed a different size/shaped central cavity which was dependant on the size/shape of the ligand's central spacer unit. As a result, the selectivity of all the produced cage assemblies was attributed to both the shape and size of the anion and how this matched the central cavity of the complex. ^{11}B and ^{19}F NMR studies were undertaken on each of the assemblies which also supported the previously observed selectivity.[69–74]

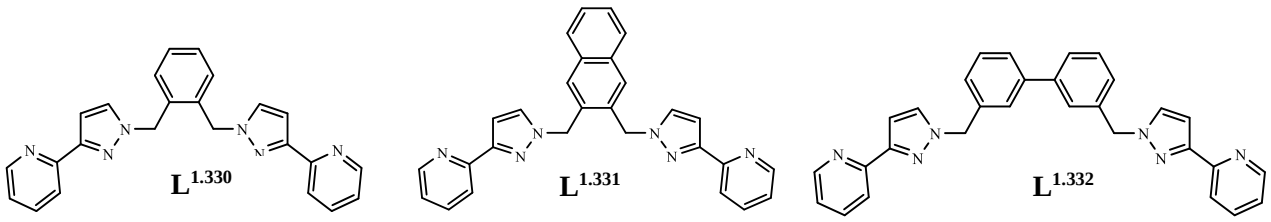

Figure 1.3.9. *Bis-pyrazolyl-pyridine ligands* ***L***$^{1.330}$, ***L***$^{1.331}$, *and* ***L***$^{1.332}$ *synthesised by Ward et. al.*[64]

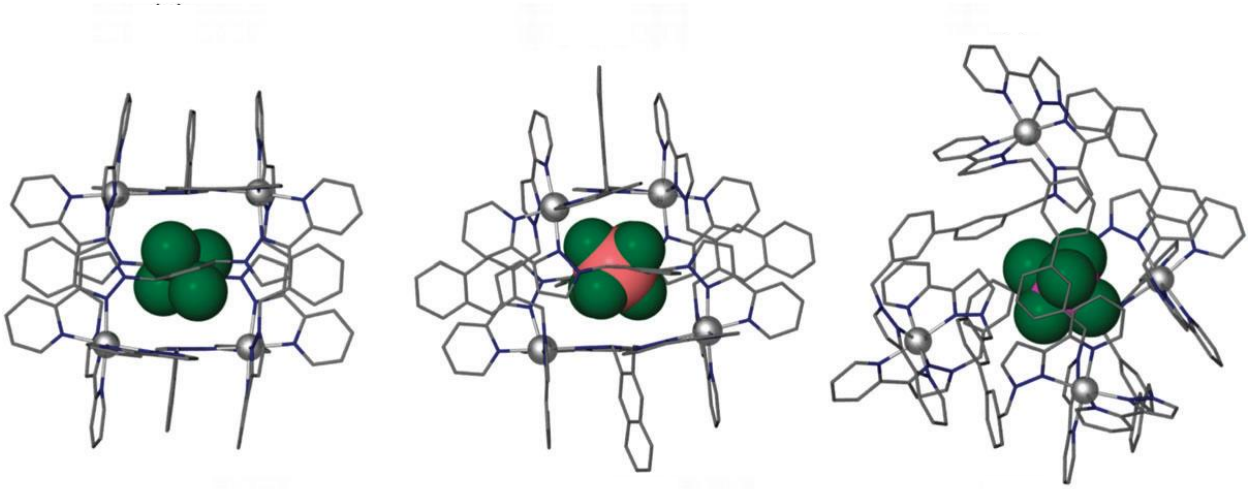

(a) (b) (c)

Figure 1.3.10. *Crystal structures of Ward et. al. {L_6M_4} cages, a) $\mathbf{L^{1.330}}$ and BF_4^-, b) $\mathbf{L^{1.331}}$ and SiF_6^{2-}, c) $\mathbf{L^{1.332}}$ and PF_6^-.*[64]

For example, the ligand $\mathbf{L^{1.330}}$ which contains a 1,2-phenylene spacer forms the $[(\mathbf{L^{1.330}})_6Co_4]^{8+}$ assembly and inside the central cavity is a ClO_4^- anion. Whereas the ligand containing the larger 3,3'-disubstituted-2,2'-diphenylene spacer forms $[(\mathbf{L^{1.331}})_6Co_4]^{8+}$ which acts as a host to the larger PF_6^- anion.[69,70] Ward *et. al.* has since gone onto use this building block for the self-assembly of a large number of different host cavities, some of which contain neutral guests including nerve agent mimics.[75–80]

One such example of anion binding has been demonstrated within the Rice *et. al.* laboratory (Fig. 1.3.11.). In this system, the reaction of the bis-bidentate ligand $\mathbf{L^{1.340}}$ with Co^{2+} resulted in the formation of a dinuclear triple helicate e.g. $[(\mathbf{L^{1.340}})_3Co_2]^{4+}$. However, the ligand also contains amide "arms" at each end of the ligand strands and the self-assembly of the helicate structure, in turn, produces two cavities that contain three –NH hydrogen bond donor units, which in this example, are ideally suited to bind perchlorate anions.

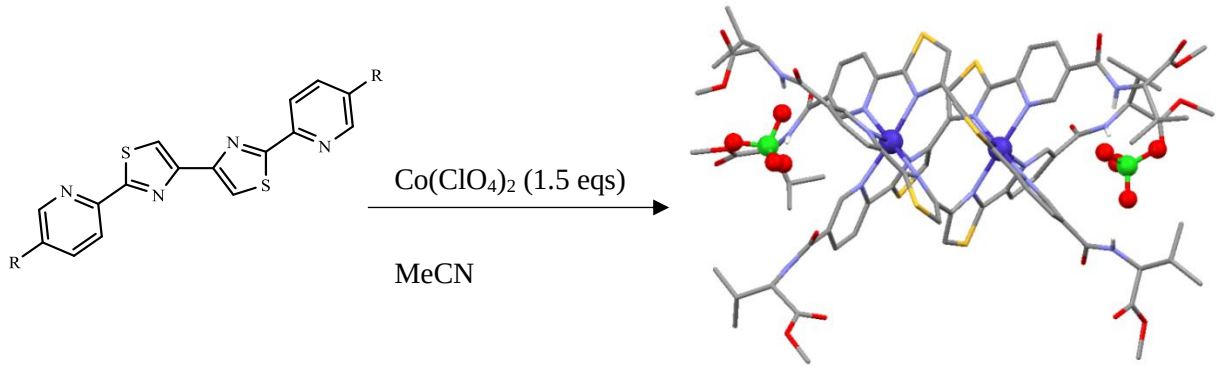

Figure 1.3.11. *Schematic of the reaction of Ligand* $\boldsymbol{L}^{1.340}$ *(where R = S CONHCH(CH(CH₃)₂)CO₂Me) with Co(II) perchlorate to give the dinuclear triple helicate showing the binding of perchlorate anions.*[81]

Reaction of $[(\mathbf{L}^{\mathbf{1.340}})_3Co_2(ClO_4)_2]^{2+}$ with two equivalents of NO_3- results in the "bound" perchlorates being displaced and a nitration anion forming hydrogen bonds to the three amide arms. Rice *et. al.* attributed the observed displacement of the perchlorate anion to the stronger hydrogen bonding interactions between the nitrate and amide units.[81]

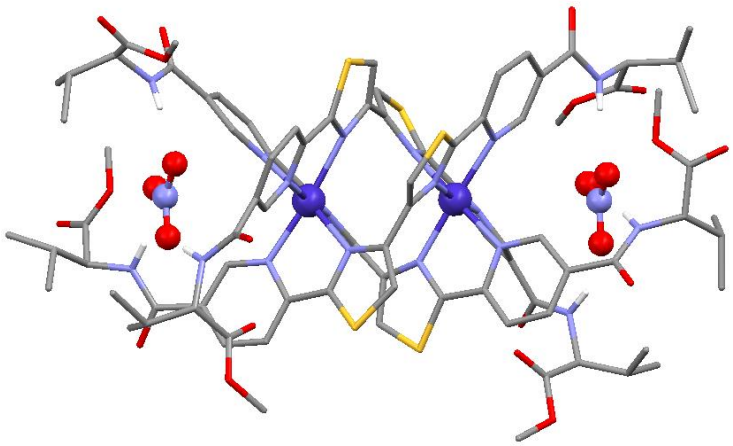

Figure 1.3.12. *Crystal structure of the* NO_3^- *containing dinuclear triple helicate assembly* $[(\boldsymbol{L}^{1.340})_3Co_2(NO_3)_2]^{2+}$*. Selected atoms omitted for clarity.*[81]

In a similar system ligand $\mathbf{L}^{\mathbf{1.341}}$ contains a tetradentate N-donor chain and contains an amide arm at the one end of the strand, making the ligand unsymmetrical. Reaction of this ligand with $Co(ClO_4)_2$ gives a dinuclear triple helicate e.g. $[(\mathbf{L}^{\mathbf{1.341}})_3Co_2]^{2+}$ but due to the unsymmetrical nature of the ligand this gives a mixture of isomers. As the ligand contains the amide substituent on only one of the pyridyl aromatic ring the ligand can be considered to have a "head" and a "tail" and as a result in the triple helicate complex "head-to-head-to-head" and "head-to-head-to-tail" isomers are present in a ratio of 1:3. However, upon addition of nitrate anions this distribution of isomers changes with only the "head-to-head-to-head" isomer present. This is attributed with the interaction of the amide hydrogen bond donors and the nitrate anions (which in the previous example are shown to interact strongly) which, as a result, orders the system.[82]

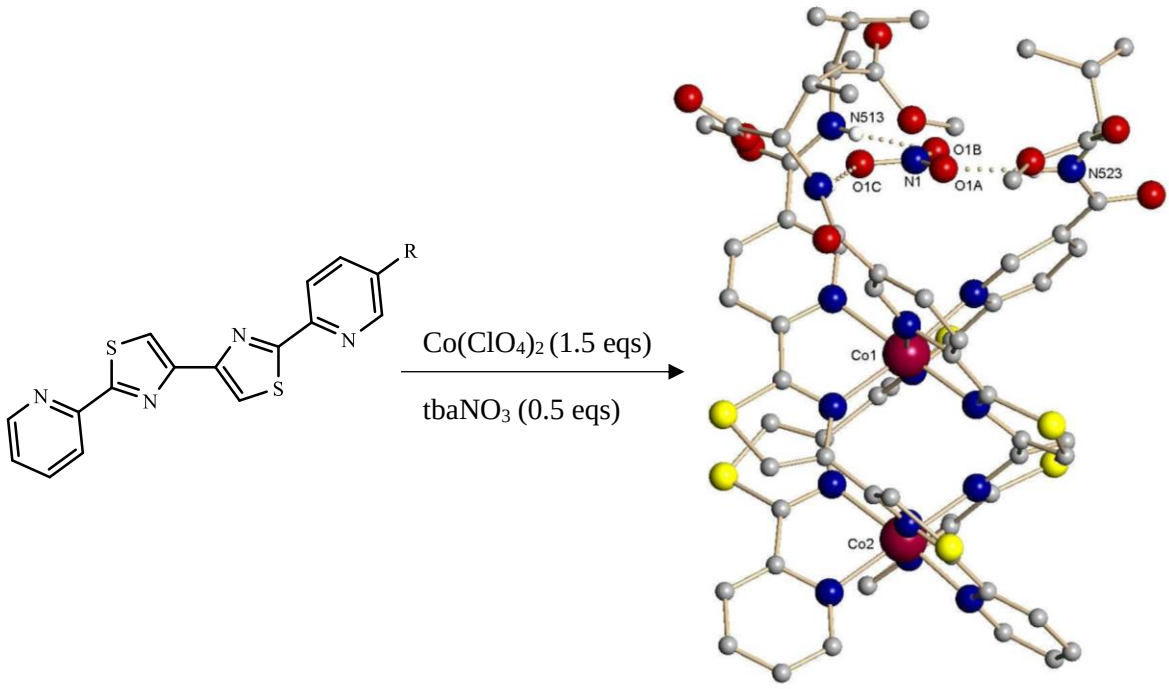

Figure 1.3.13. *Schematic of the reaction of* $\boldsymbol{L^{1.341}}$ *(where R = CONHCH(CH(CH₃)₂)CO₂Me) with Co(II) and* NO_3^- *to give the* NO_3^- *encapsulated HHH dinuclear triple helicate assembly.*[82]

In a 2014 publication by Rice *et. al.*, a ligand (**L**$^{1.342}$) featuring two thiazole-pyridyl units and two -NH hydrogen bond acceptor groups, partitioned by a 1,3-phenyl unit was synthesised (Fig. 1.3.14.). In this study, **L**$^{1.342}$ was reacted with Cu(II) ions together with a series of different anions in organic media. The solid-state structures of the resulting self-assembled complexes were analysed, and it was seen that the interactions between the ligands -NH units, and the included anion influenced both subtle and dramatic changes in the resulting structural geometry of the self-assembled complexes.[83]

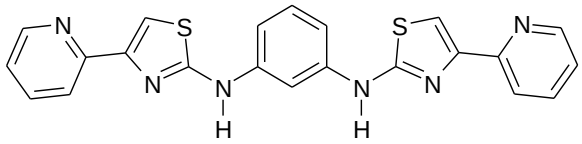

Figure 1.3.14. Ligand **L**^{1,342}

Firstly, **L**$^{1.342}$ was reacted with one equivalent of either Cu(II) perchlorate or Cu(II) tetrafluoroborate to produce a dinuclear double helicate (e.g. $[(\mathbf{L}^{1.342})_2Cu_2]^{4+}$). In this complex, each of the ligand's thiazole-pyridyl units partitioned into two separate bidentate binding domains which coordinate two separate Cu(II) metal ions to give four-coordinate metal centres (N···M 1.991(4) – 1.973(4) Å). This structural configuration resulted in the formation of a 'pocket' within the centre of the complex, which was seen to be occupied by a single anion to give $[(\mathbf{L}^{1.342})_2Cu_2A]^{3+}$ (where A is either perchlorate or tetrafluoroborate). This guest anion was observed to receive a total of four hydrogen bonding interactions from the complex arising from interaction between two -NH and two –Ar-H donors (one from each ligand, average distance of 2.847 Å) (Fig. 1.3.15.).

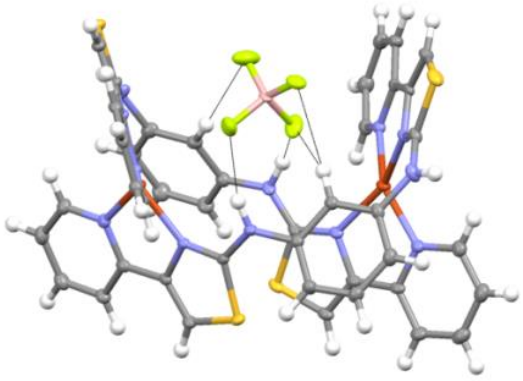

Figure 1.3.15. *Solid state structure of a) [(**L**^{1342})$_2$Cu$_2$](BF$_4$)$^{3+}$. Thermal ellipsoids shown at the 50% probability level and the remaining anions omitted for clarity.*[83]

However, when the [(**L**$^{1.342}$)$_2$Cu$_2$]$^{4+}$ complex was reacted with half a molar equivalent of dihydrogen phosphate, the dinuclear stoichiometry was retained. However, in this example the central pocket of the complex is occupied by a single phosphate anion, this forms both hydrogen bonding interactions to the ligands -NH units (average N···O of 2.745 Å), as well as bridging the two metal centres via a single O···Cu coordination bond (1.978(4) – 2.008(4) Å) to each Cu(II) metal ion to give an *unsaturated* dinuclear double helicate [(**L**$^{1.342}$)$_2$Cu$_2$(OPO$_3$H$_2$)]$^{3+}$. (Fig. 1.3.16.)

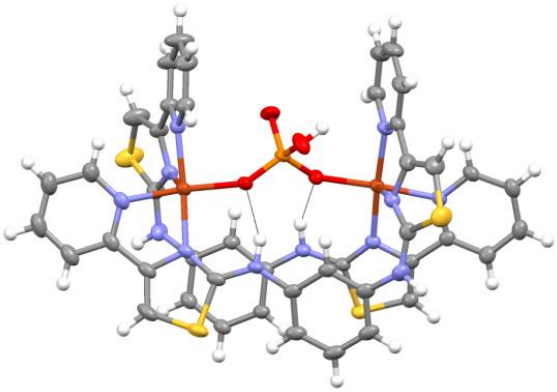

Figure 1.3.16. *Solid state structure of [(**L**$^{1.342}$)$_2$Cu$_2$(OPO$_3$H$_2$)]$^{3+}$. Thermal ellipsoids shown at the 50% probability level and the remaining anions omitted for clarity.*[83]

Interestingly, upon the addition of an additional half a molar equivalent of dihydrogen phosphate to the $[(\mathbf{L}^{1.342})_2Cu_2(OPO_3H_2)]^{3+}$ system the overall structural geometry of the complex undergoes dramatic changes to yield a trinuclear circular helicate. This higher order assembly involved the inclusion of three phosphate anions within the centre of the complex to give $[(\mathbf{L}^{1.342})_3Cu_3(OPO_3H_2)_3]^{3+}$. Each of the three phosphate guest anions was observed to be bound within the structure via a combination of both O···Cu coordination bonds as well as a complex network of hydrogen bonding interactions. Each of the phosphate anions formed one coordination bond to a single Cu(II) metal ion (1.988(5) – 2.008(4) Å), one hydrogen bonding interation to one of the ligands NH- amine units (N···O 2.890 – 3.053 Å) and one intra-molecular hydrogen bonding interaction to the neighbouring phosphate anion (2.546 – 2.605 Å) within the formed cavity (Fig 1.3.17.).

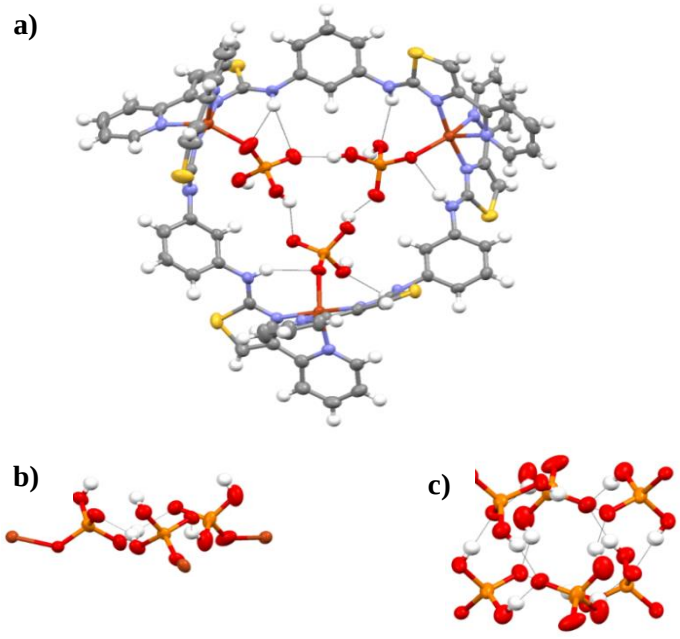

Figure 1.3.17. *Crystal structure of $[(\mathbf{L}^{1.342})_3Cu_3(OPO_3H_2)_3]^{3+}$. a) top view of the trinuclear circular helicate. b) view of the three dihydrogen phosphate anions. c) view of the six dihydrogen phosphate anions involved in both inter and intra-molecular hydrogen bonding.*[83]

Furthermore, the most interesting feature of this system is that the three central phosphate anions form a further three P=O···HO-P inter-molecular hydrogen bonding interactions (2.603 – 2.680 Å) to a second circular helicate complex, giving rise to a dimer of circular helicates *i.e.* $[(\mathbf{L}^{\mathbf{1.342}})_3Cu_3(OPO_3H_2)_3]_2^{6+}$ (Fig. 1.3.18.).

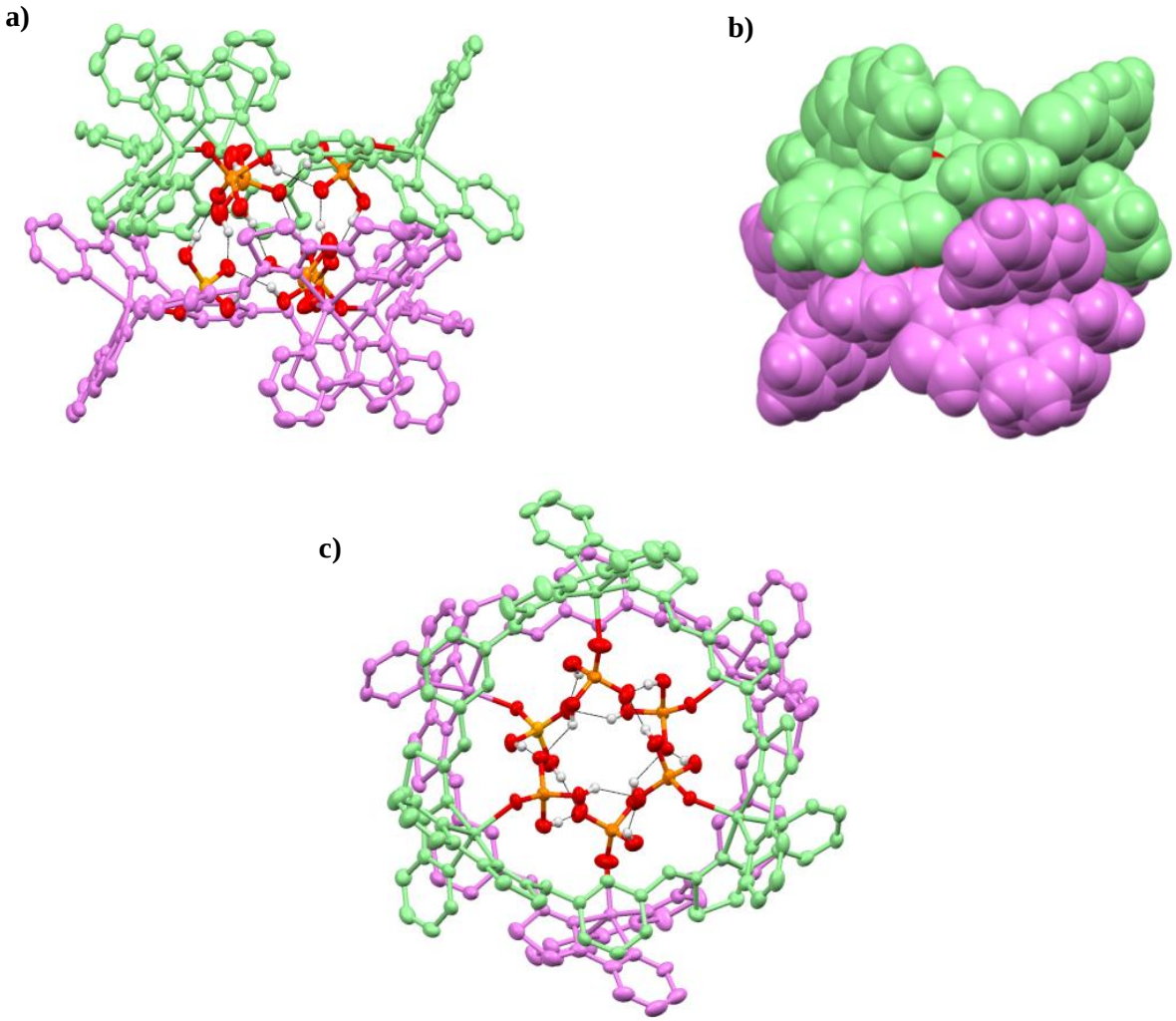

Figure 1.3.18. *Crystal structure of* $([(\boldsymbol{L}^{\boldsymbol{1.342}})_3Cu_3(OPO_3H_2)_3])_2^{6+}$. ***a)*** *side view of the dimeric structure.* ***b)*** *space-filling view of the dimer.* ***c)*** *top view of the circular helicate dimer showing the intra-molecular hydrogen bonding.*[83]

This study successfully highlights how the inclusion of amine -NH units within a ligand chain can result in a system that can adopt different coordinated molecular species dependent upon the anion and its stoichiometry. Furthermore, it is clear to see that the position of the hydrogen bonding units is vitally important. Inclusion of hydrogen bond donors at the end of a ligand chain can produce self-assembled species that act as a host for anions – but the overall self-assembly does not change. However, inclusion of hydrogen bond donors within the ligand chain can give systems that change shape / geometry on the addition of specific anions.

Drawing on the conclusions of this previous research, the work in this thesis focuses upon the synthesis of a series of ligands that contain –NH hydrogen bond donors within the ligand chain as well as the investigation of their properties both upon coordination of metal ions and interaction with a variety of different anions.

2. Carbon-carbon chain Ligands

2.1 Synthesis of $L^{2.1}$

The ligand $\mathbf{L^{2.1}}$ was synthesised in good yield from readily available materials as illustrated by the three-step procedure below (Scheme 2.1.1).

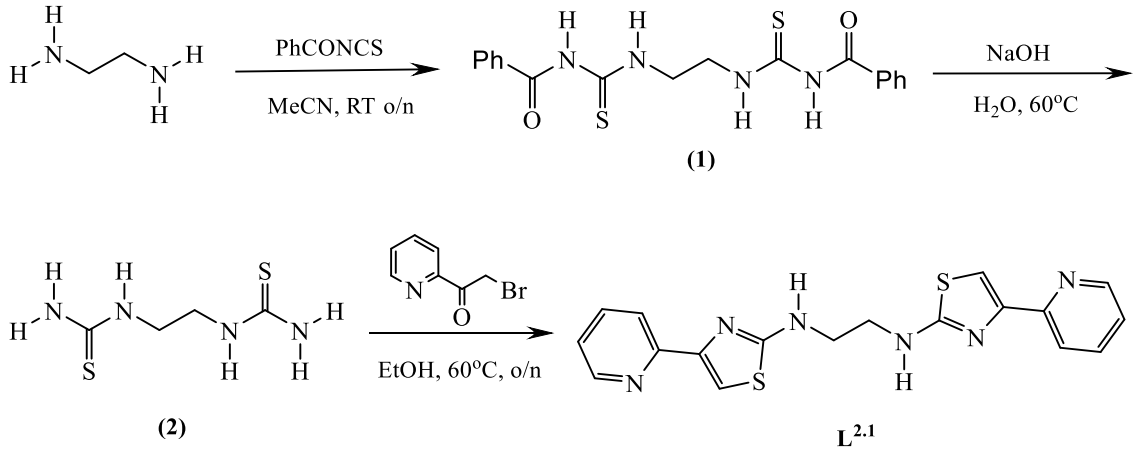

Scheme 2.1.1. *Synthesis of ligand* $\boldsymbol{L^{2.1}}$

The benzoylated bis-thiourea (**1**) was produced by a nucleophilic addition reaction of ethylenediamine with 2.1 equivalents of benzoyl isothiocyanate. The resultant yellow solid was isolated via filtration, and the crude product was then washed with methanol and dried to give the colourless powder intermediate (**1**). ^{1}H NMR showed the characteristic signals that are expected for this compound, i.e. two singlets at ~ 11 ppm corresponding to the unsymmetrical urea unit as well as three aromatic benzoyl and one aliphatic signal corresponding to the symmetrical 1, 2-ethyl bridging unit (Fig. 2.1.1). ^{13}C NMR showed the expected 9 signals and mass spectroscopic analysis gave an ion at *m/z* = 386 corresponding to the desired compound (e.g. $\{M + H\}^{+}$).

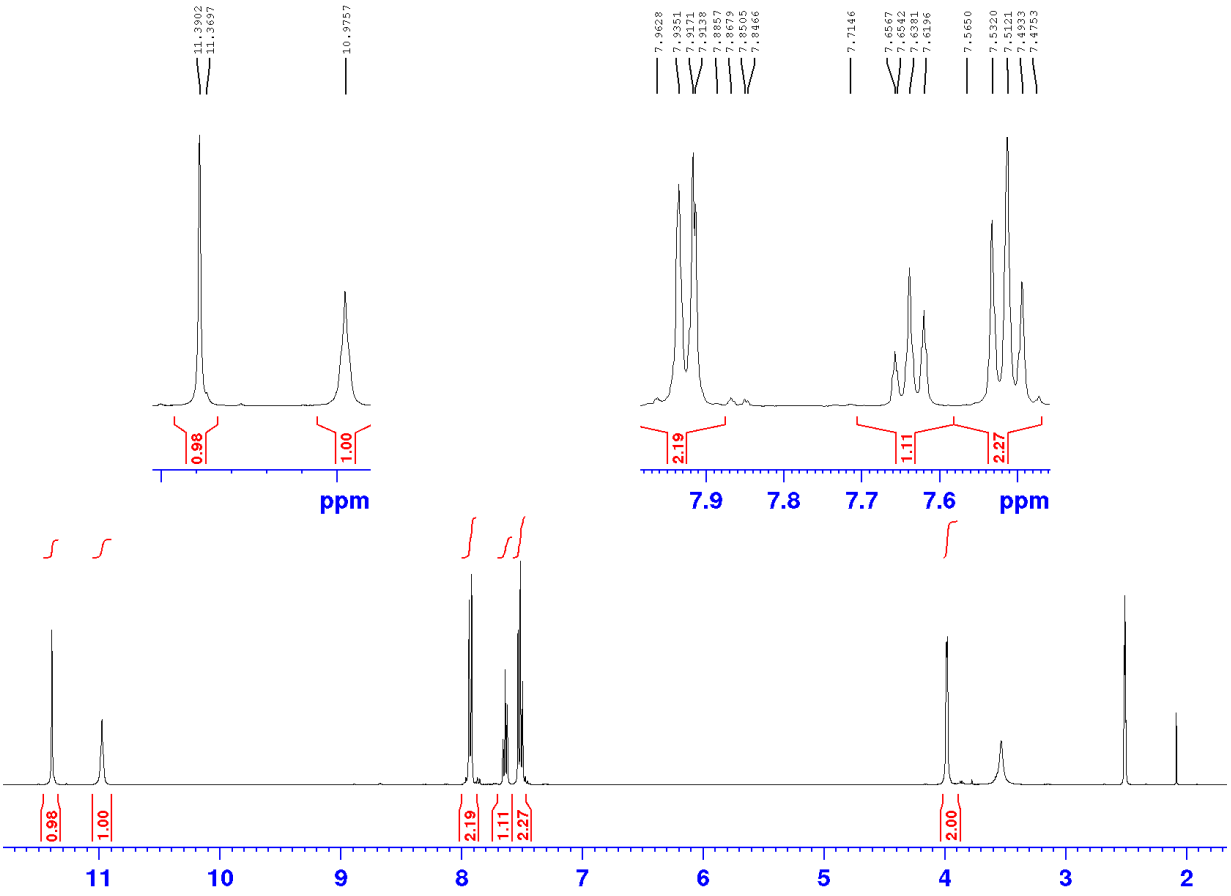

Figure 2.1.1. *^{1}H NMR of benzoylated thiourea product (**1**) a = water impurity and b = $(CD_3)(CHD_2)SO$.*

The benzoylated bis-thiourea (**1**) was then hydrolysed by treatment with 6.2 equivalents of sodium hydroxide (3.1 equivalents for each unit) in water to remove the benzoate units to give the bis-thiourea intermediate product (**2**). ^{1}H NMR for this product was broad and difficult to assign as the spectra displayed only 2 board signals (Fig. 2.1.2). Further analysis by ^{13}C NMR showed 2 signals with a signal at 183.9 ppm corresponding to the $(NH)_2C{=}S$ unit and an ion was observed in the ESI-MS at *m/z* = 179 corresponding to the desired compound (e.g. $\{M + H\}^+$). As the molecule contains both hydrogen–bond acceptor and donor units, interactions between these could result in restricted rotation, which would lead to broad signals in the ^{1}H NMR. However, with no aromatic signals from the benzoylated urea groups observed and the ^{13}C NMR and MS is as would be expected we assume that this is the correct product and it undergoes the expected

reactions. The formation of these intra- and inter-molecular hydrogen bonding interactions are confirmed by solid-state analysis (see Chapter 4)

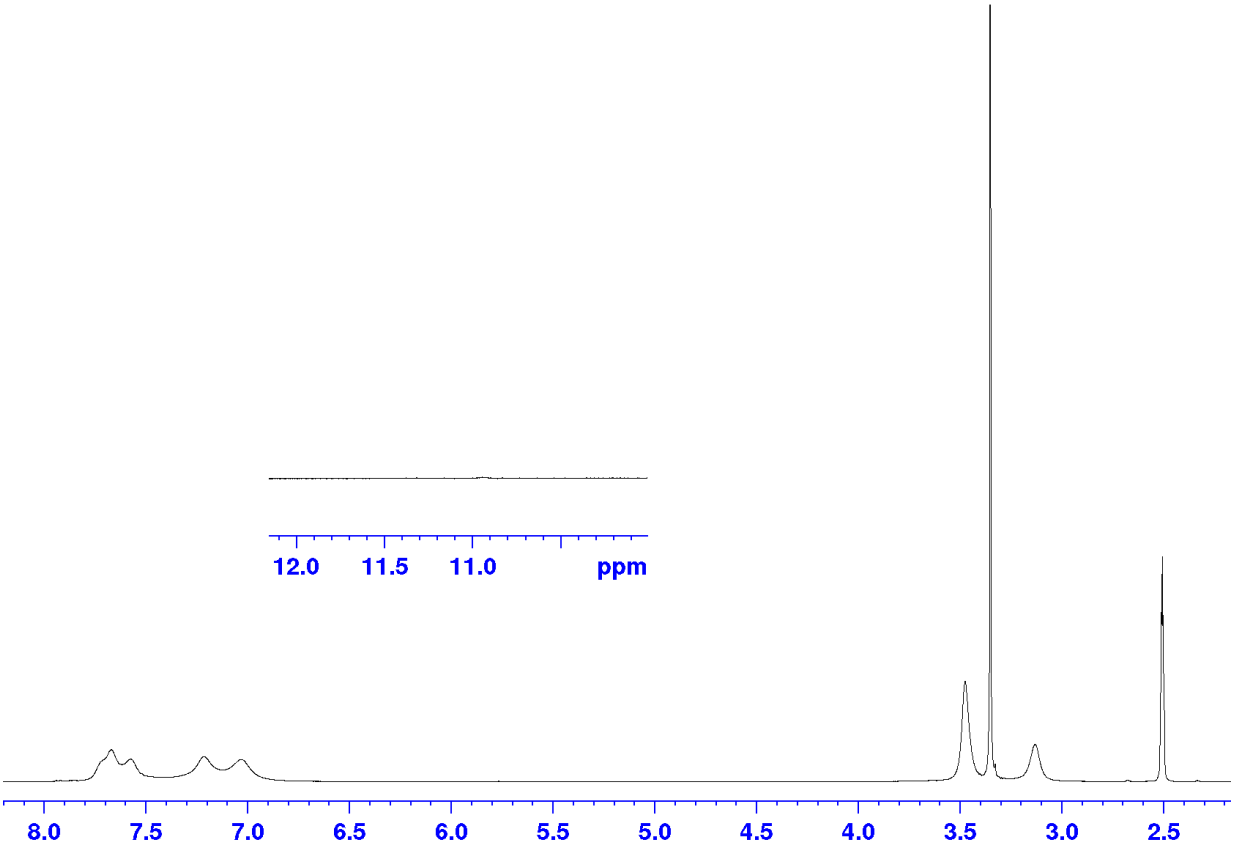

Figure 2.1.2. *^{1}H NMR of the bis-thiourea product (**2**) a = water impurity and b = $(CD_3)(CHD_2)SO$.*

The final synthetic step involved a Hantzsch thiazole synthesis type reaction of the bis-thiourea (**2**) with 2.1 equivalents of α-bromoacetylpridine, this was followed by neutralisation of the resulting hydrobromide salt with excess ammonia and gave the targeted bis-bidentate ligand ($\mathbf{L}^{\mathbf{2.1}}$). The formation of this ligand was confirmed by ^{1}H NMR (Fig. 2.1.3) which gave the signals that are indicative of this compound *i.e.* four aromatic mono-substituted pyridyl signals, one thiazole singlet, one amine (broad singlet at 6.96 ppm) and one aliphatic signal corresponding to the central 1,2-ethyl spacer unit. This was again supported by ^{13}C NMR which showed at total of 8 aromatic signals and one aliphatic signal. Further confirmation was given

by ESI-MS where an ion was observed at m/z = 381 corresponding to the desired compound ($\mathbf{L}^{2.1}$) (e.g. {M + H}$^{+}$).

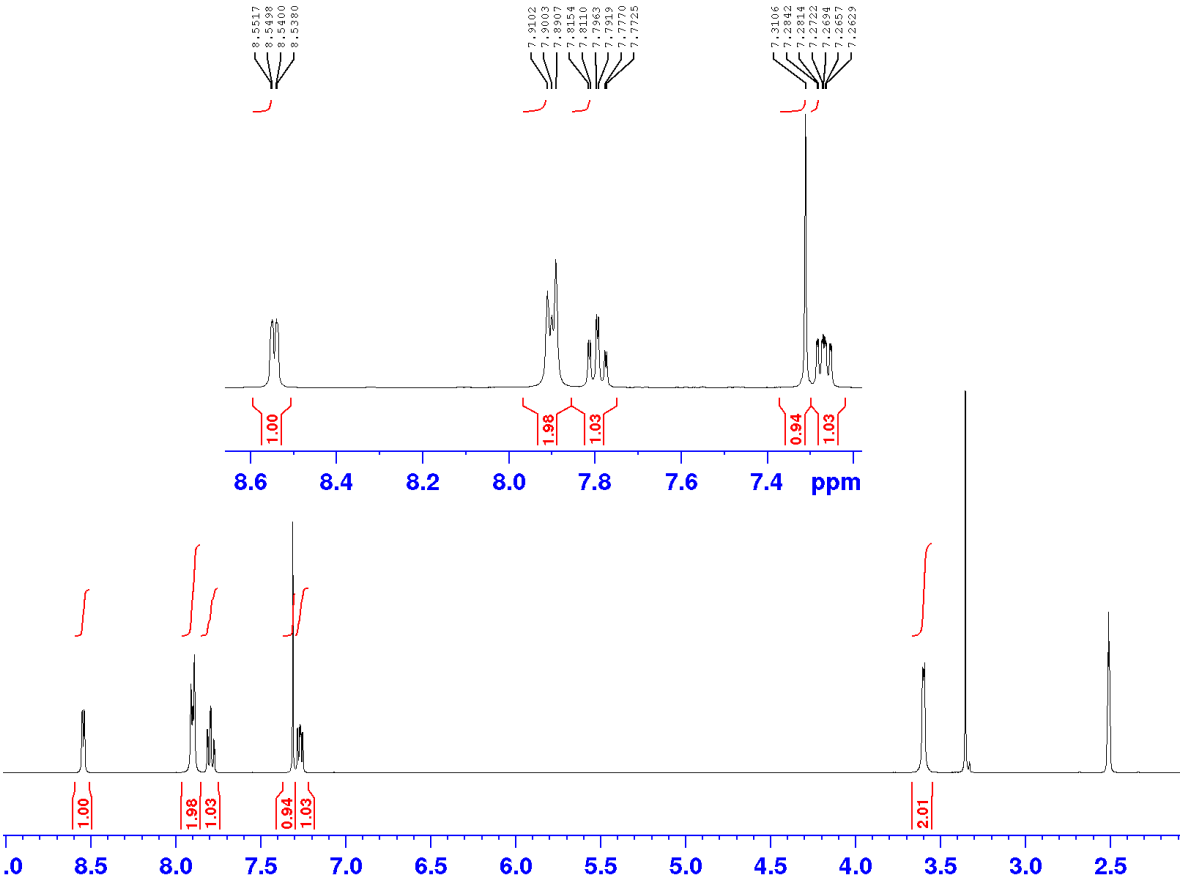

Figure 2.1.3. *^{1}H NMR of ligand $\mathbf{L}^{2.1}$ a = water impurity and b = $(CD_3)(CHD_2)SO$.*

The ligand $\mathbf{L}^{2.1}$ contains two pyridyl-thiazole domains bridged by a simple 1,2-ethyl spacer group. The two pyridyl-thiazole donor units have been previously shown to act as an excellent bidentate binding chelate to a variety of different metal ions.[84] Furthermore, also contained within the ligand strand are two secondary amine units, which are well known to act as hydrogen bond donors to anions.[83] This method of reacting diamines with benzoyl isothiocyanate, hydrolysis and reaction with α–bromoacetyl pyridine is very robust, can be applied to a variety of systems and generally works well with moderate to good yields.

2.2 Coordination Chemistry of $\mathbf{L^{2.1}}$

Reaction of $\mathbf{L^{2.1}}$ with $Cu(trif)_2$ in $MeNO_2$ gave a tan solution and analysis by ESI-MS gave an ion at *m/z* 1335 corresponding to $\{[Cu_2(\mathbf{L^{2.1}})_2](trif)_3\}^+$ as well as an ion at *m/z* 593 corresponding to $\{[Cu_2(\mathbf{L^{2.1}})_2](trif)_2\}^{2+}$ indicating the formation of a dinuclear assembly. A dark tan crystalline material was deposited upon slow diffusion of diisopropylether. Single-crystal X-ray diffraction analysis confirmed that in the solid state a dinuclear assembly compromising of two ligand strands, two Cu(II) ions and two triflate anions had formed (Fig. 2.2.1). In this structure each of the ligand strands are not intertwined as expected of the '*helicate*' architecture so the $[(\mathbf{L^{2.1}})_2Cu_2(trif)_2]^{2+}$ complex can therefore be classified as a *meso*cate as in this structure both metal ions display the same chirality. In this complex each of the two Cu(II) metal ions display a typical 5-coordinate geometry which compromises of four N···Cu coordination bonds from one of each ligand strands chelating pyridyl-thiazole units as well as receiving a O···Cu coordination bond from a triflate counter ion. This complex to anion interaction is further supplemented by hydrogen bonding interactions with the ligand strands –NH units, one to each oxygen atom from each of the two amine –NH unit of the same ligand strand (Fig. 2.2.1).

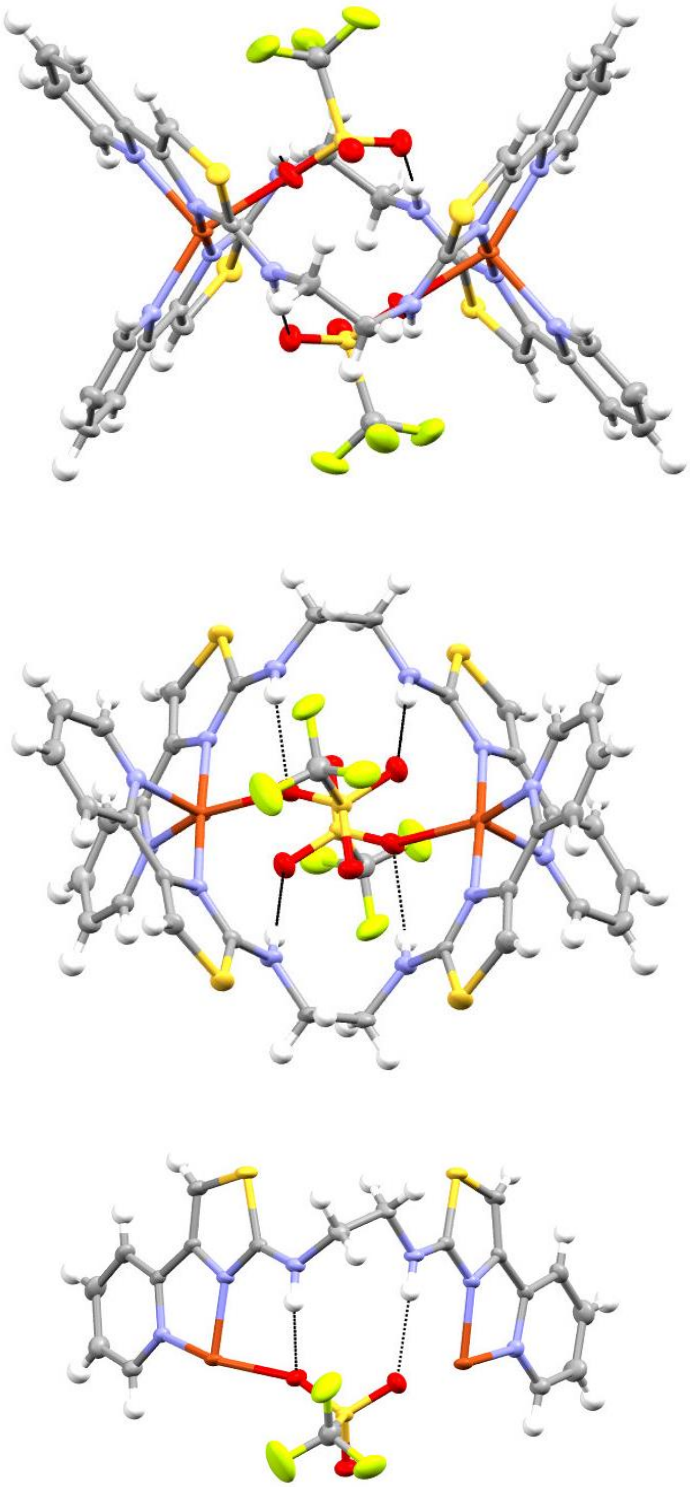

Figure 2.2.1. *X-ray structure of three different views of the X-ray structure of the major component of* $[(\mathbf{L}^{2.1})_2Cu_2(trif)_2]^{2+}$ *showing the coordination and hydrogen bonding of the triflate anion. Thermal ellipsoids shown at the 50% probability level. Selected hydrogen atoms and anions omitted for clarity.*

Reaction of $[(\mathbf{L}^{2.1})_2Cu_2]^{4+}$ with four equivalents of Bu_4NNO_3 in $MeNO_2$ resulted in the solution displaying a colour change from blue to dark green. Slow diffusion of diispropyl ether yielded a mass of large green crystals which were analysed by single crystal X-ray diffraction. In the solid state it was found that the dinuclear assembly persists but in this example each of the Cu(II) ions is coordinated by the ligand strands two bidentate pyridyl-thiazole domains as well as a single water molecule. Furthermore, within the complex there are four individual nitrate anions which are bonded to the assembly via a complex hydrogen bonding array involving a total of 15 interactions. In all four cases, the nitrate anion is bound by one –OH···O hydrogen bonding interaction (from the water molecule) and one –NH···O hydrogen bonding interaction from each of the ligand strands amine units (Fig. 2.2.2). Interestingly in this example each of the ligand strands displays a distinctive twist to give a helicate motif (as opposed to mesocate with the triflate anion). As a result, this highlights that in this system the binding of nitrate anions does change the structural assembly in the solid state, albeit subtly. The poor solubility of this complex in either $MeNO_2$ or MeCN precluded analysis by ESI-MS.

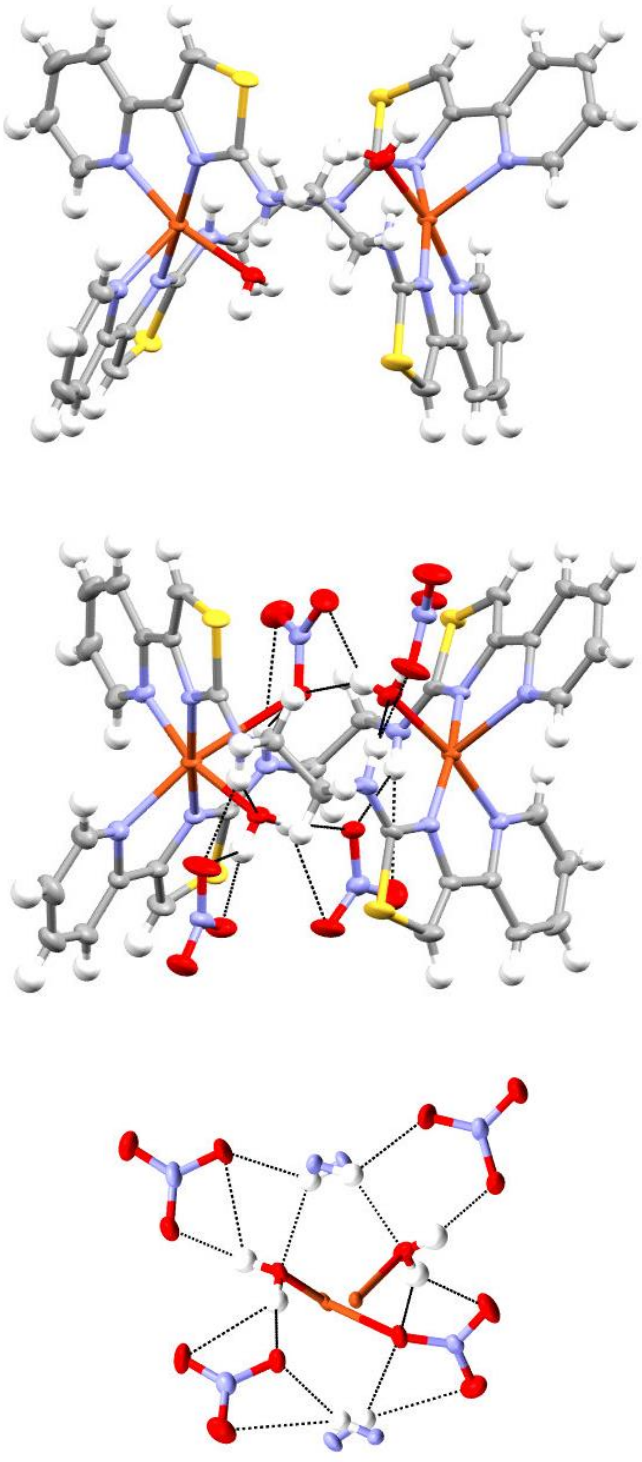

Figure 2.2.2. *Three different views of the X-ray structure of* $[(\mathbf{L}^{2.1})_2Cu_2(H_2O)_2(NO_3)_4]$ *showing the coordination and hydrogen bonding of the nitrate anion. Thermal ellipsoids shown at the 50% probability level. Selected anions omitted for clarity.*

Reaction of $[(\mathbf{L}^{2.1})_2Cu_2]^{4+}$ with two equivalents of Bu_4NI in $MeNO_2$ results in the colour of the solution initially changing from blue to red and eventually forming a dark green solution. Again, in the solid state a dinuclear species was seen to have formed. However, in this system each of the Cu(II) metal ions are coordinated by two pyridyl-thiazole units (as seen in the previous examples) and the bonding is further supplemented by an amine nitrogen atom resulting in five-coordinate metal centres (Fig. 2.2.3). The geometry of the amine and the observation that only two triflates are present per helicate assembly (e.g. $[(\mathbf{L}^{2.1})_2Cu_2]^{2+}$) indicates that the –NH unit has deprotonated. It seems reasonable to assume that this has occurred as iodide can act as a weak base (relative to triflate, perchlorate and tetrafluoroborate) which would not occur in the triflate as this is a much weaker base. Interestingly, nitrate is a stronger base than iodide but the nitrate-containing structure is presumably stabilised by the network of intramolecular hydrogen bonding interactions which prevent the deprotonation of the amine –NH units. The poor solubility of this complex in either $MeNO_2$ or MeCN precluded analysis by ESI-MS.

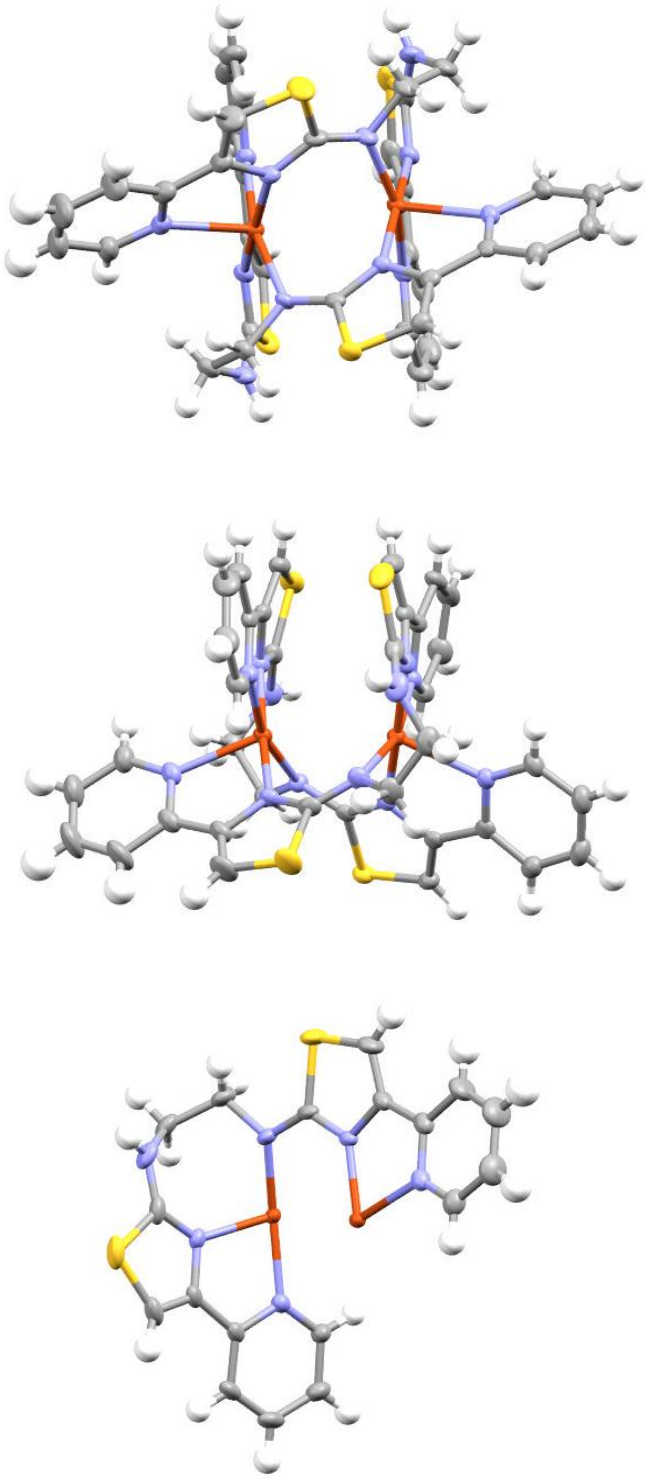

Figure 2.2.3. *Three different views of the X-ray structure of* $[(\mathbf{L}^{2.1})_2Cu_2]^{2+}$ *showing the Cu(II) coordination. Thermal ellipsoids shown at the 50% probability level. Selected anions omitted for clarity.*

Reaction of $[(\mathbf{L}^{2.1})_2Cu_2]^{4+}$ with half a molar equivalent of Na_2SeO_3 in $MeNO_2$ (containing a few drops of MeOH to aid dissolution) resulted in the colour of the solution changing from dark blue to lime-green. Single-crystal X-ray analysis determined that in the solid-state an anion-containing $[(\mathbf{L}^{2.1})_2Cu_2]^{2+}$ dinuclear double helicate assembly was present (Fig. 2.2.4). As been observed previously a dinuclear double helicate is formed and each of the two Cu(II) metal centres formed four N···Cu coordination bonds from one of the bidentate thiazole-pyridyl binding domains from each of the two ligands. However, in this example both Cu(II) metal centres were seen to adopt a 6-coordinate octahedral binding geometry with each of the two selenite anions bridging the Cu(II) ions to give a total of four O···Cu bonds (two for each Cu(II) ion). The bonding of the included anions within the complex was then further complemented by the formation of four -NH···O hydrogen bonding interactions, where each anion has two interactions from the ligand's amine units. Interestingly, on closer examination of the included selenite anions it was seen that both bridging anions have reacted to form a new -OMe bond to give the methyl ester of the selenite anion e.g. $(O_2SeOMe)^-$. This reaction is not that unusual as methanol was included within the reactions solvent system and it is known that selenite esters can be formed. However, this type of esterification reaction usually requires more forcing conditions (e.g. heat, alcohol as solvent) and as this esterification occurs at room temperature (and with limited MeOH) it seems likely that coordination of the selenite by Cu(II) increases its reactivity to nucleophiles.

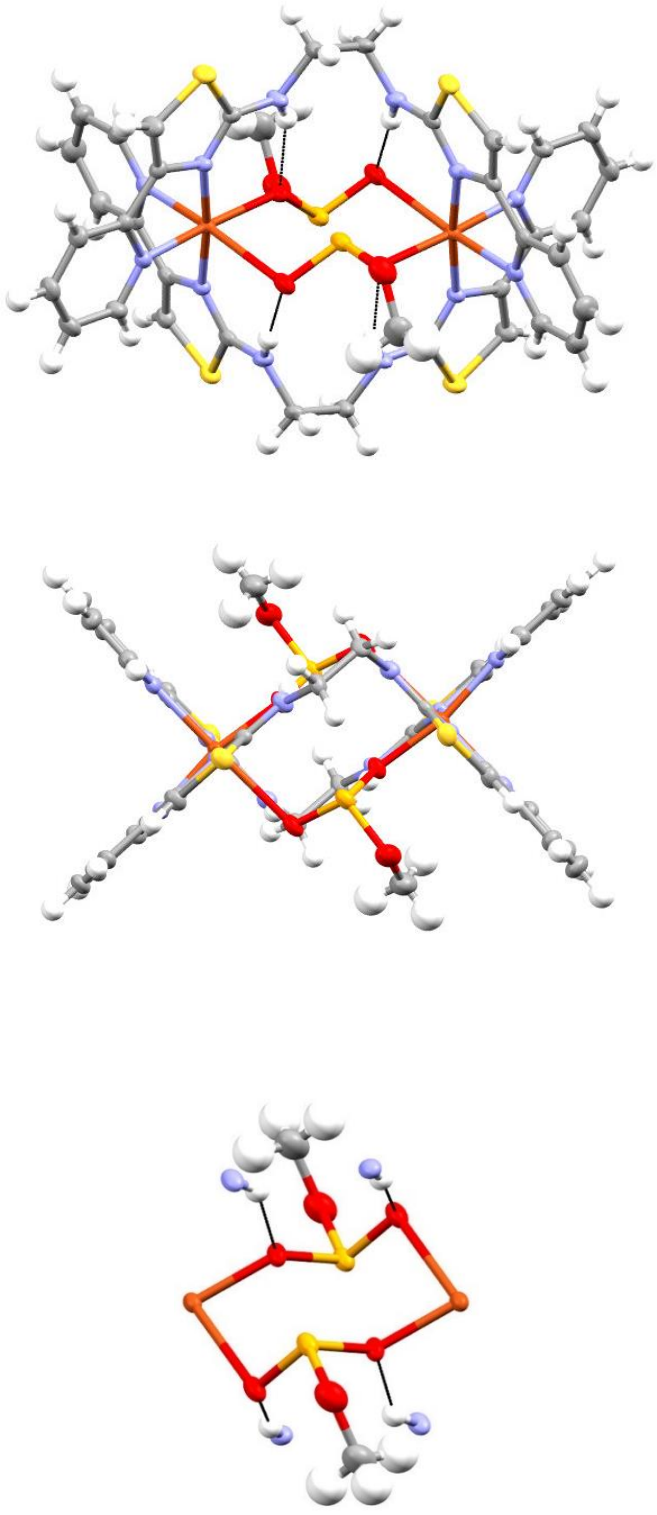

Figure 2.2.4. *Three different views of the X-ray structure of* $[(\mathbf{L}^{2.1})_2Cu_2(O_2SeOMe)]^{2+}$ *showing the coordination and hydrogen bonding of both the phosphate and triflate anions. Thermal ellipsoids shown at the 50% probability level. Selected anions and atoms omitted for clarity.*

Reaction of $[(\mathbf{L}^{\mathbf{2.1}})_2Cu_2]^{4+}$ with half a molar equivalent of $Bu_4N(H_2PO_4)$ in $MeNO_2$ resulted in the colour of the solution changing from dark blue to pale green. Single-crystal X-ray analysis determined that in the solid-state the mixed anion containing $[(\mathbf{L}^{\mathbf{2.1}})_2Cu_2(H_2PO_4)(trif)]^{2+}$ dinuclear double helicate assembly was present (Fig. 2.2.5). In this example, it was found that a single phosphate anion bridges the two Cu(II) metal centres. The O···Cu coordination bonding is further complimented by -NH···O hydrogen bonding interactions from two amine units, one from each ligand. The dihydrogen phosphate anion can be determined to be singly deprotonated (e.g. $[(\mathbf{L}^{\mathbf{2.1}})_2Cu_2(H_2PO_4)](trif)_3$). The two -OH units from the dihydrogen phosphate anion are both orientated pointing outward of the structure and intern form further -OH···O hydrogen bonding interactions to a single triflate counter anion (via the oxygen atom of the triflate). The structure also was found to persist in the gas phase with ESI-MS analysis giving ions at *m/z* 1282 and 492 corresponding to $\{[(\mathbf{L}^{\mathbf{2.1}})_2Cu_2(H_2PO_4)](trif)_2\}^+$ and $\{[(\mathbf{L}^{\mathbf{2.1}})_2Cu_2(HPO_4)]\}^{2+}$.

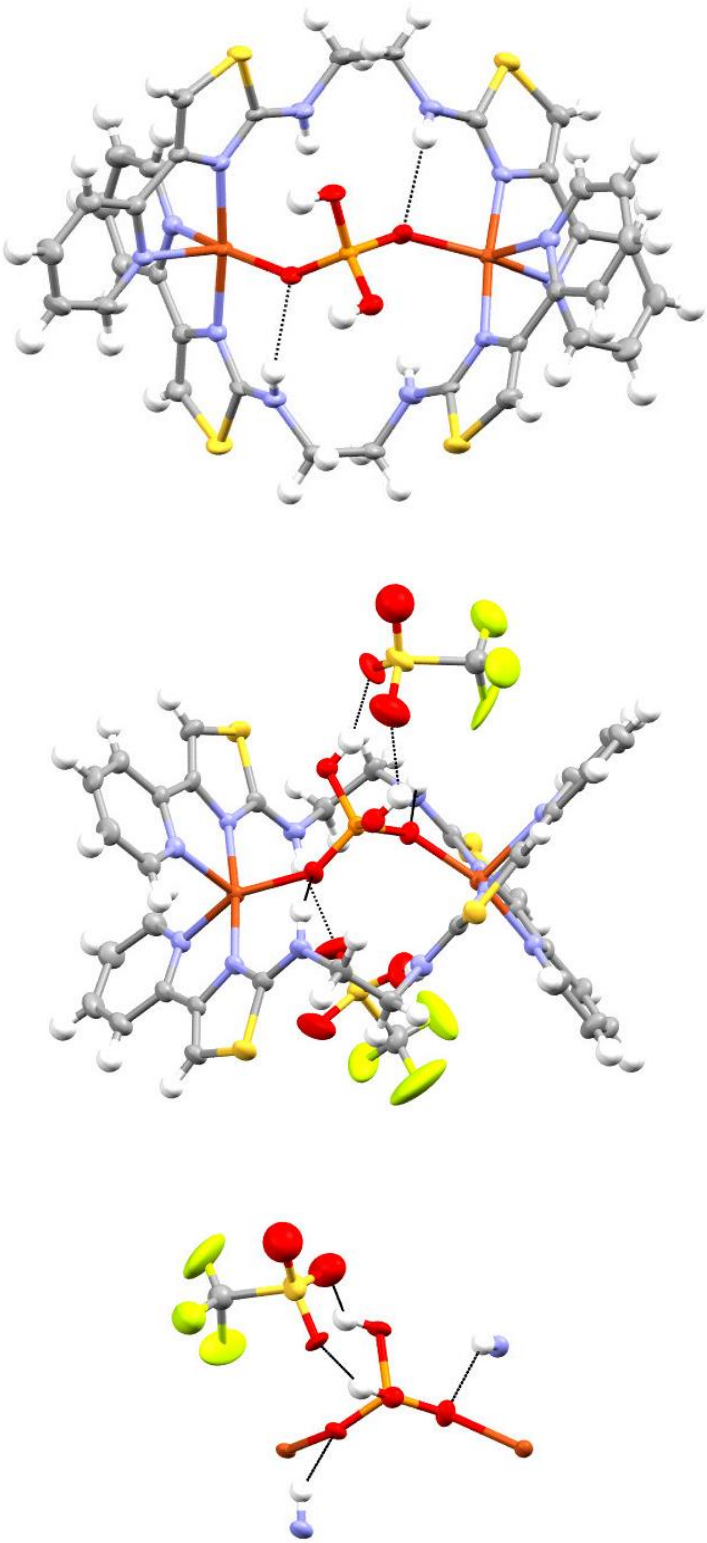

Figure 2.2.5. *Three different views of the X-ray structure of* $[(\mathbf{L}^{2.1})_2Cu_2(H_2PO_4)(trif)]^{2+}$ *showing the coordination and hydrogen bonding of both the phosphate and triflate anions. Thermal ellipsoids shown at the 50% probability level. Selected anions and atoms omitted for clarity.*

Reaction of $[(\mathbf{L}^{2.1})_2Cu_2](BF_4)_4$ with one equivalent of $Bu_4N(H_2PO_4)$ in $MeNO_2$ results in the colour of the solution changing from dark-blue to emerald-green. Slow diffusion of diisopropyl ether into the solution gave a homogenous mass of crystals that were to a sufficient standard to be analysed by single-crystal X-ray diffraction. This showed that in the solid state the dinuclear assembly was not present, instead a trinuclear circular helicate ($[(\mathbf{L}^{2.1})_3Cu_3]^{6+}$) structure had formed (Fig. 2.2.6). In this structure there are three Cu(II) ions and three ligand strands where each of the ligand strands display different individual twist geometries. Each of the three Cu(II) metal ions are coordinated by two bidentate pyridyl-thiazole unit from different ligand strands where each gain four N···Cu coordination bonds. However, in this example each of the three Cu(II) metal ions is coordinated by one of the three oxygen atoms of a single central phosphate anion which is held within the centre of the complex. The binding of the central phosphate oxygen atoms to the Cu(II) metal ions is further supplemented by three -NH···O hydrogen bonding interaction with one of the –NH units from each ligand strand (Fig 2.2.6 c). However, the most interesting feature of this structure is the fourth, uncoordinated, phosphate oxygen atom points outward of the structure and has reacted with a single molecule of tetrafluoroborate to give the molecule $[O_3PO\text{-}BF_3]^{3-}$ (Fig. 2.2.6 d). The reason a trinuclear circular helicate is formed is due to the acidity of the $[HO_3PO\text{-}BF_3]^{2-}$ unit which contains an electron withdrawing $–OBF_3$ group. This unit, although negatively charged, will increase the acidity of the POH bond and this increased acidity allows the triple deprotonation of the phosphate anion and coordination of all the oxygen atoms with the Cu(II) ions. However, the reason why tetrafluoroborate reacts with the phosphate anion is not clear. There are no previous reports of the phosphate anion reacting with tetrafluoroborate, indeed tetrafluoroborate is thought to be an inert molecule (apart from in very basic solutions) although BF_4 can be hydrolysed to F_3BOH with reactive low-valent transition metal ions and H_3PO_4 can react with $B(OH)_3$ under forcing conditions.[85–88] Close examination of the $[Cu_2(\mathbf{L}^{2.1})_2(H_2PO_4)(trif)]^{2+}$ structure (Fig. 2.2.5) shows that in this structure the triflate anion is strongly hydrogen bonded to the phosphate anion via two hydrogen bonds from the -OH units. It is therefore likely that this would occur in the tetrafluoroborate derivative and in bringing these two molecules in close

proximity would promote the reaction between the two anions. The formation of this molecule was further supported by ESI-MS which gave an ion at *m/z* 1668 corresponding to $\{[(\mathbf{L}^{2.1})_3Cu_3(O_3POBF_3)](BF_3)_2\}^+$.

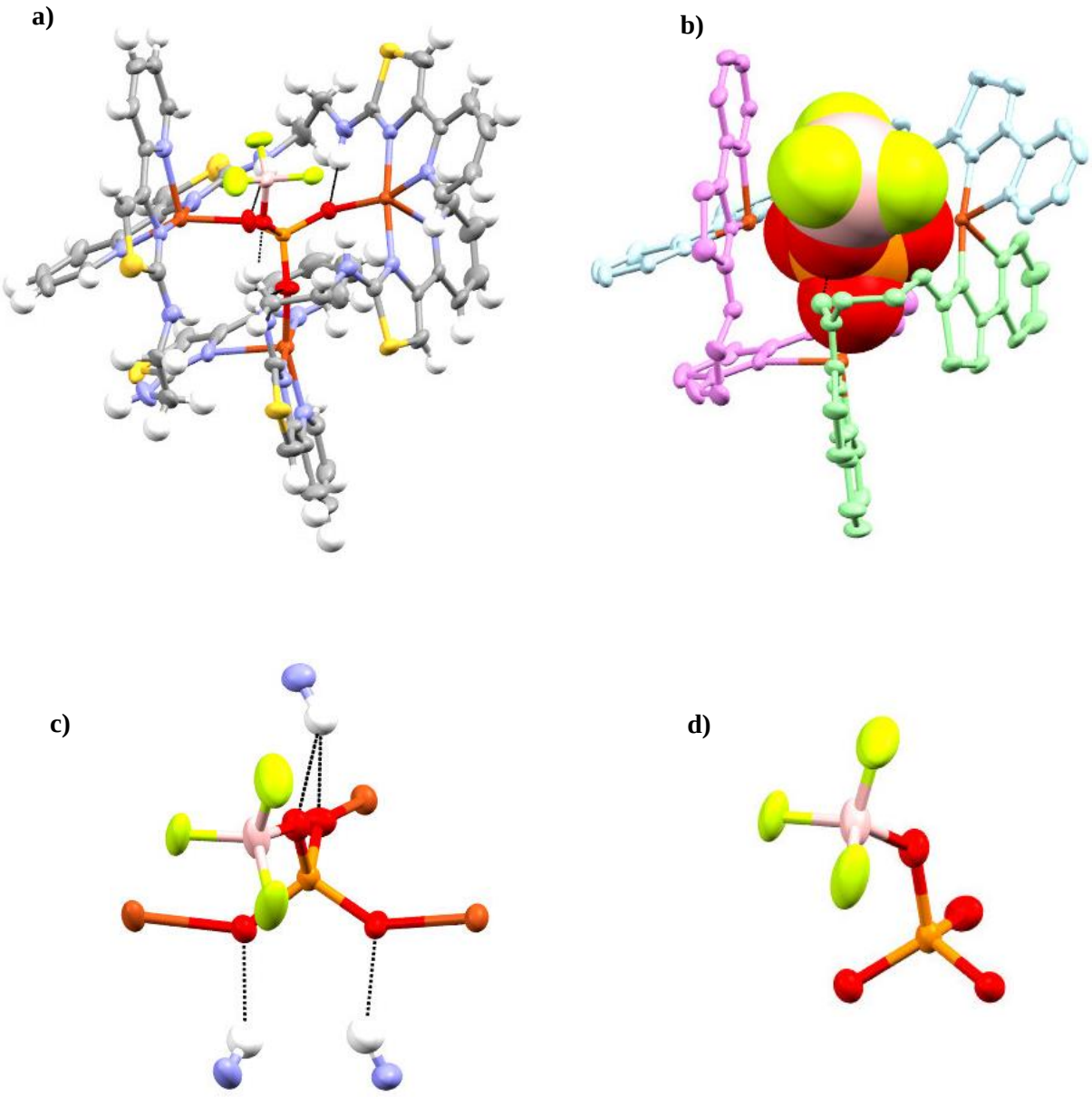

Figure 2.2.6. *Four different views of the X-ray structure of* $[(\mathbf{L}^{2.1})_3Cu_3(PO_4BF_3)]^{3+}$ *showing the coordination and hydrogen bonding of the anion. Thermal ellipsoids shown at the 50% probability level. Selected anions and atoms omitted for clarity (a-b). Partial view of the X-ray structure showing the* O_3POBF_3 *unit (d) and its bonding interactions (c).*

2.3 Coordination Chemistry of $L^{2.2}$

This reaction of tetrafluoroborate with phosphate is very unusual but it is not only limited to this $[(\mathbf{L}^{2.1})_3Cu_3(PO_4BF_3)]^{3+}$ system. Ligand $\mathbf{L}^{2.2}$ which is analogous to $\mathbf{L}^{2.1}$ but contains 1,4-butyl as opposed to 1,2-ethyl spacer and was synthesised in an analogous fashion.

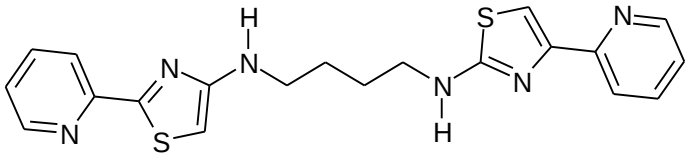

Figure 2.3.1. *Ligand* $\boldsymbol{L}^{2.2}$

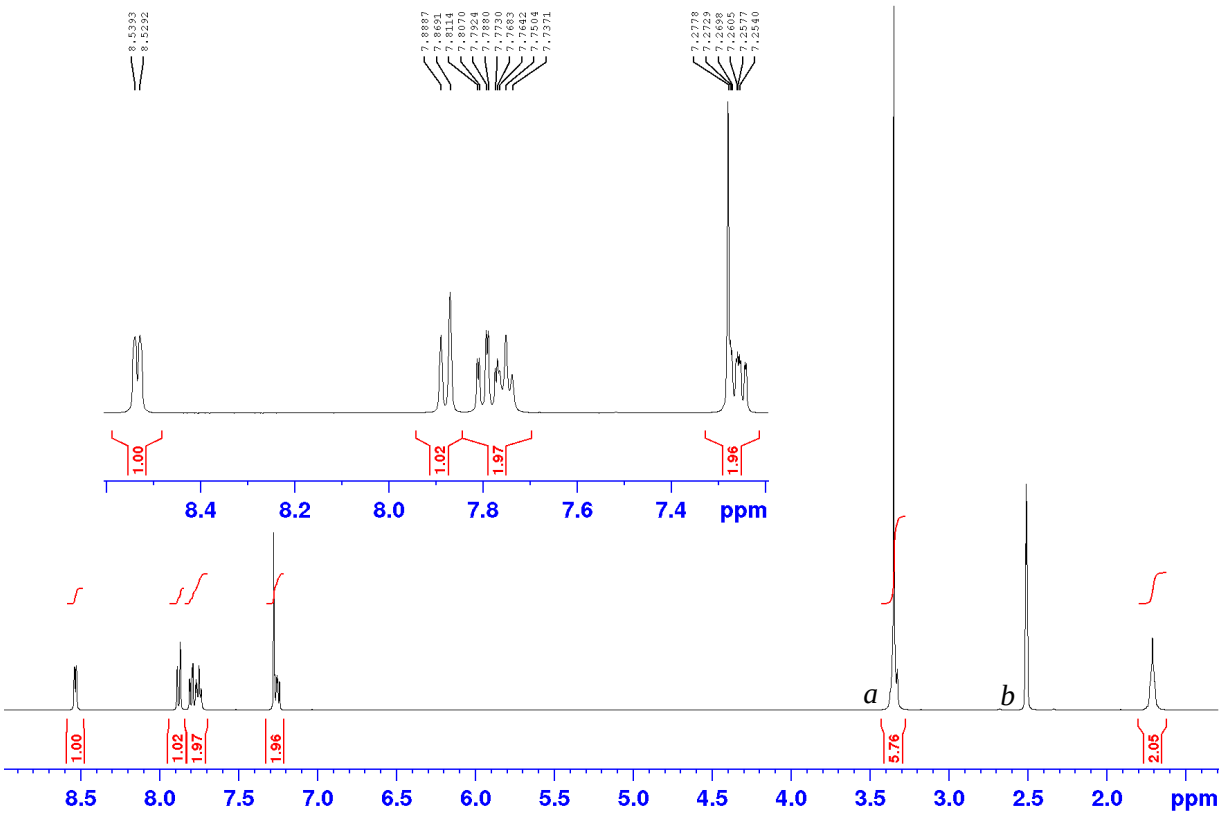

Figure 2.3.2. *^{1}H NMR of ligand* $\boldsymbol{L}^{2.2}$ *a = water impurity and b = $(CD_3)(CHD_2)SO$.*

The ligand $\mathbf{L^{2.2}}$ is similar to $\mathbf{L^{2.1}}$ but contains a butyl spacer between the two amine-bidentate domains. Reaction of $\mathbf{L^{2.2}}$ with $Cu(trif)_2$ in $MeNO_2$ gives a tan coloured solution which analysis by ESI-MS gives and ion at *m/z* 1391 and 620 which corresponds to $\{[(\mathbf{L^{2.2}})_2Cu_2](trif)_3\}^+$ and $\{[(\mathbf{L^{2.2}})_2Cu_2](trif)_2\}^{2+}$ respectively. Although we were unable to successfully grow crystals of this species the ESI-MS data, coupled with comparison with $\mathbf{L^{2.1}}$, it seems likely a dinuclear species has been formed. Ligand $\mathbf{L^{2.2}}$ reacts with $Cu(trif)_2$ and half a molar equivalent of phosphate to give a dinuclear double helicate with a central phosphate anion that bridges the two Cu^{II} metal centres (Fig. 2.3.3). In this structure the phosphate is bound by both metal ions as well as two –NH···O hydrogen bonding interactions, one from each ligand. Furthermore, in this assembly two triflate anions form hydrogen bonding interactions to both –OH units from the Cu(II) bridging phosphate anion as well as forming -NH···O hydrogen bonding interactions to the ligands amine units. The formation of this assembly was again supported by ESI-MS, giving ions at; *m/z* 1339 $\{[(\mathbf{L^{2.2}})_2Cu_2(H_2PO_4)](trif)_2\}^+$ *m/z* 1189 $\{[(\mathbf{L^{2.2}})_2Cu_2(HPO_4)](trif)\}^+$ *m/z* 520 $\{[(\mathbf{L^{2.2}})_2Cu_2(HPO_4)]\}^{2+}$ as well as lower molecular weight species such as m/z 620 $\{[(\mathbf{L^{2.2}})_2Cu](trif)\}^+$ and 470 $\{[(\mathbf{L^{2.2}})_2Cu]\}^+$.

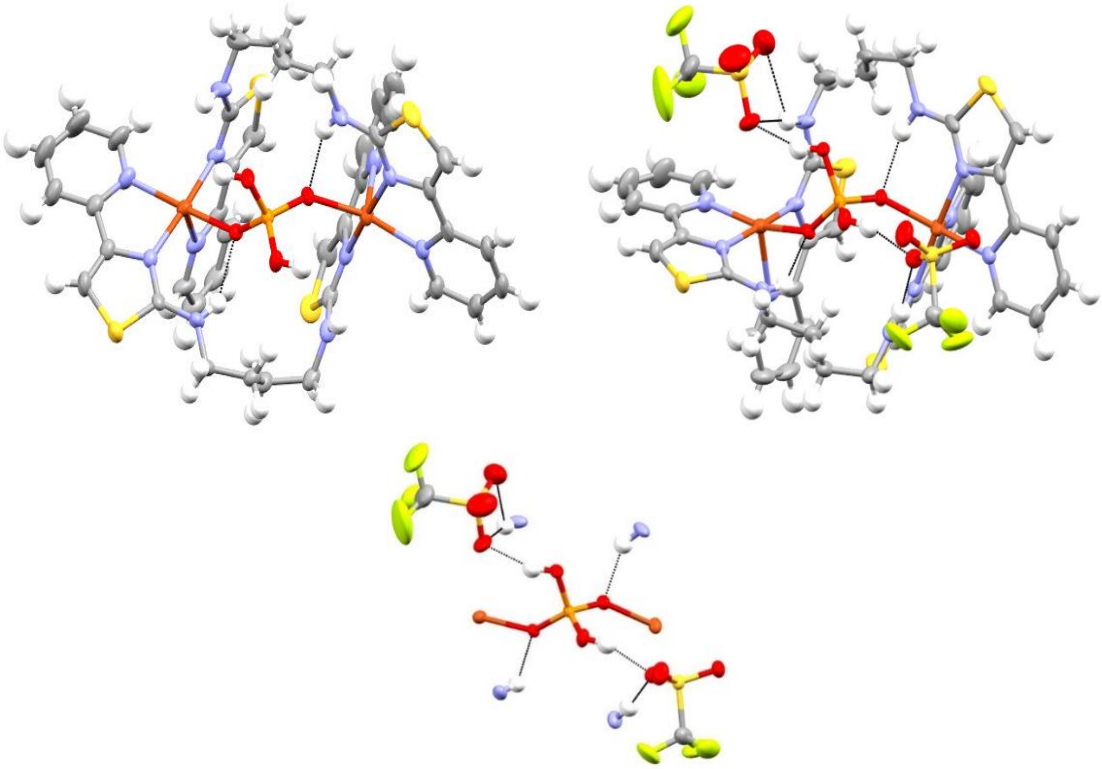

Figure 2.3.3. *Three different views of the X-ray structure of* $[(\mathbf{L}^{2.2})_2Cu_2(H_2PO_4)(trif)_2]^{2+}$ *showing the coordination and hydrogen bonding of both the phosphate and triflate anions. Thermal ellipsoids shown at the 50% probability level. Selected anions and atoms omitted for clarity*

Reaction of $Cu(BF_4)_2$ with $\mathbf{L}^{2.2}$ and half an equivalent of $Bu_4NH_2PO_4$ in $MeNO_2$ resulted in a green solution from which a crystalline material was formed upon slow diffusion of diethyl ether. It was found by X-ray diffraction that in the solid state the structure is still a dinuclear double helicate with a phosphate anion bridging the two Cu(II) metal ions (Fig. 2.3.4). However, in this example two tetrafluoroborate anions have reacted with the bound phosphate via a P-O-B bond (Fig. 2.3.5). It is probable that in this example the dinuclear assembly is retained (as opposed to the trinuclear circular structure as with $[Cu_3(\mathbf{L}^{2.1})_3(PO_4BF_3)]^{3+}$) as the butyl spacers add sufficient flexibility and can accommodate the steric bulk of the $[(F_3B\text{-}O)PO_2]^{3-}$ unit. This allows the formation of the entropically favoured *dinuclear* assembly. Examination of this material by ESI-MS showed ions at *m/z* 1175 and *m/z* 1107 $\{[(\mathbf{L}^{2.2})_2Cu_2(O_2P(OBF_3)_2)]\}^+$ and $\{[(\mathbf{L}^{2.2})_2Cu_2(O_3POBF_3)]\}^+$ respectively. Also present are smaller ions at

19 mass units higher at *m/z* 1195 and 1127 corresponding to $\{[(\mathbf{L}^{2.2})_2Cu_2(HO_3P(OBF_3))](BF_4)\}^+$ and $\{[(\mathbf{L}^{2.2})_2Cu_2(HPO_4)](BF_4)\}^+$ which we attribute to artefacts of the mass spectrometry process.

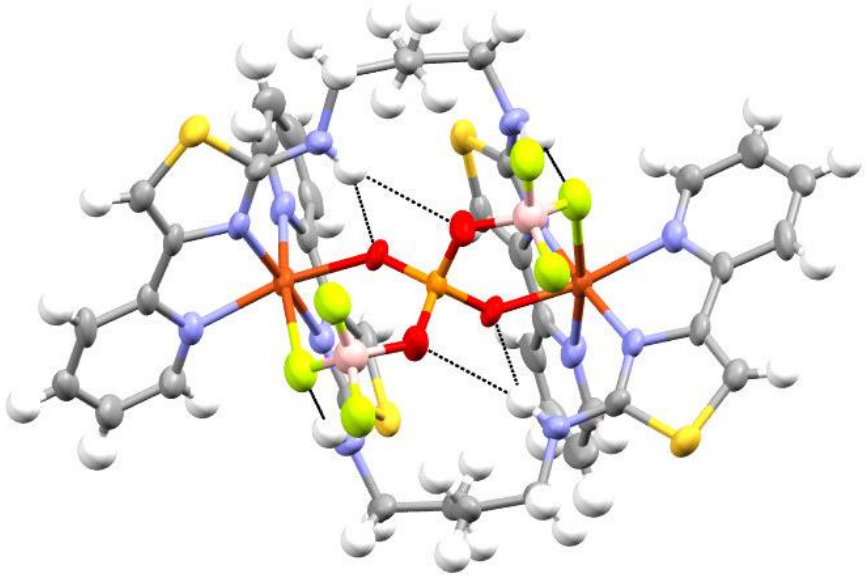

Figure 2.3.4. *X-ray structure of* $[(\boldsymbol{L}^{2.2})_2Cu_2(PO_4(BF_3)_2)]^+$ *showing the coordination and hydrogen bonding of the anion. Thermal ellipsoids shown at the 50% probability level. Selected anions and atoms omitted for clarity.*

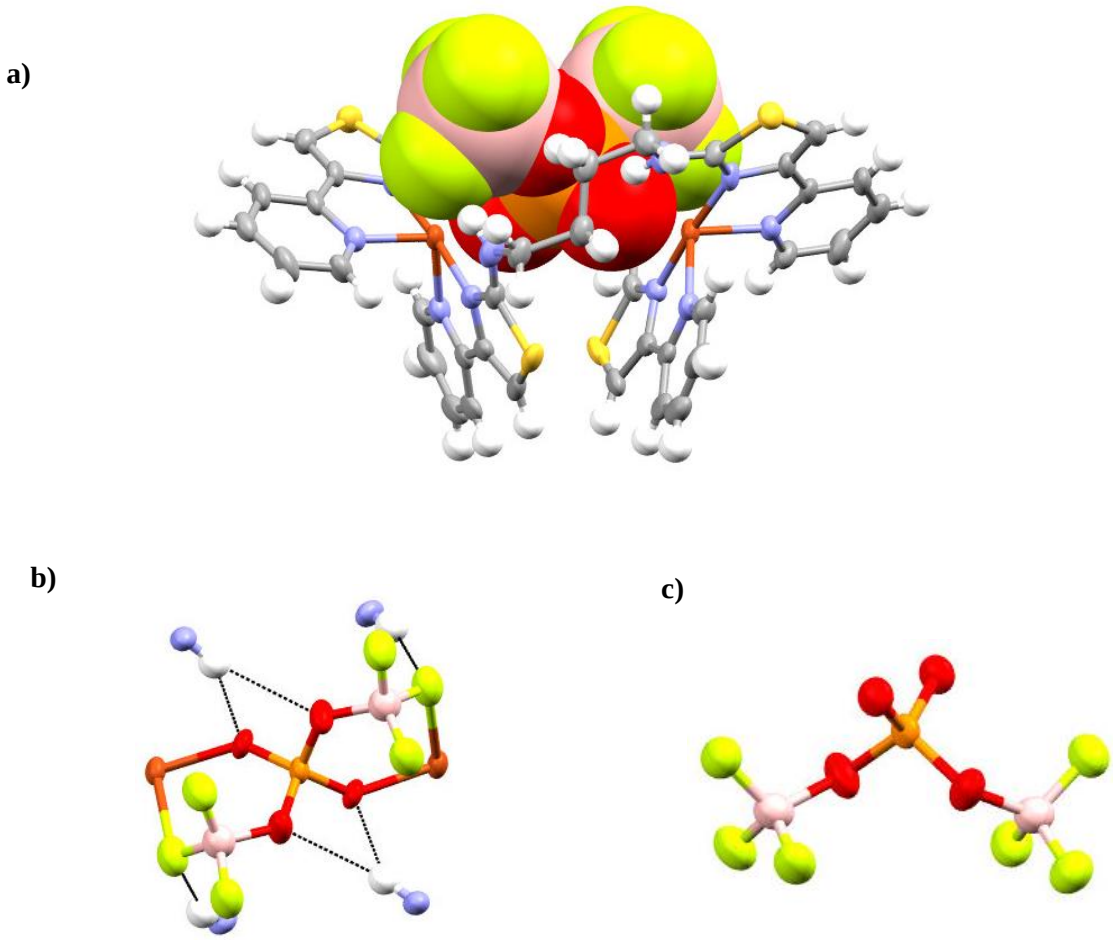

Figure 2.3.5. *Three different views of the X-ray structure of* $[(\mathbf{L}^{2.2})_2Cu_2(PO_4(BF_3)_2)]^+$ *showing the coordination and hydrogen bonding of the anion. Thermal ellipsoids shown at the 50% probability level. Selected anions and atoms omitted for clarity (a). Partial view of the X-ray structure of showing the* $\{PO_4(BF_3)_2\}$ *unit (c) and its bonding interactions (b).*

Again, this is very unusual, but it has been found that in the triflate analogue the phosphate anion forms hydrogen bonds to two triflate counter anions demonstrating that there is sufficient room in the assembly (provided by the long butyl arms) for the bridging phosphate anion to interact with two tetrafluoroborate anions.

2.4 Coordination Chemistry of $L^{2.3}$

Ligand $\mathbf{L^{2.3}}$ which is analogous to $\mathbf{L^{2.2}}$ but contains *cis*-1,4-but-2-ene spacer unit as opposed to the 1,4-butyl spacer incorporated in $\mathbf{L^{2.2}}$ and was again synthesised in an analogous fashion.

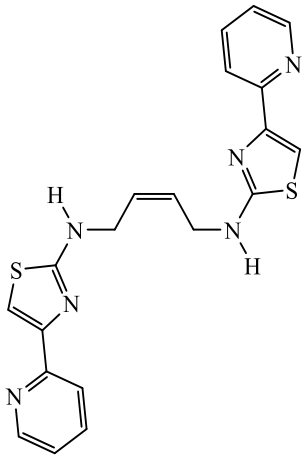

Figure 2.4.1. *Ligand* $\boldsymbol{L^{2.3}}$

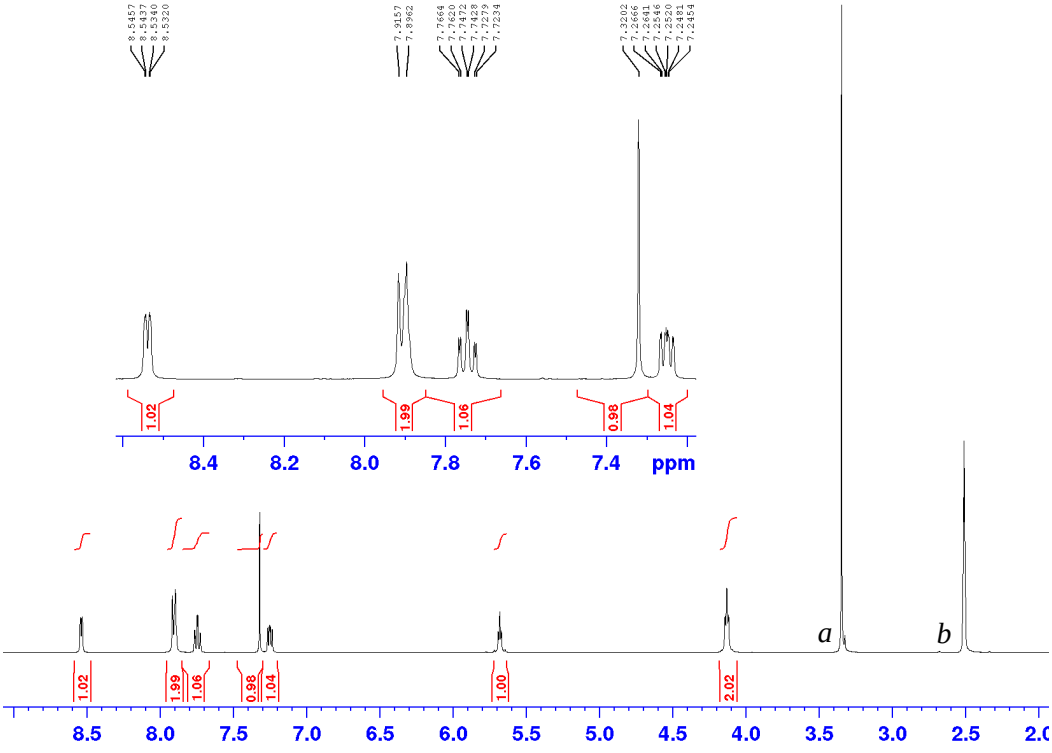

Figure 2.4.2. *^{1}H NMR of ligand* $\boldsymbol{L^{2.3}}$ *a = water impurity and b = $(CD_3)(CHD_2)SO$.*

Reaction of $\mathbf{L}^{2.3}$ with $Cu(trif)_2$ in $MeNO_2$ gave a tan coloured solution from which a dark brown crystalline material was deposited upon slow diffusion of diisopropylether. Single-crystal X-ray diffraction analysis revealed that in the solid state a dinuclear assembly compromising of two ligand strands, two Cu(II) ions and two triflate anions had formed (Fig. 2.4.3). In this structure each of the ligand strands are not seen to intertwine as expected of the '*helicate*' architecture so the $[(\mathbf{L}^{2.3})_2Cu_2(trif)_2]^{2+}$ complex can therefore be classified as a mesocate as seen previously in the $[(\mathbf{L}^{\mathbf{2.1}})_2Cu_2(trif)_2]^{2+}$ example (Fig 2.4.3). However, in this complex each of the two Cu(II) metal ions display a 6-coordinate geometry which compromises of four N···Cu coordination bonds from one of each ligand strands chelating pyridyl-thiazole units as well as two O···Cu coordination bonds, one from each bridging triflate anion. In this complex the anion interaction is further supplemented by hydrogen bonding interactions with the ligand strands amine units, one to each oxygen atom from each of the two amine –NH unit of the same ligand strand (Fig. 2.4.3). It is worth noting that in a repeat solid-state study of this reaction undertaken in identical reaction conditions similar dark blue crystal were analysed by single-crystal X-ray diffraction. The expected $[(\mathbf{L}^{\mathbf{2.3}})_2Cu_2(trif)_2)]^{2+}$complex was again confirmed although proved to have subtle differences when compared with the previous structure (Fig. 2.4.4). In this example the two triflate anions incorporated within the structure were not seen to bridge the two Cu(II) ions, intern giving the metal centres a 5-coordinate geometry which compromises of four N···Cu and one O···Cu coordination bond. However, this is a timely reminder that a crystal structure is a "snap-shot" of the molecular structure and that certainly the coordination of weakly binding anions (trif, BF_4 and ClO_4) should be treated with caution.

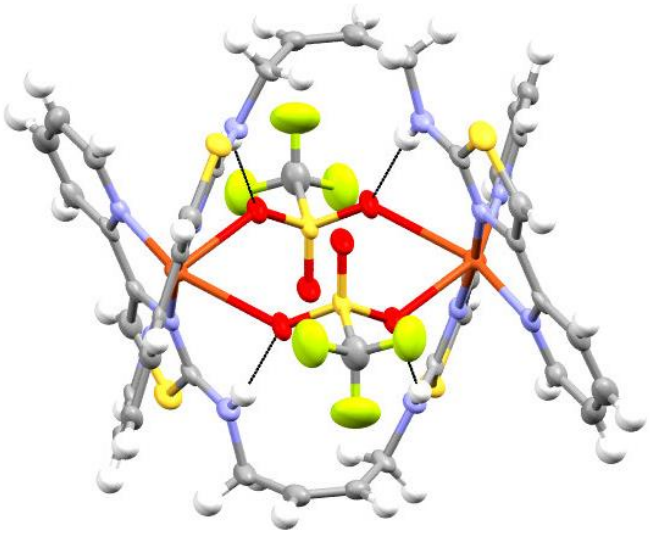

Figure 2.4.3. *The X-ray structure of* $[(\mathbf{L}^{2.3})_2Cu_2(trif)_2)]^{2+}$ *showing the coordination and hydrogen bonding of the triflate anions. Thermal ellipsoids shown at the 50% probability level. Selected anions and atoms omitted for clarity*.

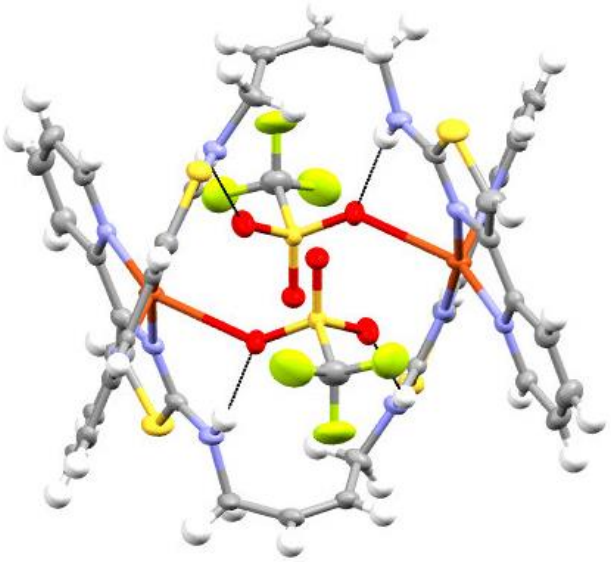

Figure 2.4.4. *The X-ray structure of* $[(\mathbf{L}^{2.3})_2Cu_2(trif)_2)]^{2+}$ *showing the coordination and hydrogen bonding of the triflate anions. Thermal ellipsoids shown at the 50% probability level. Selected anions and atoms omitted for clarity*.

2.5 Conclusion

In this work we have shown that diamines, by a simple three step synthesis procedure, can be used to produce a series of bis-bidentate ligands $\mathbf{L^{2.1}}$, $\mathbf{L^{2.2}}$ and $\mathbf{L^{2.3}}$ and these form a variety of different helicate species with Cu(II). Incorporated within each of the ligand's central spacer group are two secondary amine domains which were shown to interact with a variety of different anion species via hydrogen bonding interactions. As a result of the nature of these interactions with different anions as well as the length of the ligands central spacer unit a different array of helicate type structures can be formed i.e. helicate, mesocate, circular helicate.

Interestingly, it was also found that the examples which incorporated the use of $Cu(BF_4)_2$ salts together with phosphate anion underwent a further reaction whereby a complexed phosphate anion formed $O_{4-n}P(-O-BF_3)n$ (where n = 1 or 2) bond(s) with surrounding the tetrafluoroborate counterion(s). Specifically, it was observed that ligand $\mathbf{L^{2.1}}$ formed a trinuclear circular helicate motif which contained a central phosphate anion that had formed a P-O-B covalent bond with a single tetrafluoroborate anion to give $[(\mathbf{L^{2.1}})_3Cu_3(PO_4BF_3)]^{3+}$. The longer and more flexible butyl spacer unit contained within ligand $\mathbf{L^{2.2}}$ provided greater flexibility and resulted in a dinuclear mesocate complex which allowed the formation of two P-O-B bonds with two separate tetrafluoroborate anions to give $[(\mathbf{L^{2.2}})_2Cu_2(PO_4(BF_3)_2)]^{+}$. Quite why this unprecedented reaction is observed is difficult to rationalise. However, it is possible that the tetrafluoroborate anions are brought into close proximity to the phosphate anion by coordination to the Cu(II) ion and this close proximity facilitates reaction between the phosphate oxygen atom and the tetrafluoroborate anion. This is supported by the product complex $[(\mathbf{L^{2.2}})_2Cu_2(PO_4(BF_3)_2)]^{+}$ which contains coordination bonds between the fluoride atom and Cu(II).[89]

3. 2, 2-Diphenyl bridged Ligand $L^{3.1}$

3.1. Synthesis of Ligand $L^{3.1}$

The ligand $L^{3.1}$ was synthesised in good yield from readily available materials as illustrated by the four-step procedure below (Scheme 3.1.1).

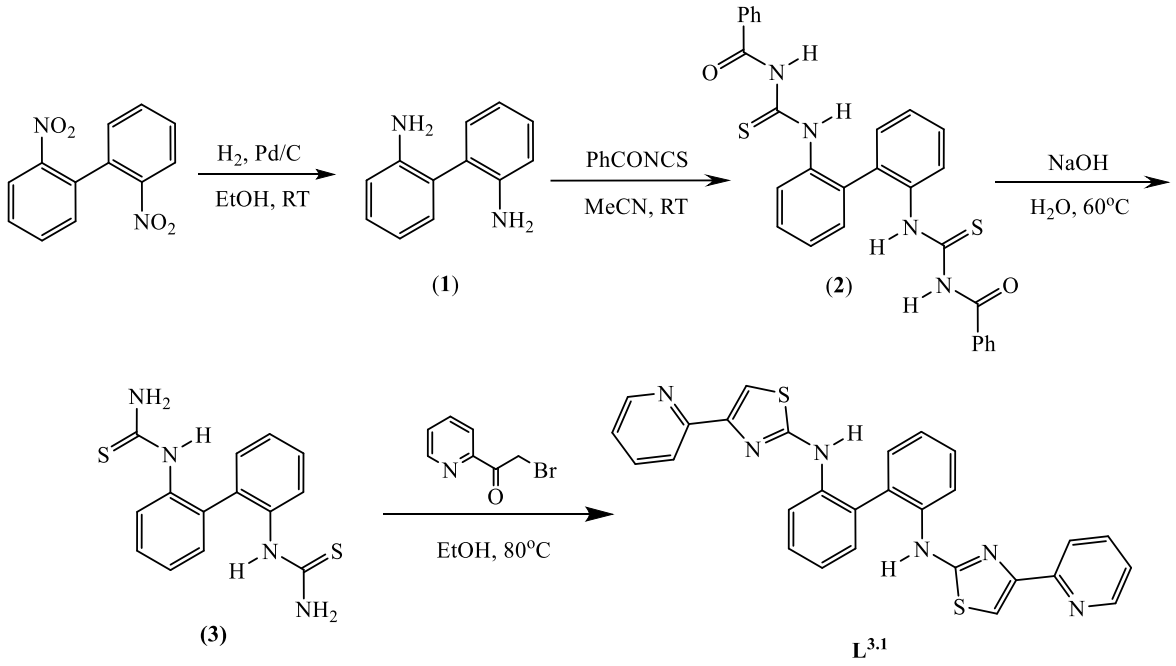

Scheme 3.1.1. *Synthesis of ligand* ***L***$^{3.1}$

The diamino-biphenyl precursor (**1**) was produced via hydrogenation of 2,2'-diamino-1,1'-biphenyl under a hydrogen gas atmosphere in absolute ethanol in the presence of a palladium on carbon catalyst. After 24 hours the absence of the staring material indicated that the reaction was complete, and the remaining insoluble catalyst was removed from the mixture by filtration and the remaining solution was reduced to dryness in *vacuo*. The resultant crude pale brown oil (**1**) showed the characteristic ^{1}H NMR signals that are expected for this compound (i.e. two multiplets at ppm respectively) and the purity was deemed sufficient for the product (**1**) to be used in the following reaction step without further purification.

The benzoylated bis-thiourea (**2**) was produced by reaction of crude 2,2'-diamino-1,1'-biphenyl[90] with 2.1 equivalents of benzoyl isothiocyanate. The resultant solid was filtered, and the crude product was then washed with methanol and dried to give intermediate (**2**). ^{1}H NMR showed the characteristic signals that are expected for this compound, i.e. two singlets at ~ 11 ppm corresponding to the unsymmetrical urea unit as well as three aromatic benzoyl and four aromatic phenyl signals (Fig. 3.1.1). Mass spectroscopic analysis gave an ion at *m/z* = 511 corresponding to the desired compound (e.g. $\{M + H\}^{+}$).

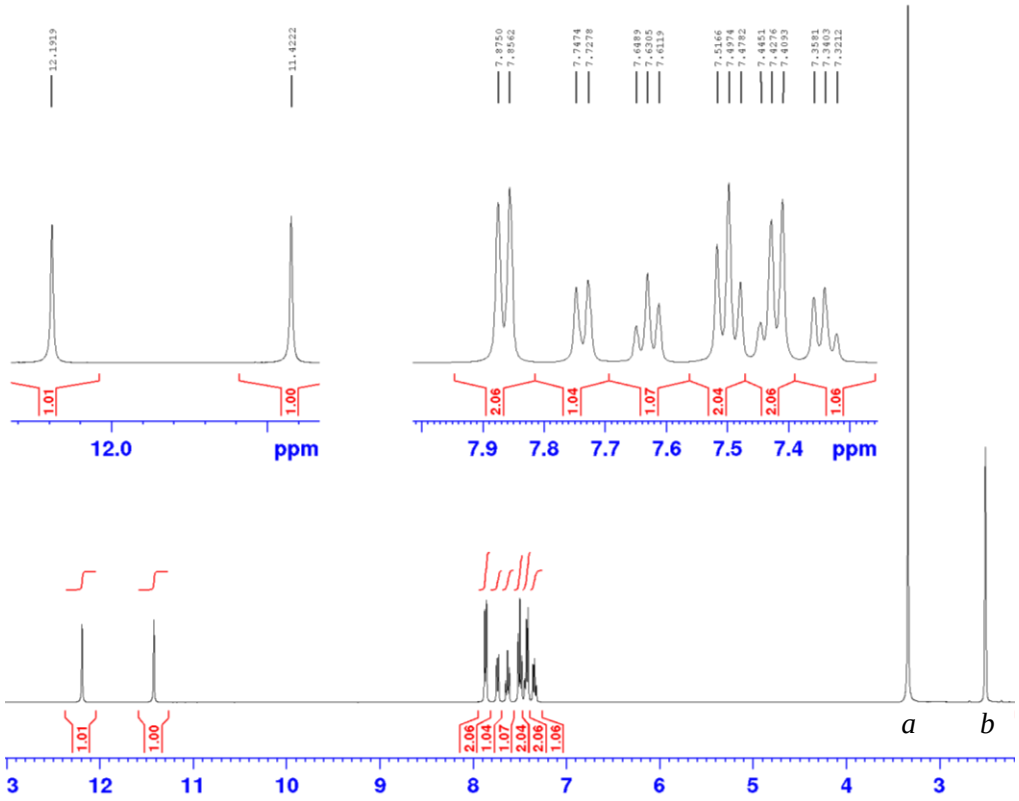

Figure 3.1.1. *^{1}H NMR of benzoylated thiourea product (**1**) a = water impurity and b = $(CD_3)(CHD_2)SO$.*

The benzoylated bis-thiourea was then hydrolysed by treatment with 6.2 equivalents of sodium hydroxide in water to give the bis-thiourea (**3**). ^{1}H NMR for this product was broad and difficult to assign (as with similar thiourea compounds described earlier) and the spectra displayed only 2 board signals (Fig. 3.1.2). This is possibly a result of restricted rotation influenced by inter-molecular and possibly intra-molecular hydrogen bonding as discussed previously. Furthermore, no aromatic signals corresponding to the benzoyl units or signals from the benzoylated urea groups were observed. Further analysis by ESI-MS observed an ion at *m/z* = 303 corresponding to the desired compound (e.g. $\{M + H\}^{+}$).

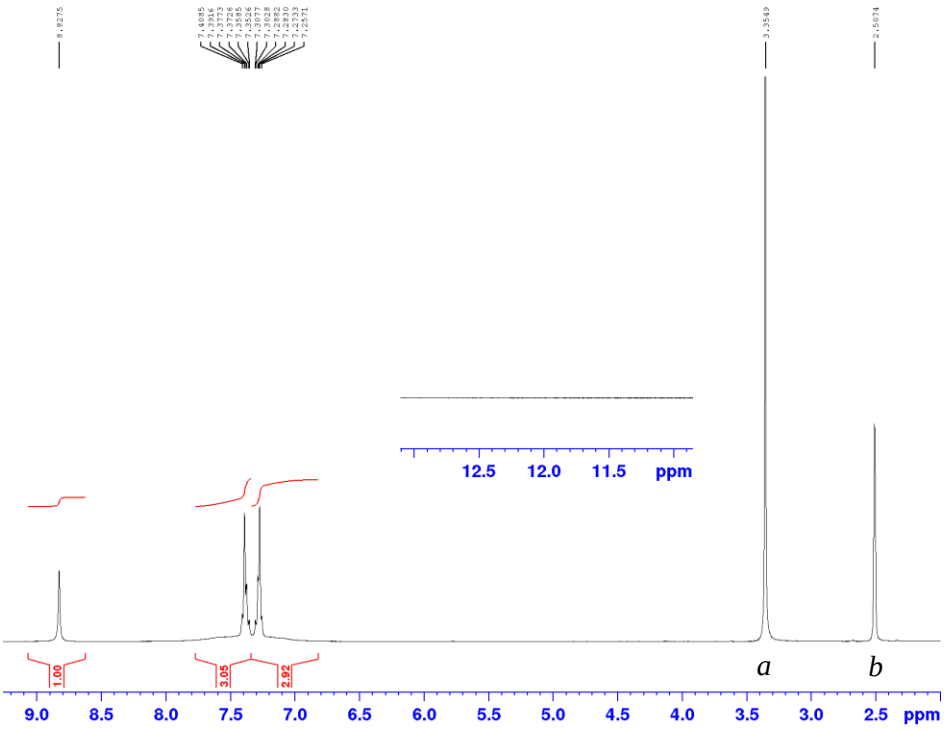

Figure 3.1.2. *^{1}H NMR of the tris-thiourea product (**2**) a = water impurity and b = $(CD_3)(CHD_2)SO$.*

The final step involved a Hantzsch thiazole type reaction of the bis-thiourea intermediate (**3**) with 2.1 equivalents of α-bromoacetylpridine followed by neutralisation of the resulting hydrobromide salt with excess ammonia and gave the targeted bis-bidentate ligand (**L**$^{3.1}$). The formation of this ligand was confirmed by ^{1}H NMR (Fig. 3.1.3) which gave the signals that are expected for this compound *i.e.* four aromatic mono-substituted pyridyl signals, one thiazole singlet, one amine (broad singlet at 6.96 ppm) and four aromatic signals corresponding to the central biphenyl spacer unit. This was again supported by ^{13}C NMR which showed at total of 14 aromatic signals and an ion was observed in the ESI-MS at m/z = 505 corresponding to the desired compound (e.g. $\{M + H\}^{+}$).

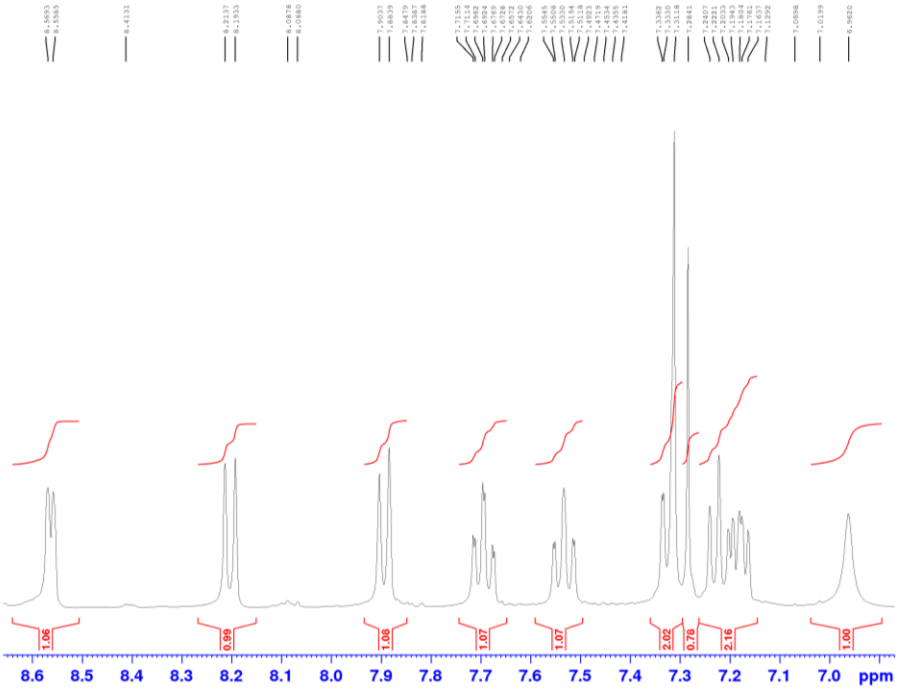

Figure 3.1.3. *Aromatic region of the ^{1}H NMR ($CDCl_3$) of ligand* ***L***$^{3.1}$.

The ligand **L**$^{3.1}$ contains two pyridyl-thiazole domains bridged by a 3,3'-diamino-2,2'-biphenyl spacer group. Furthermore, the two pyridyl-thiazole donor units have been previously shown to act as an excellent bidentate binding chelate to a variety of different metal ions.[84] Also contained within the ligand strand are two secondary amine units, which are well known to act as hydrogen bond donors to anions.[8]

3.2 Coordination Chemistry of $L^{3.1}$

Reaction of $\mathbf{L^{3.1}}$ with one equivalent of $Cu(ClO)_4$ in MeCN gave a pale blue solution from which was deposited a homogeneous blue crystalline material upon slow diffusion of diisopropyl ether. The solid-state structure was determined by single-crystal X-ray diffraction. In the solid-state a simple mono-nuclear complex is formed (i.e. $[(\mathbf{L^{3.1}})Cu]^{2+}$ with the ligand acting as a simple tetradentate donor coordinating the Cu(II) ion via four nitrogen donor atoms from the two bidentate pyridyl-thiazole domains. In the ligand strand there is a substantial twist about the central biphenyl spacer unit allowing the ligand to act as a donor to a single metal ion (Fig. 3.2.1). The Cu(II) metal ion adopts a distorted tetrahedral geometry with the Cu···N bonds ranging from 1.974(4) - 1.988(4) Å. The ligand's two amine units both point away from the complex and form -NH···O hydrogen bonding interactions with adjacent perchlorate counter anions. As has been described earlier, this type of behaviour is to be expected as ligands containing this type of amine unit have previously been shown to interact to both perchlorate and tetrafluoroborate anions.[83] Interestingly, it is worth noting that the interaction with the perchlorate anions results in the complex forming a 1-dimensional polymer chain in the solid-state (Fig 3.2.2).

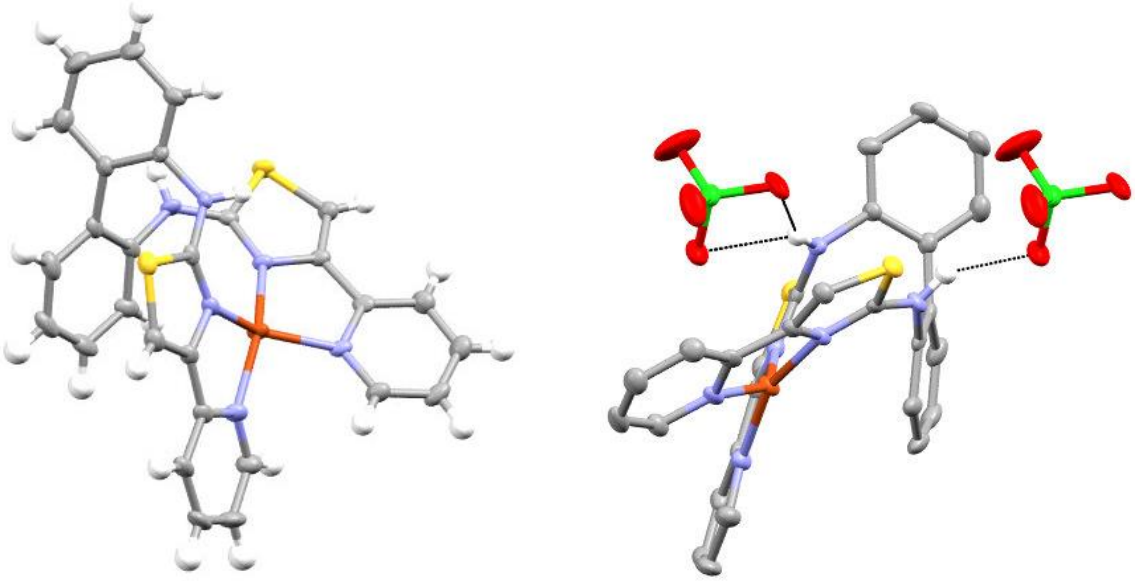

Figure 3.2.1. *X-ray structure of $[(\mathbf{L^{3.1}})Cu]^{2+}$. Thermal ellipsoids shown at the 50% probability level. Selected hydrogen atoms and anions omitted for clarity.*

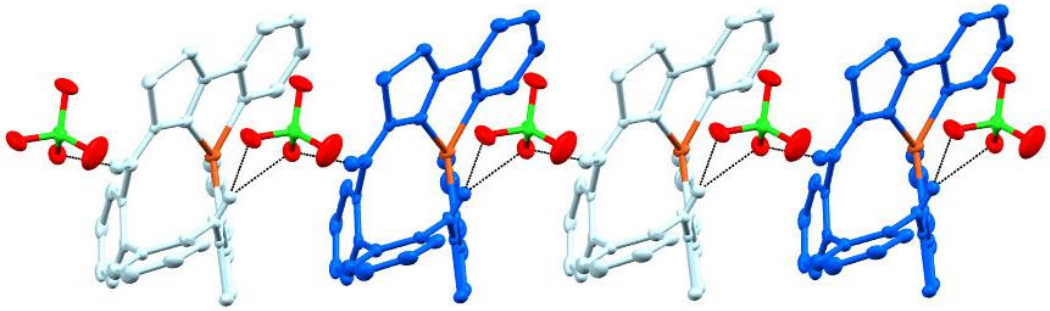

Figure 3.2.2 *X-ray structure of the interaction of a perchlorate anion with [(**L**$^{3.1}$)Cu](ClO$_4$)$_2$ resulting in a 1-dimensional polymer. Thermal ellipsoids shown at the 50% probability level. Selected hydrogen atoms omitted for clarity.*

Reaction of ligand **L**$^{3.1}$ with one equivalent of Cu(trif)$_2$ initially gives a similar blue colour to the perchlorate derivative but this significantly lightens over a period of 48 hrs. Slow diffusion of disiopropyl ether deposited a homogenous mass of light blue crystals which were examined by single crystal X-ray diffraction to reveal the structure as [(**L**^{3,2})$_4$Cu$_4$]$^{8+}$. In the solid-state this structure contains four ligand strands and four Cu(II) metal ions with the ligand partitioning into two donor domains each of which coordinates a different metal ion producing a tetranuclear circular helicate (Fig. 3.2.3 a-c). The most interesting feature of this structure is that *one* of the amine units present on the ligand strand has reacted with a molecule of acetonitrile solvent giving a new amidine-containing R$_2$N-C=NH(CH)$_3$ unit. This amidine unit is incorporated within the ligand chain producing an unsymmetrical strand containing both a bidentate pyridyl-thiazole and a tridentate amidine-pyridyl-thiazole binding domains (*i.e.* **L**$^{3.2}$ see Fig 3.3 d). In the crystal the copper ions are coordinated by a tridentate domain from one ligand and a bidentate domain for a different ligand giving a 5-coordinate metal centre which is a common coordination geometry for this metal ion (with the Cu – N bond lengths ranging from 1.926 (3) - 2.249 (4) Å). Due to the unsymmetrical nature of the ligand chain it can be considered to contain both a head and a tail and due to the copper ions preference for five coordinate geometry directional control over ligand alignment is achieved and a *head-to-tail* tetranuclear circular helicate is formed.

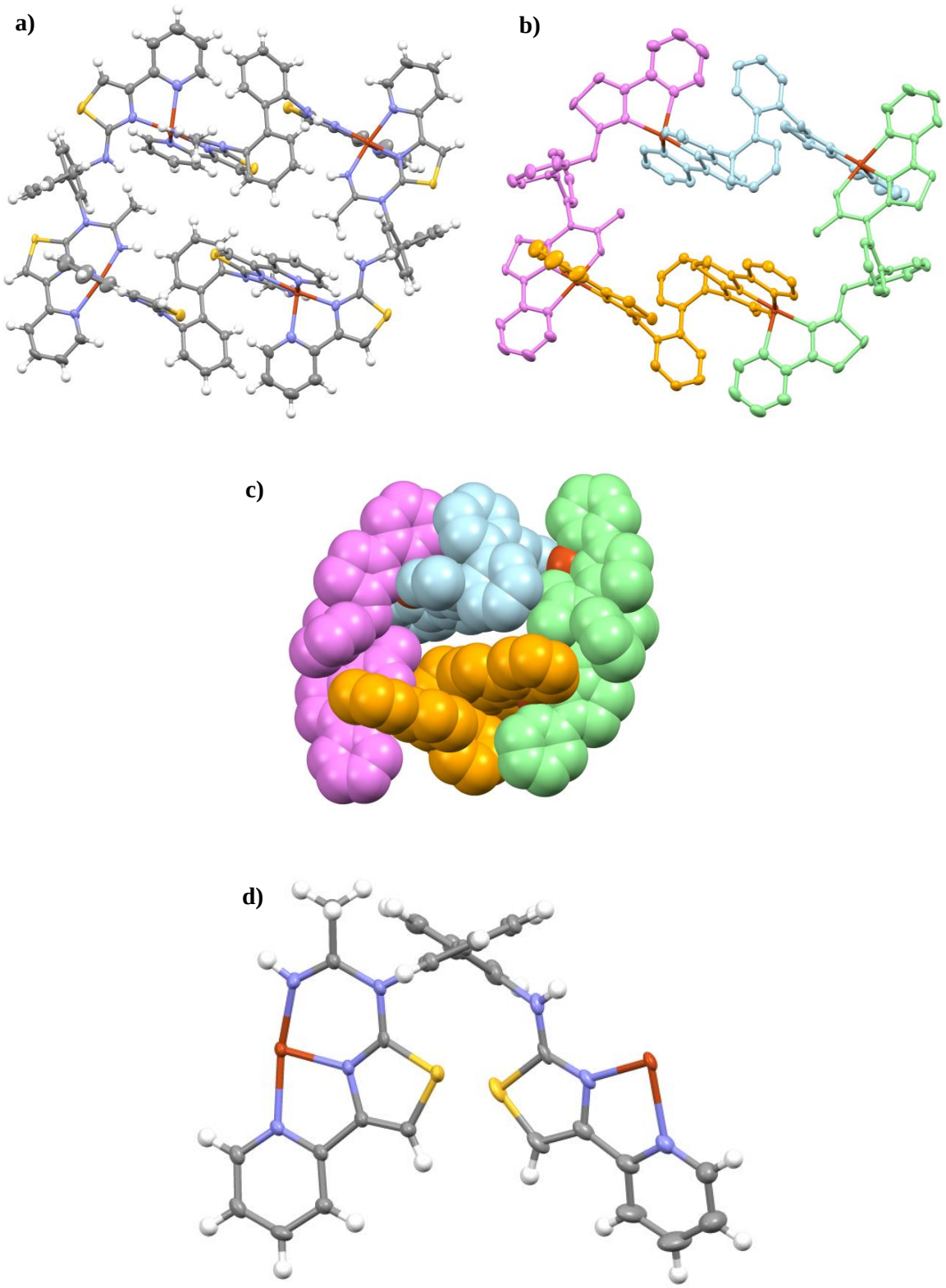

Figure 3.2.3. *Single-crystal X-ray structure of (a) – (c) $[(\mathbf{L}^{3,2})_4Cu_4]^{8+}$ and (d) view of the bidentate and tridentate domains on the ligand strand. Anions and selected hydrogen atoms omitted for clarity. Thermal ellipsoids shown at the 50% probability level.*

Examination of the ESI-MS of the reaction of $Cu(ClO_4)_2$ with $\mathbf{L^2}$ shows an ion at *m/z* = 669 corresponding to mononuclear complex $\{[(\mathbf{L^{3.1}})Cu](ClO_4)\}^+$ consistent with the solid-state observations (Fig. 3.2.4 and 3.2.5). However, also present in the ESI-MS are ions at *m/z* 1433, 2201 and 2969 which correspond to $\{[(\mathbf{L^{3.1}})_2Cu_2](ClO_4)_3\}^+$, $\{[(\mathbf{L^{3.1}})_3Cu_3](ClO_4)_5\}^+$ and $\{[(\mathbf{L^{3.1}})_4Cu_4](ClO_4)_7\}^+$. This indicates that the ligand is sufficiently flexible to adopt a number of conformations allowing a variety of polynuclear species to be accessible and in the gas phase, with the double helicate as well as the tri- and tetra- nuclear circular helicate observed. However, as would be expected due to entropic reasons, only the mononuclear species is observed in the solid-state.

Reaction of $Cu(trif)_2$ with $\mathbf{L^{3.1}}$ shows initially shows an ion at *m/z* 716 corresponding to $\{[(\mathbf{L^{3.1}})Cu](trif)\}^+$ as well as ions corresponding to the higher oligomers e.g. $\{[(\mathbf{L^{3.1}})_2Cu_2](trif)_3\}^+$, $\{[(\mathbf{L^{3.1}})_3Cu_3](trif)_5\}^+$ and $\{[(\mathbf{L^{3.1}})_4Cu_4](trif)_7\}^+$ in an analogous fashion to the perchlorate derivative (see Fig. 3.2.6). However, over the period of 48 hrs a new set of peaks, 41 mass units higher for each ligand strand, are observed in the ESI-MS indicating that the ligand has reacted with the acetonitrile solvent producing $\mathbf{L^{3.2}}$ (e.g. *m/z* 3479 corresponding to $\{[(\mathbf{L^{3.2}})_4Cu_4](trif)_7\}^+$) (Fig. 3.2.7). The most predominate peak is at *m/z* 1665 corresponding to both the singly charged dinuclear assembly $\{[(\mathbf{L^{3.2}})_2Cu_2](trif)_3\}^+$ and the doubly charged tetranuclear assembly (e.g. $\{[(\mathbf{L^{3.2}})_4Cu_4](trif)_6\}^{2+}$ (see Fig. 3.2.8). Monitoring the perchlorate derivative over a similar period of time shows no such change with all the ions corresponding to complexes containing $\mathbf{L^{3.1}}$, indicating that no reaction with acetonitrile observed (see Fig. 3.2.5).

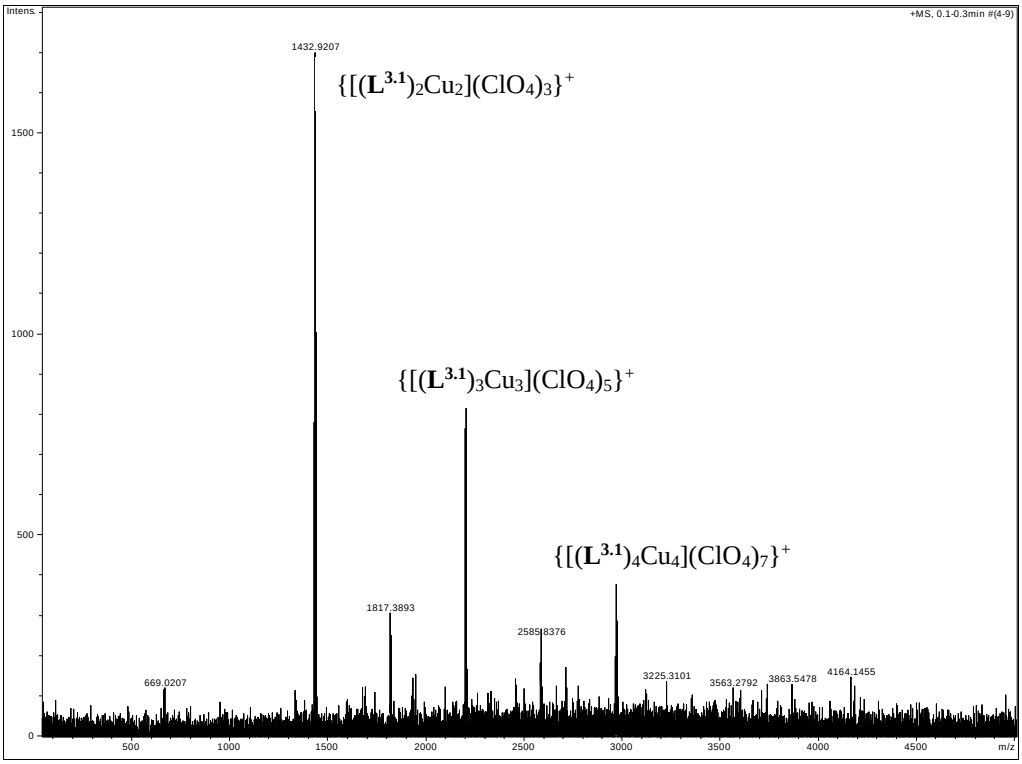

Figure 3.2.4. *ESI-MS of the reaction of $Cu(ClO_4)_2$ and* ***L*** $^{3.1}$ *(sample time 10 minutes).*

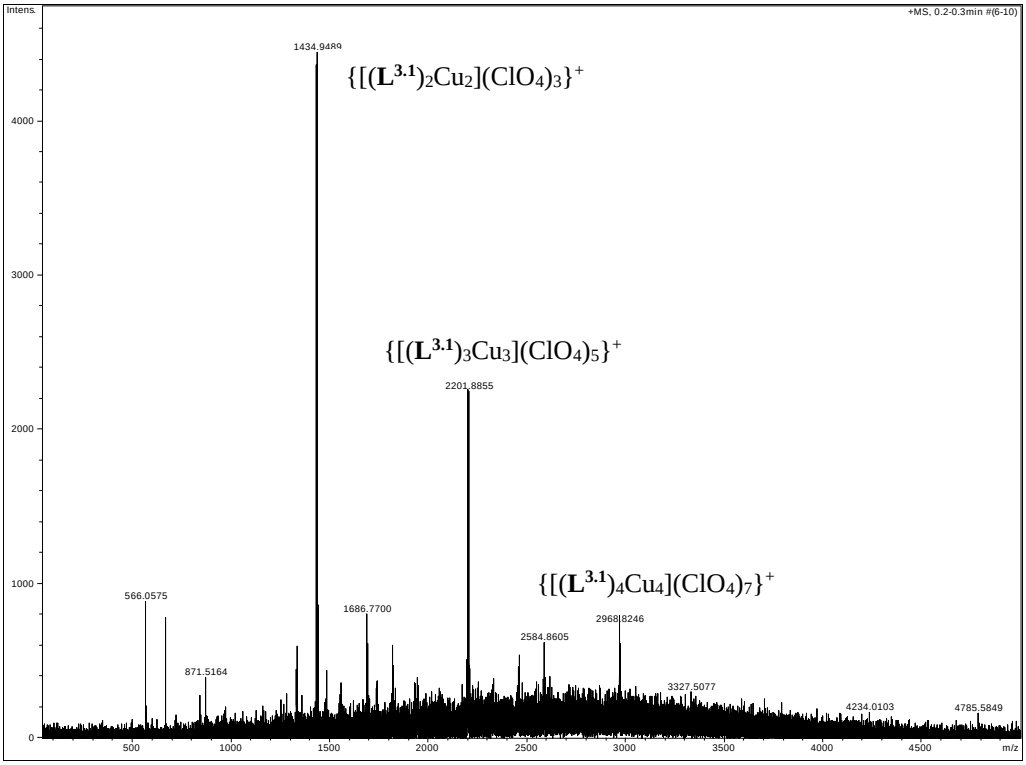

Figure 3.2.5. *ESI-MS of the reaction of $Cu(ClO_4)_2$ and* ***L*** $^{3.1}$ *(sample time 48 hrs).*

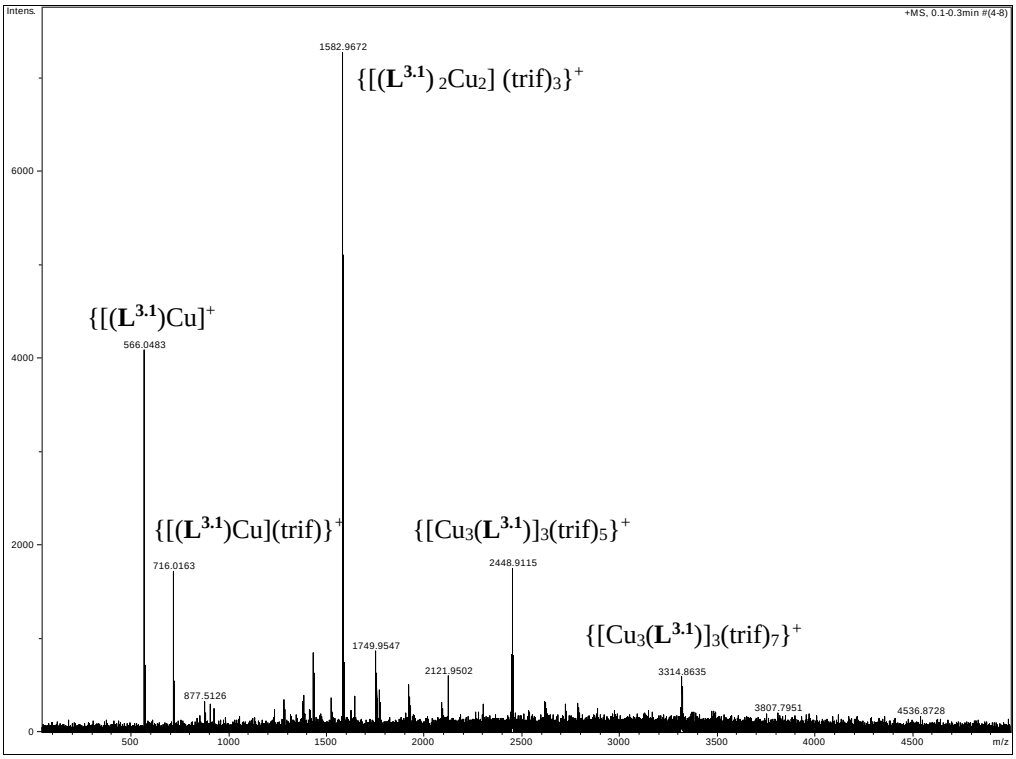

Figure 3.2.6. *ESI-MS of the reaction of Cu(triflate)$_2$ and* ***L$^{3.1}$*** *(sample time 10 minutes).*

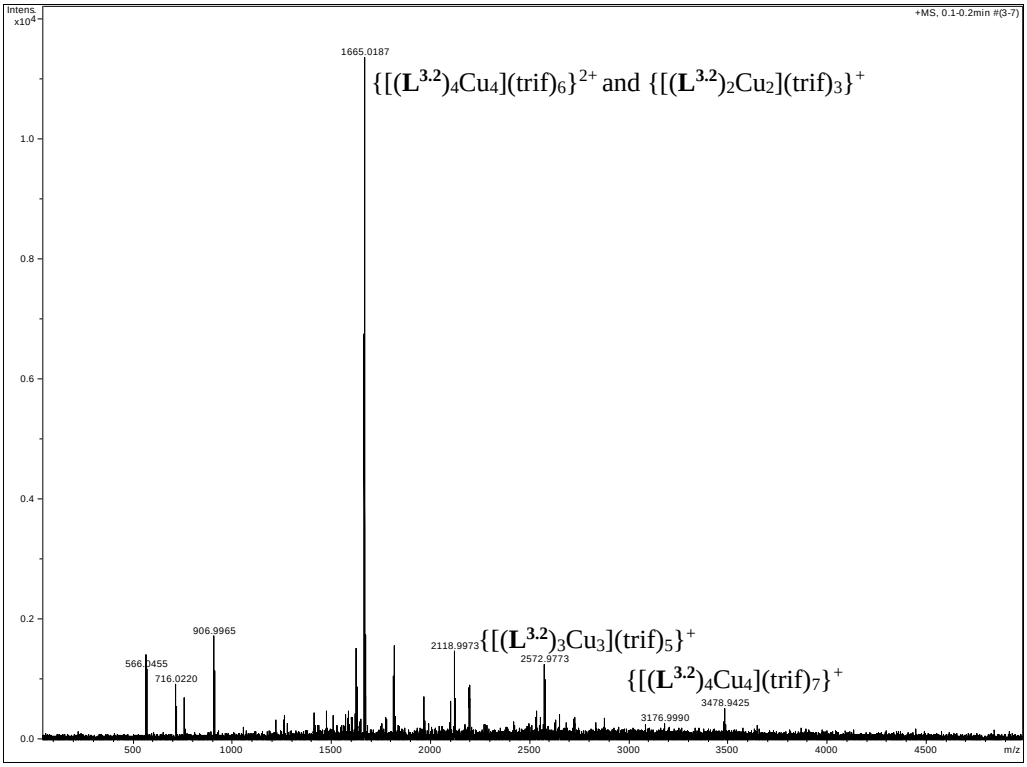

Figure 3.2.7. *ESI-MS of the reaction of Cu(triflate)$_2$ and* ***L$^{3.2}$*** *in MeCN (sample time 48 hrs).*

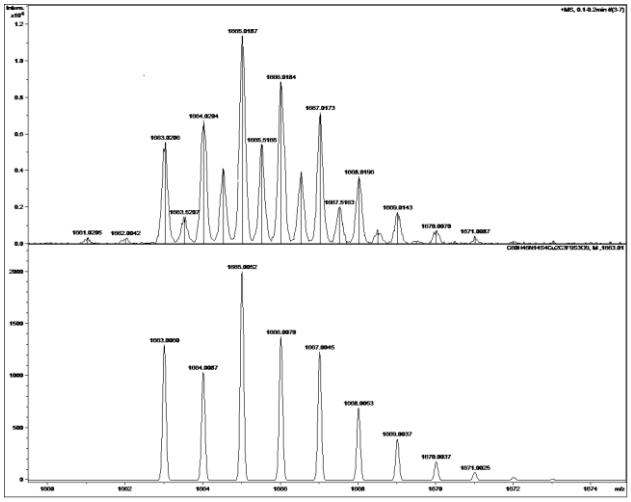

Figure 3.2.8. *ESI-MS of the reaction of Cu(triflate)$_2$ and* $\mathbf{L^{3.1}}$ *(sample time 48 hrs) showing the isotope pattern for the ion at m/z 1665 corresponding to both the singly charged {[(*$\mathbf{L^{3.2}}$*)$_2$Cu$_2$](trif)$_3$}$^+$ ion and the doubly charged {[(*$\mathbf{L^{3.2}}$*)$_4$Cu$_4$](trif)$_6$}$^{2+}$ ion.*

3.3 Conclusion

Thus, upon reaction of $\mathbf{L^{3.1}}$ with $Cu(ClO_4)_2$ the ligand acts as a simple tetradentate donor and produces a mononuclear species $[(\mathbf{L^{3.1}})Cu](ClO_4)_2$. However, upon coordination with $Cu(trif)_2$ the ligand undergoes reaction with the acetonitrile solvent producing the ligand $\mathbf{L^{3.2}}$ that contains both a bidentate and tridentate donor set. This ligand cannot now act as a simple pentadentate donor which forms the simple mononuclear complex as due to steric constraints all five *N*-donor units are unable to coordinate the same metal ion. Instead the tetranuclear *head-to-tail* circular helicate $[(\mathbf{L^{3.2}})_4Cu_4]^{8+}$ is produced. Effectively the ligand chain re-programmes itself by reaction with one equivalent of the acetonitrile solvent changing it from a tetradentate donor to one that contains both a bidentate and tridentate donor set. Exactly why the reactivity of the ligand's amine unit is anion dependant is not immediately obvious. However, we have shown that metallosupramolecular complexes that contain similar amine units strongly interact with both perchlorate and tetrafluoroborate anions and it is possible that, in forming hydrogen bonding interactions, the sp^2 hybridized nitrogen atom is stabilised reducing its nucleophilicity. Regardless, it is clear from both the mass spectrometry and X-ray studies that this reaction only occurs in the presence of the triflate anion and does not occur in the presence of perchlorate anions.

Bond	Length (Å)
Cu1⋯N7	1.974 (3)
Cu1⋯N8	1.982 (3)
Cu1⋯N10	1.985 (3)
Cu1⋯N12	1.990 (3)

Table 3.3.1. *Cu(II) bond lengths for* $[(\boldsymbol{L}^{3.1})Cu]^{2+}$

Bond	Angle (Å)
N8⋯Cu⋯N7	108.00 (11)
N10⋯Cu1⋯N7	157.67 (12)
N10⋯Cu1⋯N8.	82.29 (12)
N12⋯Cu1⋯N7	83.51 (11)
N12⋯Cu1⋯N8	144.58 (11)
N12⋯Cu1⋯N10	99.61 (12)

Table 3.3.2. *Cu(II) bond angles for* $[(\boldsymbol{L}^{3.1})Cu]^{2+}$

Bond	Length (Å)
Cu1⋯N6	1.992 (3)
Cu1⋯N7	2.249 (4)
Cu1⋯N8	2.052 (3)
Cu1⋯N9	1.926 (3)
Cu1⋯N11	1.971 (3)
Cu2⋯N1	2.048 (3)
Cu2⋯N2	1.929 (3)
Cu2⋯N4	1.961 (3)
Cu2⋯N12	2.005 (3)
Cu2⋯N13	2.245 (4)

Table 3.3.3. *Cu(II) bond lengths for* $[(\boldsymbol{L}^{3.2})_4Cu_4]^{8+}$ *(half of the molecule is generated by symmetry)*

Bond	Angle (Å)
N7···Cu1···N6	78.57 (14)
N8···Cu1···N6	96.15 (12)
N8···Cu1···N7	98.14 (12)
N9···Cu1···N6	174.72 (13)
N9···Cu1···N7	105.85 (13)
N9···Cu1···N8	80.49 (12)
N11···Cu1···N6	95.75 (13)
N11···Cu1···N7	97.81 (13)
N11···Cu1···N8	161.70 (14)
N11···Cu1···N9	86.57 (13)
N2···Cu2···N1	80.79 (13)
N4···Cu2···N1	163.25 (13)
N4···Cu2···N2	86.71 (12)
N12···Cu2···N1	98.94 (13)
N12···Cu2···N2	176.55 (13)
N12···Cu2···N4	92.87 (12)
N13···Cu2···N1	90.00 (13)
N13···Cu2···N2	104.74 (13)
N13···Cu2···N4	104.00 (13)
N13···Cu2···N12	78.69 (13)

Table 3.3.4. *Cu(II) bond angles for* $[(\mathbf{L}^{3,2})_4Cu_4]^{8+}$ *(half of the molecule is generated by symmetry).*

4. Tripodal ligand $L^{4.1}$

4.1 Synthesis of $L^{4.1}$

The tripodal ligand $L^{4.1}$ was synthesised in good yield from readily available materials as illustrated by the three-step procedure below (Scheme 4.1.1).

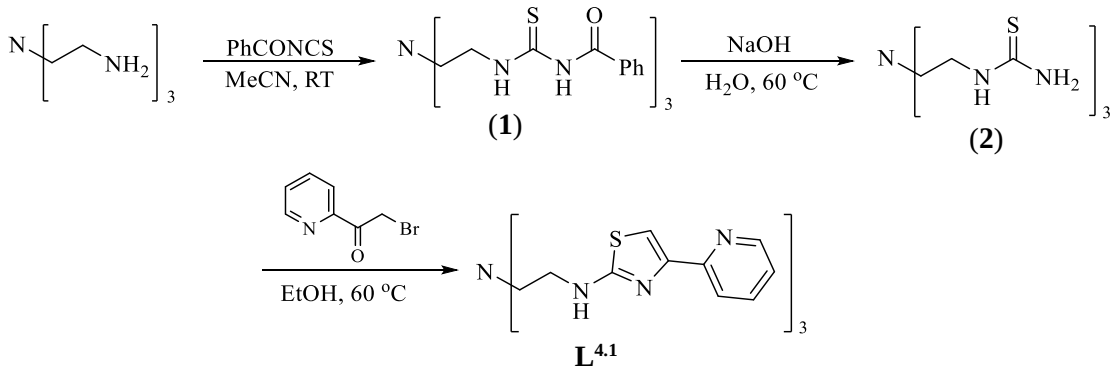

Scheme 4.1.1 *Synthesis of ligand* ***L*** $^{4.1}$

The benzoylated tris-thiourea (**1**) was produced by reaction of tris-(aminoethyl)amine with 3.2 equivalents of benzoyl isothiocyanate. The resultant solid was filtered, and the crude product was then washed with methanol and dried. ^{1}H NMR showed the characteristic signals that are indicative for this compound, i.e. two singlets at ~ 11 ppm corresponding to the unsymmetrical urea unit as well as three aromatic and two aliphatic signals (Fig. 4.1.1). ^{13}C NMR showed the expected 8 signals and mass spectroscopic analysis gave an ion at *m/z* = 636.1882 corresponding to the desired compound (e.g. $\{M + H\}^{+}$).

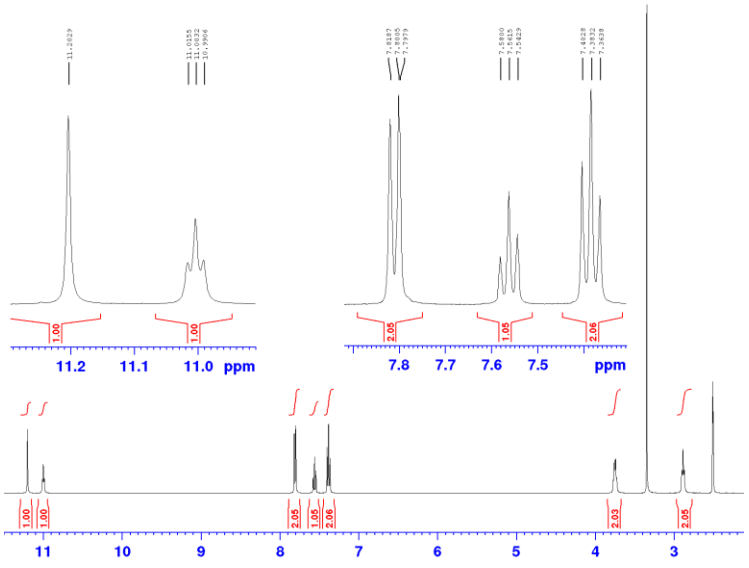

Figure 4.1.1 *^{1}H NMR of benzoylated thiourea product (**1**) a = water impurity and b = $(CD_3)(CHD_2)SO$.*

The benzoylated tris-thiourea was then hydrolysed by treatment with 10 equivalents of sodium hydroxide in water to give the tris-thiourea (**2**). ^{1}H NMR for this product was broad and difficult to assign (as with similar thiourea compounds described earlier) and the spectra displayed only four board signals (Fig. 4.1.2). This is possibly a result of restricted rotation caused by inter-molecular and intra-molecular hydrogen bonding as discussed in previous chapters. This is confirmed by single-crystal X-ray analysis, as in the solid-state an array of both intra and inter-molecular hydrogen-bonding interactions are observed (Fig 4.13). Furthermore, no aromatic signals corresponding to the phenyl unit or signals from the benzoylated urea groups were observed. Further analysis by ^{13}C NMR showed 3 signals with a signal at 183.5 ppm corresponding to the $(NH)_2C=S$ unit and an ion was observed in the ESI-MS at *m/z* = 324.1089 corresponding to the desired compound (e.g. $\{M + H\}^+$).

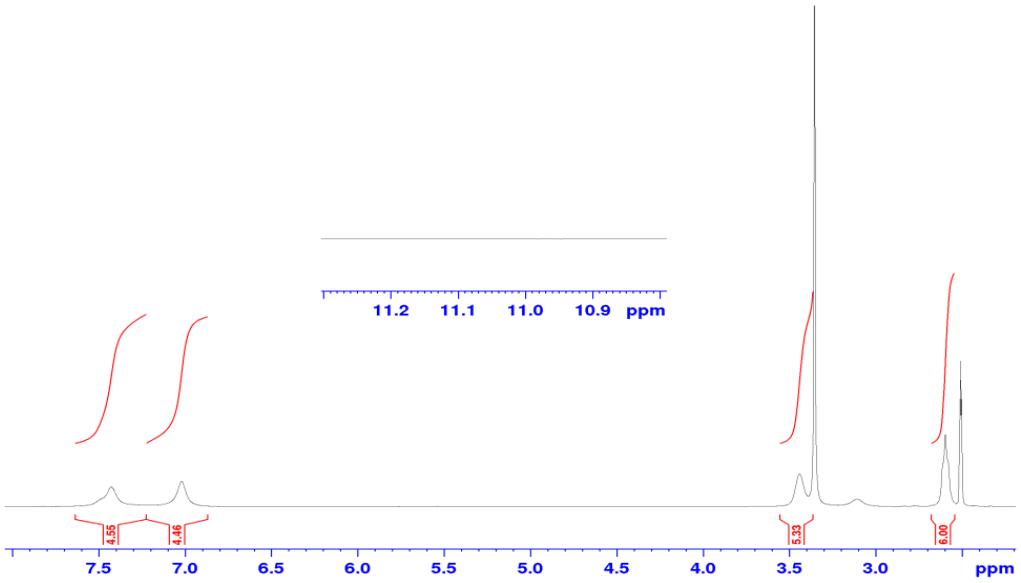

Figure 4.1.2. *^{1}H NMR of the tris-thiourea product (**2**)*

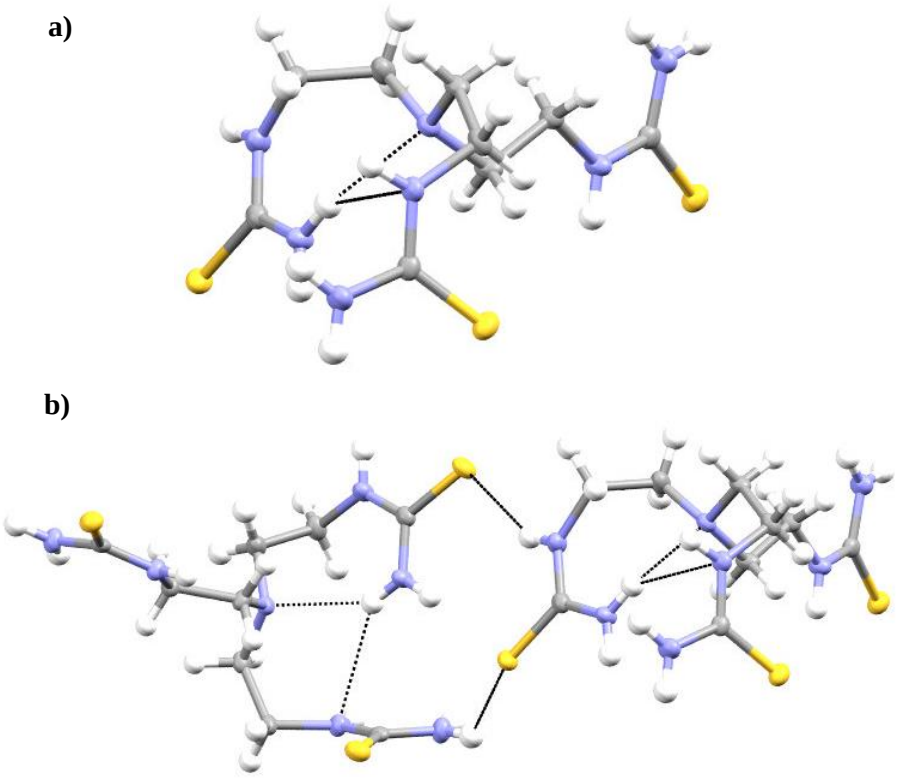

Figure 4.1.3. *Two different views of the X-ray structure of the tris-thiourea product (**2**) showing the (a) intermolecular and (b) intramolecular hydrogen bonding of the compounds thiourea groups. Thermal ellipsoids shown at the 50% probability level. Selected atoms and anions omitted for clarity.*

The final step involved a Hantzsch type reaction where the tris-thiourea intermediate was reacted with 3.1 equivalents of α-bromoacetylpridine followed by neutralisation of the resulting hydrobromide salt with excess ammonia gave the targeted tripoidal ligand (**L**$^{4.1}$). Formation of this ligand was confirmed by ^{1}H NMR (Fig. 4.1.4) which gave the signals that are expected for this compound *i.e.* four aromatic mono-substituted pyridyl signals, one thiazole singlet, one amine (triplet at 7.65 ppm) and two aliphatic methylene signals. This was again supported by ^{13}C NMR which showed at total of 8 aromatic and 2 aliphatic signals and an ion was observed in the ESI-MS at m/z = 627.1881 corresponding to the desired compound (e.g. {M + H}+).

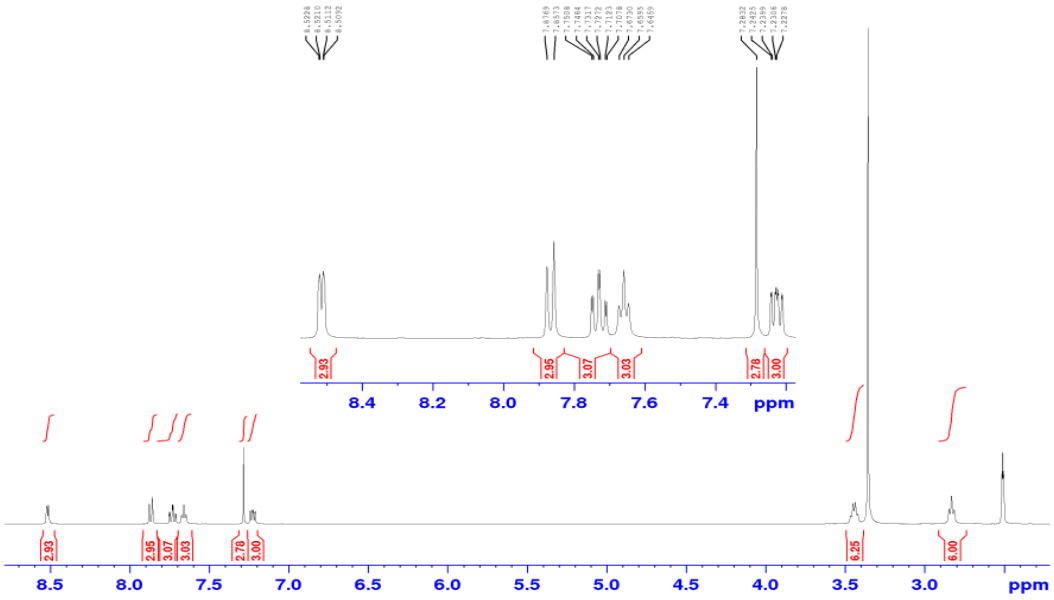

Figure 4.1.4. *^{1}H NMR of ligand* ***L***$^{4.1}$

The ligand **L**$^{4.1}$ contains three pyridyl-thiazole domains linked by a single nitrogen atom bridged via three separate amino-ethyl chains. To a degree the ligand can be thought of as ditopic as it contains three pyridyl-thiazole domor units which have been shown previous shown to act as excellent bidentate binding chelate to a variety of different metal ions. Furthermore, it also contains three amine units which are well known to act as hydrogen bond donors to anions.

4.2 Coordination chemistry of $L^{4.1}$ in organic solvents

Reaction of ligand $\mathbf{L^{4.1}}$ with 1.5 equivalents of $Cu(BF_4)_2$ in nitromethane resulted in a blue coloured solution. ESI-MS analysis of the solution gave an ion at m/z 1877 corresponding to the formation of the trinuclear assembly $\{[(\mathbf{L^{4.1}})_2Cu_3](BF_4)_5\}^+$. Upon slow diffusion of diisopropyl ether blue crystals were deposited from the solution and analysis by single-crystal X-ray diffraction confirmed the formation of the $[(\mathbf{L^{4.1}})_2Cu_3]^{6+}$ species in the solid state (Fig. 4.2.1). In this structure each of the three bidentate pyridyl-thiazole binding domains from the same ligand coordinate to three individual copper metal ions. Each copper ion is coordinated by a total of four *N*-donor atoms, two from a bidentate pyridyl-thiazole domain from each ligand strand. Within the centre of the complex a cavity is formed and is occupied by a single BF_4^- anion (Fig. 4.2.1 a and b). The encapsulated tetrahedral anion is held in place by three Cu···F coordination bonds as well as a further three -NH···F hydrogen bonding interactions from one of the ligands amine units below the tri-metallic plane (Fig. 4.2.1 c). The three remaining amine units of the ligand above the tri-metallic plane form hydrogen bonding interactions with the BF_4^- anion.

It is worth noting that in this complex the encapsulated BF_4^- anion is substitutionally disordered with a Cl^- anion (Fig. 4.2.2) and the BF_4^- anion had to be restrained using *SADI*, *SIMU*, *DELU*, and *ISOR* in the least-squares refinement. This disorder refined well and converged with an occupancy of 0.34 Cl and 0.66 BF_4. The chloride anion could arise from the original Cu(II) salt or some impurity and despite the disorder the change balance will remain the same *e.g.* $Anion^{1-}$.

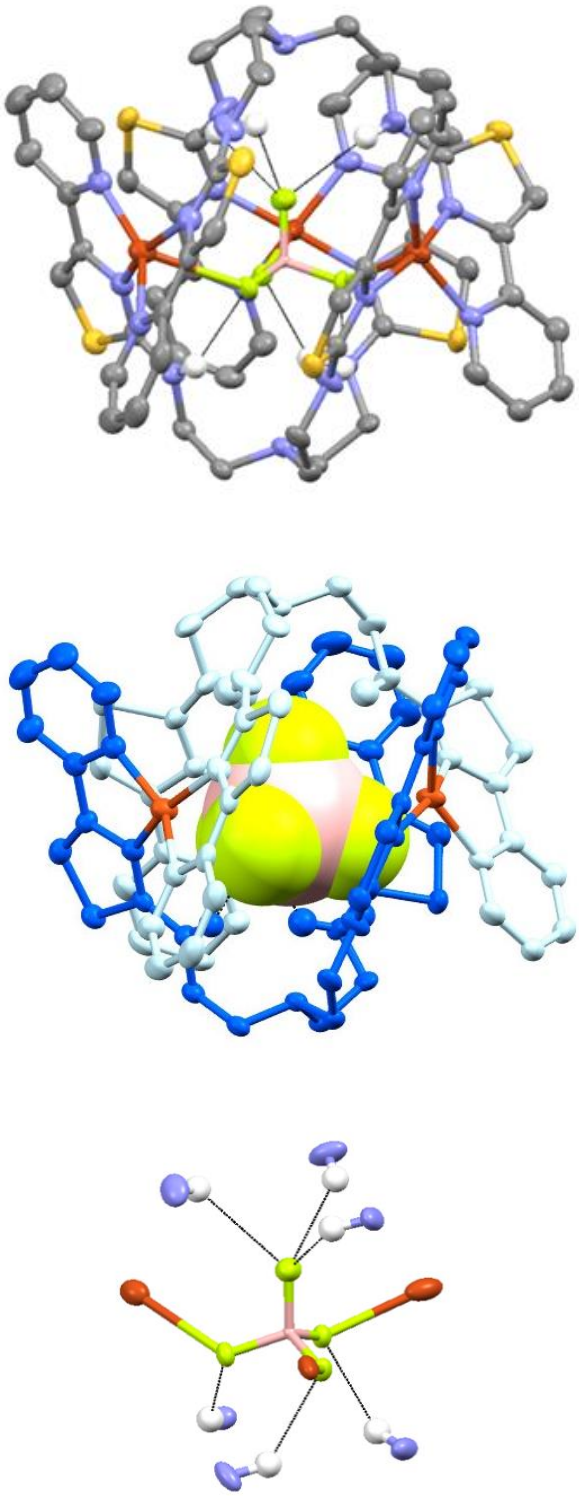

Figure 4.2.1. *a) Three different views of the X-ray structure of the major component* $[(\boldsymbol{L}^{4.1})_2Cu_3(BF_4)_{0.66}(Cl)_{0.34}]^{5+}$ *showing the coordination and hydrogen bonding of the tetrafluoroborate anion b) Thermal ellipsoids shown at the 50% probability level. Selected hydrogen atoms and anions omitted for clarity.*

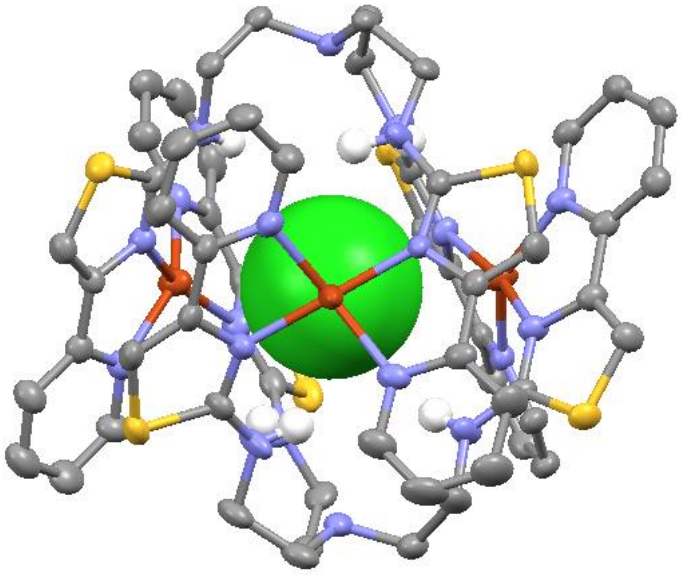

Figure 4.2.2. *The single-crystal X-ray structure of the minor Cl^- guest of the disordered $[(\mathbf{L}^{4.1})_2Cu_3(BF_4)_{0.66}(Cl)_{0.34}]^{5+}$ molecule.*

The cavity formed by the $[(\mathbf{L}^{4.1})_2Cu_3]^{6+}$ species is capable of encapsulating other anions. Reaction of the trinuclear self-assembly with half a molar equivalent of Et_4NBr in nitromethane also resulted in a dark blue solution that, when subjected to slow diffusion with diisopropyl ether, yielded a homogeneous mass of large blue crystals. Single-crystal X-ray analysis revealed that an isostructural $[(\mathbf{L}^{4.1})_2Cu_3]^{6+}$ motif had formed but, in this molecule, the encapsulated BF_4^- anion within the core cavity had been displaced by a bromide anion to give $[(\mathbf{L}^{4.1})_2Cu_3(Br)]^{5+}$ (Fig. 4.2.3). The comparably smaller radii of the bromide anion results in the anion being positioned to one side of the formed cavity. Therefore, this anion is unable to simultaneously form coordination bonds to all three copper ions and only coordinates to two of the metals (Cu···Br coordination distance = 2.8842(9) Å and remaining Cu···Br distance = 3.414 Å). Again, in this molecule the bonding of the anion is supplemented by hydrogen bonding interactions from the ligand's amine units. However, in this complex two of the amine units from both ligands (above and below the tri-metallic plane) form interactions to the anion.

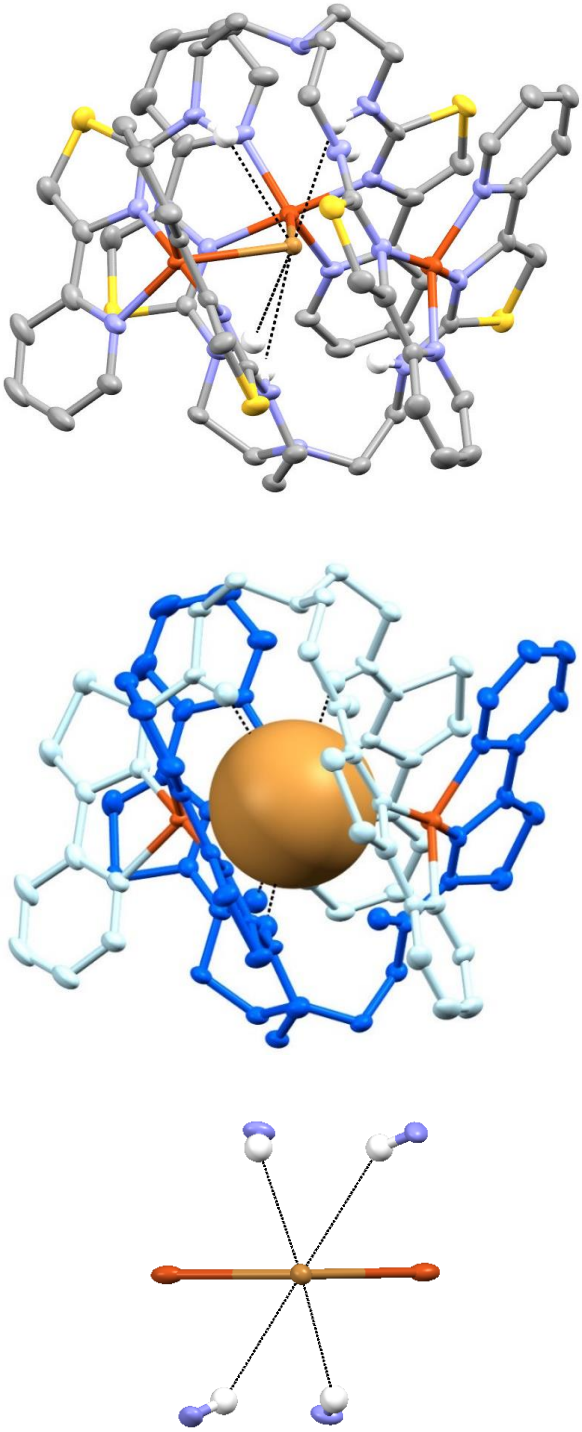

Figure 4.2.3. *Three different views of the X-ray structure of* $[(\mathbf{L}^{4.1})_2Cu_3(Br)]^{5+}$ *showing the coordination and hydrogen bonding of the anion. Thermal ellipsoids shown at the 50% probability level. Selected hydrogen atoms and anions omitted for clarity.*

The cavity formed within the $[(\mathbf{L}^{4.1})_2Cu_3]^{6+}$ complex does not exclusively act as a host to tetrahedral and spherical anions. Upon reaction with one equivalent of Na_2SiF_6 in nitromethane resulted in a dark taupe coloured solution after a period of 24 hrs. When exposed to slow diffusion of diisopropyl ether, a homogeneous mass of large, dark brown crystals was deposited. Analysis by single-crystal X-ray diffraction revealed the octahedral divalent SiF_6^{2-} anion was encapsulated within the central cavity to give $[(\mathbf{L}^{4.1})_2Cu_3(SiF_6)]^{4+}$ (Fig. 4.2.4). In this complex three of the hexafluorosilicate fluorine atoms point upward and are above the tri-metallic plane and three point downward below the tri-metallic plane. Again the anion is bound within the cavity by both Cu···F coordination bonds as well as -NH···F hydrogen bonding interactions. Each of the three copper metal ions forms two coordination bonds with two of the anions fluorine atoms, resulting in the copper metal centres being six-coordinate. In this complex all three amine units from both ligands provide hydrogen bonding interactions to the anion resulting in the SiF_6^{2-} anion receiving a total of six Cu···F coordination bonds and six -NH···F hydrogen bonding interactions.

Complex	$[(\mathbf{L}^{4.1})_2Cu_3(BF_4)]^{5+}$	$[(\mathbf{L}^{4.1})_2Cu_3(Br)]^{5+}$	$[(\mathbf{L}^{4.1})_2Cu_3(SiF_6)]^{4+}$
Cu···N bond length (Å)	1.947(4) - 2.020(4)[a]	1.934(4) - 2.079(4)[a]	1.948(4) - 2.072(4)[a]
Cu···Anion bond length (Å)	2.365(4)[b]	2.8842(9)[b]	2.386(3) - 2.430(3)[c]
-NH···Anion bond length (Å)	2.373-2.531[c] 2.274-2.302[d]	3.156[c] 2.894-2.869[d]	2.219-2.253[c] 2.239-2.304[d]

Table 4.2.1. Bond lengths of a series of encapsulation products of trimetallic host $[(\mathbf{L}^{4.1})_2Cu_3]^{6+}$.

[a] = range of bond lengths; [b] = average of the bond lengths; [c] = average bond length above the Cu_3 plane; [d] = average bond length below the Cu_3 plane

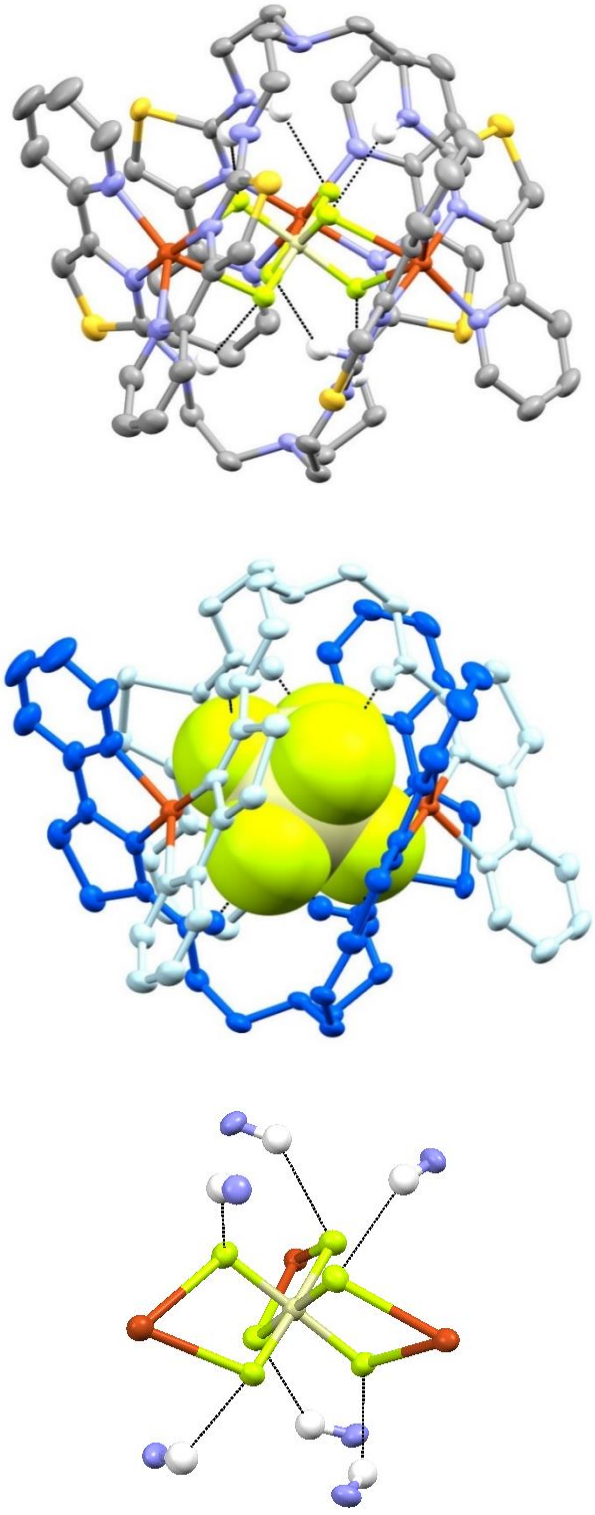

Figure 4.2.4. *Three different views of the X-ray structure of* $[(\mathbf{L^{4.1}})_2Cu_3(SiF_6)]^{4+}$ *showing the coordination and hydrogen bonding of the anion. Thermal ellipsoids shown at the 50% probability level. Selected hydrogen atoms and anions omitted for clarity.*

4.3 Coordination chemistry in aqueous media.

Most interestingly, the self-assembled $[(\mathbf{L}^{\mathbf{4.1}})_2Cu_3]^{6+}$ species will form and have the capability to encapsulate a range of different anions in competitive aqueous media. When assembled these systems display a variety of different coloured solutions (Fig. 4.3.1 a). For example, it was seen that when two equivalents of $\mathbf{L}^{\mathbf{4.1}}$ was reacted with three equivalents of $Cu(ClO_4)_2.6H_2O$ in $MeCN/H_2O$ (1:4) a pale brown/tan solution was formed. However, on addition of one molar equivalent (per $[(\mathbf{L}^{\mathbf{4.1}})_2Cu_3]^{6+}$ unit) of $Bu_4NH_2PO_4$ to this system resulted in an intense lime coloured solution. This solution was slowly allowed to reduce (*i.e.* evaporation of the organic solvent) which resulted in a large homogenous mass of lime green crystals and a colourless solution.

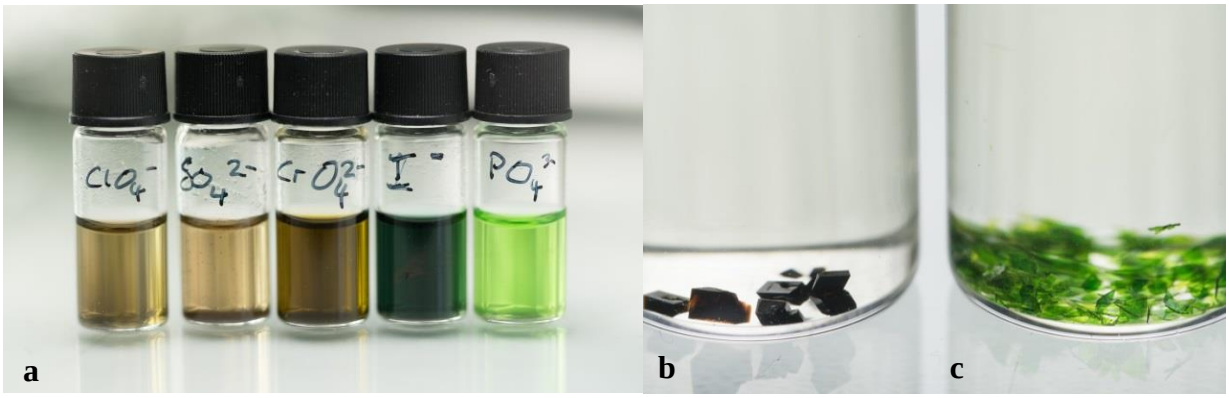

Figure 4.3.1. *Aqueous solutions of the $[(\mathbf{L}^{\mathbf{4.1}})_2Cu_3]^{6+}$ species with a variety of different anions displaying the variety of colours (a). A solution of $[(\mathbf{L}^{\mathbf{4.1}})_2Cu_3]^{6+}$ which was reacted with (b) HSO_4^- and (c) $H_2PO_4^-$ and deposits brown and green crystals respectively.*

Analysis by single-crystal X-ray diffraction confirmed the formation of the $[(\mathbf{L}^{\mathbf{4.1}})_2Cu_3]^{6+}$ species, however this example featured a single phosphate anion encapsulated within the central cavity to give $[(\mathbf{L}^{\mathbf{4.1}})_2Cu_3(PO_4)]^{3+}$ (Fig. 4.3.2). The structure of this complex is analogous to that seen previously with the tetrafluoroborate anion with Cu···O coordination bonds and -NH···O hydrogen bonding interactions. It is worth noting that the reaction was carried out using mono basic $Bu_4NH_2PO_4$ and the anion has undergone full deprotonation to form the tri-basic species. This was confirmed by the presence of three perchlorate counter ions in the solid-state structure e.g. $[(\mathbf{L}^{\mathbf{4.1}})_2Cu_3(PO_4)](ClO_4)_3$.

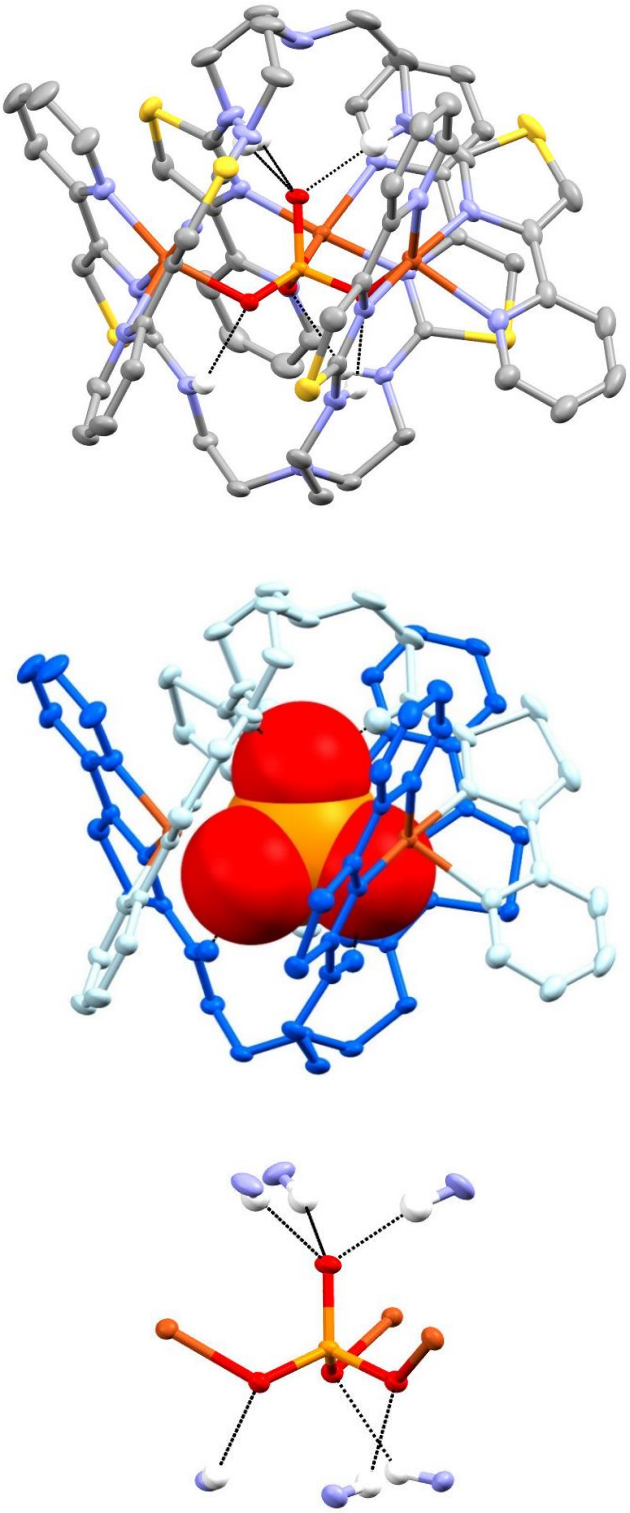

Figure 4.3.2. *Three different views of the X-ray structure of* $[(\mathbf{L}^{4.1})_2Cu_3(PO_4)]^{3+}$ *showing the coordination and hydrogen bonding of the anion. Thermal ellipsoids shown at the 50% probability level. Selected hydrogen atoms and anions omitted for clarity.*

In addition to the $[(\mathbf{L}^{4.1})_2Cu_3(PO_4)]^{3+}$ complex other examples of encapsulated tetrahedral anions have also been observed to form in aqueous solutions. These included VO_4^{3-}, WO_4^{2-}, CrO_4^{2-}, SO_4^{2-} and AsO_4^{3-} (Fig. 4.3.3 – Fig. 4.3.7). The listed complexes were prepared in an identical fashion by the addition of one molar equivalent of counter ion to one molar equivalent of the $[(\mathbf{L}^{4.1})_2Cu_3]^{6+}$ complex. All these EO_4^{n-} complexes displayed isostructural anion encapsulation motifs to the $[(\mathbf{L}^{4.1})_2Cu_3(PO_4)]^{3+}$ species *i.e.* three Cu···Anion coordination bonds and three -NH···Anion hydrogen bonds. In all these examples similar solubility characteristics were observed when the solutions were prepared in $MeCN/H_2O$ (1:4). Upon slow evaporation of the organic solvent crystalline material was deposited within a matter of minutes or days depending on what counter ion and/or concentration was used.

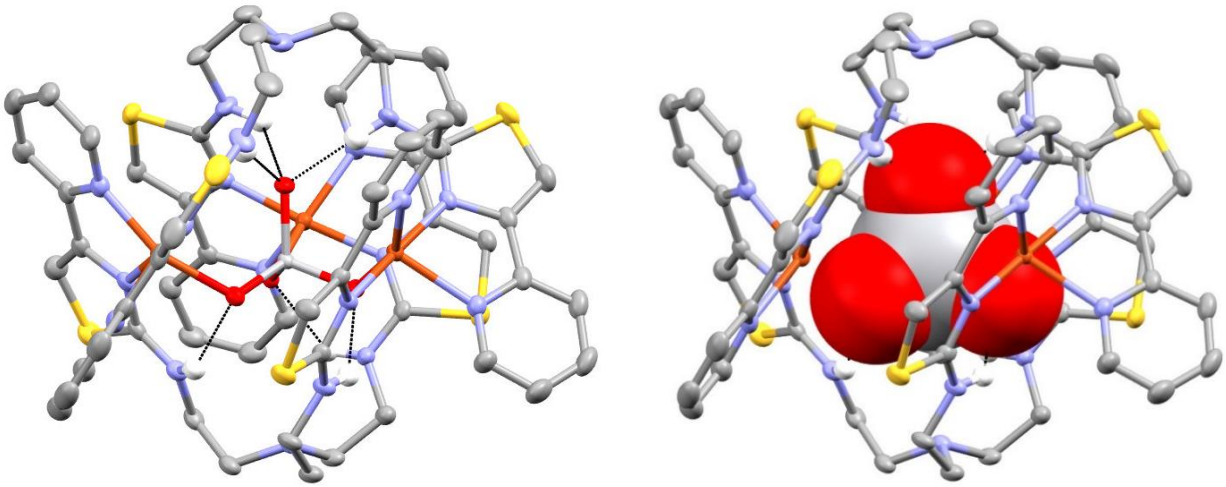

Figure 4.3.3. *Two different views of the X-ray structure of* $[(\boldsymbol{L}^{4.1})_2Cu_3(VO_4)]^{3+}$. *Thermal ellipsoids shown at the 50% probability level. Selected hydrogen atoms and anions omitted for clarity.*

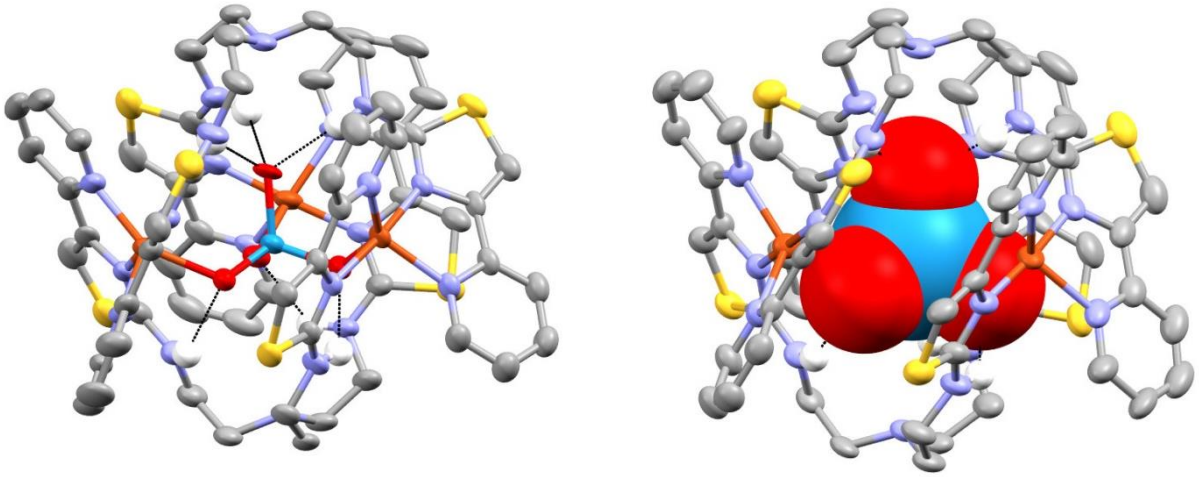

Figure 4.3.4. *X-ray structure of* $[(\mathbf{L}^{4.1})_2Cu_3(WO_4)]^{4+}$. *Thermal ellipsoids shown at the 50% probability level. Selected hydrogen atoms and anions omitted for clarity.*

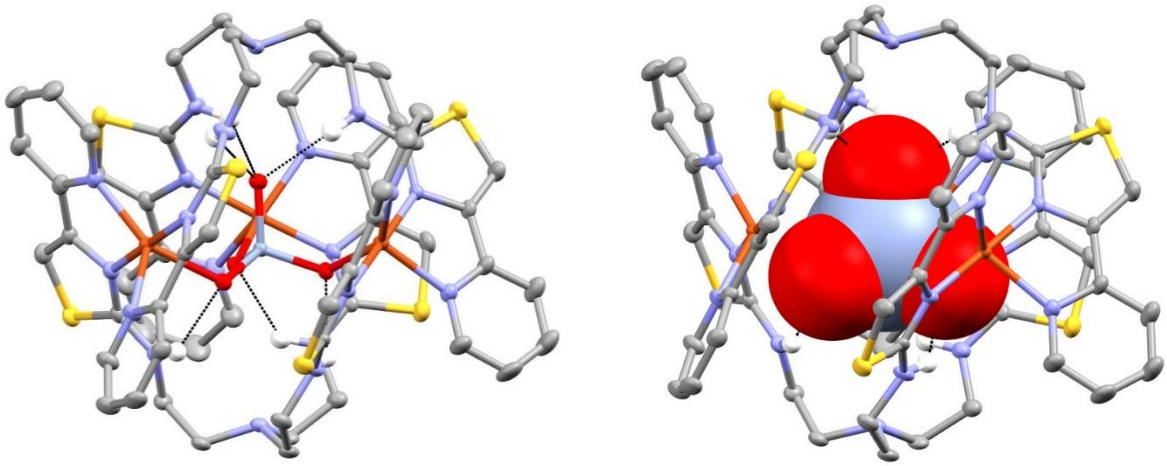

Figure 4.3.5. *Two different views of the X-ray structure of* $[(\mathbf{L}^{4.1})_2Cu_3(CrO_4)]^{4+}$. *Thermal ellipsoids shown at the 50% probability level. Selected hydrogen atoms and anions omitted for clarity.*

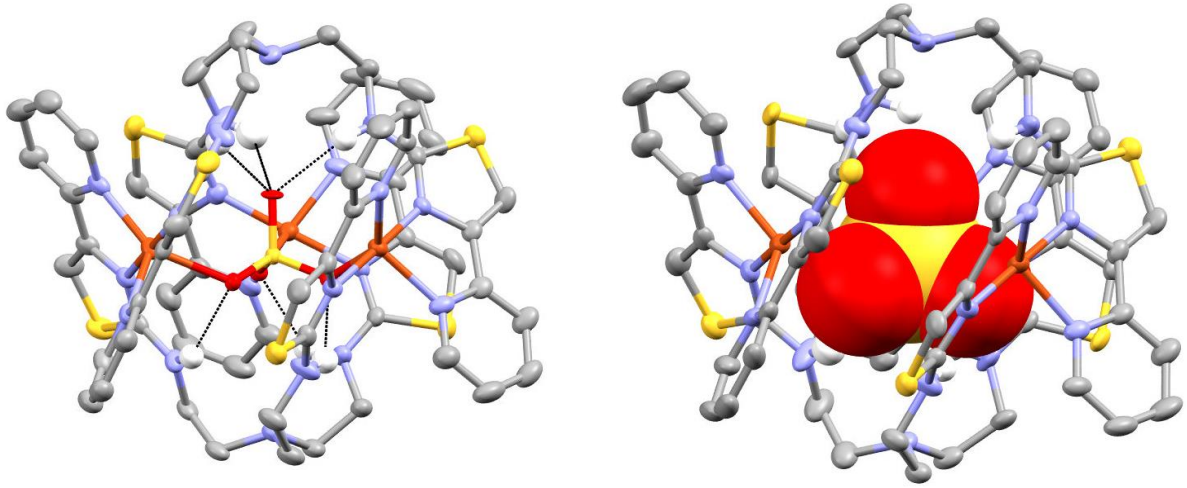

Figure 4.3.6. *Two different views of the X-ray structure of* $[(\mathbf{L}^{4.1})_2Cu_3(SO_4)]^{4+}$. *Thermal ellipsoids shown at the 50% probability level. Selected hydrogen atoms and anions omitted for clarity.*

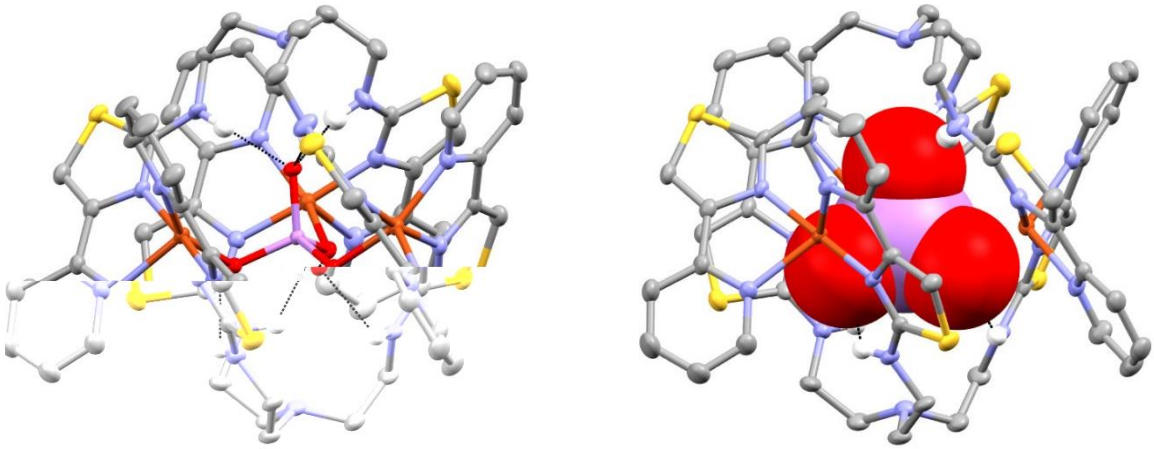

Figure 4.3.7. *Two different views of the X-ray structure of* $[(\mathbf{L}^{4.1})_2Cu_3(AsO_4)]^{3+}$. *Thermal ellipsoids shown at the 50% probability level. Selected hydrogen atoms and anions omitted for clarity.*

However, the inclusion of the tetrahedral IO_4^- anion to the $[(\mathbf{L^{4.1}})_2Cu_3]^{6+}$ system resulted in a different encapsulation motif as the trinuclear assembly is replaced with a tetranuclear species e.g. "$[(\mathbf{L^{4.1}})_2Cu_4]^{8+}$". When one molar equivalent of $NaIO_4$ was reacted with one molar equivalent of the $[(\mathbf{L^{4.1}})_2Cu_3]^{6+}$ complex, the anion undergoes hydrolysis to form the octahedral IO_6^{2-} anion which is encapsulated within a tetranuclear $[(\mathbf{L^{4.1}})_2Cu_4(IO_6)(H_2O)_2]^{4+}$ assembly (Fig. 4.3.8).[91,92] In this structure two of each ligand's bidentate pyridyl-thiazole binding domains coordinate two copper metal ions as seen in the previous $[(\mathbf{L^{4.1}})_2Cu_3]^{6+}$ complexes. Whilst, the remaining pyridyl-thiazole bidentate domain from each ligand coordinates its own copper metal ion as well as a molecule of water on each completing the five-coordinate motif. The central encapsulated IO_6^{2-} anion is held within the self-assembled cavity via all four copper ions providing Cu···O coordination bonds to two separate oxygen atoms. This is again further complimented by the formation of six -NH···O hydrogen bonding interactions (three above and three below the tri-metallic plane). In this structure the inner cavity of the complex has significantly expanded when compared with the previous examples c.f. $[(\mathbf{L^{4.1}})_2Cu_3(SiF_6)]^{4+}$. This increase in the cavity volume is a consequence of the complex accommodating the larger anion and displays that the flexibility within the ligand allows such a change in the self-assembly process to take place.

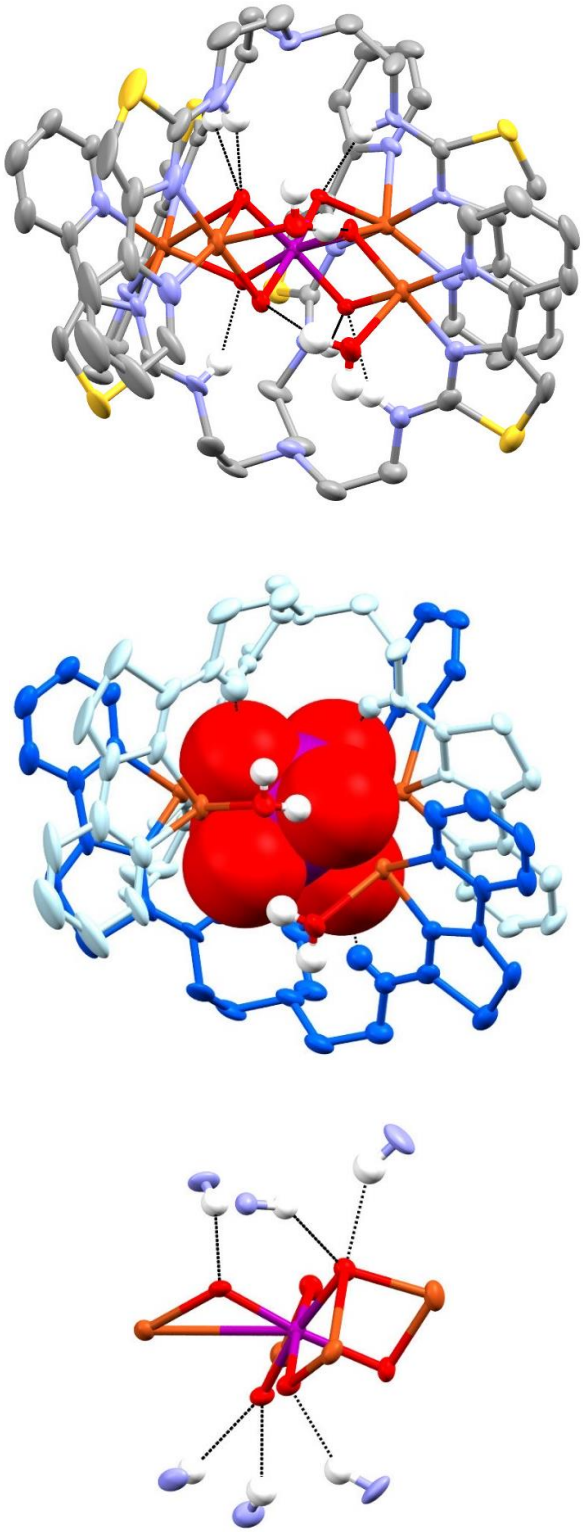

Figure 4.3.8. *Three different views of the X-ray structure of* $[(\mathbf{L}^{4.1})_2Cu_4(IO_6)(H_20)_2]^{4+}$ *showing the coordination and hydrogen bonding of the anion. Thermal ellipsoids shown at the 50% probability level. Selected hydrogen atoms and anions omitted for clarity.*

As previously seen in organic media, the $[(\mathbf{L^{4.1}})_2Cu_3]^{6+}$ molecule is also capable of encapsulating halide anions in a competitive aqueous solvent. Reaction of $[(\mathbf{L^{4.1}})_2Cu_3]^{6+}$ with one molar equivalent of Et_4NI in $MeCN/H_2O$ (1:4) produced a dark blue solution that when subject to slow evaporation yielded a colourless solution and a mass of homogeneous dark blue crystals. The $[(\mathbf{L^{4.1}})_2Cu_3(I)]^{5+}$ structure was again determined by single-crystal X-ray diffraction (Fig. 4.3.9). In this example the molecules structure is analogous to the $[(\mathbf{L^{4.1}})_2Cu_3(Br)]^{5+}$ complex with the substitution of the bromide anion for an iodide anion. The $[(\mathbf{L^{4.1}})_2Cu_3(I)]^{5+}$ complex differs from the prior halide example in that the larger atomic radii of the iodide anion enables the anion to occupy a more central position within the molecules cavity and therefore gaining coordination bonds from *all three* Cu(II) ions. However, the spherical geometry of the anion limits it to only gaining four hydrogen bonding interactions with the ligands -NH donor units (two from each ligand as seen in the $[(\mathbf{L^{4.1}})_2Cu_3(Br)]^{5+}$ complex) (Fig. 4.3.5 c).

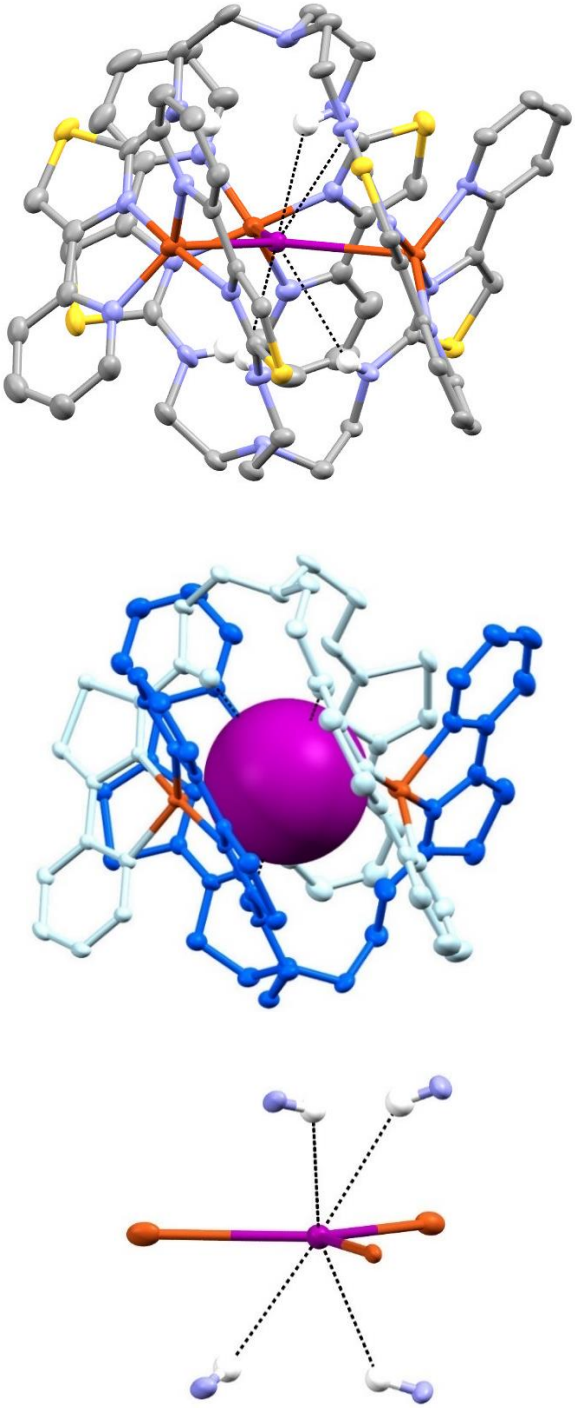

Figure 4.3.9. *Three different views of the X-ray structure of* $[\mathbf{L^{4.1}}_2Cu_3I]^{5+}$ *showing the coordination and hydrogen bonding of the anion. Thermal ellipsoids shown at the 50% probability level. Selected hydrogen atoms and anions omitted for clarity.*

In an effort to examine if the host would encapsulate mono-anionic third-row oxoanions, two equivalents of $\mathbf{L^{4.1}}$ and three equivalents of Cu(trif)$_2$ were combined with one equivalent Bu_4NHReO_4 in MeCN/H_2O (1:4). Upon slow evaporation over 48 hours dark blue crystals were deposited and analysed by single-crystal X-ray diffraction. Again, the expected $[(\mathbf{L^{4.1}})_2Cu_3]^{6+}$ motif was observed. However, in this system ReO_4 was not found to be encapsulated within the $[(\mathbf{L^{4.1}})_2Cu_3]^{6+}$ cavity but was only present as a simple counter ion. In this example a single CO_3^{2-} anion was found to be present within the assembly's central cavity giving $[(\mathbf{L^{4.1}})_2Cu_3(CO_3)]^{4+}$. In this system the central CO_3^{2-} anion was orientated pointing upward, perpendicular to the tri-metallic plane and receiving two Cu···O coordination bonds from two of the Cu(II) ions. This was intern supplemented by six -NH···O hydrogen bonding interactions to all the ligands -NH donor units. It is worth noting that a virtually identical species is observed from a system prepared from two equivalents of $\mathbf{L^{4.1}}$ with three equivalents of Cu(trif)$_2$ in MeCN/H_2O (1:4) when allowed to stand for 48 hours. It seems likely to suggest that the inclusion of the CO_3^{2-} anion arose from the presence of CO_2 within the aqueous media which undergoes hydrolysis and is encapsulated within the $[(\mathbf{L^{4.1}})_2Cu_3]^{6+}$ molecule. This type of behaviour is not unique to this system and has previously been observed in other supramolecular systems.[93–96] It is worth noting that UV-Vis studies have shown that when one equivalent of dihydrogen phosphate is added to a $[(\mathbf{L^{4.1}})_2Cu_3CO_3]^{4+}$ sample the carbonate anion is displaced in favour of the tri-anionic guest (Fig. 4.3.10). Reactions with CO_2 are not observed with the tetrafluoroborate salt and we attribute this to the low solubility of CO_2 in $MeNO_2$ (the solvent from which the crystals were deposited) rather than a strong interaction between the BF_4^- anion and the host.

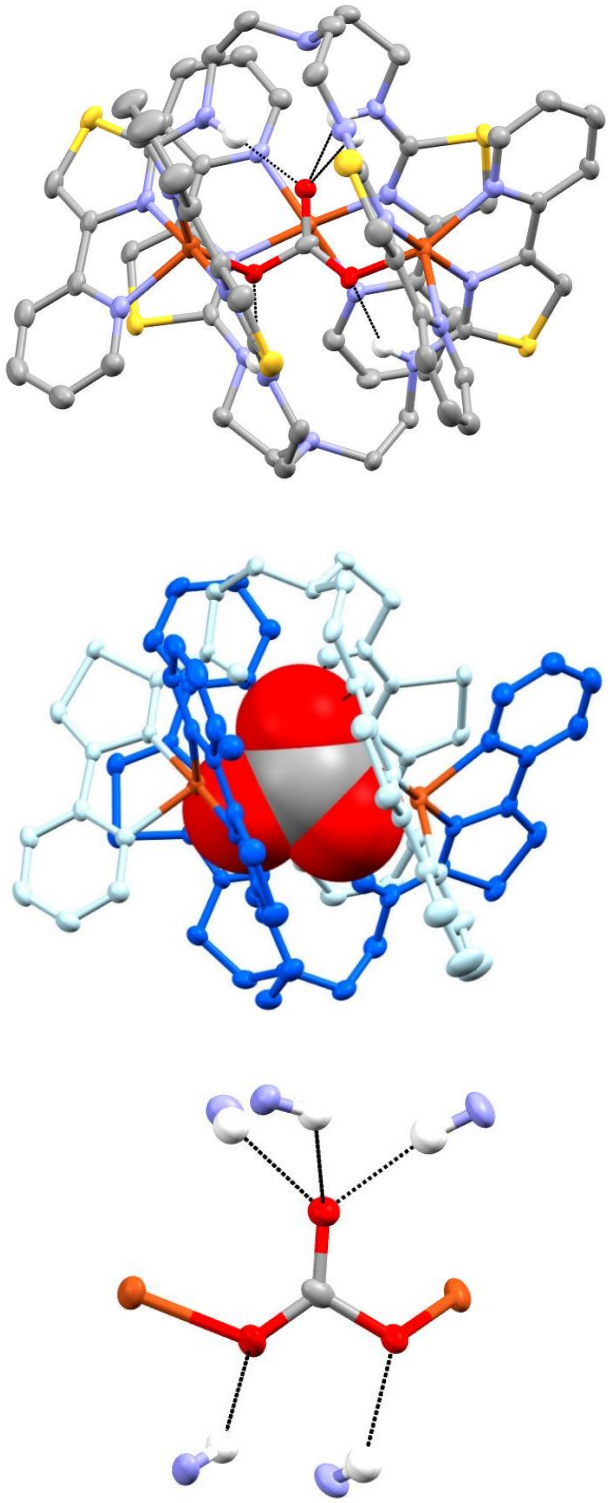

Figure 4.3.10. *Three different views of the X-ray structure of* $[(\mathbf{L}^{4.1})_2Cu_3CO_3]^{4+}$ *showing the coordination and hydrogen bonding of the anion. Thermal ellipsoids shown at the 50% probability level. Selected hydrogen atoms and anions omitted for clarity.*

Complex	$[(\mathbf{L}^{4.1}{}_2Cu_3(PO_4)]^{3+}$	$[\mathbf{L}^{4.1}{}_2Cu_3(VO_4)]^{3+}$	$[\mathbf{L}^{4.1}{}_2Cu_3(WO_4)]^{4+}$	$[\mathbf{L}^{4.1}{}_2Cu_3(CrO_4)]^{4+}$	$[\mathbf{L}^{4.1}{}_2Cu_3(SO_4)]^{4+}$
Cu···N bond length (Å)	1.967(3) – 2.233(3)[a]	1.969(2) – 2.220(2)[a]	1.942(6) – 2.120(6)[a]	1.955(3) – 2.116(3)[a]	1.951(4) – 2.100(4)[a]
Cu···Anion bond length (Å)	1.945[a]	1.953[b]	2.117[b]	2.092[b]	2.138[b]
NH···Anion bond length (Å)	2.001[c] 2.190[d]	1.999[c] 2.160[d]	2.148[c] 2.274[d]	2.206[c] 2.239[d]	2.270[c] 2.271[d]

Table 4.3.1. Bond lengths of a series of encapsulation products of trimetallic host $[(\mathbf{L}^{4.1})_2Cu_3]^{6+}$.

[a] = range of bond lengths; [b] = average of the bond lengths; [c] = average bond length above the Cu_3 plane; [d] = average bond length below the Cu_3 plane [e] = remaining Cu ···· anion bonds generated by symmetry.

Complex	$[\mathbf{L}^{4.1}{}_2Cu_3(AsO_4)]^{3+}$	$[\mathbf{L}^{4.1}{}_2Cu_4(IO_6)(H_20)_2]^{4+}$	$[\mathbf{L}^{4.1}{}_2Cu_3I]^{5+}$	$[\mathbf{L}^{4.1}{}_2Cu_3CO_3]^{4+}$
Cu···N bond length (Å)	1.972(3) – 2.194(3)[a]	1.923(7) – 2.230(6)[a]	1.938(3) – 2.005(4)[a]	1.958(3) – 2.195(3)[a]
Cu···Anion bond length (Å)	1.956[b]	1.971[b]	3.0383(7)[e]	1.963[b]
-NH···Anion bond length (Å)	1.946[c] 2.266[d]	2.200[c] 2.200[d]	3.088[c] 3.104[d]	2.156[c] 2.082[d]

Table 4.3.2. Bond lengths of a series of encapsulation products of trimetallic host $[(\mathbf{L}^{4.1})_2Cu_3]^{6+}$.

[a] = range of bond lengths; [b] = average of the bond lengths; [c] = average bond length above the Cu_3 plane; [d] = average bond length below the Cu_3 plane.

Unsymmetrical tetrahedral anions can also be included within the self-assembled cavity. For example, when the $[(\mathbf{L^{4.1}})_2Cu_3]^{6+}$ system was reacted with half a molar equivalent of $S_2O_3^{2-}$ the expected $[(\mathbf{L^{4.1}})_2(A)Cu_3]^{n+}$ capsulation motif was observed (Fig.4.3.11). Interestingly, in this example the central anion orientated itself in fashion where the sulphur atom lies along the Cu(II) plane forming a coordination bond to one of the Cu(II) metal centres and one hydrogen bonding interaction with the lower ligands -NH- unit. This results in the remaining two Cu(II) centres being coordinated by two separate oxygen atoms whilst the third oxygen atom points upward of the metallic plane forming three hydrogen bonding interactions with the upper ligands -NH- units. The formation of this encapsulated geometry is due to the localisation of the negative charge on the sulphur atoms which results in it coordinating the Cu(II) cation, as opposed to hydrogen bonding to the amine atoms.

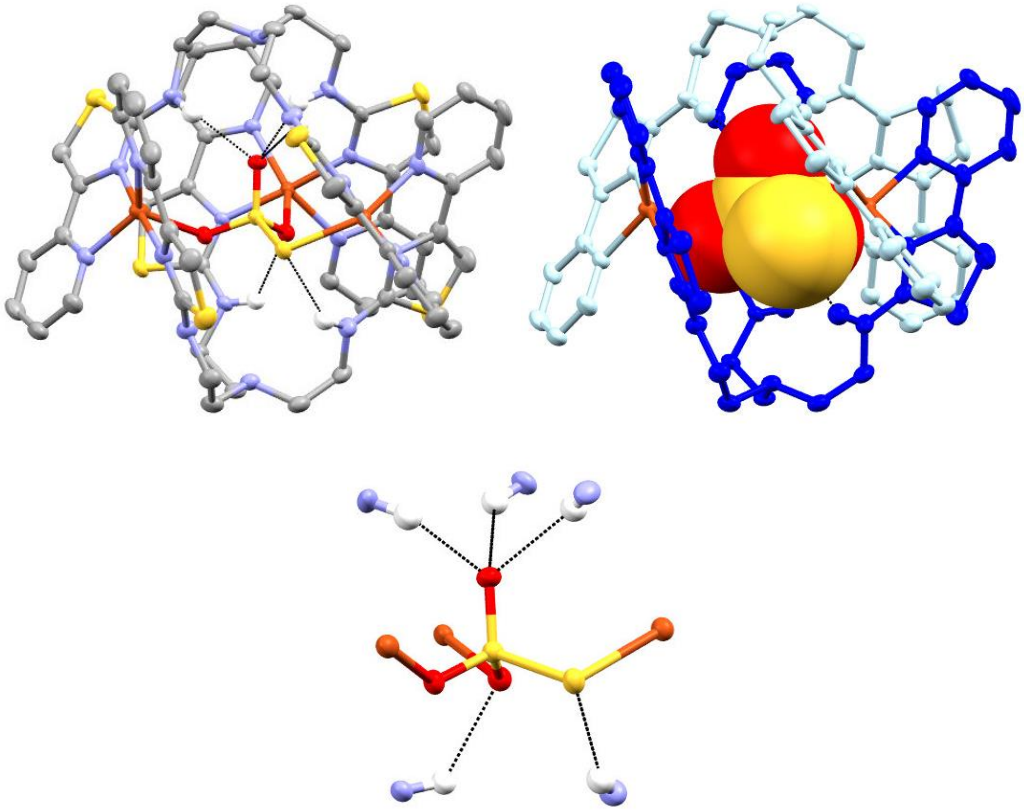

Figure 4.3.11. *Three different views of the X-ray structure of* $[(\mathbf{L^{4.1}})_2Cu_3(S_2O_3)]^{4+}$ *showing the coordination and hydrogen bonding of the anion. Thermal ellipsoids shown at the 50% probability level. Selected hydrogen atoms and anions omitted for clarity.*

4.4 Solution state studies and phosphate sequestering

Analysis by ESI-MS of the $[(\mathbf{L^{4.1}})_2Cu_n(A)]^{n+}$ complexes was undertaken and this demonstrated that the anion encapsulated structures observed in the solid state were also present in the gas phase. For example, the ESI-MS of complexes containing the sulphate anion (Fig. 4.4.1) gave an ion at *m/z* 1839 which corresponds to $\{[(\mathbf{L^{4.1}})_2Cu_3(SO_4)](ClO_4)_3]^+\}$ as well as the phosphate containing species which gave an ion at *m/z* 1838. Similar data was collected for the VO_4^{3-}, WO_4^{2-} and SiF_6^{2-} examples. Importantly, the carbonate containing example was also analysed by ESI-MS and gave an ion at *m/z* 1952 which corresponds to $\{[(\mathbf{L^{4.1}})_2Cu_3(CO_3)](trif)_3]^+\}$ confirming the CO_3^{2-} observed in the solid state analysis (Fig. 4.4.3). Examples such as the halide containing complexes gave much less simple spectra. The iodide encapsulated species gave ions at m/z 1967 for $\{[(\mathbf{L^{4.1}})_2Cu_3(I)](ClO_4)_4]^+\}$ as well as at m/z 1940 for $\{[(\mathbf{L^{4.1}})_2Cu_3(I)](ClO_4)_4]^+\}$ (Fig. 4.4.4). This highlights that when in the gas phase the spherical monoanionic iodide anion can be easily displaced. Spectra obtained for the complexes containing both IO_6^- and CrO_4^- gave complicated signals that proved difficult to assign. This can possibly be a result of the reactive nature of these anions interfering with the mass spectroscopic process.

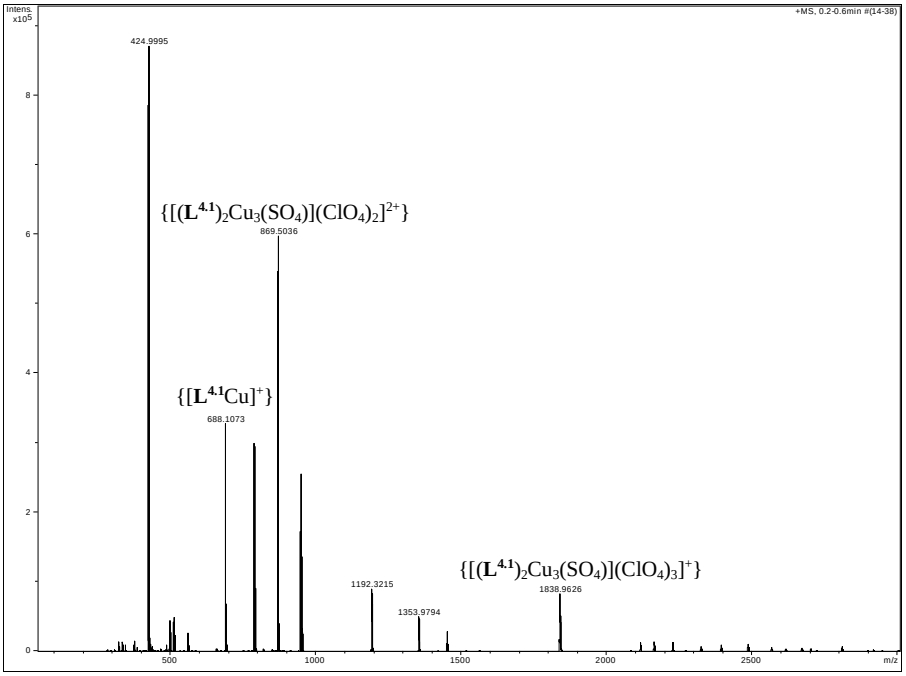

Figure 4.4.1. *ESI-MS of* $[(\mathbf{L^{4.1}})_2Cu_3(SO_4)](ClO_4)_4$

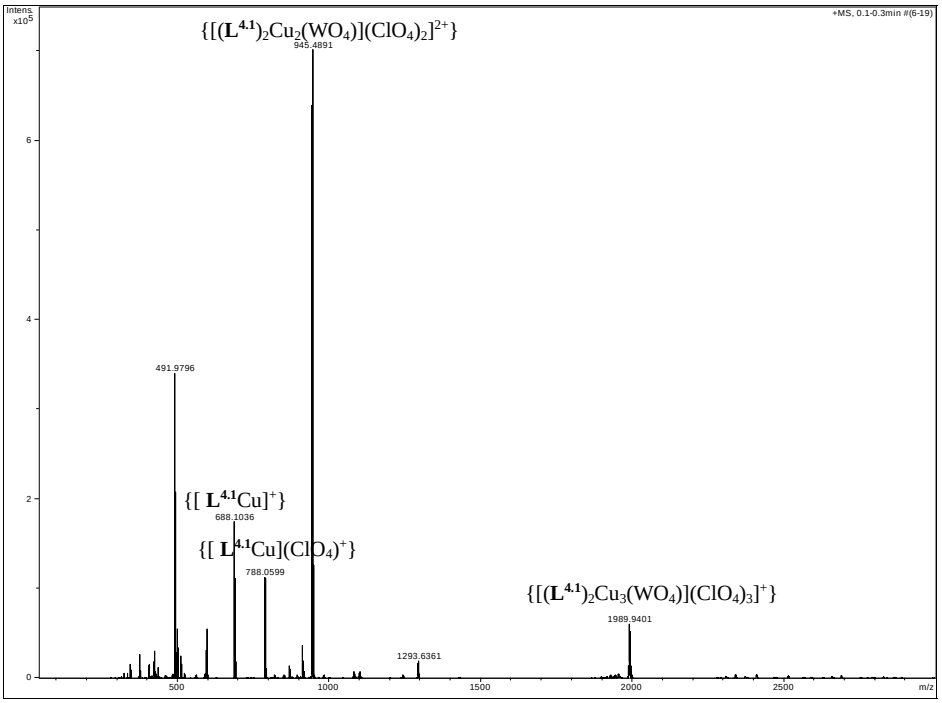

Figure 4.4.2. *ESI-MS of [(**L**$^{4.1}$)$_2$Cu$_3$(WO$_4$)](ClO$_4$)$_3$].*

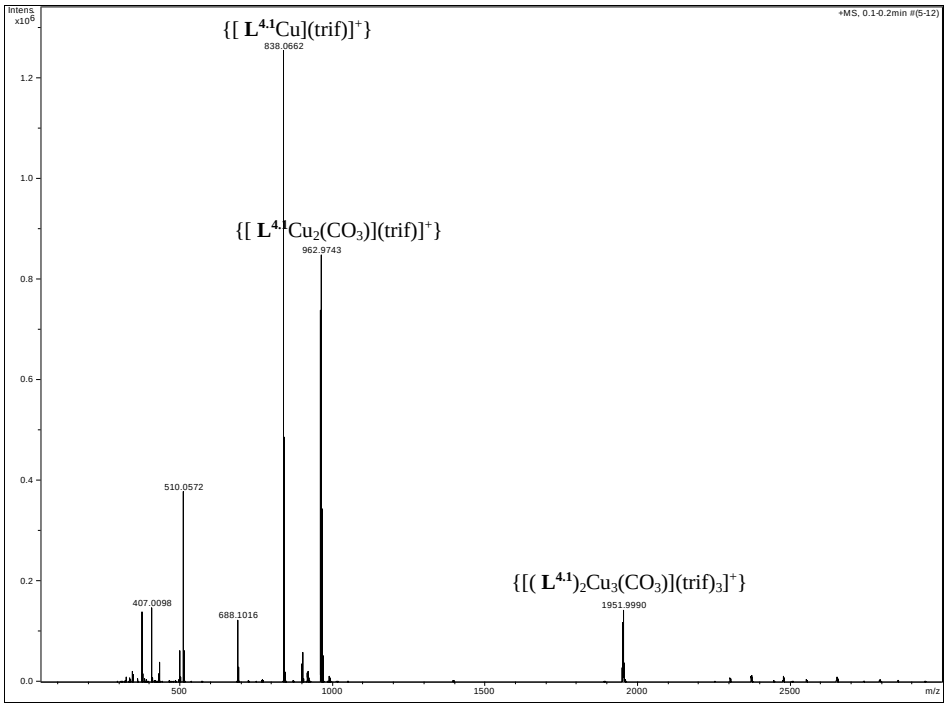

Figure 4.4.3. *ESI-MS of [(**L**$^{4.1}$)$_2$Cu$_3$(CO$_3$)](trif)$_3$]*

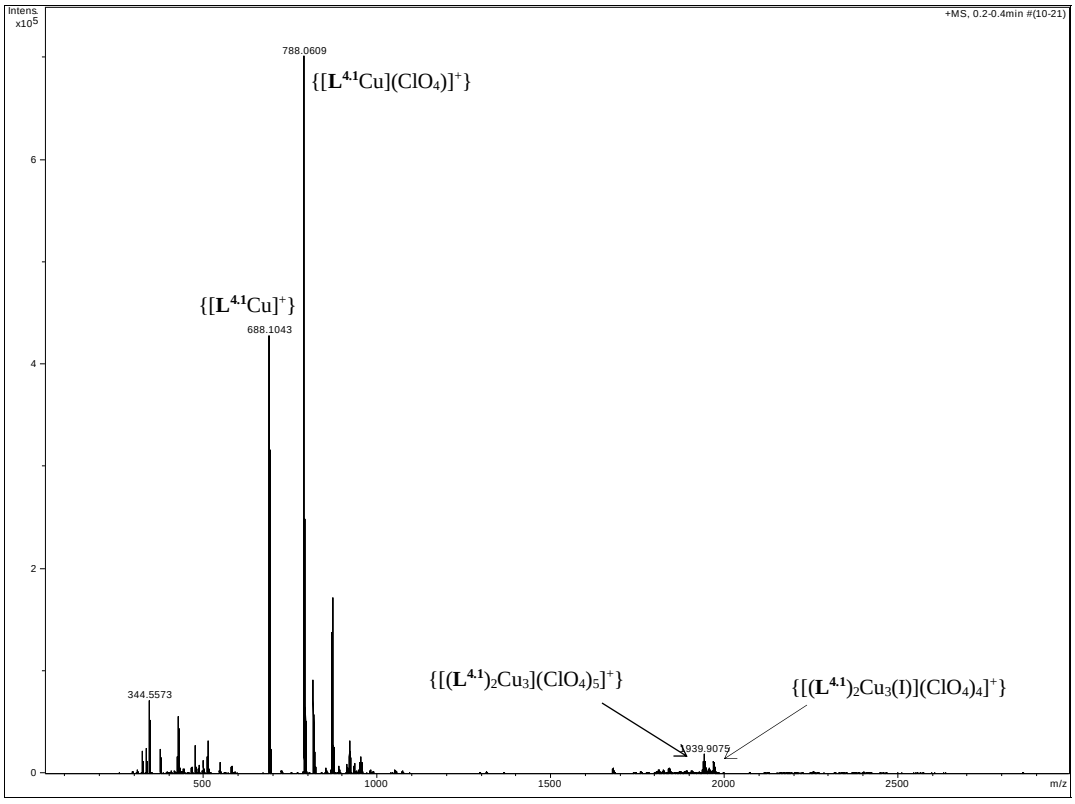

Figure 4.4.4. *ESI-MS of [(**L**$^{4.1}$)$_2$Cu$_3$(I)](trif)$_5$]*

UV-Vis spectroscopy studies were also carried out for the different anion containing complexes by reaction of **L**$^{4.1}$ with the appropriate equivalents of Cu(II) (either BF_4^-, ClO_4^- or triflate salts) in aqueous media ($MeCN/H_2O$, 1:1 v/v to avoid precipitation). This basic system (e.g. of [(**L**$^{4.1}$)$_2$Cu$_3$](A)$_6$) resulted in a pale tan colour and gave a λ_{max} absorption at 810 nm. Upon the addition of a variety of different anions to this system a change to the UV-Vis spectrum occurred which was mirrored in the solutions colour/intensity changes (Fig. 4.3.1). For example, the addition of iodide induced a dramatic increase in the λ_{max} absorption whereas the addition of H_2PO_4 resulted in the λ_{max} absorption undergoing a blue shift to higher energies (740 nm). These changes to the systems UV-Vis spectra highlight that the coordination of the encapsulated anion to the Cu(II) metal ions modulates the response of the complexes chromogenic ion. It is also worth noting that on addition of the nitrate ion, no changes in the UV-Vis spectra occurred indicating that this anion was not encapsulated in aqueous media.

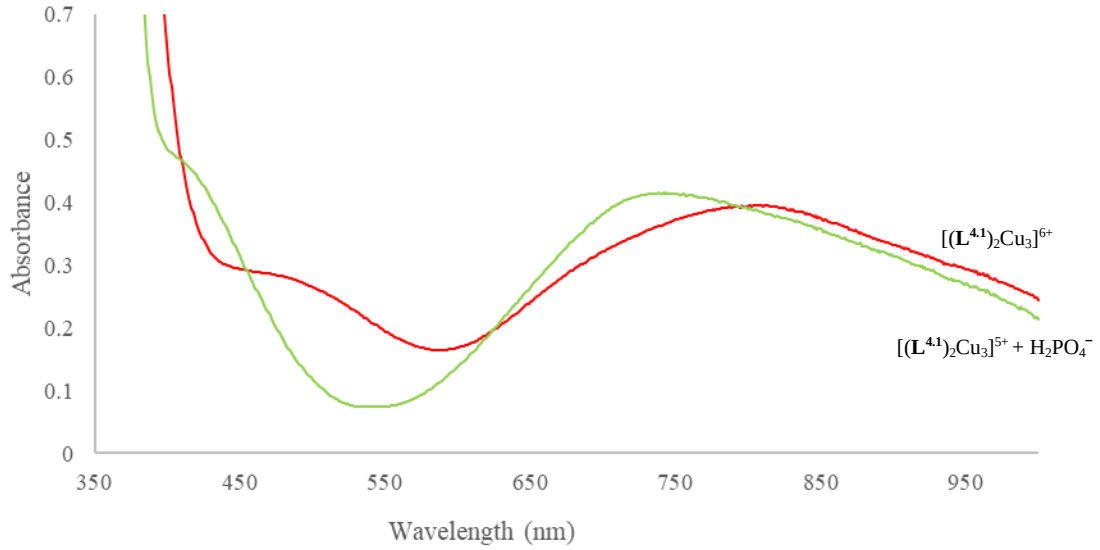

Figure 4.4.5. *UV-Vis absorption spectra of $[(\mathbf{L^{4.1}})_2Cu_3]^{6+}$; $[(\mathbf{L^{4.1}})_2Cu_3]^{6+}$ plus one equivalent of phosphate. $[(\mathbf{L^{4.1}})_2Cu_3]^{6+}$ 1.33 x 10^{-3} M.*

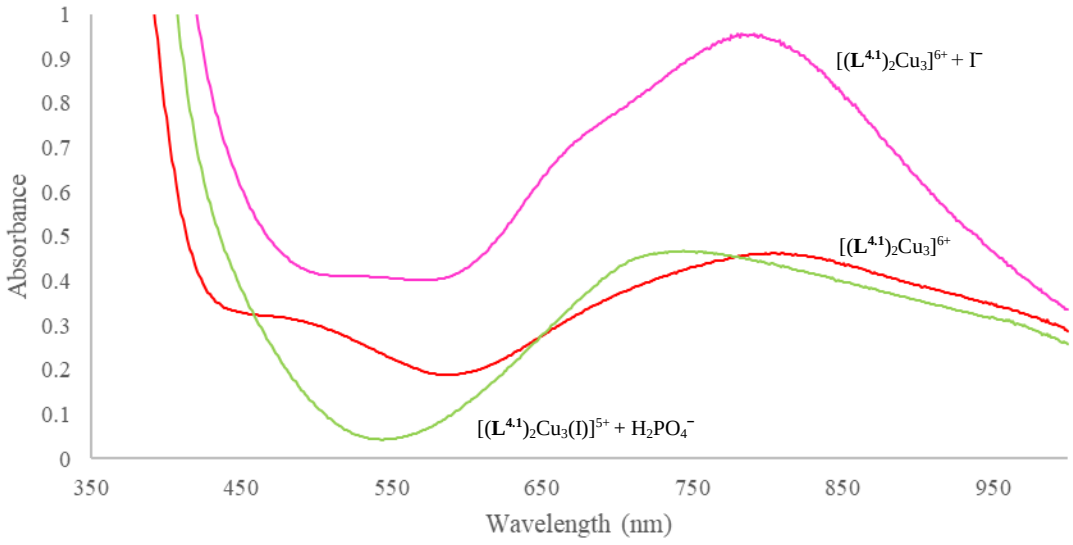

Figure 4.4.6. *UV-Vis absorption spectra of $[(\mathbf{L^{4.1}})_2Cu_3]^{6+}$; $[(\mathbf{L^{4.1}})_2Cu_3]^{6+}$ plus one equivalent of iodide; $[(\mathbf{L^{4.1}})_2Cu_3(I)]^{6+}$ plus one equivalent of hydrogen phosphate. $[(\mathbf{L^{4.1}})_2Cu_3]^{6+}$ 1.33 x 10^{-3} M.*

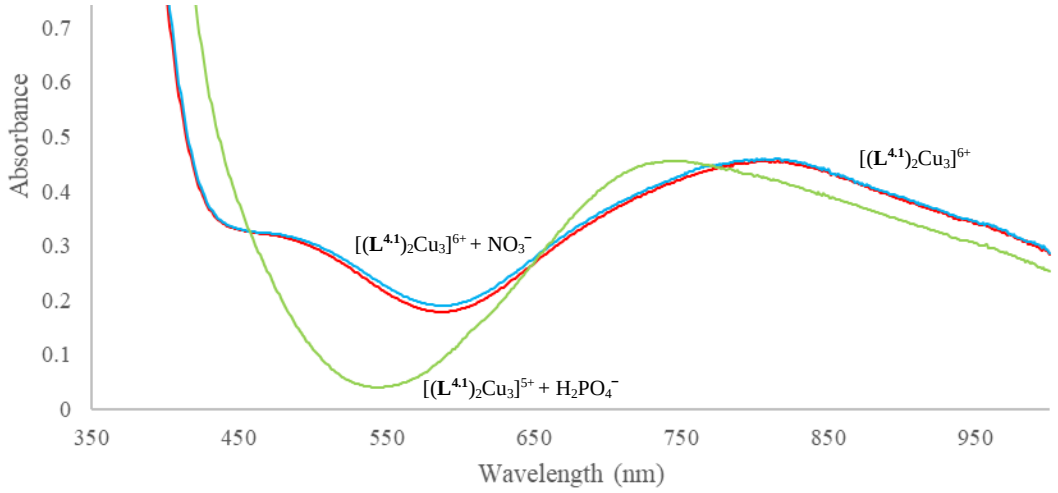

Figure 4.4.7. *UV-Vis absorption spectra of $[(\mathbf{L^{4.1}})_2Cu_3]^{6+}$; $[(\mathbf{L^{4.1}})_2Cu_3]^{6+}$ plus one equivalent of nitrate; $[L_2Cu_3]^{6+}$ plus one equivalent of nitrate and then one equivalent of hydrogen phosphate. $[(\mathbf{L^{4.1}})_2Cu_3]^{6+}$ 1.33 x 10^{-3} M. Notice that there is no change in the UV-Vis spectrum upon addition of nitrate 1.33 x 10^{-3} M.*

In addition to the initial UV-Vis spectroscopy studies a series of competitive experiments were undertaken. In these each of these cases, a series of $[(\mathbf{L^{4.1}})_2Cu_3]$ complexes were again prepared in aqueous media ($MeCN/H_2O$, 1:1 v/v) with the addition of one equivalent of Cl^-, Br^-, I^-, NO_3^- and SO_4^{2-} and the UV-Vis spectra was obtained. To each of these samples was added one equivalent of $H_2PO_4^-$ which in the cases of Br^-, I^- and NO_3^- resulted in a colour change from their original colour to lime-green. The UV-Vis spectra were then obtained and gave an almost identical response to that of the initial PO_4^{3-} encapsulated complex. Interestingly, in the case of addition of $H_2PO_4^-$ to the sulphate containing complex no colour change or change in the UV-Vis spectra occurred. This indicates that in this case the SO_4^{2-} anion was not displaced. However, when a similar sulphate containing solution was treated with one equivalent of HPO_4^{2-} the solution underwent the characteristic colour change to lime-green and the obtained UV-Vis spectra also showed a similar blue shift in λ_{max} absorption to that was witnessed for the initial PO_4^{3-} encapsulated complex. This suggests that at a higher *p*H the complex is selective to the phosphate anion.

Rationalizing the selectivity of the complex's inner cavity towards different guest anions can be considered in terms of both the shape and charge of the guest species. Monoanionic spherical, trigonal planar and tetrahedral are easily displaced due to the low charge density of the anion species with the trigonal planar NO_3^- anion not encapsulated within the complex at all. Whereas all di-anionic guests, including the trigonal planar CO_3^{2-} (*c.f.* NO_3^-) species as well as all di-anionic tetrahedral anions are readily encapsulated by the $[(\mathbf{L}^{4.1})_2Cu_3]^{6+}$ complex and both tri-anionic PO_4^{3-} species displacing all other low-charged examples. However, the selectivity between sulfate and phosphate is not as clear cut. Both examples are polyprotic tetrahedral anions, but the selectivity of the cavity prefers HSO_4^- over $H_2PO_4^-$, whereas the selectivity is reversed for SO_4^{2-} over HPO_4^{2-}, with the cavity now preferring the phosphate guest. This behavior can be rationalized in terms of the pH dependency of the anion. The acidity of the HSO_4^- mono-ion (pK_a = 1.81) is significantly more acidic than the $H_2PO_4^-$ mono-ion (pK_a = 7.21) and the HSO_4^- anion is therefore deprotonated much more readily than the $H_2PO_4^-$ anion and in turn will occupy the cavity. However, when HPO_4^{2-} is used initially the charge of the guests are matched. In this case the phosphate anion only requires a single deprotonation to achieve the tri-anionic PO_4^{3-} species and this increase in charge density of the anion leads to the di-anionic SO_4^{2-} being easily displaced.

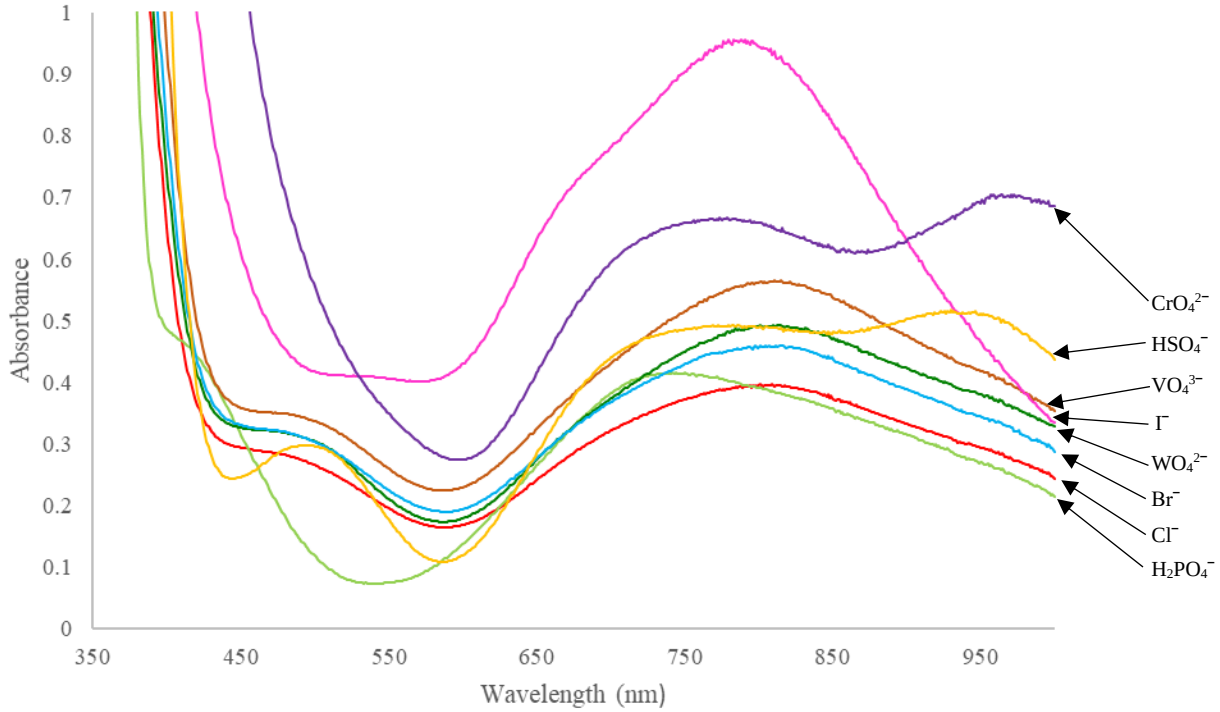

Figure 4.4.8. *UV-Vis absorption spectra $[(\mathbf{L}^{4.1})_2Cu_3](trif)_6$ plus one equivalent of Cl^-, Br^-, I^-, VO_4^{3-}, WO_4^{2-}, CrO_4^{2-}, HSO_4^- and $H_2PO_4^-$. All experiments were carried out in MeCN/H_2O (1:1 v/v to avoid precipitation) with the concentration of $[(\mathbf{L}^{4.1})_2Cu_3](trif)_6$ = 1.33 mM.*

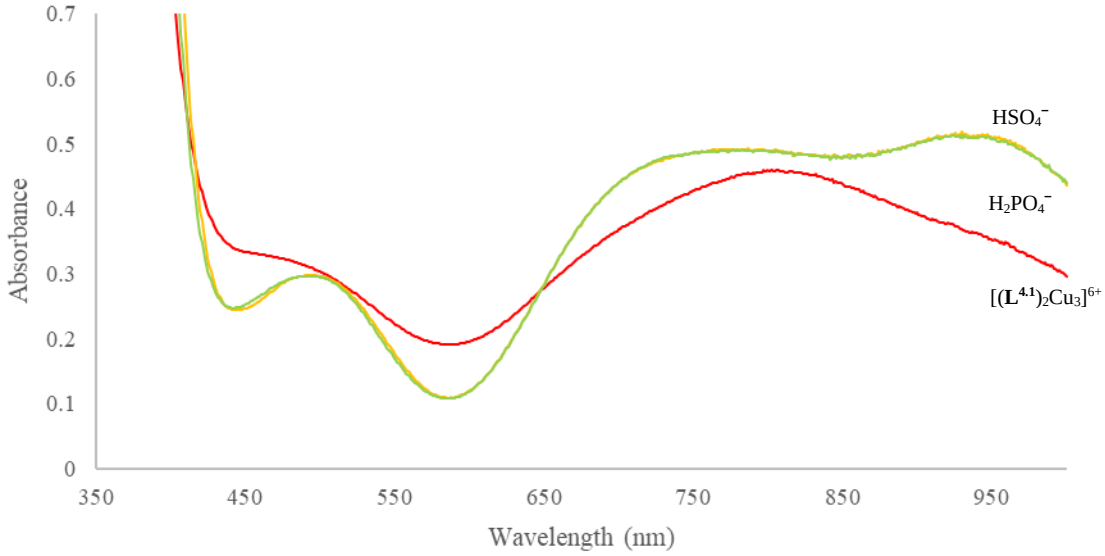

Figure 4.4.9. *UV-Vis absorption spectra of $[(\mathbf{L}^{4.1})_2Cu_3](trif)_6$ plus one equivalent of HSO_4^- and then $H_2PO_4^-$.*

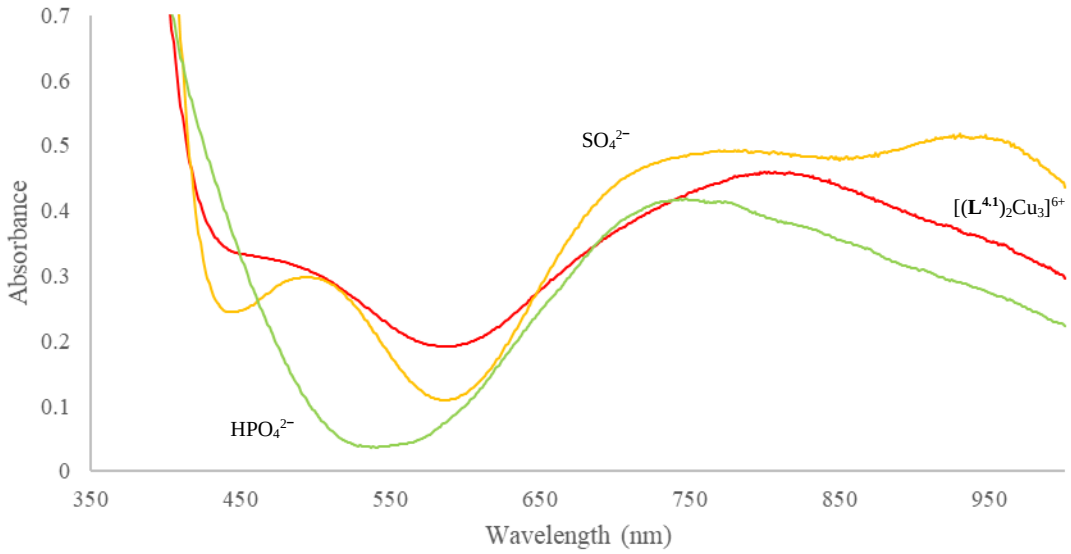

Figure 4.4.10. *UV-Vis absorption spectra of $[(L^{4.1})_2Cu_3](trif)_6$ plus one equivalent of Na_2SO_4 and then Na_2HPO_4.*

The preparation of these complex is not limited to only perchlorate, triflate and tetrafluoroborate Cu(II) salts, $[(\mathbf{L}^{4.1})_2Cu_3(PO_4)](NO_3)_3$ from which the "$[(\mathbf{L}^{4.1})_2Cu_3]^{6+}$" unit was initially prepared from reaction of two equivalents of $\mathbf{L}^{4.1}$ and three equivalents of $Cu(NO_3)_2$ has been isolated in both the solid and gas phase (**Appendix**, **6.3**). Furthermore, complexes prepared from $Cu(OAc)_2$ and $CuCl_2$ with Na_2HPO_4 result in the same characteristic lime green solution that gives the expected λ_{max} absorption at 740 nm in the UV-Vis spectra. However, to date, solid state characterisation of these complexes has not been obtained due to the observed increase in solubility of the complex that arises from the use of OAc^- and Cl^- counter ions.

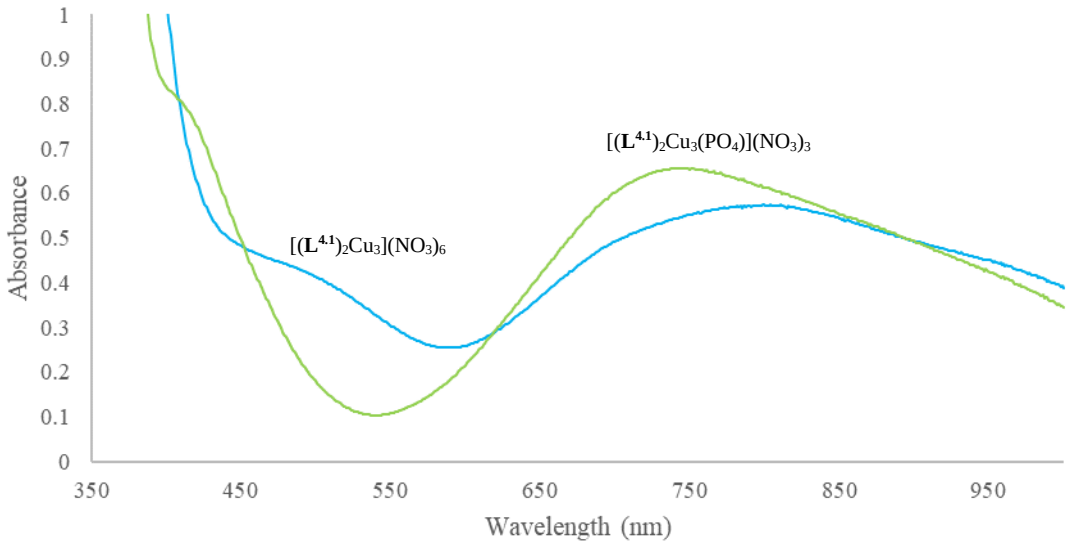

Figure 4.4.11. *UV-Vis absorption spectra of $[(\mathbf{L^{4.1}})_2Cu_3](NO_3)_6$; $[(\mathbf{L^{4.1}})_2Cu_3](NO_3)_6$ plus one equivalent of $Bu_4NH_2PO_4$; giving $[(\mathbf{L^{4.1}})_2Cu_3(PO_4)](NO_3)_3$. $[(\mathbf{L^{4.1}})_2Cu_3]^{6+}$ 1.33 x 10^{-3} M.*

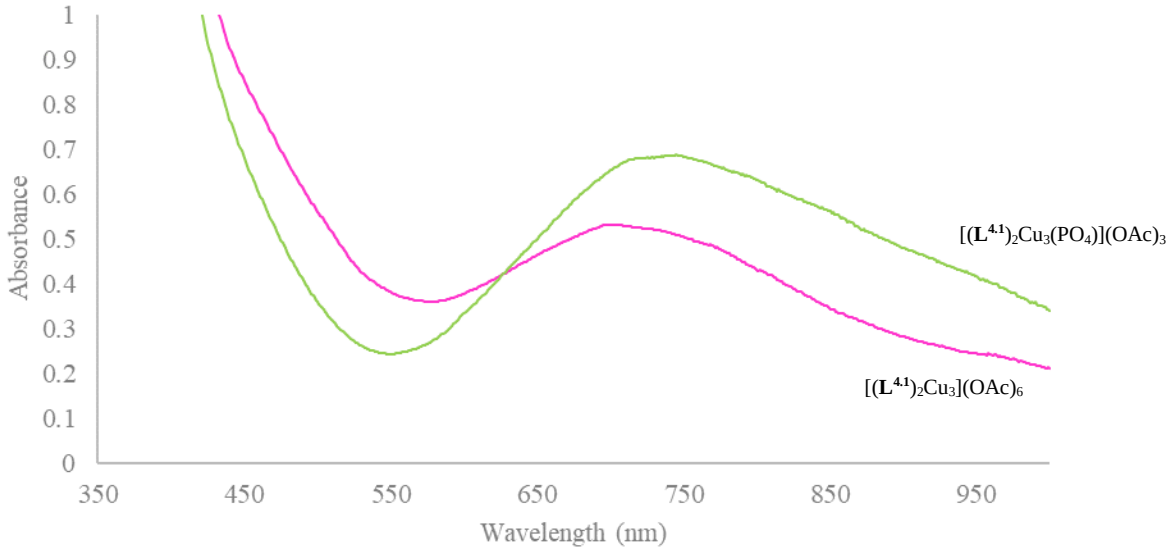

Figure 4.4.12. *UV-Vis absorption spectra of $[(\mathbf{L^{4.1}})_2Cu_3](OAc)_6$; $[(\mathbf{L^{4.1}})_2Cu_3](OAc)_6$ plus one equivalent of $Bu_4NH_2PO_4$; giving $[(\mathbf{L^{4.1}})_2Cu_3(PO_4)](OAc)_3$. $[(\mathbf{L^{4.1}})_2Cu_3]^{6+}$ 1.33 x 10^{-3} M.*

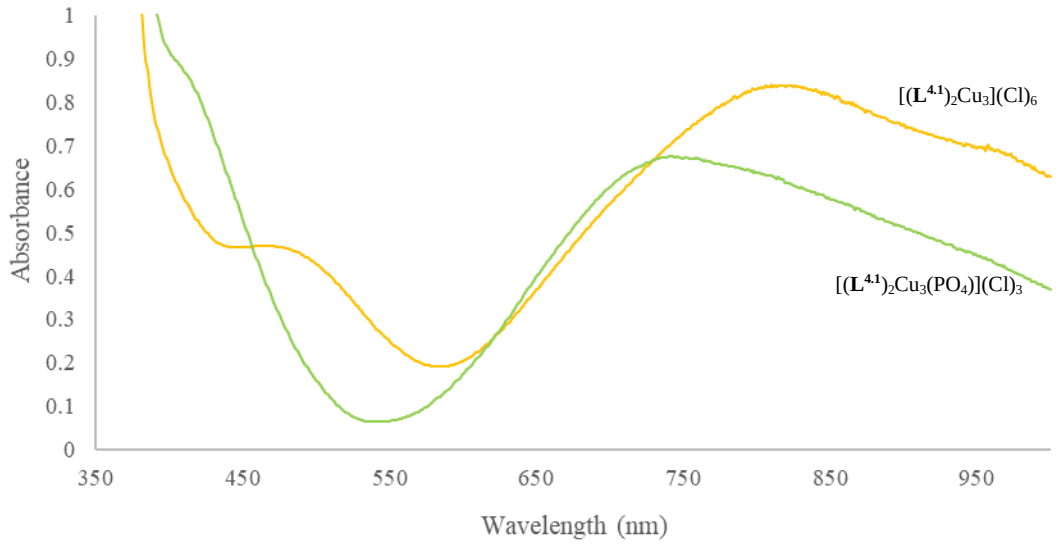

Figure 4.4.13. *UV-Vis absorption spectra of* $[(\mathbf{L}^{4.1})_2Cu_3](Cl)_6$*;* $[(\mathbf{L}^{4.1})_2Cu_3](Cl)_6$ *plus one equivalent of* $Bu_4NH_2PO_4$*; giving* $[(\mathbf{L}^{4.1})_2Cu_3(PO_4)](Cl)_3$*.* $[(\mathbf{L}^{4.1})_2Cu_3]^{6+}$ *1.33 x* 10^{-3} *M.*

Finally, an ion chromatography (IC) study was undertaken to investigate to what amount of the phosphate anion could be removed from a solution by the $[(\mathbf{L}^{4.1})_2Cu_3]^{6+}$ complex. The procedure involved a 1000 ppm solution of HPO_4^{2-} in water to which was added one equivalent of $[(\mathbf{L}^{4.1})_2Cu_3](ClO_4)_6$ in acetone (~ 1 mL) and the solution was allowed to stand for 48 hours during which time a lime-green crystalline precipitate was formed. Analysis of the remaining colourless solution by IC revealed that the initial phosphate concentration had significantly reduced to < 0.1 ppm. An identical system was set up in tandem produced a similar lime-green precipitate that when isolated and dried showed a ~99% recovery of the $[(\mathbf{L}^{4.1})_2Cu_3(PO_4)](ClO_4)_3$ complex. These two procedures indicate that the $[(\mathbf{L}^{4.1})_2Cu_3]^{6+}$ can achieve a near quantitative removal and recovery of the phosphate anion from a solution of water. In a competitive experiment, a solution containing 50 ppm of each of chloride, nitrate, sulphate and phosphate anions was reacted with one equivalent of $[(\mathbf{L}^{4.1})_2Cu_3](trif)_6$ and the solution allowed to stand for 1 week during which time a green crystalline precipitate formed. The solution was then analysed by ion chromatography and it was found to contain 47 ppm of chloride, 46 ppm nitrate, 41 ppm sulfate and 10 ppm phosphate. This

demonstrates that the complex is highly selective to phosphate, in the presence of a series of common anions in aqueous media, removing ~80% of this anion.

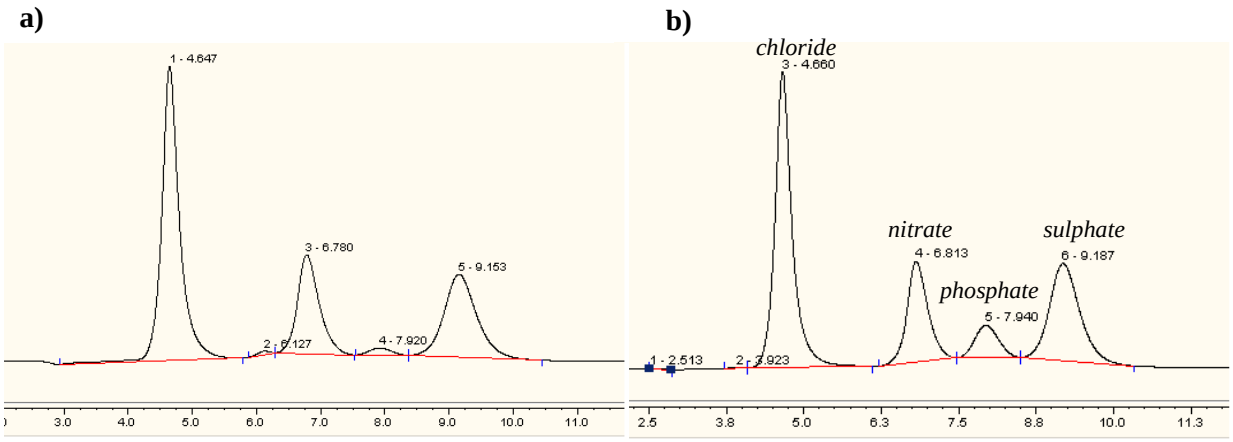

Figure 4.4.14. *IC experimental data a) 50 ppm solution of each of chloride, nitrate, phosphate and sulfate exposed to* $[(\mathbf{L}^{4.1})_2Cu_3](trif)_6$ *and b) 50 ppm standard.*

4.5 Conclusion

In this work we have shown that a simple three step synthesis procedure can be used to produce a tripodal ligand $\mathbf{L}^{4.1}$ that forms a trinuclear species with Cu(II). Incorporated within the trinuclear structure $[(\mathbf{L}^{4.1})_2Cu_3]^{6+}$ a central cavity is formed and can act as a host to a variety of different anions. The trinuclear host can form up to a total of three Cu···A^{n-} coordinate bonds and six -NH··· A^{n-} hydrogen bonding interactions within the cavity. This behaviour of forming nine bonding interactions in a 3-dimensional manner which is like that of the thoroughly documented cation binding cryptate ligand, although in this example the charge of the guest is reversed, resulting in an *anti*-cryptate. UV-Vis experiments have shown that the self-assembled host displays a high degree of selectivity to shape, size and charge of the guest, with the highly charged phosphate anion being of preference to the system. Importantly, this study has shown that the $[(\mathbf{L}^{4.1})_2Cu_3]^{6+}$ host system is capable of both forming and encapsulating phosphate anions in a competitive aqueous solvent (*i.e.* water) and removing them in a stoichiometric manner even at low concentrations. With these characteristics in mind, this system and other similar architectures could prove

useful in the remediation and removal of phosphate anion in aquatic system and will be of definite interest for further study.[97]

4.6 Encapsulation of third row chalcogenides

Third row chalcogenides can also be encapsulated within the self-assembled host. For example, reaction of two equivalents of $\mathbf{L^{4.1}}$ and three equivalents of $Cu(ClO_4)_2$ were reacted with half an equivalent of Na_2SeO_3 in $MeCN/H_2O$ (1:4). Upon slow evaporation over 24 hours light green crystals were deposited and analysed by single-crystal X-ray diffraction. Surprisingly, in this system the expected $[(\mathbf{L^{4.1}})_2Cu_3A)]^{n+}$ encapsulating motif was not observed but instead the system had formed a substantially different octanuclear assembly e.g. $[(\mathbf{L^{4.1}})_4Cu_8(SeO_3)_4]^{8+}$ (Fig. 4.6.1).

In this octanuclear complex each of the four $\mathbf{L^{4.1}}$ ligand strands adopt a under and over motif and coordinate three different Cu(II) metal ions via each of the three bidentate pyridyl-thiazole binding domains to form a three by three octanuclear Cu(II) grid-type architecture. This results in the formation of a large central cavity within the structure which is host to a total of four SeO_3^{2-} guest anions. In this complex each of the Cu(II) metal centres are again five-coordinate but four of the eight receive four N···Cu coordinate bonds from two separate ligand strands as well as one O···Cu coordinate bond from a SeO_3^{2-} guest anion. Whilst the remaining four Cu(II) ions form only two N···Cu coordination bonds from one of each ligands bidentate pyridyl-thiazole binding domains and a total of three O···Cu coordination bonds from a SeO_3^{2-} guest anion. The central four SeO_3^{2-} guest anions are held within the central cavity by a combination of four O···Cu coordinate bonds (two from a single Cu(II) ion and two to two separate Cu(II) ions) as well as three -NH···O hydrogen bonding interactions (two from one ligand strand and one from a separate ligand strand).

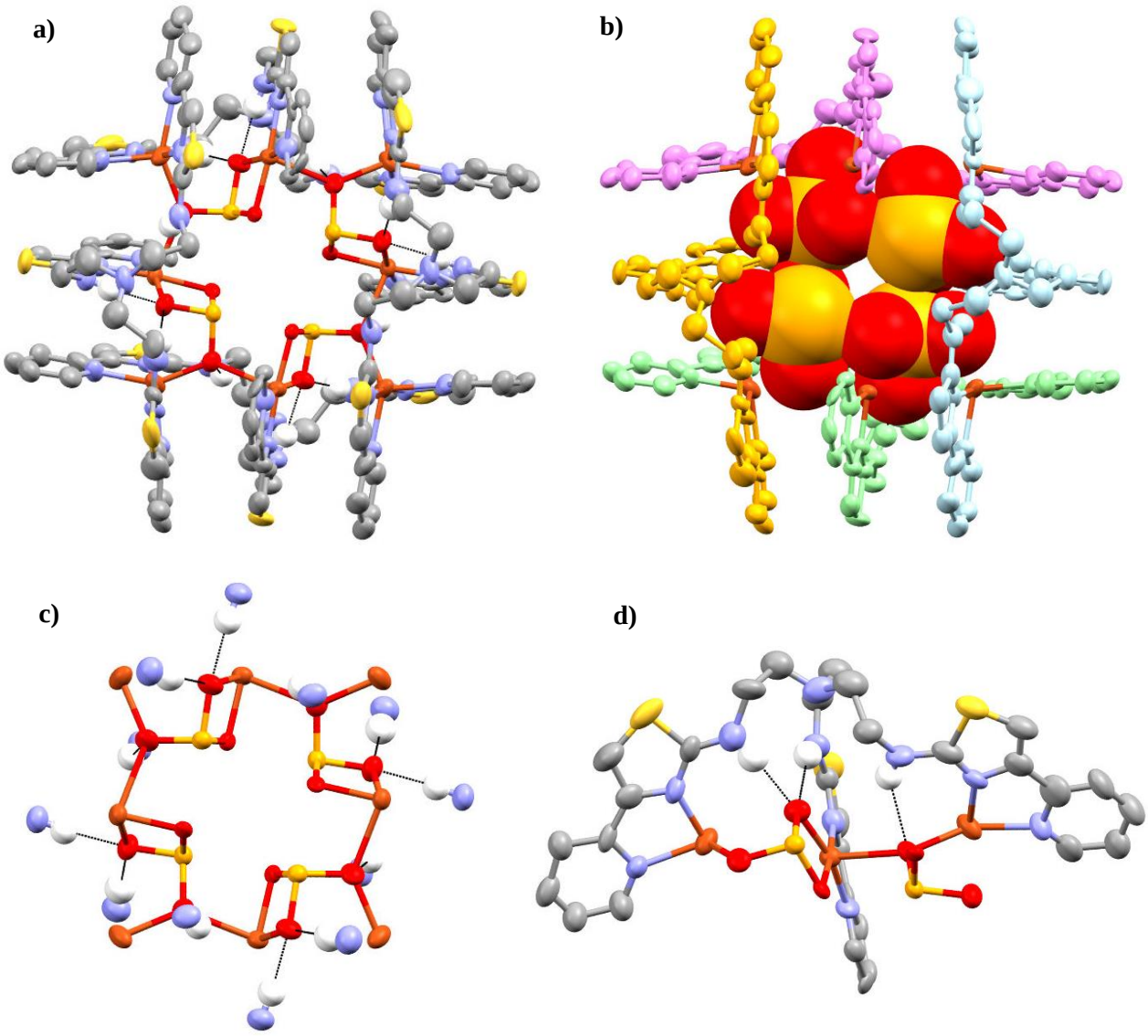

Figure 4.6.1. *Four different views of the X-ray structure of* $[(\mathbf{L}^{4.1})_4Cu_8(SeO_3)_4]^{8+}$ *(a - b) showing the coordination and hydrogen bonding of the anion (c – d). Thermal ellipsoids shown at the 50% probability level. Selected hydrogen atoms and anions omitted for clarity*

However, as similar reaction to that discussed about but where $Cu(BF_4)_2$ is used instead of $Cu(ClO_4)_2$ results in a different structure and this gave the expected tri-nuclear $[(\mathbf{L^{4.1}})_2Cu_3)]^{6+}$ complex and this incorporated the SeO_3^{2-} anion giving $[(\mathbf{L^{4.1}})_2Cu_3(SeO_4)]^{4+}$ (Fig. 4.6.2). In this example the two ligand strands and three Cu(II) ions adopt a similar geometry to what was seen previously described with other oxoanions. The central SeO_3^{2-} anion guest is held within the cavity in a similar manner to that of the CO_3^{2-} example where by the anion forms a total of two Cu···O coordination bonds and five -NH···O hydrogen bonding interactions.

It is worth noting that the trimetallic species $[(\mathbf{L^{4.1}})_2Cu_3(SeO_4)]^{4+}$ is formed as a minor component with only one or two crystals (which were dark green – allowing differentiation between the bulk material) were observed in the crystallisation process but in both the BF_4^- and ClO_4^- reactions the octanuclear species (light-green crystals) were present as by far the major product. A possible explanation of why the octanuclear complex is the preferred self-assembled species is due to the combination of the coordination bonds and hydrogen bonding interactions between the ligand/copper host complex with the guest anion. In $[(\mathbf{L^{4.1}})_2Cu_3(SeO_4)]^{4+}$ the selenite anion coordinates two copper atoms and these two coordination bonds are supplemented by –NH interactions by the adjacent amine units. The oxygen atom of the SeO_3^{2-} anion (which point upward of the Cu_3 core) also interacts with the three –NH bonds (in a similar manner to all the other oxoanion hosts). However, one of the Cu(II) ions is not coordinated via the anion and no hydrogen bonding is observed with the adjacent amine unit. In $[(\mathbf{L^{4.1}})_4Cu_8(SeO_3)_4]^{8+}$ all of the Cu(II) atoms are coordinated to either one or two anion oxygen atoms and all the amine units form –NH···anion interactions. As a result, the octanuclear species is formed preferentially as all Cu(II) atoms are five-coordinate (formed from either 4 *N*- and 1 *O*-donor or 2 *N*- and 3 *O*-donor units) and all the amine units form hydrogen bond interactions to oxygen atoms. The small amount of $[(\mathbf{L^{4.1}})_2Cu_3(SeO_4)]^{4+}$ is possibly a consequence of the stoichiometry of the reaction.

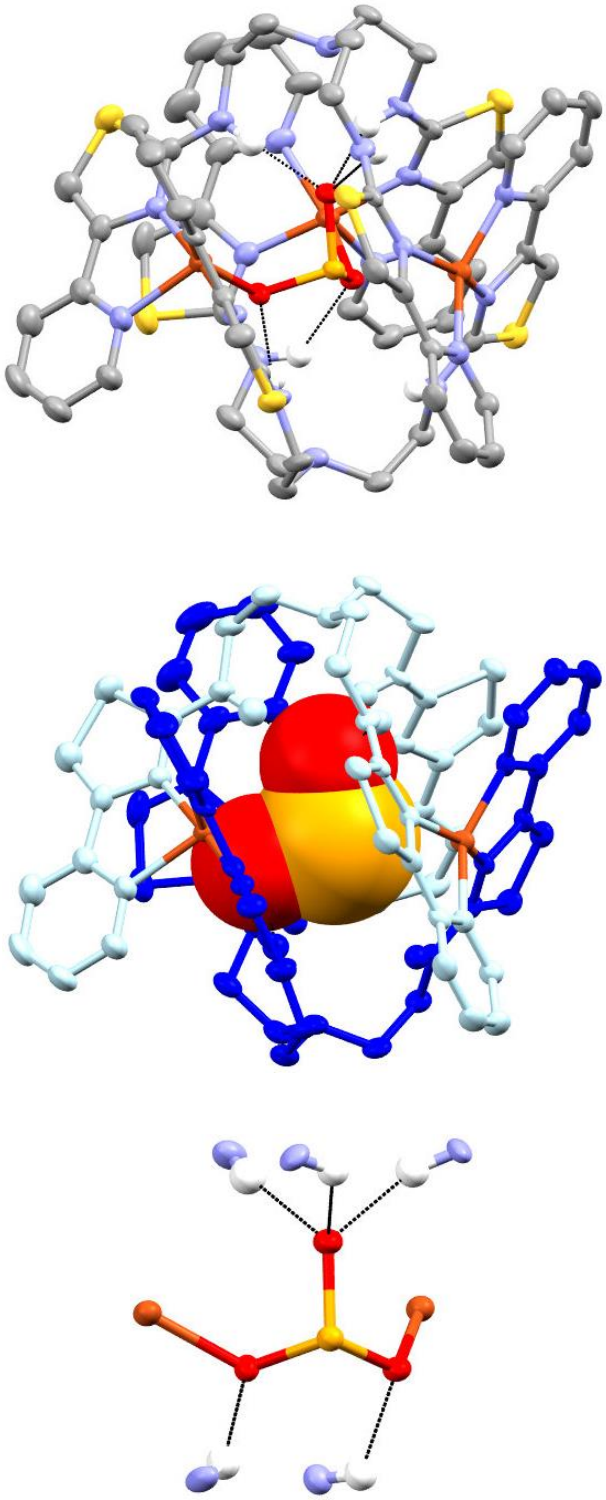

Figure 4.6.2. *Three different views of the X-ray structure of* $[(\mathbf{L}^{4.1})_2Cu_3(SeO_3)]^{4+}$ *showing the coordination and hydrogen bonding of the anion. Thermal ellipsoids shown at the 50% probability level. Selected hydrogen atoms and anions omitted for clarity.*

5. Experimental

5.1 Experimental

Chemicals were purchased and used without further purification. ^{1}H and ^{13}C NMR spectra were recorded on a 400MHz Bruker Avance DP X400. Mass spectra were obtained on an Agilent 6210 TOF MS for the organic species with the metal complexes run on a Bruker MicroQTOF LC.

5.11 $L^{2.1}$

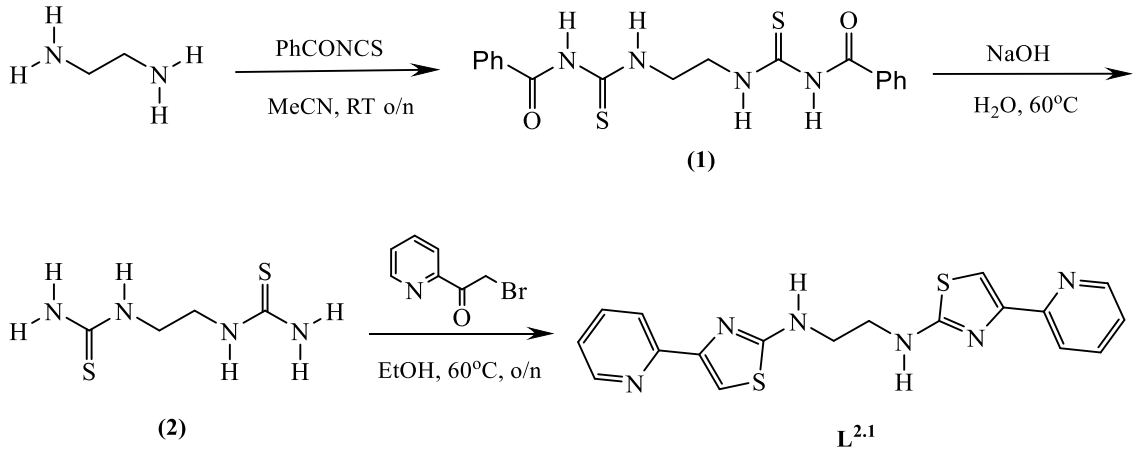

Scheme 5.1.1. *Synthesis route of ligand* ***L*** $^{2.1}$

To a 250 mL RBF charged with ethylenediamine (1 mL, 0.9 g, 15 mmol) and MeCN (50 mL) was added a solution of benzoyl isothiocyanate (5 mL, 6.1 g, 37.5 mmol) in MeCN (50 mL) slowly over 30 mins with constant stirring. The reaction mixture was then stirred at RT for a further 12 hrs during which time a heavy white precipitate was formed. The resulting mixture was the added dropwise, whilst stirring, to deionised water (300 mL) to yield a white/yellow precipitate which was then isolated via vacuum filtration. The solid was then suspended in MeOH (50 mL) in a 100 mL conical flask and sonicated (5 mins). The white/yellow suspension was then once again filtered under vacuum to yield a fine white solid which was washed with further portions of MeOH (3 x 10 mL) to give the pure *bis*-benzoylated thiourea (**1**) as a fine white powder

(3.5 g, 60 %). ^{1}H NMR (400 MHz, $(CD_3)_2SO$) δ (ppm) 11.45 (s, 2H, NH), 11.03 (s, 2H, NH), 7.98 (d, *J* = 7.5, 4H, Ph), 7.64 (dt, *J* = 7.5, 1.0, 2H, Ph), 7.64 (t, *J* = 7.5, 4H, Ph), 4.04 (s, *J* = 2.4 Hz, 4H, -CH_2-). ^{13}C NMR [400 MHz, DMSO-*d*^{6}]: δ_C = 183.5 (C=S), 168.4 (C=O), 133.4 (CH), 132.7 (Q), 129.0 (CH), 128.9 (CH), 128.7 (CH), 127.6 (CH), 44.8 (CH_2), 25.6 (CH_2). ESI-MS *m/z* 386 (M + H^+), HR ESI-MS found 387.0927 $C_{18}H_{18}N_4S_2O_2$ requires 387.0944 (error 4.5 ppm). Whilst the ESI-MS analysis did give an accurate ion the compound did decompose rapidly in the ESI MS process and only a small M^+ ion was observed. This behaviour is common to all the aliphatic bridged disubstituted thioamines and their derivatives.

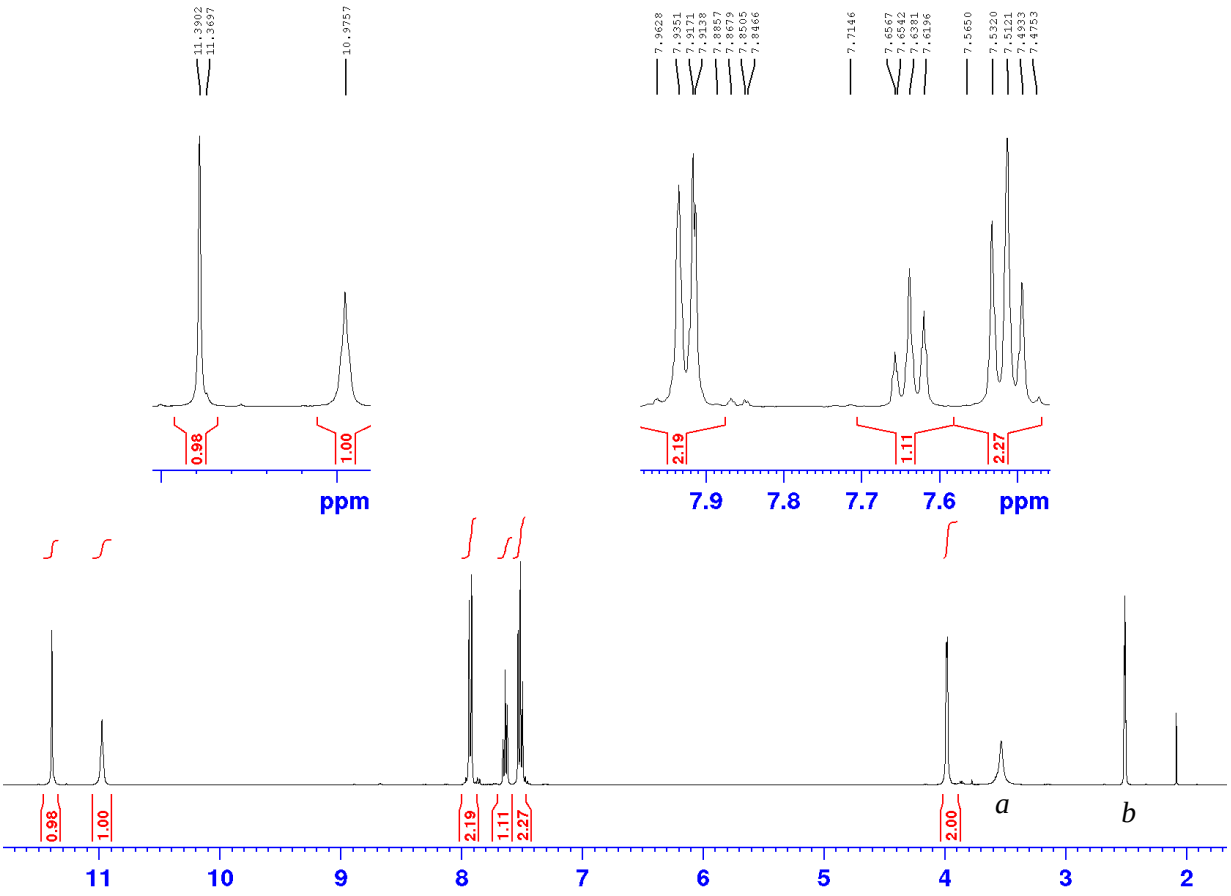

Figure 5.1.1. *^{1}H NMR of benzoylated thiourea product (**1**) a = water impurity and b = $(CD_3)(CHD_2)SO$.*

In a 100 ml RBF was combined the *bis*-benzoylated dithiourea (1 g, 2.6 mmol), deionised water (30 mL) and a magnetic stir bar. A solution of NaOH (0.63 g, 15.8 mmol) in H_2O (15 mL) was then added to the reaction mixture whilst stirring at 60°C. After 12hrs the resulting colourless solution was then cooled to RT during which time a fine white precipitate was formed. The precipitate was then collected via vacuum filtration and then washed with ice cold deionised water (3 x 5 mL). To give the *bis*-thiourea (**2**) as a fine white powder (0.43 g, 93 %). The ^{1}H NMR gives four broad signals in the aromatic region and two broad signals at ~ 3.5 ppm. It is suspected that intra-molecular hydrogen bonding is inducing broad peaks in the ^{1}H NMR. However, both the ^{13}C and ESI-MS are exactly as expected. ^{13}C NMR [400 MHz, DMSO-d^6]: δ_C = 183.9 (C=S), 43.7 (CH_2). ESI-MS *m/z* 179 ($M + H^+$). HR ESI-MS found 179.0415 $C_4H_{10}N_4S_2$ requires 179.042 (error 2.61 ppm).

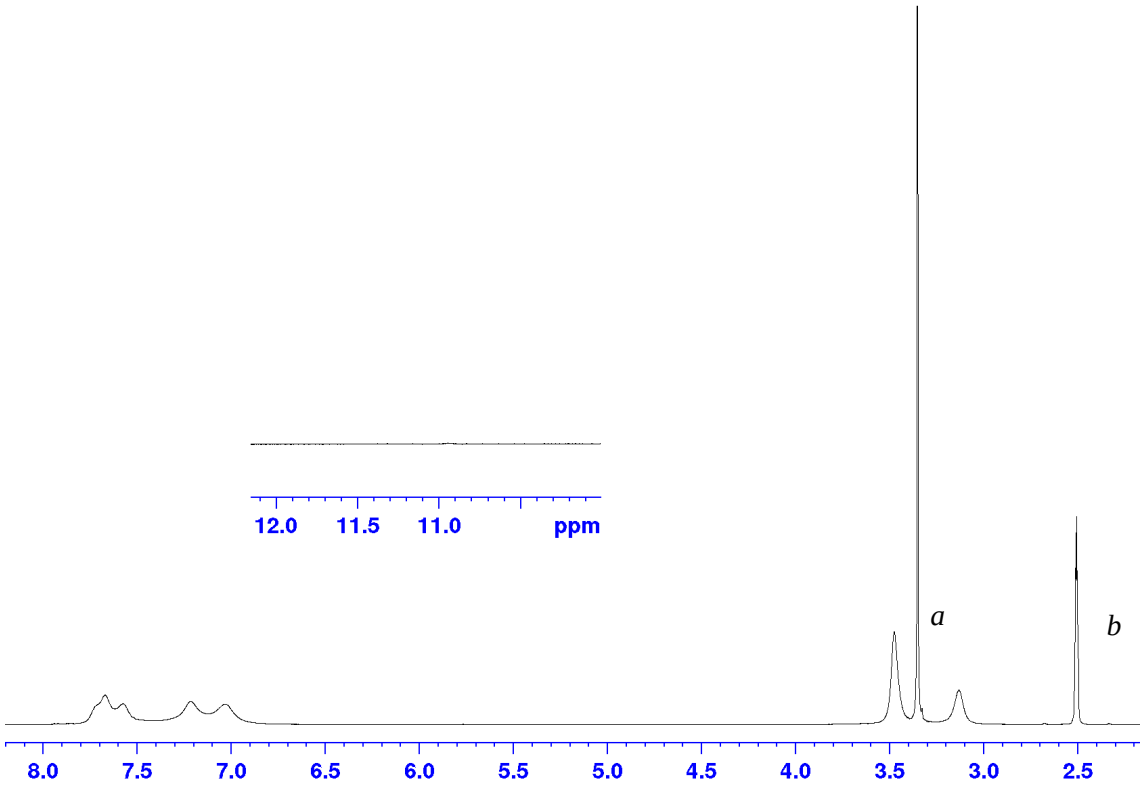

Figure 5.1.2. *^{1}H NMR of the bis-thiourea product (**2**) a = water impurity and b = $(CD_3)(CHD_2)SO$. The expansion shows the absence of amide peaks at ~ 11 ppm.*

A 25 mL RBF was charged with dithiourea (228 mg, 1.3 mmol), EtOH (10 mL) and magnetic stir bar. The mixture was then heated to 60 °C and to this was added α-bromoacetyl pyridine (540 mg, 2.7 mmol) as a solution in EtOH (2 mL). Heating was continued for a further 8 hrs during which time a heavy yellow precipitate was formed. This was then isolated via vacuum filtration and the filtrand washed with equal portions of EtOH (3 x 2 mL) to give the protonated product. The free-base ligand was then isolated by suspending in concentrated ammonia (15 mL) for 24 hrs. The resulting colourless suspension was then sonicated (5mins) and was filtered under vacuo and the solid washed with equal portions of deionised water (5 x 2 mL), giving the product (**L**$^{2.1}$) as a fine off-white powder (402 mg 81 %). ^{1}H NMR (400 MHz, $(CD_3)_2SO$) δ (ppm) 8.55 (d, *J* = 4.7, 2H, py), 7.90 (m, overlapping, 4H, py and -NH), 7.79 (dt, *J* = 7.8, 1.8, 2H, py), 7.31 (s, 2H, tz), 7.26 (dd, *J* = 4.8, 1.1, 2H, py), 3.60 (t, *J* = 2.5 Hz, 4H, -CH_2-). ^{13}C NMR (100 MHz d^6-DMSO) δ 169.0, 152.9, 150.7, 149.7, 137.4, 122.8, 120.8, 105.4 and 44.1 ppm. ESI-MS *m/z* 381 ($M + H^+$). HR ESI-MS found 381.0934 $C_{18}H_{17}N_6S_2$ requires 381.0951 (error 4.79 ppm).

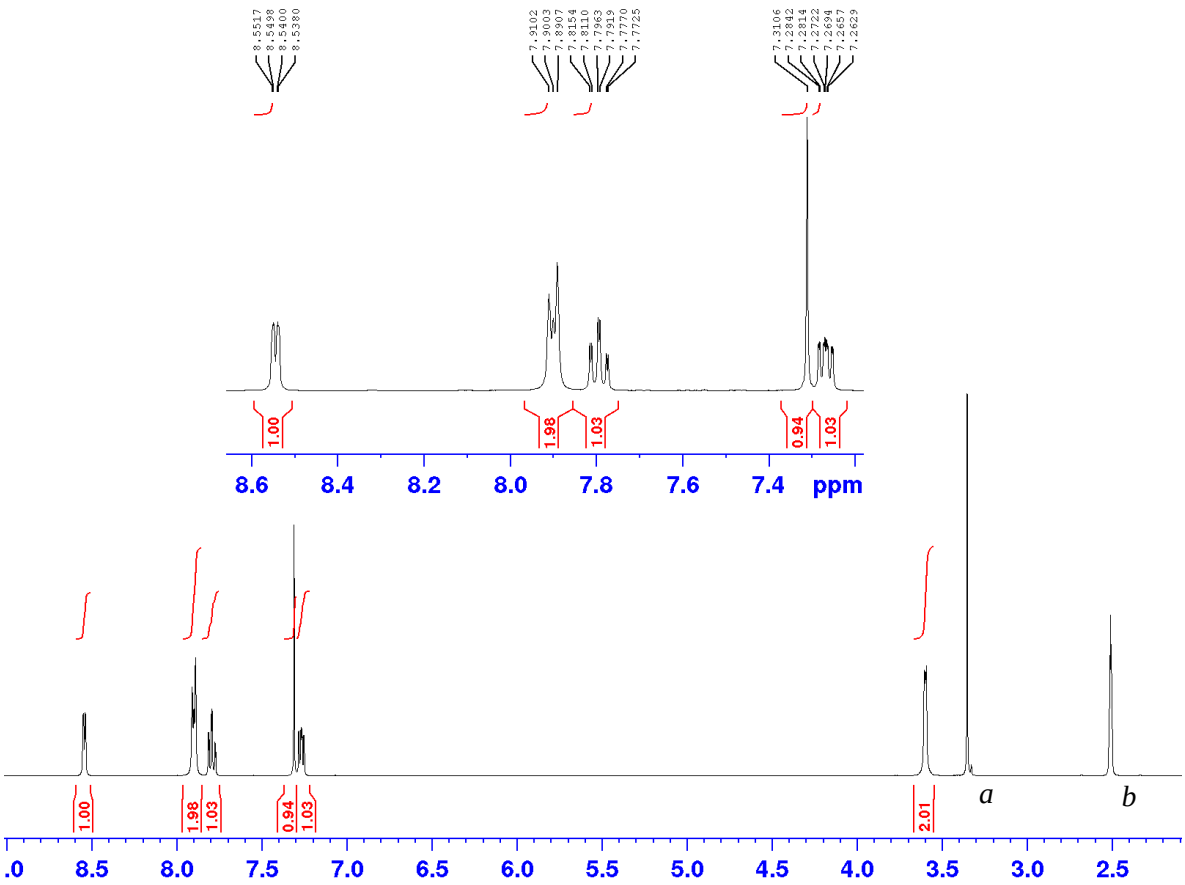

Figure 5.1.3. *^{1}H NMR of ligand $\boldsymbol{L^{2.1}}$ a = water impurity and b = $(CD_3)(CHD_2)SO$.*

Synthesis of $[(\mathbf{L}^{2.1})_2Cu_2(trif)_2](trif)_2$

To a solution of $Cu(trif)_2 \cdot 6H_2O$ (10 mg. 0.027 mmol) in $MeNO_2$ (1 ml) was added a suspension of ligand $\mathbf{L}^{2.1}$ (9.5 mg, 0.025 mmol) in $MeNO_2$ and the reaction warmed and sonicated until a clear dark blue solution had formed. Di-isopropyl ether was slowly allowed to diffuse into the solution resulting in dark blue block-like crystals after several days. Filtration and washing with diisopropyl ether (1 ml) and diethyl ether (1 ml) gave dark blue crystals which lost solvent rapidly (yield = 46%).

Synthesis of $[(\mathbf{L}^{2.1})_2Cu_2(H_2O)_2(NO_2)_4]$

To a solution of $Cu(trif)_2 \cdot 6H_2O$ (10 mg. 0.027 mmol) in $MeNO_2$ (1 ml) was added a suspension of ligand $\mathbf{L}^{2.1}$ (9.5 mg, 0.025 mmol) in $MeNO_2$ and the reaction warmed and sonicated until a clear dark blue solution had formed. To this was added a solution of Bu_4NNO_3 (7.6 mg, 0.025 mmol) in $MeNO_2$ (0.5 ml) during which the colour changed from dark blue to dark green. Diisopropyl ether was slowly allowed to diffuse into the solution resulting in dark green needle-like crystals after several days. Filtration and washing with diisopropyl ether (1 ml) and diethyl ether (1 ml) gave dark green crystals which lost solvent rapidly (yield = 38%).

Synthesis of $[(\mathbf{L}^{2.1})_2Cu_2](trif)_4$.

To a solution of $Cu(trif)_2 \cdot 6H_2O$ (10 mg. 0.027 mmol) in $MeNO_2$ (1 ml) was added a suspension of ligand $\mathbf{L}^{2.1}$ (9.5 mg, 0.025 mmol) in $MeNO_2$ and the reaction warmed and sonicated until a clear dark blue solution had formed. To this was added a solution of Bu_4NI (4.4 mg, 0.012 mmol) in $MeNO_2$ (0.5 ml) during which the colour changed from dark blue to dark red and after a 24 hrs dark green. Diisopropyl ether was slowly allowed to diffuse into the solution resulting in lime green needle-like crystals after several days. Filtration and washing with diisopropyl ether (1 ml) and diethyl ether (1 ml) gave dark red crystals which lost solvent rapidly (yield = 44%).

Synthesis of $[(\mathbf{L}^{2.1})_2Cu_2H_2PO_4(trif)_2](trif)$.

To a solution of $Cu(trif)_2 \cdot 6H_2O$ (10 mg. 0.027 mmol) in $MeNO_2$ (1 ml) was added a suspension of ligand $\mathbf{L}^{2.1}$ (9.5 mg, 0.025 mmol) in $MeNO_2$ and the reaction warmed and sonicated until a clear dark blue solution had formed. To this was added a solution of $Bu_4NH_2PO_4$ (4 mg, 0.012 mmol) in $MeNO_2$ (0.5 ml) during which the colour changed from dark blue to lime green. Diisopropyl ether was slowly allowed to diffuse into the solution resulting in lime green needle-like crystals after several days. Filtration and washing with diisopropyl ether (1 ml) and diethyl ether (1 ml) gave lime green crystals which lost solvent rapidly (yield = 39%).

Synthesis of $[(\mathbf{L}^{2.2})_3Cu_3(O_3POBF_3)](BF_4)_3$.

To a solution of $Cu(BF_4)_2 \cdot 6H_2O$ (10 mg. 0.029 mmol) in $MeNO_2$ (1 ml) was added a suspension of ligand $\mathbf{L}^{2.1}$ (10 mg, 0.026 mmol) in $MeNO_2$ and the reaction warmed and sonicated until a clear dark blue solution had formed. To this was added a solution of $Bu_4NH_2PO_4$ (4 mg, 0.015 mmol) in $MeNO_2$ (0.5 ml) during which the colour changed from dark blue to lime green. Diisopropyl ether was slowly allowed to diffuse into the solution resulting in lime green needle-like crystals after several days. Filtration and washing with diisopropyl ether (1 ml) and diethyl ether (1 ml) gave lime green crystals which lost solvent rapidly (yield = 37%).

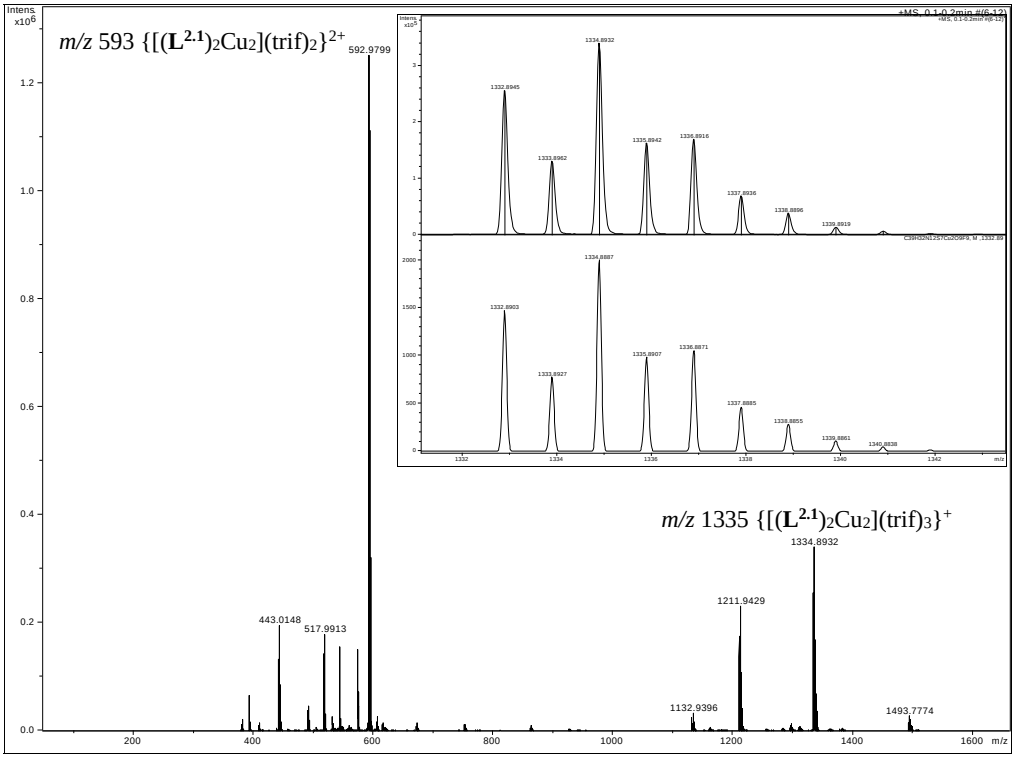

Figure 5.1.4. *ESI-MS of [(**L**$^{2.1}$)$_2$Cu$_2$(trif)](trif)$_2$ with the obtained isotope pattern (inset top) and calculated (inset bottom) for m/z 1335 {[(**L**$^{2.1}$)$_2$Cu$_2$](trif)$_3$}$^+$.*

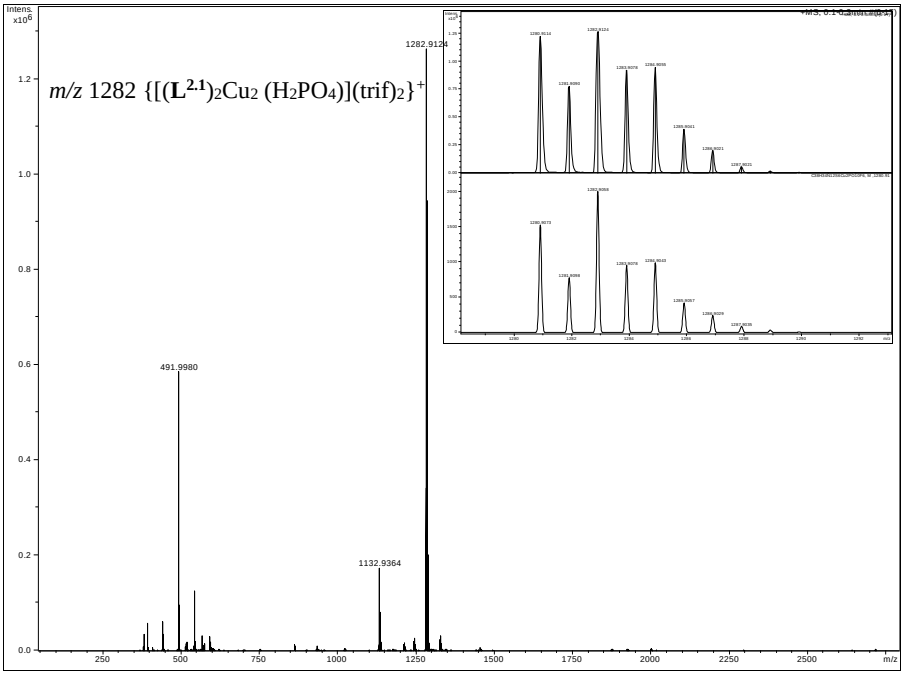

Figure 5.1.5. *ESI-MS of [(**L**$^{2.1}$)$_2$Cu$_2$(H$_2$PO$_4$)](trif)$_3$ with the obtained isotope pattern (inset top) and calculated (inset bottom) for m/z 1282 {[(**L**$^{2.1}$)$_2$Cu$_2$(H$_2$PO$_4$)](trif)$_2$}$^+$*

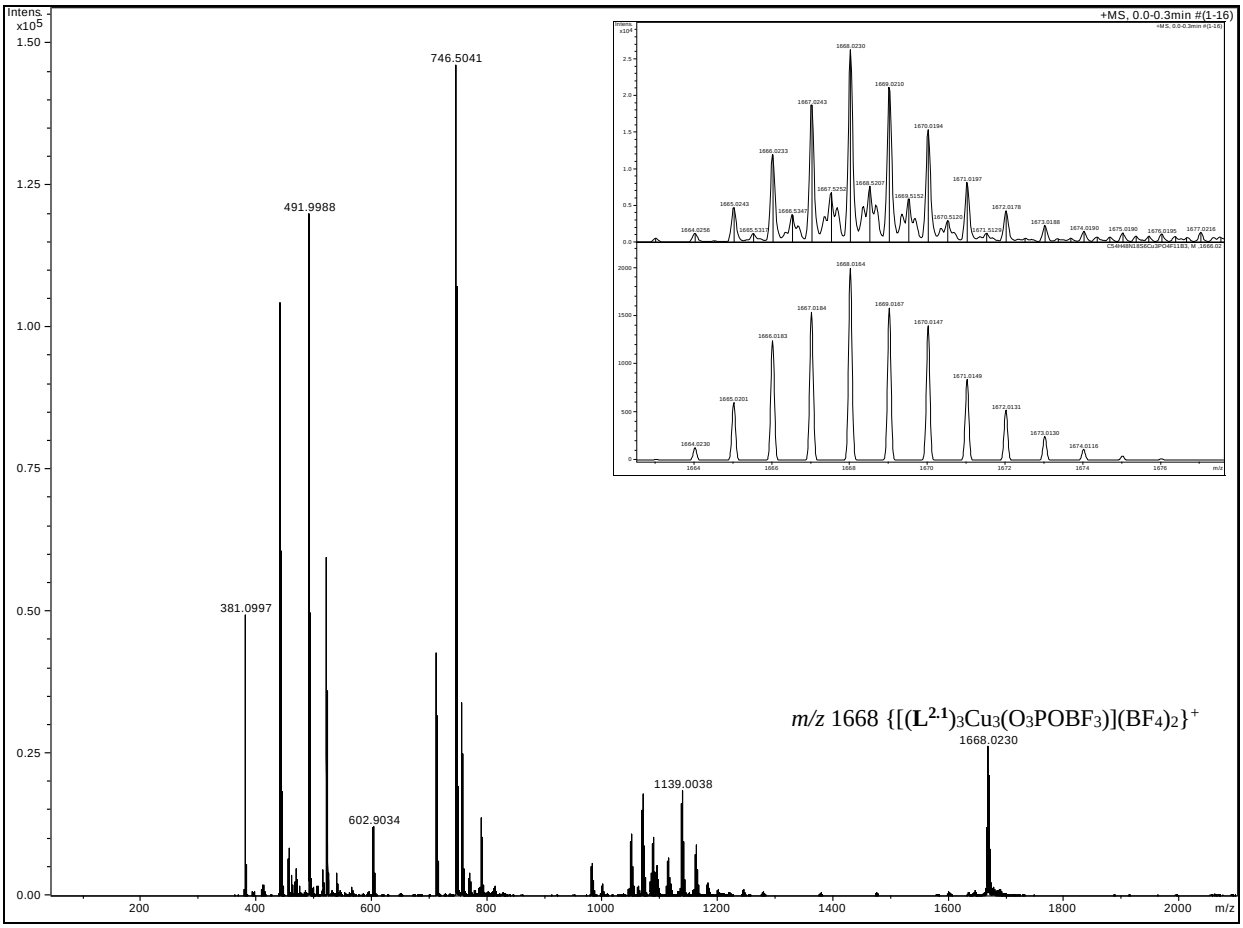

Figure 5.1.6. *ESI-MS of [(**L**$^{2.1}$)$_3$Cu$_3$(O$_3$POBF$_3$)](BF$_4$)$_3$ with the obtained isotope pattern (inset top) and calculated (inset bottom) for m/z 1668 {[(**L**$^{2.1}$)$_3$Cu$_3$(O$_3$POBF$_3$)](BF$_3$)$_2$}$^+$.*

5.12. $L^{2.2}$

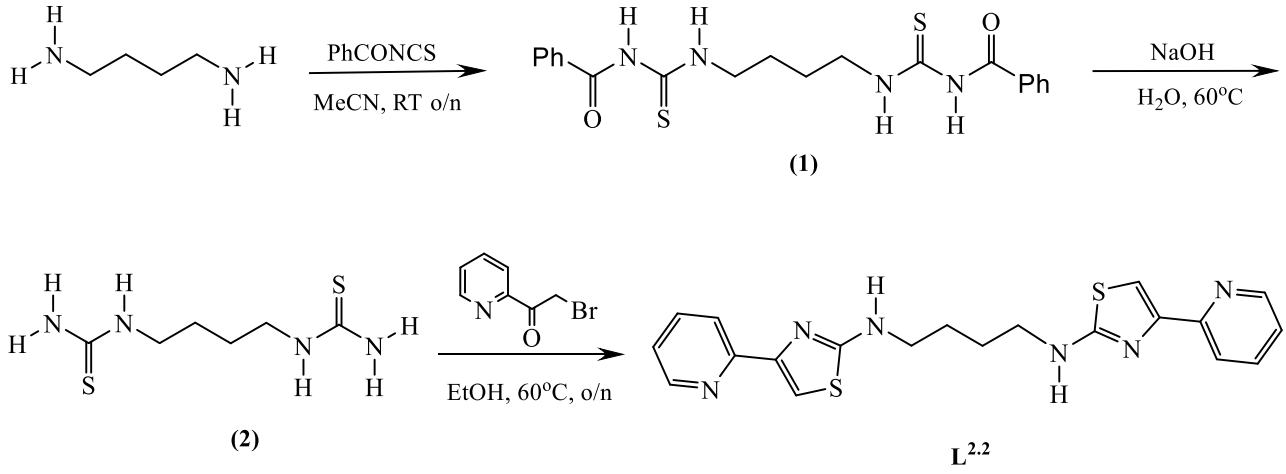

Scheme 5.1.2. *Synthesis route of ligand* ***L*$^{2.2}$**

To a 100 mL RBF was charged with putrescine (butane-1,4-diamine) (0.35 g, 3.9 mmol) and MeCN (25 mL) was added a solution of benzoyl isothiocyanate (1.3 mL, 1.59 g, 9.8 mmol) in MeCN (25 mL) slowly over 30 mins with constant stirring. The reaction mixture was then stirred at RT for a further 12 hrs during this time a heavy white precipitate was formed. The resulting mixture was the added dropwise whilst stirring to deionised water (100 mL) to yield a white/yellow precipitate which was then isolated via vacuum filtration. The solid was then suspended in MeOH (20 mL) in a 50 mL conical flask and sonicated (5 mins). The white/yellow suspension was then once again filtered under vacuum to yield a fine white solid which was washed with further portions of MeOH (3 x 5 mL) to give the *bis*-benzoylated thiourea (**1)** as a fine white powder (0.90 g, 55 %). ^{1}H NMR (400 MHz, $(CD_3)_2SO$) δ (ppm) 11.30 (s, 2H, NH), 10.92 (t, *J* = 5.4, 2H, -CH_2N*H*-), 7.92 (d, *J* = 7.2, 4H, Ph), 7.64 (t, *J* = 7.4, 2H, Ph), 7.51 (t, *J* = 7.8, 4H, Ph), 3.68 (d, *J* = 5.4 Hz, 4H, -C*H*$_2$NH-), 1.72 (brs, 4H, -C*H*$_2$$CH_2$NH-). ^{13}C NMR [400 MHz, DMSO-*d*^{6}]: δ_C = 183.5 (C=S), 168.4 (C=O), 133.4 (CH), 132.7 (Q), 129.0 (CH), 128.9 (CH), 128.7 (CH), 127.6 (CH), 44.8 (CH_2), 25.6 (CH_2). ESI-MS *m/z* 415 (M + H^+), HR ESI-MS found 415.1257 $C_{20}H_{22}N_4S_2O_2$ requires 414.1184 (error 0.49 ppm). Whilst the ESI-MS analysis did give an accurate ion the compound did decompose rapidly in

the ESI MS process and only a small M^+ ion was observed. This behaviour is common to all of the aliphatic bridged dithioamines and their derivatives.

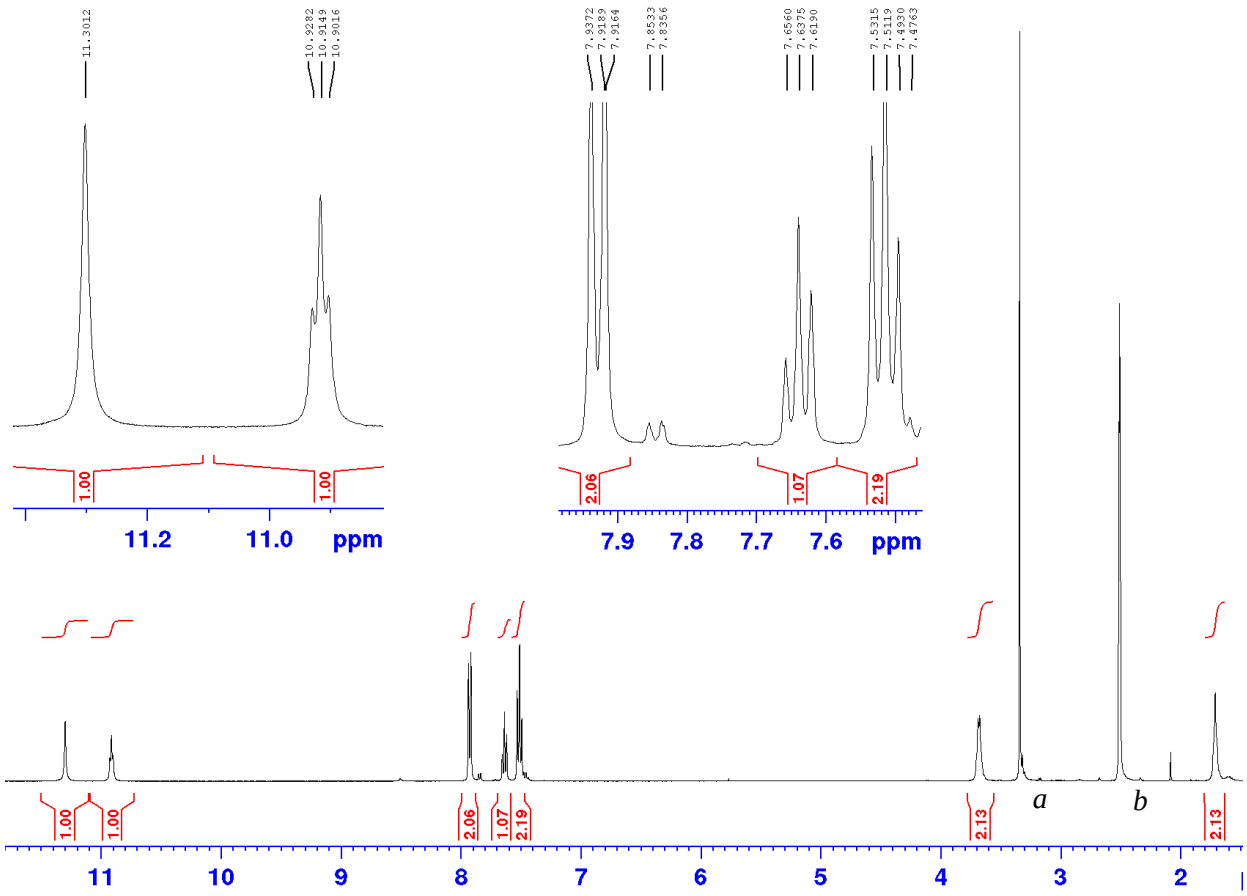

Figure 5.1.7. *^{1}H NMR of benzoylated thiourea product (**1**) a = water impurity and b = $(CD_3)(CHD_2)SO$.*

In a 50 ml RBF was combined the *bis*-benzoylated dithiourea (510 mg, 1.23 mmol), deionised water (10 mL) and a magnetic stir bar. A solution of NaOH (290 mg, 7.4 mmol) solution in H_2O (10 mL) was then added to the reaction mixture whilst stirring at 60°C. After 12 hrs the resulting colourless solution was then cooled to RT during which time a fine white precipitate was formed. The precipitate was then collected via vacuum filtration and then washed with ice cold deionised water (3 x 3 mL) giving the di-thiourea (**2**) as a

fine white powder (210 mg, 83 %). The ^{1}H NMR gives three broad signals in the aromatic region and two broad signals at 3.0 and 1.4 ppm. As has been mentioned previously is suspected that intra-molecular hydrogen bonding is inducing broad peaks in the ^{1}H NMR. However, the ^{13}C and ESI-MS is exactly as expected. ^{13}C NMR [400 MHz, DMSO-d^6]: δ_C = 183.5 (C=S), 44.1 (CH_2), 26.9 (CH_2). ESI-MS *m/z* 207 ($M + H^+$). HR ESI-MS found 207.0735 $C_6H_{14}N_4S_2$ requires 207.0733 (error 1.48 ppm).

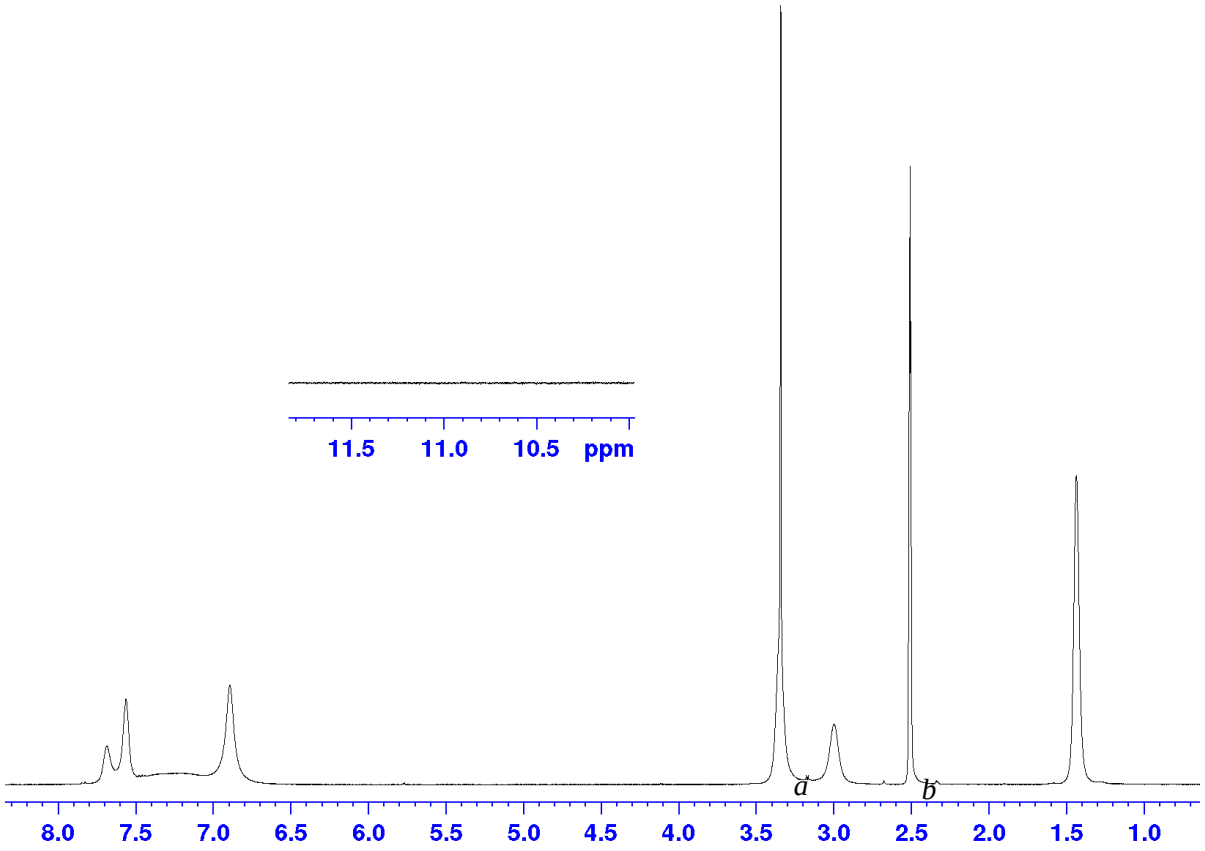

Figure 5.1.8. *^{1}H NMR of the bis-thiourea product (**2**) a = water impurity and b = $(CD_3)(CHD_2)SO$. The expansion shows the absence of amide peaks at ~11 ppm.*

A 25 mL RBF was charged with the *bis*-thiourea (**2**) (150 mg, 0.73 mmol), EtOH (10 mL) and magnetic stir bar. The mixture was then heated to 60 °C and to this added α-bromoacetyl pyridine (0.30 mg, 1.5 mmol) as a solution in EtOH (2 mL). Heating was continued for a further 8 hrs during which time a heavy yellow precipitate was formed. This was then isolated via vacuum filtration and the filtrand was then washed with equal portions of EtOH (3 x 2 mL) to give the protonated product. The free-base ligand was then isolated by suspending in concentrated ammonia (15 mL) for 24 hrs. The resulting colourless suspension was then sonicated (5mins) and was filtered under vacuum and the solid washed with equal portions of deionised water (5 x 2 mL) giving the product ($\mathbf{L}^{\mathbf{3.2}}$) as a fine off-white powder (180 mg 60 %). ^{1}H NMR (400 MHz, $(CD_3)_2SO$) δ (ppm) 8.53 (d, *J* = 4, 2H, py), 7.88 (d, *J* = 7.8, 2H, py), 7.79 (dt, 7.6, *J* = 1.7, 2H, py), 7.75 (t, *J* = 5.4, 2H, -NH), 7.28 (s, 2H, tz), 7.25 (dd, *J* = 5.7, 2H, py), 3.33 (brs, 4H, -C*H*$_2$NH-, overlapping with H_2O), 1.71 (brs, 4H, -C*H*$_2$CH$_2$NH-). ^{13}C NMR (400 MHz d^6-DMSO) δ 169.2, 153.0, 150.7, 149.7, 137.5, 122.8, 120.7, 104.9, 44.6 and 26.7 ppm. ESI-MS *m/z* 409 ($M + H^+$), HR ESI-MS found 409.1261 $C_{20}H_{20}N_6S_2$ requires 409.1264 (error 0.97 ppm).

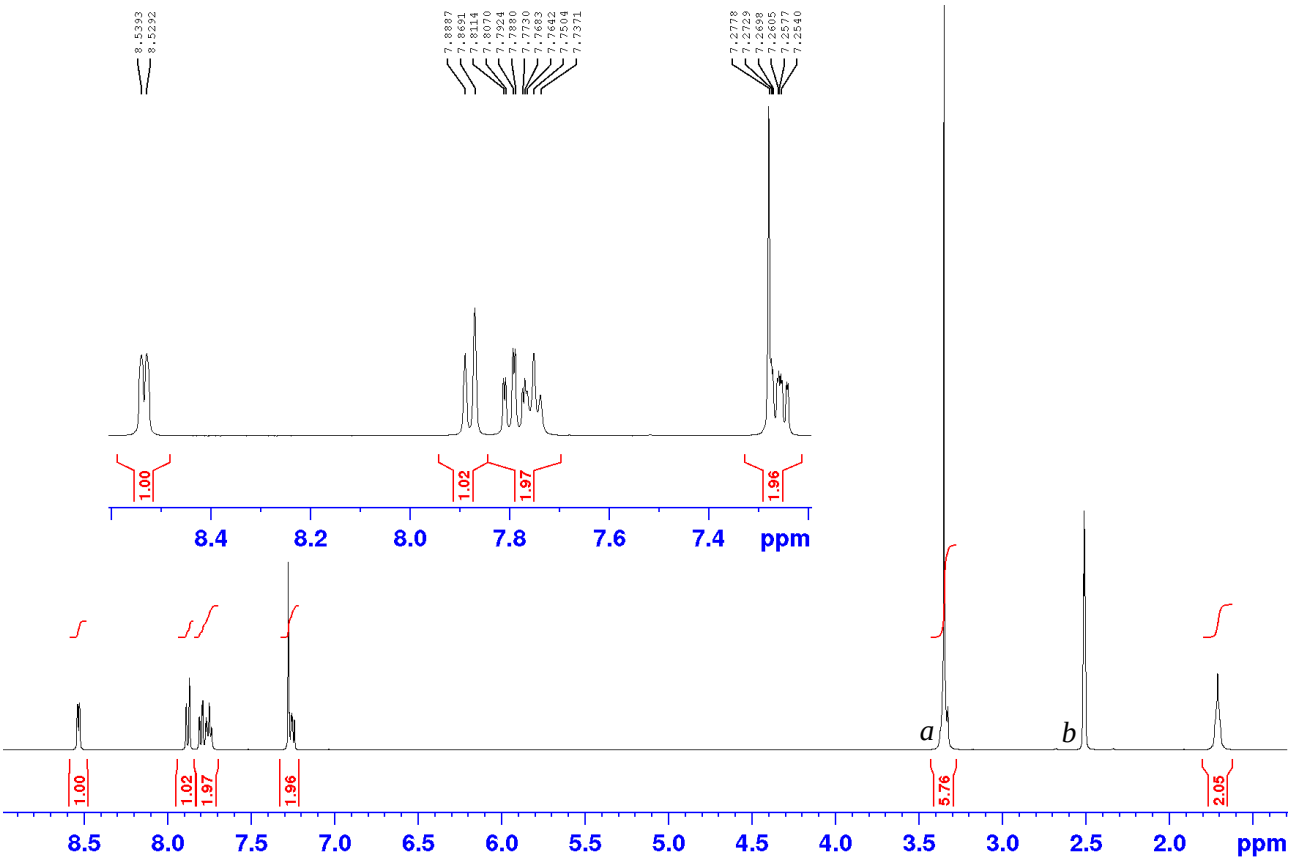

Figure 5.1.9. *^{1}H NMR of ligand $\boldsymbol{L^{2,2}}$ a = water impurity and b = $(CD_3)(CHD_2)SO$.*

Synthesis of $[(\mathbf{L}^{2.2})_2Cu_2H_2PO_4(trif)_2](trif)$.

To a solution of $Cu(trif)_2 \cdot 6H_2O$ (10 mg. 0.029 mmol) in $MeNO_2$ (1 ml) was added a suspension of ligand $\mathbf{L}^{2.2}$ (10 mg, 0.027 mmol) in $MeNO_2$ and the reaction warmed and sonicated until a clear dark blue solution had formed. To this was added a solution of $Bu_4NH_2PO_4$ (6.4 mg, 0.027 mmol) in $MeNO_2$ (0.5 ml) during which the colour changed from dark blue to lime green. Diisopropyl ether was slowly allowed to diffuse into the solution resulting in lime green needle-like crystals after several days. Filtration and washing with diisopropyl ether (1 ml) and diethyl ether (1 ml) gave lime green crystals which lost solvent rapidly (yield = 41%).

Synthesis of $[(\mathbf{L}^{2.2})_2Cu_2(HO_2P(OBF_3)_2](BF_4)$.

To a solution of $Cu(BF_4)_2 \cdot 6H_2O$ (10 mg. 0.029 mmol) in $MeNO_2$ (1 ml) was added a suspension of ligand $\mathbf{L}^{2.2}$ (10 mg, 0.027 mmol) in $MeNO_2$ and the reaction warmed and sonicated until a clear dark blue solution had formed. To this was added a solution of $Bu_4NH_2PO_4$ (6.4 mg, 0.027 mmol) in $MeNO_2$ (0.5 ml) during which the colour changed from dark blue to lime green. Diisopropyl ether was slowly allowed to diffuse into the solution resulting in lime green needle-like crystals after several days. Filtration and washing with diisopropyl ether (1 ml) and diethyl ether (1 ml) gave lime green crystals which lost solvent rapidly (yield = 38%).

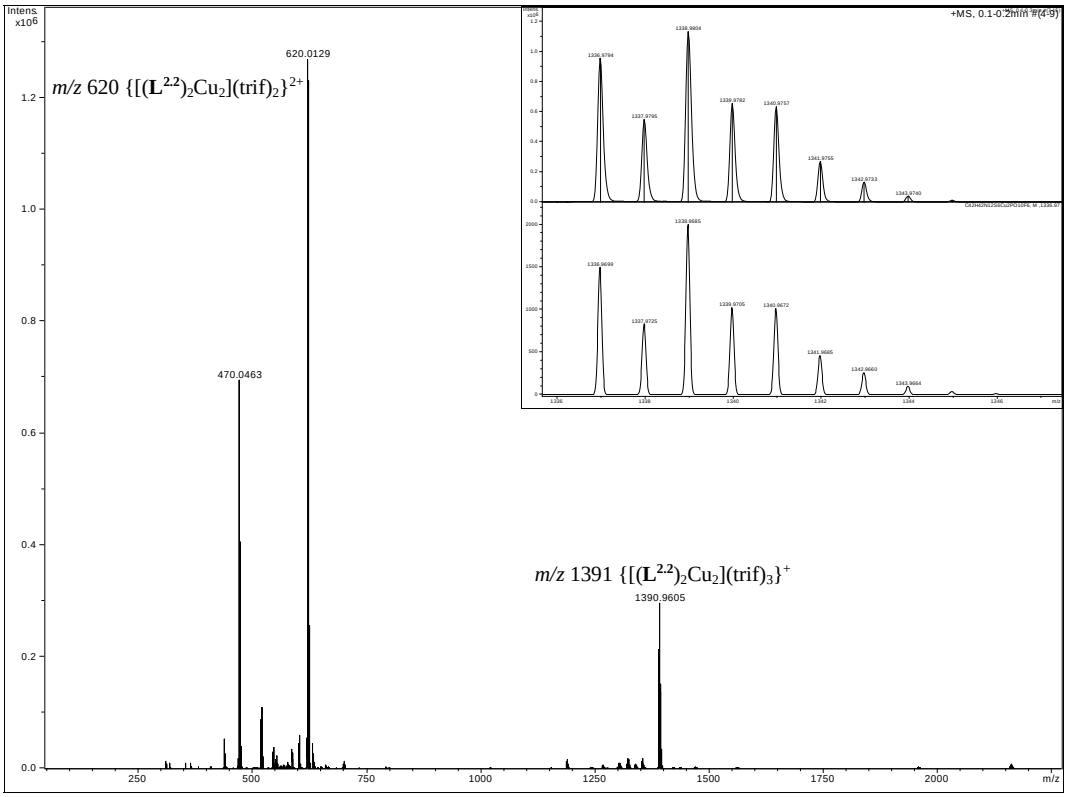

Figure 5.1.10. *ESI-MS of [(**L**$^{2.2}$)$_2$Cu$_2$](trif)$_4$ with the obtained isotope pattern (inset top) and calculated (inset bottom) for m/z 1391 {[(**L**$^{2.2}$)$_2$Cu$_2$](trif)$_3$}$^+$.*

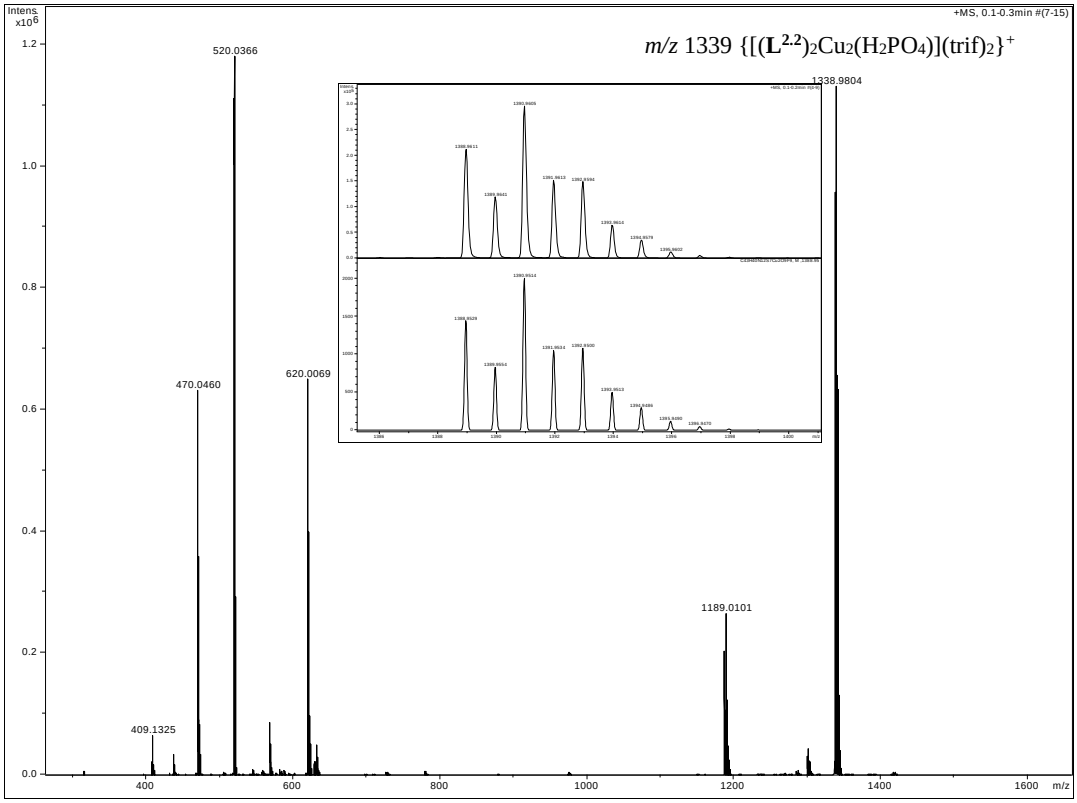

Figure 5.1.11. *ESI-MS of [(**L**$^{2.2}$)$_2$Cu$_2$(HPO$_4$)](trif)$_2$ with the obtained isotope pattern (inset top) and calculated (inset bottom) for m/z 1339 {[(**L**$^{2.2}$)$_2$Cu$_2$(H$_2$PO$_4$)](trif)$_2$}$^+$.*

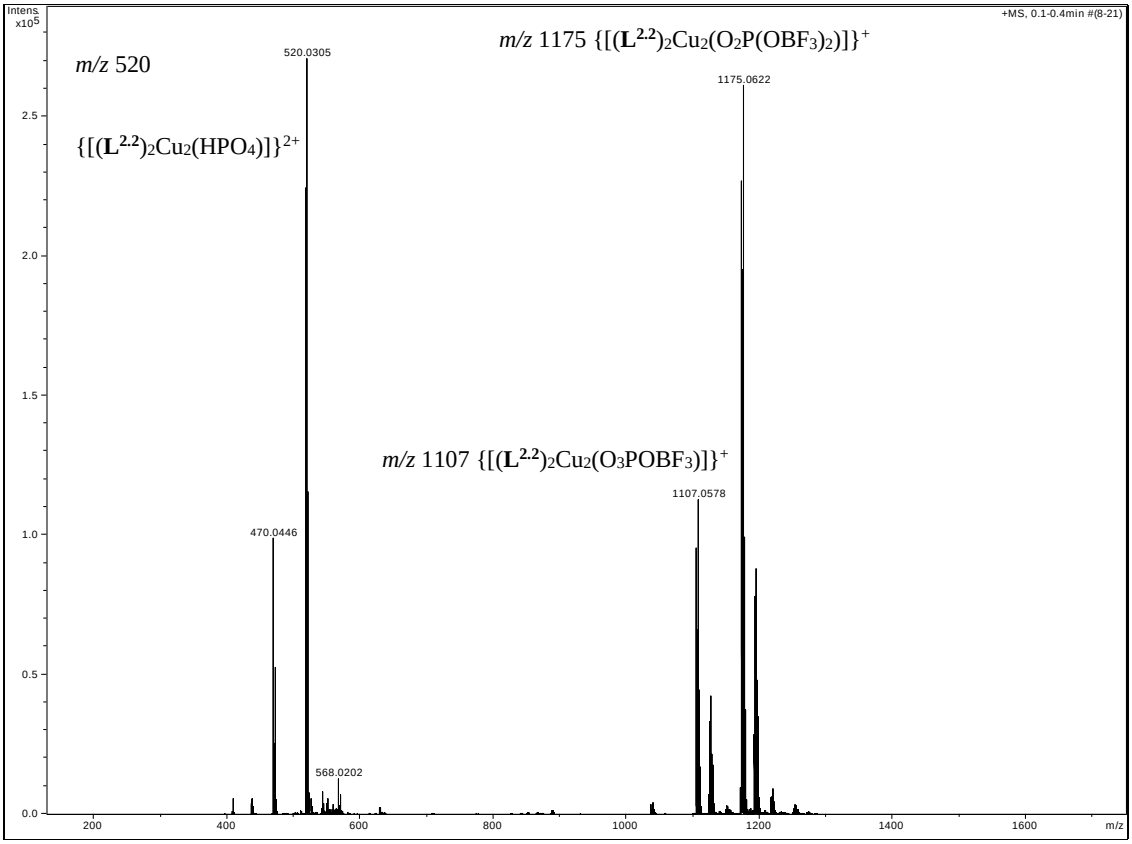

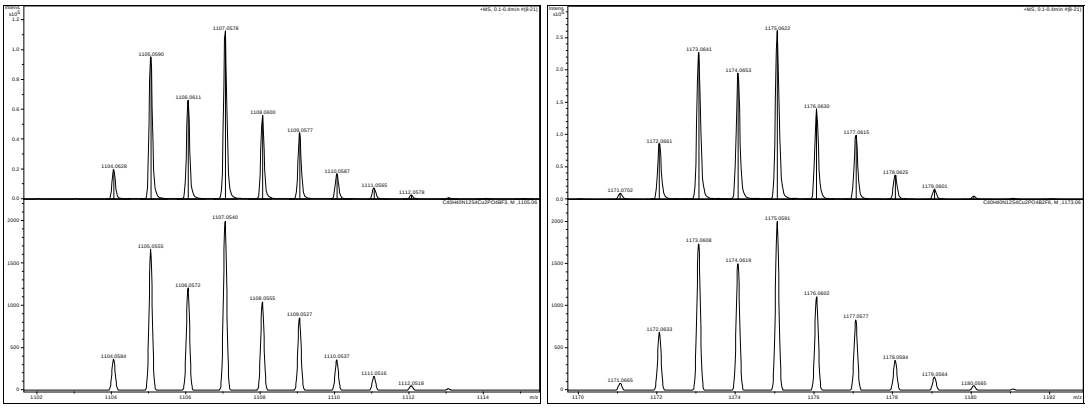

Figure 5.1.12. *ESI-MS of [(**L**$^{2.2}$)$_2$Cu$_2$(O$_3$POBF$_3$)](trif)$_2$ with the b) obtained isotope pattern and a) calculated for m/z 1107 {[(**L**$^{2.2}$)$_2$Cu$_2$(O$_3$POBF$_3$)]}$^+$.*

5.13. $L^{2.3}$

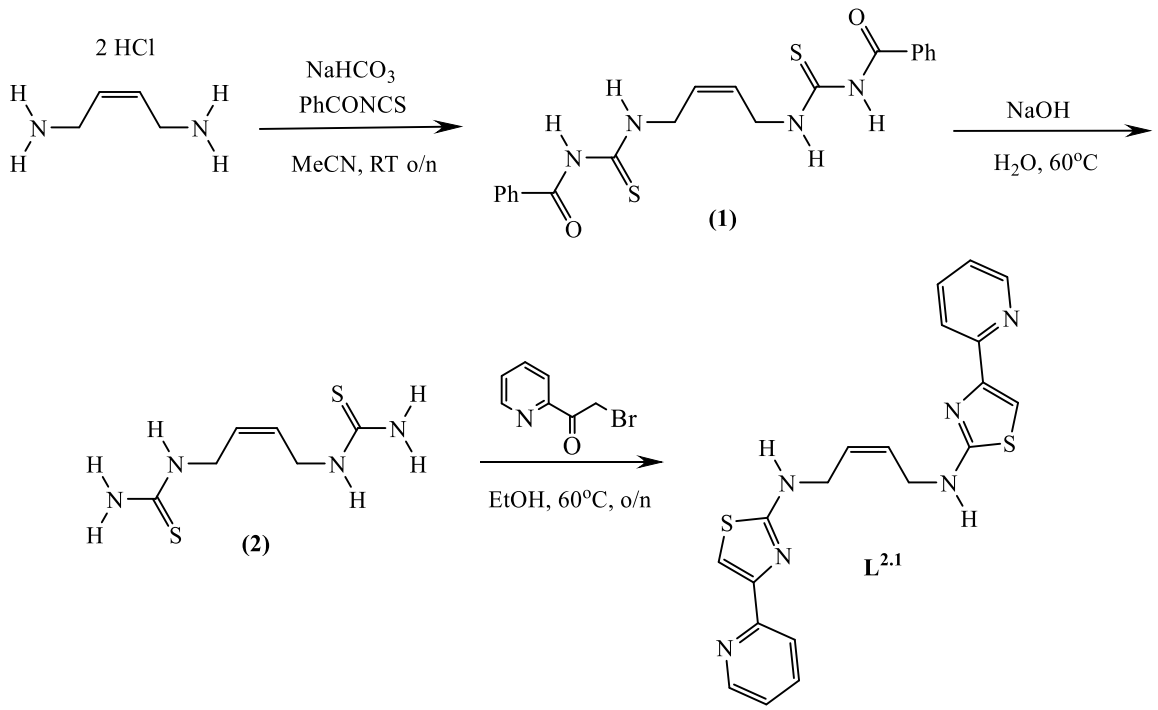

Scheme 5.1.3 *Synthesis route of ligand* ***L*$^{2.3}$**

To a 250 mL RBF charged with *cis*-1,4-diamino-2-butene dihydrochloride (0.7 g, 4.4 mmol) and MeCN (40 mL) was added $NaHCO_3$ (0.744 g, 8.8 mmol). The mixture was then sonicated (10 mins) followed by the addition of a solution of benzoyl isothiocyanate (1.3 mL, 1.58 g, 9.69 mmol) in MeCN (5 mL) slowly over 40 mins with constant stirring. The reaction mixture was then stirred at RT for a further 3 days during which time a heavy white precipitate was formed. The resulting mixture was the added dropwise whilst stirring to deionised water (300 mL) to yield a white/yellow precipitate which was then isolated via vacuum filtration. The solid was then suspended in MeOH (50 mL) in a 100 mL conical flask and sonicated (5 mins). The white/yellow suspension was then once again filtered under vacuum to yield a fine white solid which was washed with further portions of MeOH (3 x 10 mL) to give the *bis*-benzoylated di-thiourea (1) as a fine white powder (1.16 g, 62 %). ^{1}H NMR (400 MHz, $(CD_3)_2SO$) δ (ppm) 11.38 (s, 2H, NH), 10.95 (t, J = 5.4, 2H, NH), 7.91 (d, J = 8.52, 4H, Ph), 7.66 (t, J = 7.44, 2H, Ph), 7.51 (t, J = 7.48, 4H, Ph), 5.72 (t, J = 4.36 Hz, 2H, =CH-), 4.42 (t, J = 5.12, 4H, -CH_2-)). ^{13}C NMR [400 MHz, DMSO-d^6]: δ_C = 180.57 (C=S),

168.2 (C=O), 133.1 (CH), 132.7 (Q), 128.9 (CH), 128.6 (CH), 51.9 (CH_2), 42.6 (CH_2). ESI-MS *m/z* 413 ($M + H^+$), HR ESI-MS found 413.1111 $C_{30}H_{33}N_7S_3O_3$ requires 413.1100 (error 2.66 ppm). Whilst the ESI-MS analysis did give an accurate ion the compound did decompose rapidly in the ESI MS process and only a small M^+ ion was observed. This behaviour is common to all the aliphatic bridged dithioamines and their derivatives.

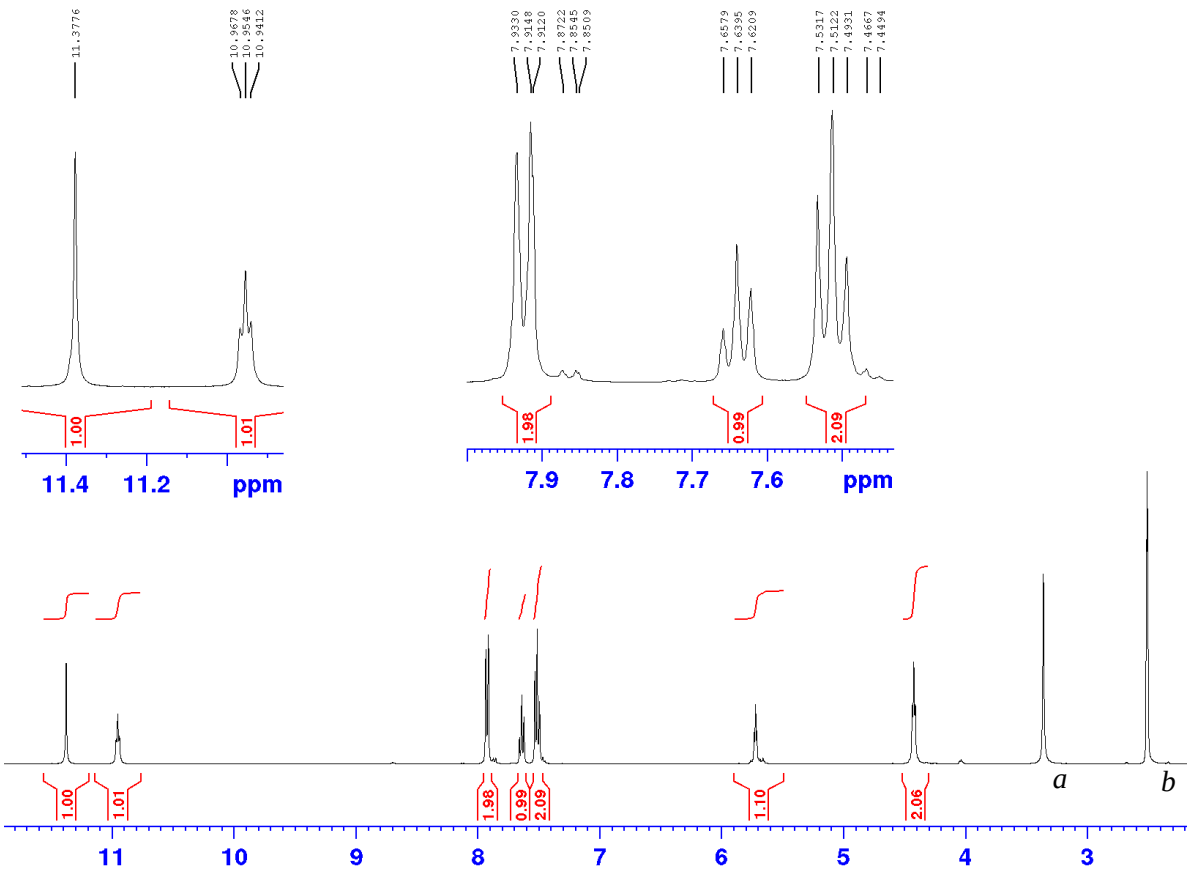

Figure 5.1.13. *^1H NMR of bis-benzoylated thiourea product (**1**) a = water impurity and b = $(CD_3)(CHD_2)SO$.*

In a 100 ml RBF was combined the benzoylated dithiourea (0.8 g, 1.94 mmol), deionised water (20 mL) and a magnetic stir bar. A solution of NaOH (0.47 g, 11.8 mmol) solution in H_2O (5 mL) was then added to the reaction mixture whilst stirring at 60°C. After 12 hrs the resulting colourless solution was then cooled to RT during which time a fine white precipitate was formed. The precipitate was then collected via vacuum filtration and then washed with ice cold deionised water (3 x 5 mL) giving the dithiourea (**2**) as a fine white powder (0.35 g, 89 %). The ^{1}H NMR gives one broad signal in the aromatic region and two broad signals at ~5.8 ppm and ~3.5 ppm. Again, it is suspected that intra-molecular hydrogen bonding is inducing broad peaks in the ^{1}H NMR, however the ^{13}C and ESI-MS is exactly as expected. ^{13}C NMR [400 MHz, DMSO-d^6]: δ_C = 183.5 (C=S), 128.8 (CH), 41.7 (CH_2).ESI-MS *m/z* 205 ($M + H^+$). HR ESI-MS found 205.0581 $C_6H_{12}N_4S_2$ requires 205.0576 (error 2.67 ppm).

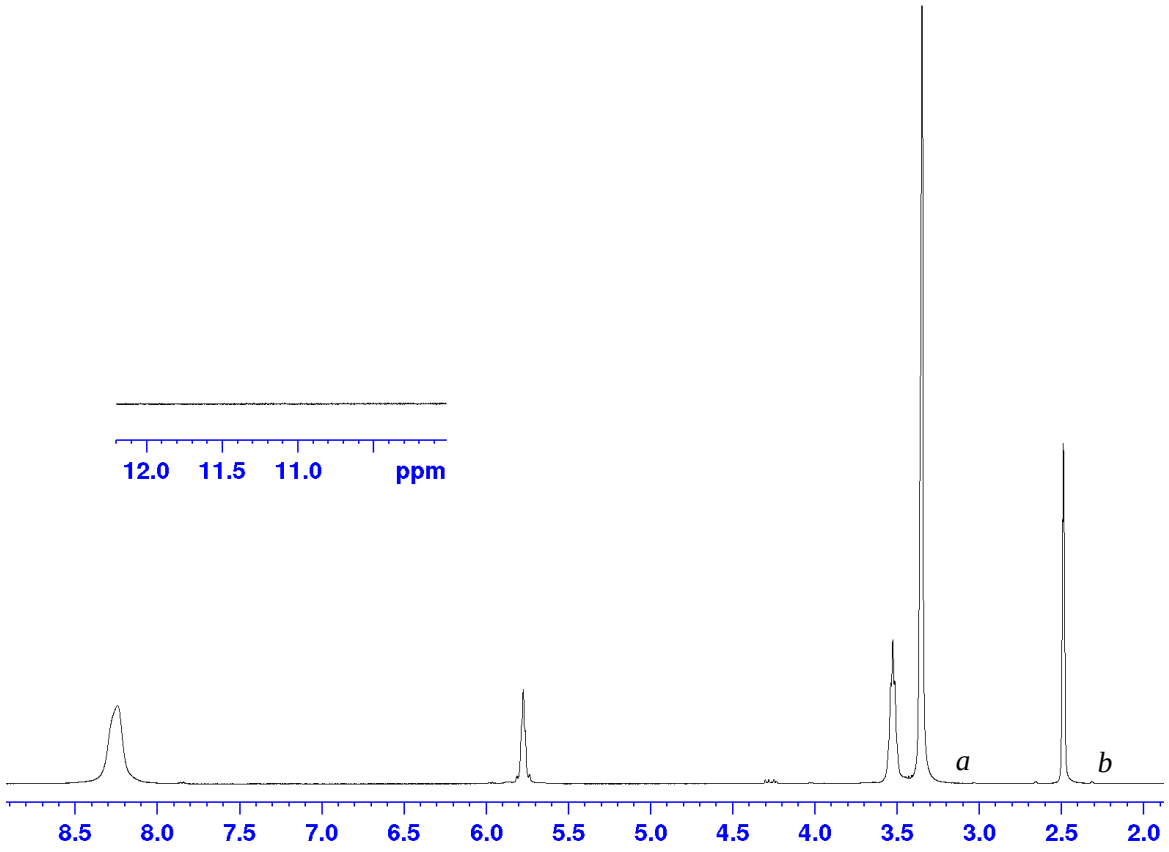

Figure 5.1.14. *^{1}H NMR of the bis-thiourea product (**2**) a = water impurity and b = $(CD_3)(CHD_2)SO$.*

Synthesis of $L^{2.3}$

A 25 mL RBF was charged with dithiourea (0.2 g, 0.98 mmol), EtOH (10 mL) and magnetic stir bar and the mixture was then heated to 60 °C. To this was slowly added α-bromoacetyl pyridine (0.41 g, 2.1 mmol) in a solution in EtOH (2 mL). Heating was continued for a further 16 hrs during which time a heavy yellow precipitate was formed. This was then isolated via vacuum filtration and the filtrand was then washed with equal portions of EtOH (3 x 2 mL) to give the protonated product. The free-base ligand was then isolated by suspending in concentrated ammonia (15 mL) for 24 h. The resulting colourless suspension was then sonicated (5mins) and was filtered under vacuum and the solid washed with equal portions of deionised water (5 x 2 mL). Giving the product (**$L^{2.3}$**) as a fine off-white powder (0.33 g, 83 %). ^{1}H NMR (400 MHz, $(CD_3)_2SO$) δ (ppm) 8.54 (dd, *J* = 4.0, 0.8, 2H, py), 7.90 (m, overlapping, 4H, py and -NH), 7.74 (dt, *J* = 7.8, 1.6, 2H, py), 7.32 (s, 2H, tz), 7.26 (ddd, *J* = 5.7, 4.8, 0.8, 2H, py), 5.68 (t, *J* = 4.2, 2H, =CH-), 4.13 (t, *J* = 4.9 Hz, 4H, $-CH_2-$). ^{13}C NMR (400 MHz d^6-DMSO) δ 168.7, 152.9, 150.7, 149.7, 137.4, 129.0, 122.8, 120.8, 105.5 and 41.9 ppm. ESI-MS *m/z* 407 ($M + H^+$). HR ESI-MS found 407.1108 $C_{20}H_{18}N_6S_2$ requires 407.1107 (error 0.29 ppm).

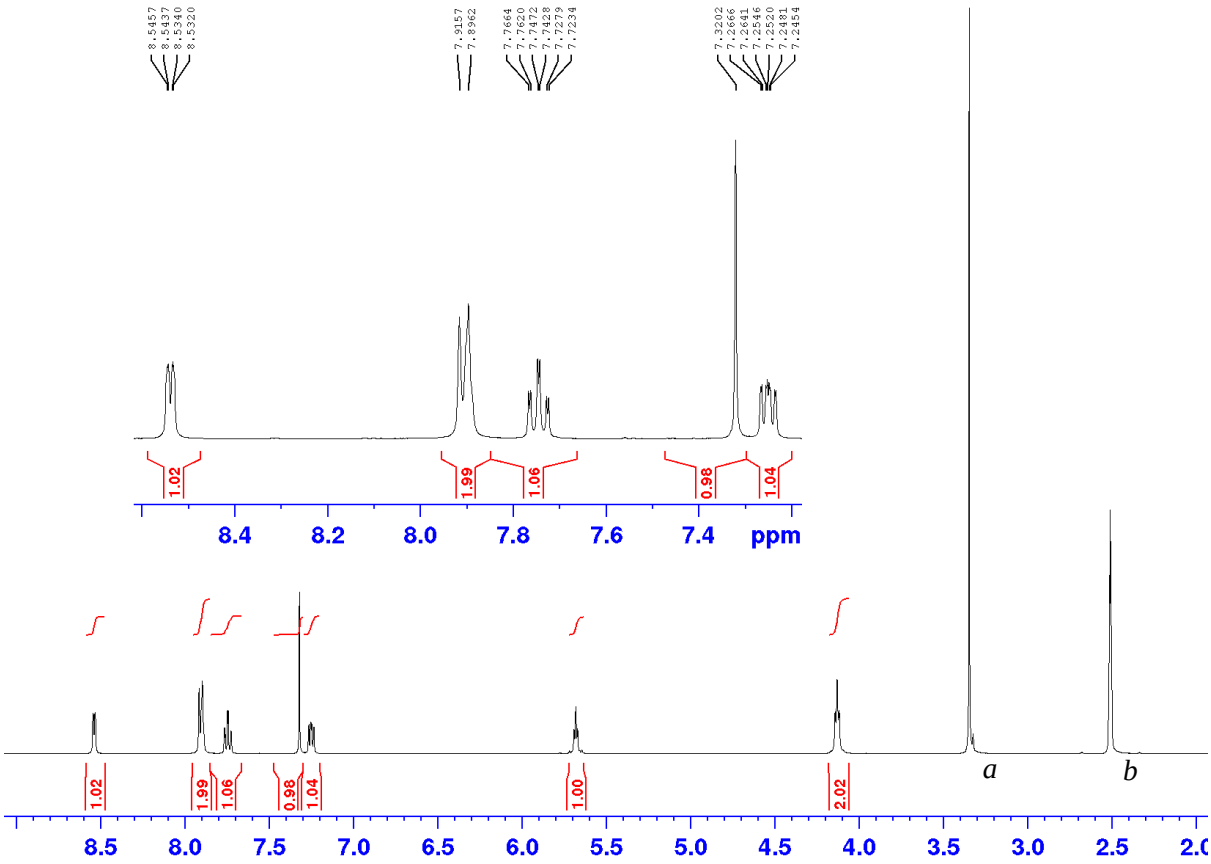

Figure 5.1.15. *^{1}H NMR of ligand $\mathbf{L}^{2.3}$ a = water impurity and b = $(CD_3)(CHD_2)SO$.*

Synthesis of $[(\mathbf{L}^{2.3})_2Cu_2(trif)_2](trif)_2$.

To a solution of $Cu(trif)_2 \cdot 6H_2O$ (10 mg. 0.027 mmol) in $MeNO_2$ (1 ml) was added a suspension of ligand $\mathbf{L}^{2.3}$ (10 mg, 0.025 mmol) in $MeNO_2$ and the reaction warmed and sonicated until a clear dark tan solution had formed. Di-isopropyl ether was slowly allowed to diffuse into the solution resulting in dark brown needle-like crystals after several days. Filtration and washing with diisopropyl ether (1 ml) and diethyl ether (1 ml) gave brown crystals which lost solvent rapidly (yield = 51%). A similar isolation was carried out using CHCl3 as the anti-solvent (see discussion) (yield = 47%).

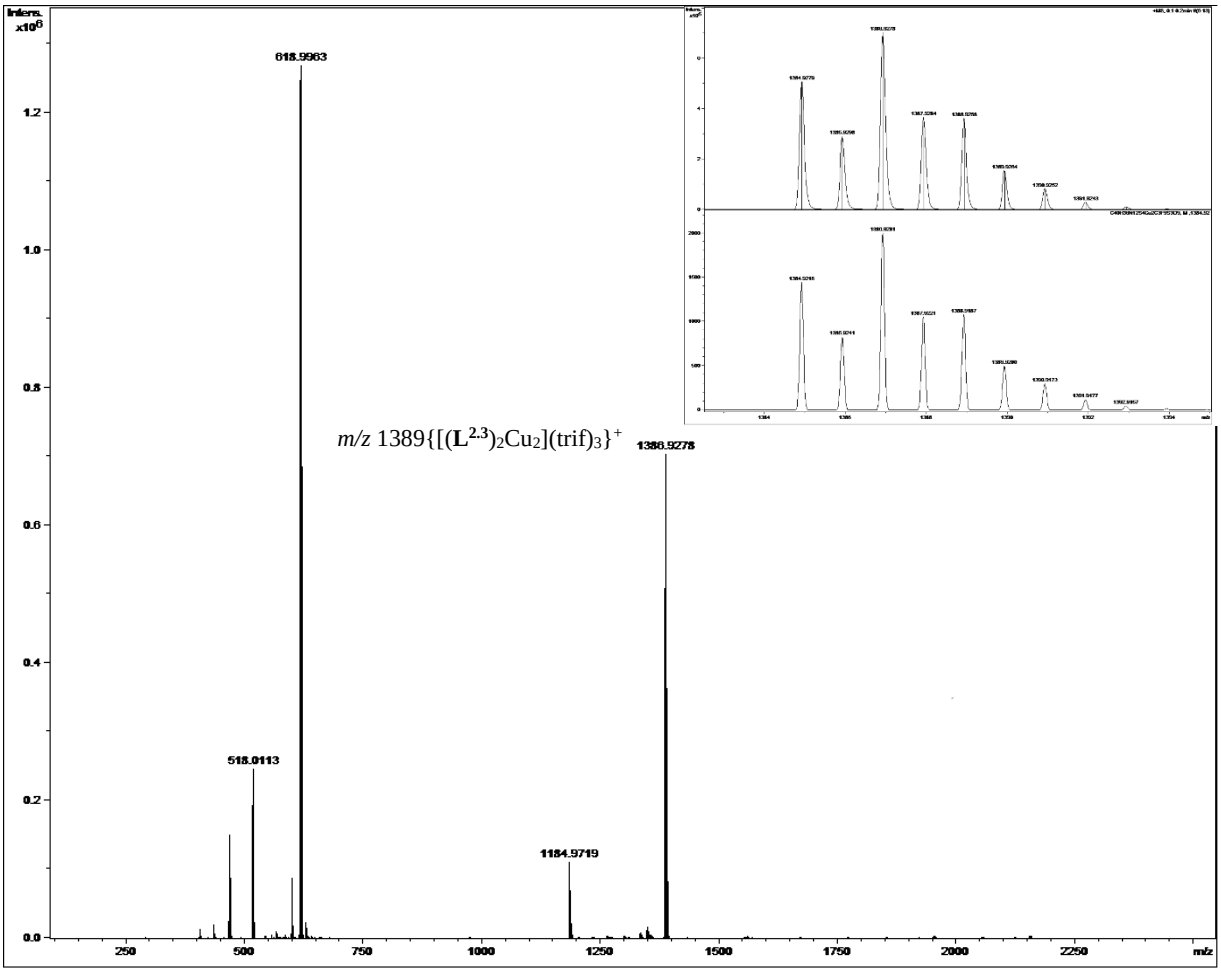

Figure 5.1.16. *ESI-MS of* $[(\mathbf{L}^{2.3})_2Cu_2](trif)_4$ *with the obtained isotope pattern (inset top) and calculated (inset bottom) for m/z 1389* $\{[(\mathbf{L}^{2.3})_2Cu_2](trif)_3\}^+$.

5.2 Experimental $L^{3.1}$

Chemicals were purchased and used without further purification. ^{1}H and ^{13}C NMR spectra were recorded on a 400MHz Bruker Avance DP X400. Mass spectra were obtained on an Agilent 6210 TOF MS for the organic species with the metal complexes run on a Bruker MicroQTOF LC.

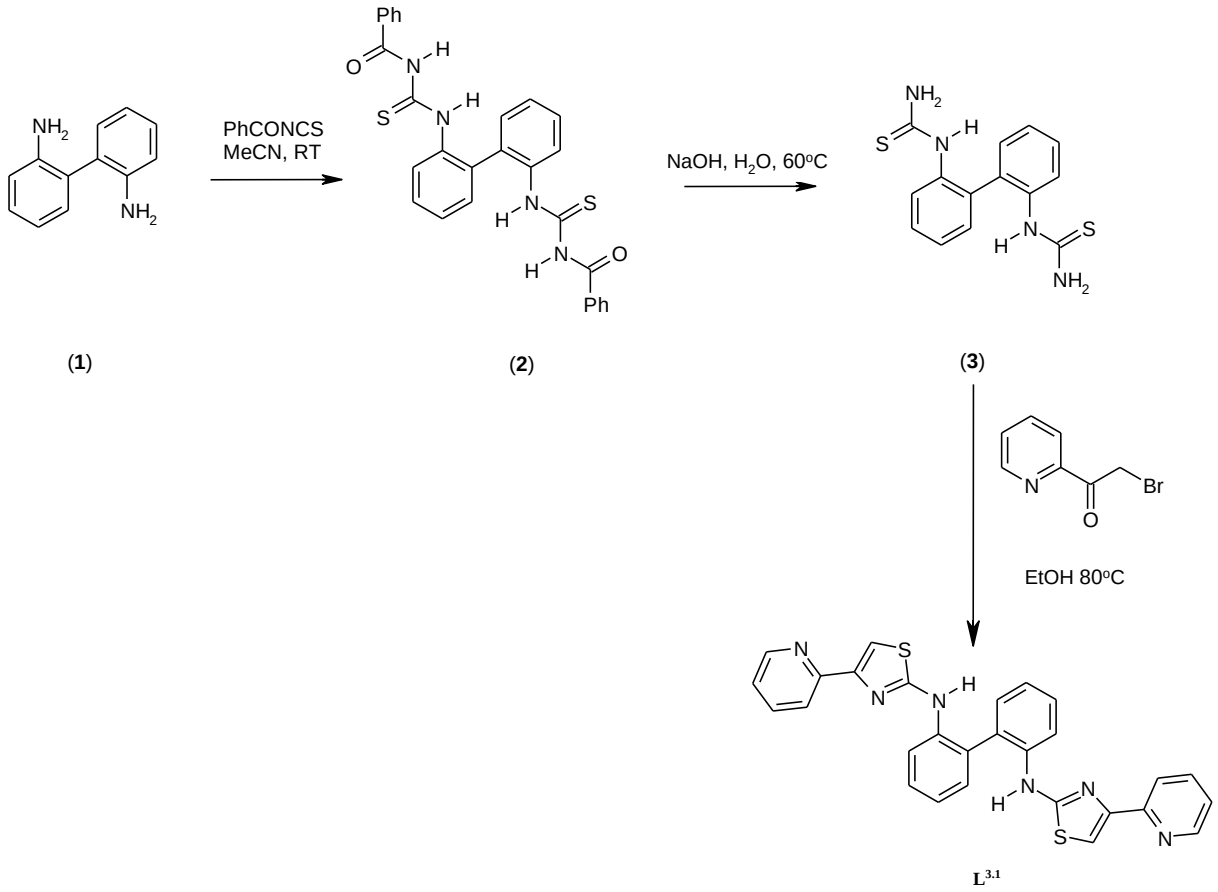

Scheme 5.2.1. *Synthetic route for ligand* ***L**$^{3.1}$*

Synthesis of (**2**).

To a solution of 1,1'-biphenyl-2,2'-diamine (**1**) (410 mg, 2.23 mmol) in acetonitrile (50 mL) was added benzoyl isothiocyanate (794 mg, 4.90 mmol) and the reaction stirred for 3 days at RT, during which time a colourless precipitate formed which was isolated by filtration, washed with MeCN (3 × 5 mL) and Et_2O (3

× 5 mL) giving (**2**) as a while solid. Yield = 743 mg (65 %). ^{1}H NMR (400MHz, DMSO-d^6) δ (ppm) 12.2 (s, 2H, -NH), 11.4 (s, 2H, -NH), 7.86 (d, 4H, *J* = 7.52), 7.74 (d, 2H, *J* = 7.8), 7.63 (t, 2H, *J* = 7.4), 7.50 (t, 4H, *J* = 7.68), 7.43 (m, overlapping, 4H), 7.34 (t, 2H *J* = 7.38 Hz). ESI-MS *m/z* 511 (M + H^+), HR ESI-MS found 511.1251 $C_{28}H_{22}N_4O_2S_2$ requires 511.1257 (error 0.93 ppm).

Synthesis of (**3**)

The diurea derivative (**2**) (400 mg, 0.784 mmol) was suspended in water (20 mL) and NaOH (191 mg, 4.78 mmol) added. The reaction was then heated to 60°C and MeOH slowly added dropwise until all the solid dissolved (1 ~ 2 mL). After 24 hrs the solution was allowed to cool to room temperature and then immersed in an ice bath, after which time a colourless solid precipitated. Isolation by filtration and washing with ice cold water (2 x 1 mL) gave the dithiourea (**3**) as a colourless solid. Yield = 140 mg (59 %). ^{1}H NMR (400MHz, DMSO-d^6) δ (ppm) 8.81 (s, 2H, -NH), 7.33 (m, broad, overlapping, 12H). ESI-MS *m/z* 303 (M + H^+), HR ESI-MS found 303.0732 $C_{14}H_{14}N_4S_2$ requires 303.0733 (error 0.41 ppm).

Synthesis of $\mathbf{L^{3.1}}$.

The dithiourea containing compound (**3**) (141 mg, 0.47 mmol) was suspend in EtOH (20 mL) and to this, α-bromoacetylpyridine hydrobromide (393 mg, 1.40 mmol) was added and the reaction heated at 80 °C overnight. During this time a yellow precipitate had formed which was isolated by filtration and washed with EtOH (2 x 1 mL) and Et_2O (2 x 1 mL). This yellow solid was suspended in ammonia (sp. gr 0.88, 10 mL) and stirred for 24 hrs. The solid was then filtered, washed with H_2O (2 x 1 mL), EtOH (2 x 1 mL) and Et_2O (2 x 1 mL) to give $\mathbf{L^{3.1}}$ as a cream solid. Yield = 120 mg (51 %).^{1}H NMR (400MHz, DMSO-d^6) δ (ppm) 8.56 (d, 2H, *J* = 4.32), 8.20 (d, 2H, *J* = 8.16), 7.89 (d, 2H, *J* = 7.92 Hz), 7.69 (td, 2H, *J* = 7.72, 1.6), 7.53 (td, 2H, *J* = 7.81, 1.4 Hz), 7.33 (m, overlapping, 4H), 7.23 (t, 2H, *J* = 7.44), 7.18 (dd, 2H, *J* = 7.02, 4.96 Hz), 6.96 (2H, br s, -NH). ^{13}C NMR (500 MHz, DMSO-d^6) δ (ppm) = 165.6 (Q), 151.7 (Q), 149.6,

139.2 (Q), 137.6, 131.9, 130.8 (Q), 129.5 (Q), 129.0, 123.9, 122.9, 122.0, 120.8, 107.2. ESI-MS *m/z* 505 ($M + H^+$), HR ESI-MS found 505.1256 $C_{28}H_{20}N_6S_2$ requires 505.1264 (error 1.24 ppm).

Synthesis of $[(\mathbf{L}^{3.1})Cu](ClO_4)_2$.

To a solution of $Cu(ClO_4)_2 \cdot 6H_2O$ (10 mg. 0.027 mmol) in MeCN (1 ml) was added a suspension of ligand $\mathbf{L}^{3.1}$ (13 mg, 0.026 mmol) in MeCN and the reaction warmed and sonicated until a clear light blue solution had formed. Diisopropyl ether was slowly allowed to diffuse into the solution resulting in blue plate-like crystals after several days. Filtration and washing with diisopropyl ether (1 ml) and diethyl ether (1 ml) gave blue crystals which lost solvent rapidly (yield = 52%). ESI-MS *m/z* 669 corresponding to $\{Cu(\mathbf{L}^{3.1})(ClO_4)\}^+$ along with higher molecular species (see **3. Discussion**, Fig. 3.2.4 and 3.2.5.).

Synthesis of $[(\mathbf{L}^{3.2})_4Cu_4](trif)_8$.

To a solution of $Cu(trif)_2$ (10 mg. 0.028 mmol) in MeCN (1 ml) was added a suspension of ligand $\mathbf{L}^{3.1}$ (14 mg, 0.026 mmol) in MeCN and the reaction warmed and sonicated until a clear light blue solution had formed. Diisopropyl ether was slowly allowed to diffuse into the solution resulting in pale blue block crystals after several days. Filtration and washing with diisopropyl ether (1 ml) and diethyl ether (1 ml) gave blue crystals which lost solvent rapidly (yield = 68%). ESI-MS *m/z* 3479 corresponding to $\{[Cu_4(\mathbf{L}^{3.2})_4](trif)_7\}^+$), along with a ion at *m/z* 1665 corresponding to both the singly charged dinuclear assembly $\{[Cu_2(\mathbf{L}^{3.2})_2](trif)_3\}^+$ and the doubly charged tetranuclear assembly (e.g. $\{[Cu_4(\mathbf{L}^{3.2})_4](trif)_6\}^{2+}$). Found: C, 41.4; H, 2.6; N, 10.0%; $C_{128}H_{92}N_{28}S_{16}Cu_4F_{24}O_{24} \cdot 2H_2O$ requires C, 41.9; H, 2.6; N, 10.7%.

5.3 $L^{4.1}$ Experimental

Chemicals were purchased and used without further purification. ^{1}H and ^{13}C NMR spectra were recorded on a 400MHz Bruker Avance DP X400. Mass spectra were obtained on an Agilent 6210 TOF MS for the organic species with the metal complexes run on a Bruker MicroQTOF LC. UV-Vis spectra were run on an Agilent Cary 60 UV-Vis. Ion chromatography was run on a Metrohm 850 IC system.

Synthesis of $L^{4.1}$

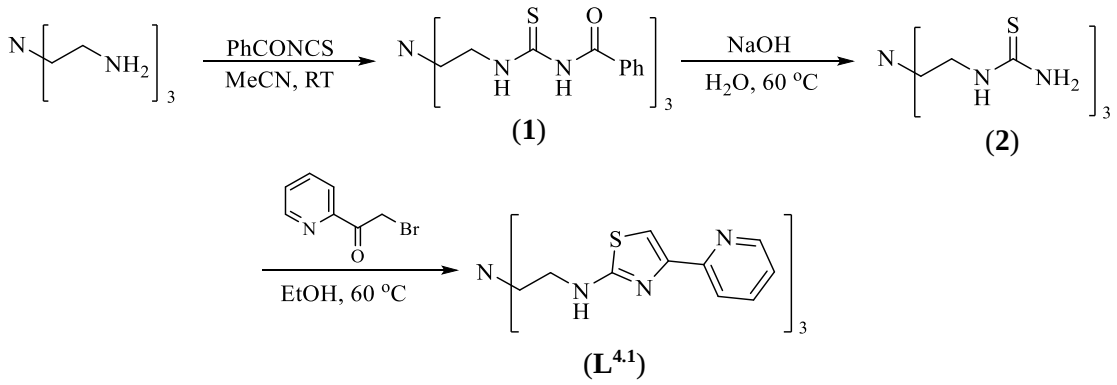

Scheme 5.3.1. *Synthetic route for the synthesis of* ***L$^{4.1}$***

Synthesis of (**1**).

To a solution of tris(2-aminoethyl)amine (0.5 g, 3.42 mmol) in acetonitrile (50 mL) was added benzoyl isothiocyanate (1.8 g, 11.3 mmol) and the reaction stirred for 4 days at RT, during which time a small amount of a yellow precipitate formed. The suspension was then slowly added to water (50 mL) which gave a heavy colourless precipitate which was isolated by filtration washed with acetone (3 × 5 mL) giving (**1**) as a white solid. Yield = 1.05 g (48 %). ^{1}H NMR (400 MHz, DMSO-d^6) δ (ppm) 11.20 (s, 3H, -NH), 11.0 (t, 3H, *J* = 4.8, -CH_2NH), 7.81 (d, 6H, *J* = 7.2, Ph), 7.56 (t, 3H, *J* = 7.4, Ph), 7.38 (t, 6H, *J* = 7.6, Ph), 3.75 (q, 6H, *J* = 5.7, -CH_2CH_2NH), 2.89 (t, 6H, *J* = 6.0 Hz, -CH_2CH_2NH). ^{13}C NMR [100 MHz, DMSO-d^6]: δ_C = 180.5 (C=S), 168.2 (C=O), 133.1 (CH), 132.7 (Q), 128.9 (CH), 128.6 (CH), 51.9 (CH_2), 42.6 (CH_2). ESI-MS *m/z* 636 ($M + H^+$), HR ESI-MS found 636.1882 $C_{30}H_{33}N_7S_3O_3$ requires 636.1880 (error 0.46 ppm).

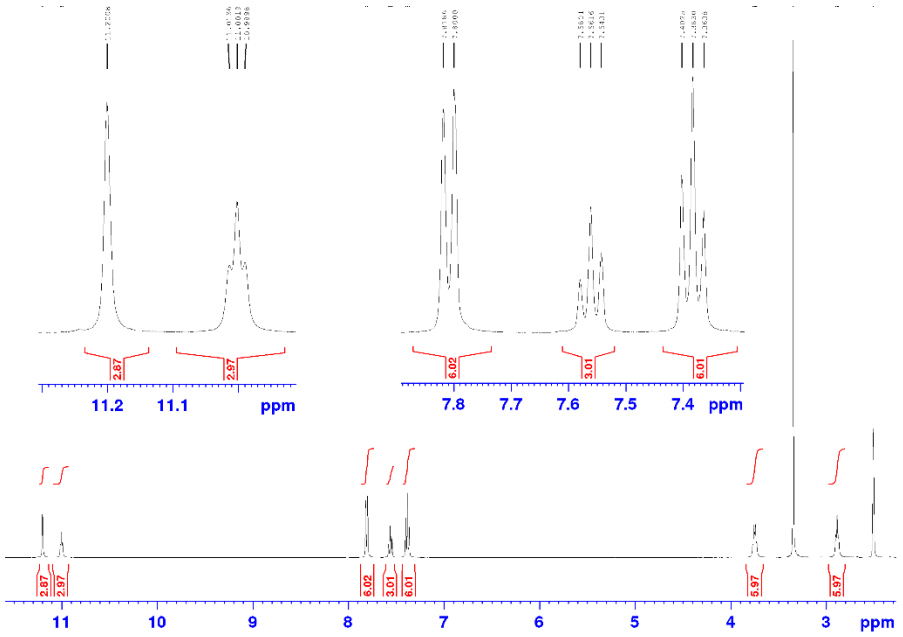

Figure 5.3.1. *^{1}H NMR of the benzoylated urea derivative (**1**)*

Synthesis of (**2**)

The benzoylated urea derivative (**1**) (500 mg, 0.787 mmol) was suspended in water (20 mL) and NaOH (307 mg, 7.87 mmol) added. The reaction was then heated to 60 °C and MeOH slowly added dropwise until all the solid dissolved (1 ~ 2 mL). After 48 hrs the solution was allowed to cool to room temperature and then immersed in an ice bath, after which time a colourless solid precipitated. Isolation by filtration and washing with ice cold water (2 x 1 mL) gave the tri-thiourea (**2**) as a colourless solid. Yield = 120 mg (47 %). ^{1}H NMR (400 MHz, DMSO-d^6) δ (ppm) 7.55 (brs, 3H, -NH), 7.08 (brs, 6H, -NH_2), 3.44 (brs, 6H, -CH_2CH_2NH), 2.58 (brs, 6H, -CH_2CH_2NH). ^{13}C NMR [100 MHz, DMSO-d^6]: δ_C = 183.5 (C=S), 52.9 (CH_2), 42.3 (CH_2). ESI-MS *m/z* 324 (M + H^+), HR ESI-MS found 324.1089 $C_9H_{21}N_7S_3$ requires 324.1093 (error 1.03 ppm).

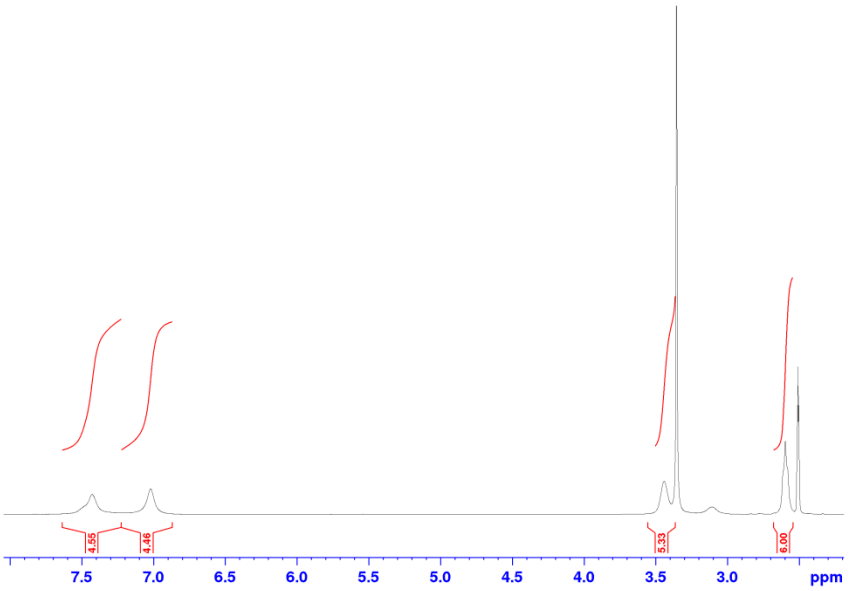

Figure 5.3.2. *^{1}H NMR of the trithiourea compound (**2**)*

Synthesis of **L**$^{4.1}$.

The trithiourea containing compound (**2**) (100 mg, 0.31 mmol) was suspend in EtOH (20 mL) and to this α-bromoacetylpyridine (205 mg, 1.02 mmol) was added and the reaction heated at 80 °C overnight. During this time a yellow precipitate had formed which was isolated by filtration and washed with EtOH (2 x 1 mL) and Et_2O (2 x 1 mL). This yellow solid was suspended in ammonia (sp. gr 0.88, 10 mL) and stirred for 24 hrs. The solid was then filtered, washed with H_2O (2 x 1 mL), EtOH (2 x 1 mL) and Et_2O (2 x 1 mL) to give **L** as a tan solid. Yield = 120 mg (62 %). ^{1}H NMR (400MHz, DMSO-*d*^{6}) δ (ppm) 8.52 (dd, 3H, *J* = 4.0, 0.8, Py), 7.87 (d, 3H, *J* = 7.9, Py), 7.73 (td, 3H, *J* = 7.8, 1.7, Py), 7.66 (t, 3H, *J* = 5.4, -NH), 7.28 (s, 3H, tz), 7.23 (ddd, 3H, J = 5.7, 4.8, 0.8, Py), 3.44 (q, 6H, *J* = 6.2, -CH_2CH_2NH), 2.83 (t, 6H, *J* = 6.4 Hz, -CH_2CH_2NH). ^{13}C NMR [100 MHz, DMSO-*d*^{6}]: δ_C = 169.1 (Q), 152.9 (Q), 150.7 (Q), 149.7 (CH), 137.4 (CH), 122.7 (CH), 120.7 (CH), 105.2 (CH), 53.3 (CH_2), 43.2 (CH_2). ESI-MS *m/z* 627 (M + H^+), HR ESI-MS found 627.1881 $C_{30}H_{30}N_{10}S_3$ requires 627.1890 (error 0.16 ppm).

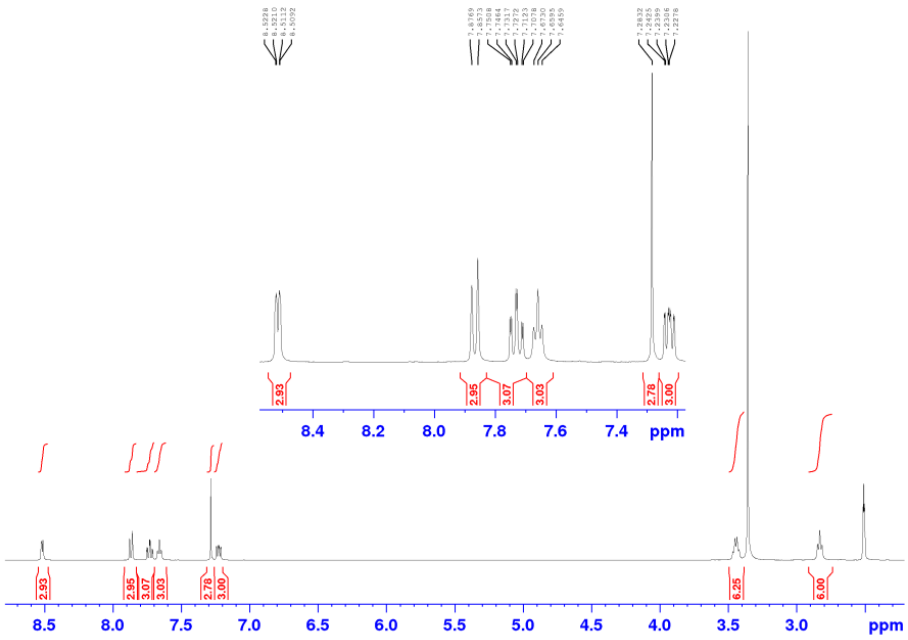

Figure 5.3.3. *^{1}H NMR of ligand* ***L*$^{4.1}$**.

Synthesis of $[(\mathbf{L}^{4.1})_2Cu_3(BF_4)](BF_4)_5$.

To a solution of $Cu(BF_4)_2{\cdot}6H_2O$ (10 mg. 0.029 mmol) in $MeNO_2$ (1 ml) was added a suspension of ligand $\mathbf{L}^{4.1}$ (27 mg, 0.043 mmol) in $MeNO_2$ and the reaction warmed and sonicated until a clear slate blue solution had formed. Diethyl ether was slowly allowed to diffuse into the solution resulting in blue block-like crystals after several days. Filtration and washing with diethyl ether (1 ml) and diethyl ether (1 ml) gave blue crystals which lost solvent rapidly (yield = 52%).

The bromide $[(\mathbf{L}^{4.1})_2Cu_3(Br)](BF_4)_5$ and hexafluorosilicate $[(\mathbf{L}^{4.1})_2Cu_3(SiF_6)](BF_4)_4$ complexes were all made in an analogous fashion but a half of an equivalent of Et_4NBr and Na_2SiF_6 was added (w.r.t ligand $\mathbf{L}^{4.1}$ i.e. 0.022 mmol) to the nitromethane solution. In the case of hexafluorosilicate the solution was allowed to stand for 24 hrs to allow dissolution of the anion and then exposed to ethyl acetate.

$[(\mathbf{L}^{4.1})_2Cu_3(PO_4)](ClO_4)_3$. $Cu(ClO_4)_2{\cdot}6H_2O$ (11 mg. 0.029 mmol) was dissolved in MeCN (0.25 ml) and added to ligand $\mathbf{L}^{4.1}$ (12.1 mg, 0.019 mmol) and the reaction sonicated until all the ligand has dissolved. To this was added a solution of $Bu_4NH_2PO_4$ (3.2 mg, 0.009 mmol) in water (0.5 ml) during which the colour

changed from blue to lime green. The reaction was then allowed to stand and after between 1 – 2 hrs lime green plate-like crystal were formed. Filtration and washing with water (1 ml) gave lime-green crystals which were dried under vacuum overnight. (yield = 99%). Found: C, 38.47; H, 3.24; N, 14.91%; $C_{60}H_{60}N_{20}S_6Cu_3PCl_3O_{16}\cdot H_2O$ requires C, 38.84; H, 3.37; N, 15.10%.

The remaining structures were all prepared in an identical manner using Et_4NI, $NaIO_4$, Na_3VO_4, Na_2WO_4, Na_2CrO_4, Et_4NHSO_4, $NaReO_4$ and NaH_2AsO_4 and either $Cu(ClO_4)_2\cdot 6H_2O$, $Cu(BF_4)_2\cdot 6H_2O$, Cu(triflate)$_2$ or $Cu(NO_3)_2\cdot 2H_2O$ were used (see crystal data table). For $[(\mathbf{L}^{\mathbf{4.1}})_2Cu_3(CO_3)](CF_3SO_3)_4$ no secondary anion was added but the solution was allowed to concentrate over 36 hrs.

$[(\mathbf{L}^{\mathbf{4.1}})_2Cu_3(CrO_4)](ClO_4)_4$. Yield = 78%. Found: C, 35.42; H, 2.99; N, 13.59%; $C_{60}H_{60}N_{20}S_6Cu_3CrCl_4O_{20}\cdot 3H_2O$ requires C, 35.82; H, 3.31; N, 13.92%.

$[(\mathbf{L}^{\mathbf{4.1}})_2Cu_3(SO_4)](ClO_4)_4$. Yield = 76%. Found: C, 36.19; H, 3.03; N, 13.89%; $C_{60}H_{60}N_{20}S_7Cu_3Cl_4O_{20}\cdot 2H_2O$ requires C, 36.5; H, 3.27; N, 14.19%.

$(\mathbf{L}^{\mathbf{4.1}})$ $[_2Cu_3(CO_3)](ReO_4)(trif)_3$. Yield = 53%. Found: C, 34.88; H, 2.97; N, 13.21%; $C_{64}H_{60}N_{20}S_9Cu_3O_{16}F_9Re$ requires C, 34.91; H, 2.75; N, 12.72%.

$[(\mathbf{L}^{\mathbf{4.1}})_2Cu_3(VO_4)](ClO_4)_3$. Yield = 70%. Found: C, 36.58; H, 3.23; N, 13.58%; $C_{60}H_{60}N_{20}S_6Cu_3VCl_3O_{16}\cdot 6H_2O$ requires C, 36.66; H, 3.69; N, 14.25%.

$[(\mathbf{L}^{\mathbf{4.1}})_2Cu_4(IO_6)(H_2O)_2](ClO_4)_5$. Yield = 70%. Found: C, 32.79; H, 3.03; N, 12.76%; $C_{60}H_{64}N_{20}S_6Cu_4ICl_5O_{26}$ requires C, 32.29; H, 2.89; N, 12.55%.

$[(\mathbf{L}^{\mathbf{4.1}})_2Cu_3(AsO_4)](trif)_3$. Yield = 81%. Found: C, 36.90; H, 2.98; N, 13.60%; $C_{63}H_{60}N_{20}F_9S_9Cu_3AsO_{13}$ requires C, 37.27; H, 2.98; N, 13.80%.

$[(\mathbf{L}^{\mathbf{4.1}})_2Cu_3(I)](ClO_4)_5$. Yield = 77%. Found: C, 34.06; H, 3.23; N, 12.72%; $C_{60}H_{60}N_{20}S_6Cu_3ICl_5O_{20}\cdot 3H_2O$ requires C, 33.95; H, 3.13; N, 13.20%.

$[(\mathbf{L}^{4.1})_2Cu_3(WO_4)](ClO_4)_4$. Yield = 77%. Found: C, 34.43; H, 2.89; N, 13.16%; $C_{60}H_{60}N_{20}S_6Cu_3WCl_4O_{20}$ requires C, 34.48; H, 2.89; N, 13.40%.

$[(\mathbf{L}^{4.1})_2Cu_3(SiF_6)](ClO_4)_4$. Yield = 69%. Found: C, 35.61; H, 2.98; N, 13.58%; $C_{60}H_{60}N_{20}S_6Cu_3SiF_6Cl_4O_{16}\cdot 2H_2O$ requires C, 35.67; H, 3.19; N, 13.87%.

5.4 UV-Vis studies.

Solutions were prepared by dissolving ligand $\mathbf{L^{4.1}}$ (6.26 mg, 0.01 mmol) and $Cu(ClO_4)_2 \cdot 6H_2O$ (5.56 mg. 0.015 mmol) in 1:1 $MeCN/H_2O$ (1 ml) and adding the relevant anion (0.5 equiv w.r.t. ligand) as a solution in the same solvent (1 ml) the solvent was then adjusted to 3 ml giving 1.66 x 10^{-3} M solutions of $[(\mathbf{L^{4.1}})_2Cu_3](ClO_4)_6$ or $[(\mathbf{L^{4.1}})_2Cu_3](trif)_6$.

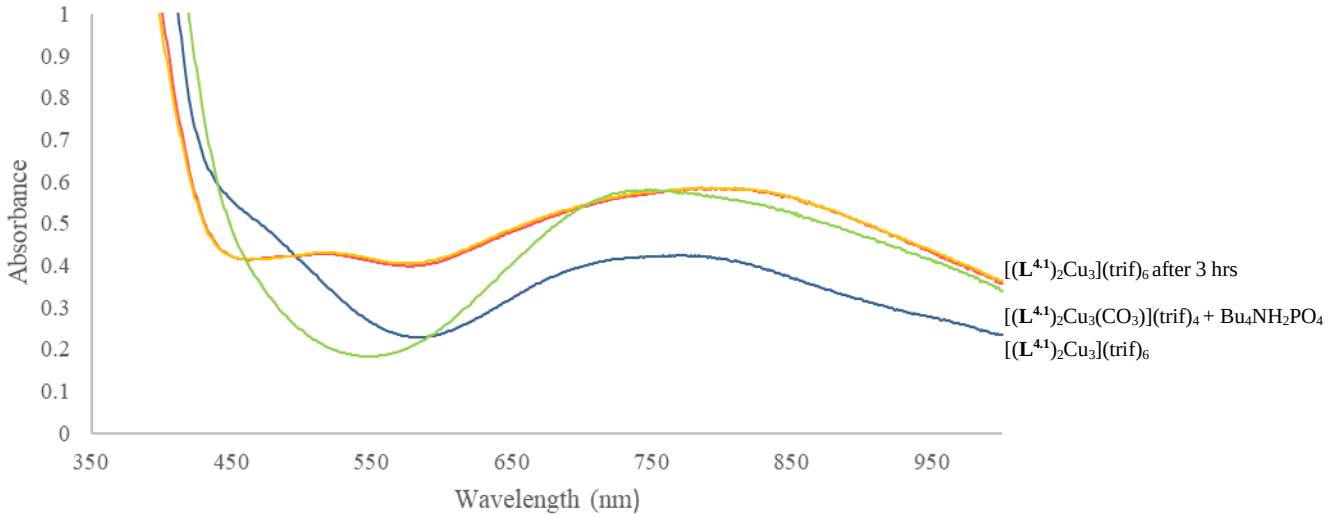

Figure 5.4.1. *UV-Vis absorption spectra of* $[(\mathbf{L^{4.1}})_2Cu_3](trif)_6$; $[(\mathbf{L^{4.1}})_2Cu_3](trif)_6$ *after 1 and 3 hrs giving* $[(\mathbf{L^{4.1}})_2Cu_3(CO_3)](trif)_4$; $[(\mathbf{L^{4.1}})_2Cu_3(CO_3)](trif)_4$ *plus one equivalent of* $Bu_4NH_2PO_4$ *giving* $[(\mathbf{L^{4.1}})_2Cu_3(PO_4)](trif)_3$. $[(\mathbf{L^{4.1}})_2Cu_3]^{6+}$ *1.33 x* 10^{-3} *M.*

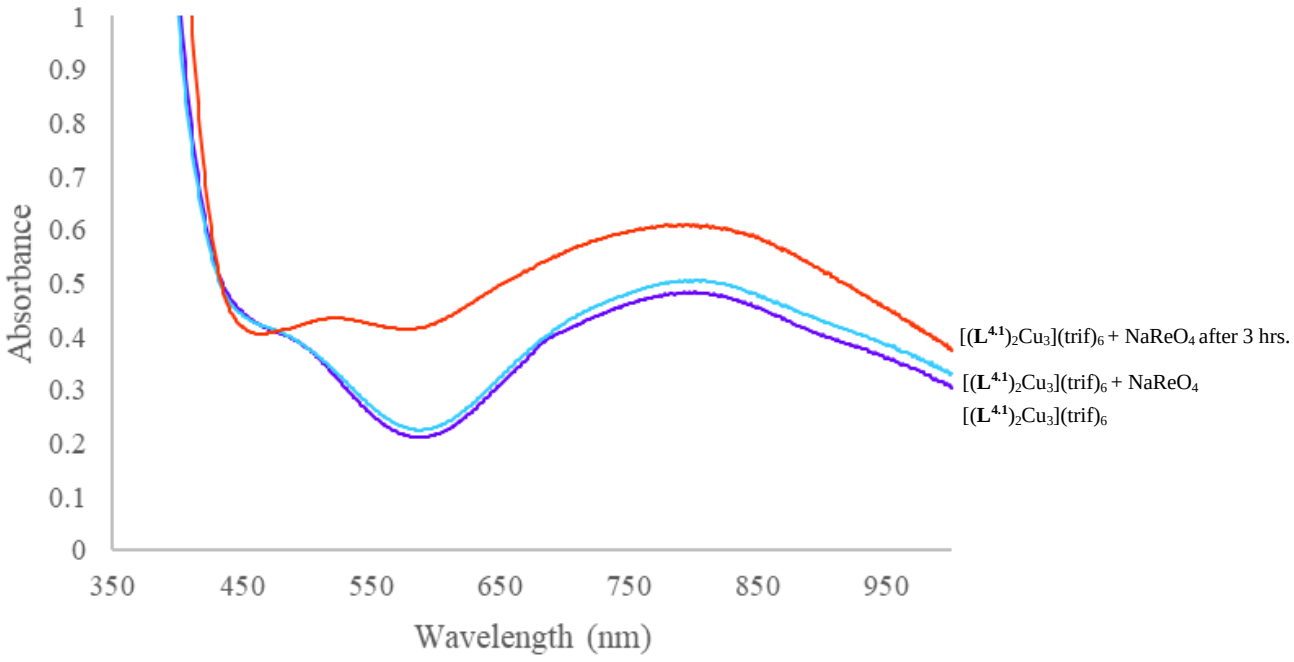

Figure 5.4.2. *UV-Vis absorption spectra of [(**L**$^{4.1}$)$_2$Cu$_3$](trif)$_6$; [(**L**$^{4.1}$)$_2$Cu$_3$](trif)$_6$ plus 1 equiv. NaReO$_4$; [(**L**$^{4.1}$)$_2$Cu$_3$](trif)$_6$ plus 1 equiv. NaReO$_4$ after 3 hrs giving [(**L**$^{4.1}$)$_2$Cu$_3$(CO$_3$)](trif)$_4$; [(**L**$^{4.1}$)$_2$Cu$_3$]$^{6+}$ 1.33 x 10^{-3} M.*

5.5. Quantitative yield and ion chromatography experiments.

$Cu(ClO_4)_2 \cdot 6H_2O$ (11.5 mg. 0.021 mmol) was dissolved in MeCN (0.25 ml) and added to ligand L (13 mgs, 0.021 mmol) and the reaction sonicated until all the ligand has dissolved. To this was added a 1000 ppm solution of $NaH_2PO_4 \cdot 2H_2O$ (prepared from 0.164 g in 100 ml water = 1000 ppm of $H_2PO_4^-$) in water (1 ml = 0.01 mmol of phosphate) upon which a lime-green coloured solution was formed (more MeCN was added if a precipitate formed ~ 0.1 ml) and the organic solvent was allowed to evaporate over two days. The solution was carefully removed, and the precipitate washed with water and the aqueous solvent collected and the volume adjusted to 2 ml by the addition of water if necessary. The phosphate concentration was then examined by IC.

IC		
Instrument	Metrohm 850 IC system	
Column	Metrohm A Supp 5 column (150 mm x 4.6 mm)	
Oven (ºC)	30ºC	
Pump	Mobile Phase A	5.0 mM Sodium Carbonate
	Mobile Phase B	N.A.
	Flow (mls/min)	0.70
	Isocratic/Gradient	Isocratic
	Runtime (mins)	30
Injector	Volume (□l)	10
Suppressor	Regenerant Solution	0.1 M Oxalic acid / 0.1 M Sulfuric acid in 10% acetone
Detector	Conductance / PAD	Conductance

Table 5.5.1 *Ion Chromatography; Conditions and Instrumentation.*

[Phosphate]/ppm	Phosphate Peak Area
10	0.477
25	1.136
50	2.302
100	4.943
200	10.12

Table 5.5.2 *Phosphate calibration.*

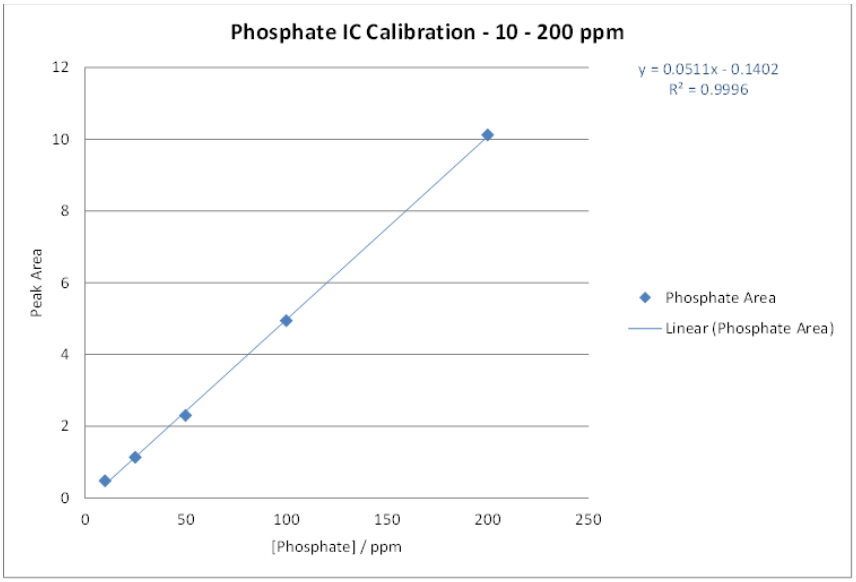

Figure 5.5.1. *IC calibration cure of 10 - 200 ppm solutions of* $Bu_4NH_2PO_4$.

The sample was analysed, and no phosphate was detected. A spiked sample (~10 ppm) was analysed immediately after spiking with phosphate (injected ~10 mins after spike) which confirmed phosphate could be detected in the sample matrix, however, the peak shape was significantly broader than the standard solutions. This may be due to the low pH of the sample. Example chromatograms are detailed below.

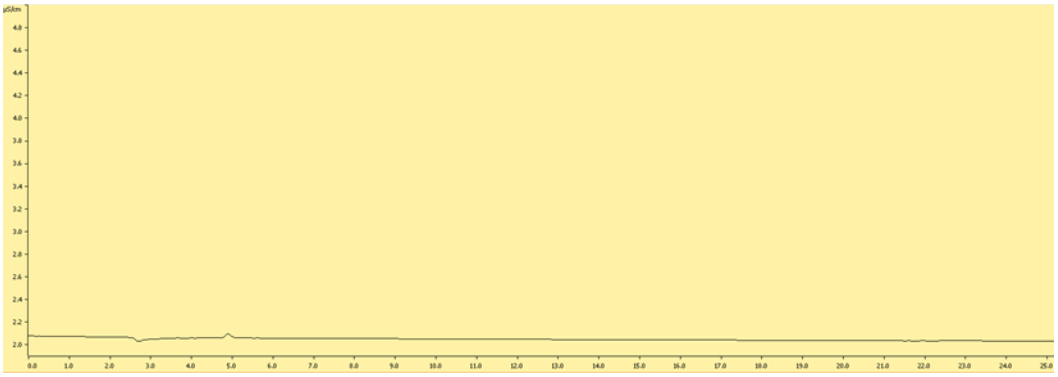

Figure 5.5.2 *Blank Solution.*

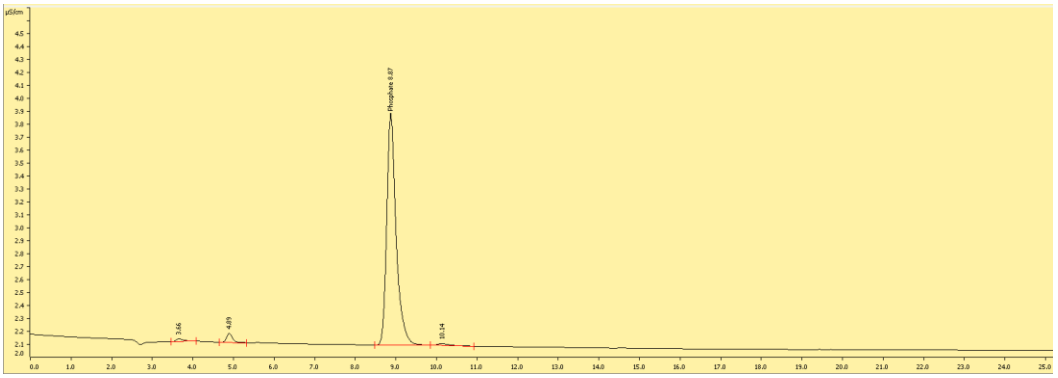

Figure 5.5.3 *10 ppm Phosphate Standard.*

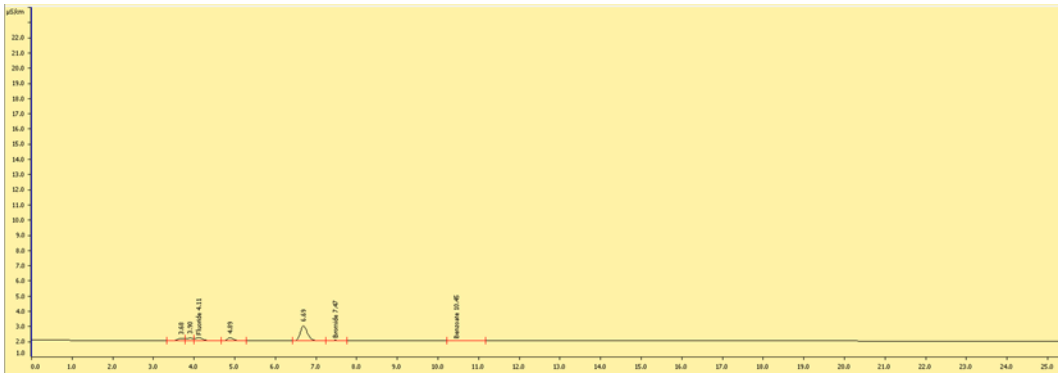

Figure 5.5.4 *Sample Solution.*

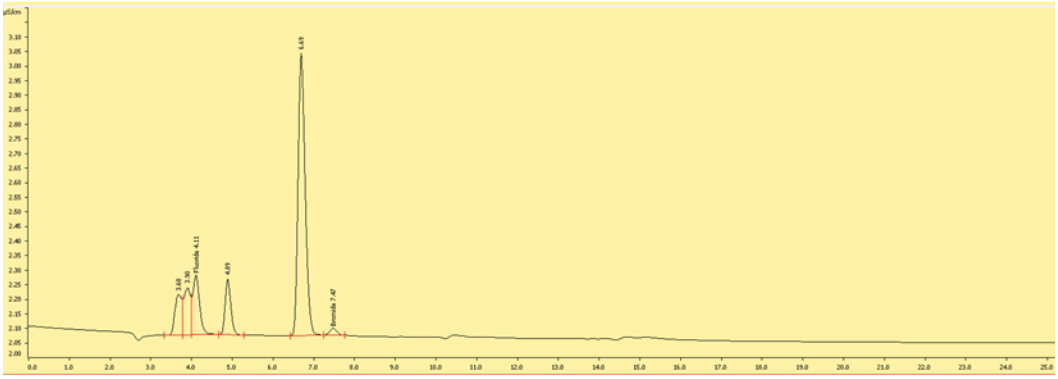

Figure 5.5.5 *Expanded Sample Solution.*

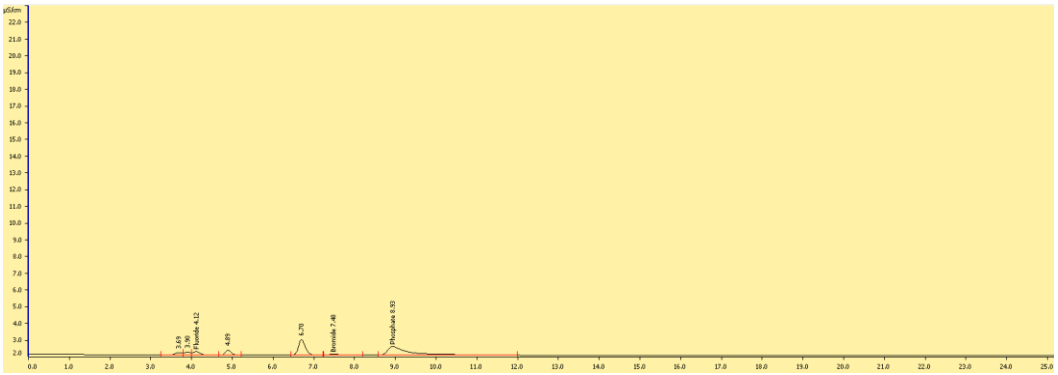

Figure 5.5.6 *Spiked Sample Solution.*

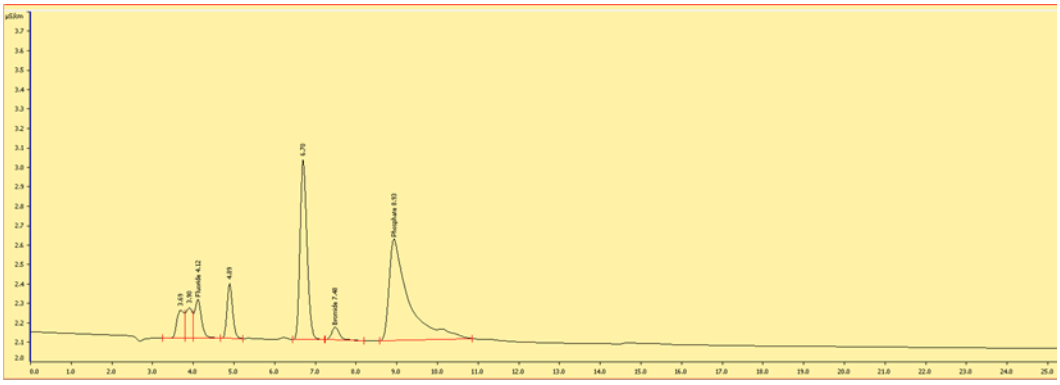

Figure 5.5.7 *Expanded Spiked Sample Solution.*

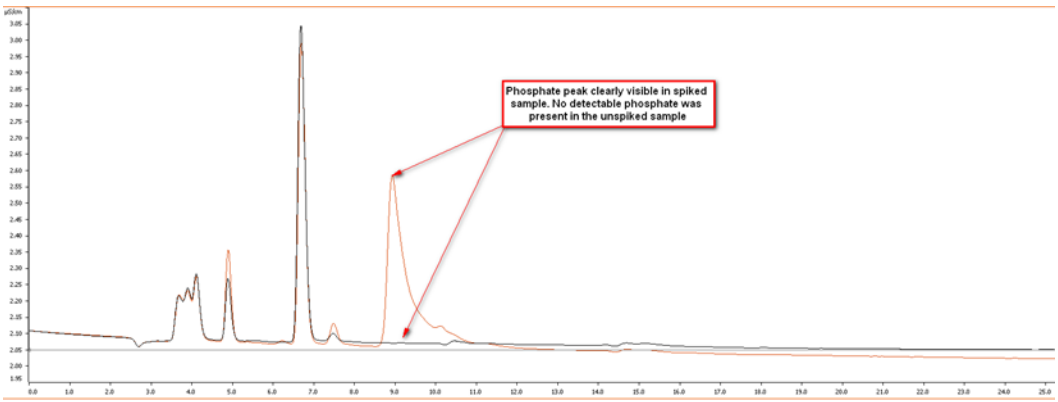

Figure 5.5.8 IC experimental data.

In an identical experiment to that above the phosphate containing complex ($[(\mathbf{L}^{\mathbf{4.1}})_2Cu_3(PO_4)](ClO_4)_3$) was isolated by filtration and washed with water and dried for several days in a desiccator giving 19.1 mgs of sample (99% yield). Theoretical yield = 19.3 mgs based on a molecular weight of 1855.616 from the elemental analysis (see above) which suggested the monohydrate e.g. $C_{60}H_{60}N_{20}S_6Cu_3PCl_3O_{16}\cdot H_2O$. This was repeated four times and the yield was similar in each case.

5.6 Ion Chromatography Competitive Experiment

To a 10 ml solution of chloride, nitrate, phosphate and sulfate (50 ppm of each) was added a solution of $[(\mathbf{L}^{\mathbf{4.1}})_2Cu_3](trif)_6$ (prepared from 6.59 mgs $\mathbf{L}^{\mathbf{4.1}}$ and 5.71 mg $Cu(trif)_2$ *i.e.* enough to encapsulate and precipitate one of the anions) in acetone (2 ml) and the solution allowed to stand over ~ 1 week during which time a lime-green precipitate formed. The solution was then filtered, the solid washed with water and the volume of the pooled aqueous fractions was carefully adjusted to 10 ml. Examination by IC gave values of 47 ppm of chloride, 46 ppm nitrate, 41 ppm sulfate and 10 ppm phosphate. It is worth noting that repeats of this experiment show that fast precipitation (1 ~ 2 days) of the anion reduces the selectivity and we attribute this two to factors: firstly, the selectivity of the cavity, which upon fast precipitation doesn't allow sufficient time to selectively form the thermodynamic product i.e. $[(\mathbf{L}^{\mathbf{4.1}})_2Cu_3(PO_4)](trif)_3$. Secondly, anions may precipitate as counter anions e.g. $[(\mathbf{L}^{\mathbf{4.1}})_2Cu_3(PO_4)](trif)_2(NO_3)$ or $[(\mathbf{L}^{\mathbf{4.1}})_2Cu_3(PO_4)](trif)_2Cl$ etc. as a result it is possible that further optimisation of the precipitation may increase the amount of phosphate removed.

References

1 J. W. Steed and J. L. Atwood, in *Supramolecular Chemistry*, 2009, pp. 591–706.

2 T. Gunnlaugsson, *Nat. Chem.*, 2016, 8, 6–7.

3 J.-M. Lehn, *Supramolecular Chemistry*, 1995.

4 V. Percec and G. Ungar, *Science (80-.).*, 2006, 313, 55–56.

5 F. M. Menger, *Proc. Natl. Acad. Sci.*, 2002, **99**, 4818–4822.

6 M. Fujita, *Yuki Gosei Kagaku Kyokaishi/Journal Synth. Org. Chem.*, 1995, **53**.

7 D. J. Cram, J. Lehn and C. J. Pedersen, *Nobel Prize Chem. 1987*, 1987, 1.

8 F. L. Dickert, *Sensors (Switzerland)*, 2014, 14, 22525–22531.

9 D. Pasini and A. Kraft, in *Current Opinion in Solid State and Materials Science*, 2004, vol. 8, pp. 157–163.

10 T. W. Ebbesen and C. Mioskowski, *Science (80-.).*, 2003, **9**, 775–778.

11 N. Kimizuka, *Adv. Polym. Sci.*, 2008, 219, 1–26.

12 Z. Dong, Yongguo Wang, Y. Yin and J. Liu, *Curr. Opin. Colloid Interface Sci.*, 2011, 16, 451–458.

13 C. K. McLaughlin, G. D. Hamblin and H. F. Sleiman, *Chem. Soc. Rev.*, 2011, 40, 5647–5656.

14 M. Teresa Albelda, J. C. Frías, E. García-España and H. J. Schneider, *Chem. Soc. Rev.*, 2012, 41, 3859–3877.

15 J. Buffle, M. Filella and J. W. Zhang, *Chimia (Aarau).*, 1995, **49**, 102–109.

16 K. Ariga, S. Ishihara, H. Abe, M. Li and J. P. Hill, *J. Mater. Chem.*, 2012, **22**, 2369–2377.

17 N. P. Org, *ScienceDaily*, 2016.

18 B. L. Feringa, *Angew. Chemie - Int. Ed.*, 2017, 56, 11060–11078.

19 P. D. Beer, P. A. Gale and D. K. Smith, in *Supramolecular Chemistry*, 1999, p. 92.

20 C. L. D. Gibb and B. C. Gibb, in *Supramolecular Chemistry*, 2012.

21 A. Bianchi and E. García-España, *Supramol. Chem. Anions*, 1997, 217–275.

22 A. N. Sokolov and L. R. MacGillivray, *Cryst. Growth Des.*, 2006, 6, 2615–2624.

23 B. R. Hall, L. E. Manck, I. S. Tidmarsh, A. Stephenson, B. F. Taylor, E. J. Blaikie, D. A. Vander Griend and M. D. Ward, *Dalton Trans.*, 2011, **40**, 12132–45.

24 M. J. Hannon and L. J. Childs, *Supramol. Chem.*, 2004, **16**, 7–22.

25 A. M. Stadler, N. Kyritsakas, G. Vaughan and J. M. Lehn, *Chem. - A Eur. J.*, 2007, **13**, 59–68.

26 M. Schmittel, V. Kalsani and J. W. Bats, *Inorg. Chem.*, 2005, **44**, 4115–4117.

27 V. Kalsani, H. Bodenstedt, D. Fenske and M. Schmittel, *Eur. J. Inorg. Chem.*, 2005, 1841–1849.

28 T. Riis-Johannessen, G. Bernardinelli, Y. Filinchuk, S. Clifford, N. D. Favera and C. Piguet, *Inorg. Chem.*, 2009, **48**, 5512–5525.

29 E. Terazzi, L. Guénée, J. Varin, B. Bocquet, J. F. Lemonnier, D. Emery, J. Mareda and C. Piguet, *Chem. - A Eur. J.*, 2011, **17**, 184–195.

30 T. K. Ronson, H. Adams, T. Riis-Johannessen, J. C. Jeffery and M. D. Ward, *New J. Chem.*, 2006, **30**, 26–28.

31 P. V. Bernhardt, P. Chin and D. R. Richardson, *Dalt. Trans.*, 2004, 3342–3346.

32 M. Albrecht, *Nat. Chem.*, 2014, 6, 761–762.

33 J. Xu, T. N. Parac and K. N. Raymond, *Angew. Chemie - Int. Ed.*, 1999, **38**, 2878–2882.

34 M. Wenzel, S. R. Bruere, Q. W. Knapp, P. A. Tasker and P. G. Plieger, *Dalt. Trans.*, 2010, **39**, 2936–2941.

35 B. Hasenknopf, J. M. Lehn, N. Boumediene, A. Dupont-Gervais, A. Van Dorsselaer, B. Kneisel and D. Fenske, *J. Am. Chem. Soc.*, 1997, **119**, 10956–10962.

36 C. J. Baylies, J. C. Jeffery, T. A. Miller, R. Moon, C. R. Rice and T. Riis-Johannessen, *Chem. Commun.*, 2005, 4158–4160.

37 J. C. Jeffery, C. R. Rice, L. P. Harding, C. J. Baylies and T. Riis-Johannessen, *Chem. - A Eur. J.*, 2007, **13**, 5256–5271.

38 D. J. Cooke, J. M. Cross, R. V Fennessy, L. P. Harding, C. R. Rice and C. Slater, *Chem. Commun. (Camb).*, 2013, **49**, 7785–7.

39 J. M. Cross, R. V. Fennessy, L. P. Harding, C. R. Rice, M. J. Hardie and C. Slater, *Chem. Commun.*, 2013, **49**, 11290–11292.

40 A. Stephenson and M. D. Ward, *Chem. Commun.*, 2012, **48**, 3605.

41 J. Hamblin, F. Tuna, S. Bunce, L. J. Childs, A. Jackson, W. Errington, N. W. Alcock, H. Nierengarten, A. Van Dorsselaer, E. Leize-Wagner and M. J. Hannon, *Chem. - A Eur. J.*, 2007, **13**, 9286–9296.

42 M. Albrecht, *Chem. Rev.*, 2001, **101**, 3457–3497.

43 O. R. Clegg, R. V. Fennessy, L. P. Harding, C. R. Rice, T. Riis-Johannessen and N. C. Fletcher, *Dalt. Trans.*, 2011, **40**, 12381–12387.

44 K. E. Allen, R. a. Faulkner, L. P. Harding, C. R. Rice, T. Riis-Johannessen, M. L. Voss and M.

Whitehead, *Angew. Chemie - Int. Ed.*, 2010, **49**, 6655–6658.

45 A. J. Metherell and M. D. Ward, *RSC Adv.*, 2013, **3**, 14281–14285.

46 P. A. Gale, *Acc. Chem. Res.*, 2011, **44**, 216–226.

47 P. A. Gale and C. Caltagirone, in *Chemosensors: Principles, Strategies, and Applications*, 2011, pp. 395–427.

48 P. A. Gale, E. N. W. Howe and X. Wu, *Chem*, 2016, 1, 351–422.

49 P. A. Gale, *Chem. Soc. Rev.*, 2010, **39**, 3746–3771.

50 S. O. Kang, J. M. Llinares, V. W. Day and K. Bowman-James, *Chem. Soc. Rev.*, 2010, 39, 3980–4003.

51 K. Choi and A. D. Hamilton, *Coord. Chem. Rev.*, 2003, **240**, 101–110.

52 J. Ju, M. Park, J. M. Suk, M. S. Lah and K. S. Jeong, *Chem. Commun.*, 2008, 3546–3548.

53 J.-Y. Lee, M.-H. Lee and K.-S. Jeong, *Supramol. Chem.*, 2007, **19**, 257–263.

54 P. A. Gale, J. R. Hiscock, C. Z. Jie, M. B. Hursthouse and M. E. Light, *Chem. Sci.*, 2010, **1**, 215–220.

55 Y. Zhang, R. Zhang, Y. Zhao, L. Ji, C. Jia and B. Wu, *New J. Chem.*, 2013, **37**, 2266–2270.

56 C. H. Park and H. E. Simmons, *J. Am. Chem. Soc.*, 1968, 90, 2431–2432.

57 H. E. Simmons and C. H. Park, *J. Am. Chem. Soc.*, 1968, 90, 2428–2429.

58 B. Dietrich, J. M. Lehn and J. P. Sauvage, *Tetrahedron Lett.*, 1969, 2889–2892.

59 J.-M. Lehn, E. Sonveaux and A. K. Willard, *J. Am. Chem. Soc.*, 1978, 4916–4918.

60 D. Pelleteret, N. C. Fletcher and A. P. Doherty, *Inorg. Chem.*, 2007, **46**, 4386–4388.

61 C. Piguet, *J. Incl. Phenom. Mol. Recognit. Chem.*, 1999, **34**, 361–391.

62 F. Cui, S. Li, C. Jia, J. S. Mathieson, L. Cronin, X. J. Yang and B. Wu, *Inorg. Chem.*, 2012, **51**, 179–187.

63 J. F. Ayme, J. E. Beves, C. J. Campbell, G. Gil-Ramírez, D. A. Leigh and A. J. Stephens, *J. Am. Chem. Soc.*, 2015, **137**, 9812–9815.

64 R. Custelcean, *Chem. Soc. Rev.*, 2014, 43, 1813–1824.

65 R. Custelcean, P. V. Bonnesen, N. C. Duncan, X. Zhang, L. A. Watson, G. Van Berkel, W. B. Parson and B. P. Hay, *J. Am. Chem. Soc.*, 2012, **134**, 8525–8534.

66 C. Raposo, M. Almaraz, M. Martín, V. Weinrich, M. L. Mussóns, V. Alcázar, M. C. Caballero and J. R. Morán, *Chem. Lett.*, 1995, **24**, 759–760.

67 R. Custelcean, B. A. Moyer and B. P. Hay, *Chem. Commun.*, 2005, 5971–5973.

68 A. Rajbanshi and R. Custelcean, in *Supramolecular Chemistry*, 2012, vol. 24, pp. 65–71.

69 B. R. Hall, L. E. Manck, I. S. Tidmarsh, A. Stephenson, B. F. Taylor, E. J. Blaikie, D. A. V. Griend and M. D. Ward, *Dalt. Trans.*, 2011, **40**, 12132–12145.

70 R. L. Paul, S. P. Argent, J. C. Jeffery, L. P. Harding, J. M. Lynam and M. D. Ward, *Dalt. Trans.*, 2004, 3453–3458.

71 J. S. Fleming, K. L. V. Mann, C. A. Carraz, E. Psillakis, J. C. Jeffery, J. A. McCleverty and M. D. Ward, *Angew. Chemie - Int. Ed.*, 1998, **37**, 1279–1281.

72 R. L. Paul, Z. R. Bell, J. C. Jeffery, J. A. McCleverty and M. D. Ward, *Proc. Natl. Acad. Sci.*, 2002, **99**, 4883–4888.

73 R. L. Paul, Z. R. Bell, J. C. Jeffery, L. P. Harding, J. A. McCleverty and M. D. Ward, *Polyhedron*, 2003, **22**, 781–787.

74 I. S. Tidmarsh, B. F. Taylor, M. J. Hardie, L. Russo, W. Clegg and M. D. Ward, *New J. Chem.*, 2009, **33**, 366.

75 A. J. Metherell and M. D. Ward, *Chem. Sci.*, 2016, **7**, 910–915.

76 W. Cullen, S. Turega, C. A. Hunter and M. D. Ward, *Chem. Sci.*, 2015, **6**, 2790–2794.

77 W. Cullen, K. A. Thomas, C. A. Hunter and M. D. Ward, *Chem. Sci.*, 2015, **6**, 4025–4028.

78 W. Cullen, S. Turega, C. A. Hunter and M. D. Ward, *Chem. Sci.*, 2015, **6**, 625–631.

79 S. Turega, W. Cullen, M. Whitehead, C. A. Hunter and M. D. Ward, *J. Am. Chem. Soc.*, 2014, **136**, 8475–8483.

80 C. G. P. Taylor, J. R. Piper and M. D. Ward, *Chem. Commun.*, 2016, **52**, 6225–6228.

81 L. P. Harding, J. C. Jeffery, T. Riis-Johannessen, C. R. Rice and Z. Zeng, *Chem. Commun.*, 2004, **3**, 654–655.

82 L. P. Harding, J. C. Jeffery, T. Riis-Johannessen, C. R. Rice and Z. Zeng, *Dalt. Trans.*, 2004, 2396–2397.

83 R. a. Faulkner, L. P. Harding, J. Higginson, C. R. Rice and C. Slater, *Angew. Chemie - Int. Ed.*, 2014, **53**, 13540–13543.

84 L. Bain, S. Bullock, L. Harding, T. Riis-Johannessen, G. Midgley, C. R. Rice and M. Whitehead, *Chem. Commun. (Camb).*, 2010, **46**, 3496–8.

85 M. G. Freire, C. M. S. S. Neves, I. M. Marrucho, J. A. P. Coutinho and A. M. Fernandes, *J. Phys. Chem. A*, 2010, **114**, 3744.

86 J. C. Dewan and L. K. Thompson, *Can. J. Chem.*, 1982, **60**, 121.

87 A. Styskalik, M. Babiak, P. Machac, B. Relichova and J. Pinkas, *Inorg. Chem.*, 2017, **56**, 10699–10705.

88 F. Mylius and A. Meusser, *Berichte der Dtsch. Chem. Gesellschaft*, 1904, **37**, 397–401.

89 R. A. Faulkner, N. J. Patmore, C. R. Rice and C. Slater, *Chem. Commun.*, 2018, **54**, 9159–9162.

90 C. C. Scarborough, B. V. Popp, I. A. Guzei and S. S. Stahl, *J. Organomet. Chem.*, 2005, **690**, 6143–6155.

91 Y. D. Feikema, *Acta Cryst.*, 1966, **20**, 765–769.

92 A. S. Ivanov, I. A. Popov, A. I. Boldyrev and V. V. Zhdankin, *Angew. Chemie - Int. Ed.*, 2014, **53**, 9617–9621.

93 W. Leitner, *Coord. Chem. Rev.*, 1996, **153**, 257–284.

94 X. Yin and J. R. Moss, *Coord. Chem. Rev.*, 1999, **181**, 27–59.

95 A. M. García-Deibe, C. Portela-García, M. Fondo, A. J. Mota and J. Sanmartín-Matalobos, *Chem. Commun.*, 2012, **48**, 9915–9917.

96 S. K. Dey, R. Chutia and G. Das, *Inorg. Chem.*, 2012, **51**, 1727–1738.

97 C. R. Rice, C. slater, R. Faulkner and R. Allan, *Angew. Chemie Int. Ed.*, 2018.

6. Appendix

6.1 Crystal Data $L^{2.1}$, $L^{2.2}$ and $L^{2.3}$

Single crystal X-ray diffraction data was collected at 150(2) K on a Bruker D8 Venture diffractometer equipped with a graphite monochromated Mo(Kα) radiation source and a cold stream of N_2 gas. Solutions were generated by conventional heavy atom Patterson or direct methods and refined by full-matrix least squares on all F^2 data, using SHELXS-97 and SHELXL software respectively.[A1] Absorption corrections were applied based on multiple and symmetry-equivalent measurements using SADABS.[A2]

The crystal structures $[(\mathbf{L^{2.1}})_2Cu_2(trif)_2](trif)_2$ and $[(\mathbf{L^{2.1}})_2Cu_2(H_2O)_2(NO_3)_4]$ were treated as standard. $[(\mathbf{L^{2.1}})_2Cu_2](trif)_2$ $[(\mathbf{L^{2.1}})_2Cu_2(H_2PO_4)(trif)](trif)_2$, $[(\mathbf{L^{2.3}})_2Cu_2(trif)_2](trif)_2$ (bridging triflate) had either disordered solvent molecule and/or counter anions. There were modelled over two positions and assigned their own free variable. In most cases *DELU, SIMU* and *ISOR* were used to constrain the adp's in the lest-squares refinement. The remaining structures contained further disorder which was modelled over two positions. However, also present was solvent disorder that despite attempts could not be successfully modelled and as a result the diffuse electron density was removed using the solvent mask facility in Olex2, resulting in voids in the crystal structure.[3] $[(\mathbf{L^{2.1}})_3Cu_3(O_3P(OBF_3)](BF_4)_3$ contained voids of 2515 Å^3 (629 Å^3 or 227 electrons per circular helicate which corresponds to one BF_4 anion and 6 $MeNO_2$ molecules). $[(\mathbf{L^{2.2}})_2Cu_2(H_2PO_4)(trif)_2](trif)_2$ contained voids of 1176 Å^3 which corresponds to 545 electrons. This accounts for 5 molecules of DIPE per asymmetric unit. $[(\mathbf{L^{2.2}})_2Cu_2(O_2P(OBF_3)_2](BF_4)$ contained voids of 335 Å^3 which corresponds to 131 electrons. This accounts for 2 molecules of $MeNO_2$ per asymmetric unit. $[(\mathbf{L^{2.3}})_2Cu_2(trif)_2](trif)_2$ (non-bridging triflate) contained voids of 1036 Å^3 which corresponds to 82 electrons, this accounts for 1 molecule of $MeNO_2$ per asymmetric unit.

Compound	$[(\mathbf{L}^{2.1})_2Cu_2(trif)_2](trif)_2$	$[(\mathbf{L}^{2.1})_2Cu_2(H_2O)_2(NO_3)_4]$	$[(\mathbf{L}^{2.1})_2Cu_2](trif)_2$	$[(\mathbf{L}^{2.1})_2Cu_2(H_2PO_4)(trif)](trif)_2$
Formula	$C_{40}H_{32}Cu_2F_{12}N_{12}O_{12}S_8$	$C_{37}H_{39}Cu_2N_{17}O_{16}S_4$	$C_{84}H_{70}Cu_4F_{12}N_{24}O_{15}S_{12}$	$C_{40}H_{34}Cu_2F_9N_{13.858}O_{15.743}PS_7$
M	1484.33	1233.18	2522.52	1514.22
Crystal system	triclinic	triclinic	triclinic	triclinic
Space group	P -1	P -1	P -1	P -1
a (Å)	9.7479(10)	11.6824(7)	13.0430(9)	11.358(4)
b (Å)	10.8987(11)	12.4937(7)	13.5163(10)	16.280(5)
c (Å)	14.1786(14)	18.6876(11)	17.0569(13)	16.681(7)
α (˚)	67.525(3)	104.3388(18)	79.424(2)	99.030(16)
β (˚)	73.066(3)	90.974(2)	71.004(2)	108.218(16)
γ (˚)	83.669(3)	112.5228(18)	61.611(2)	92.693(12)
V (Å^3)	1331.6(2)	2421.9(3)	2499.8(3)	2878.4(18)
Z	1	2	1	2
ρ_{calc} (Mg cm^{-1})	1.851	1.6909	1.676	1.7470
F(000)	746	1262.9016	1278	1530.0797
Crystal dimensions (mm)	0.15, 0.1, 0.1		0.1, 0.1, 0.05	0.25, 0.2, 0.1
Reflections measured	22989	66816	55348	80975
Range	$2.072 \leq \theta \geq 30.578$	$1.84 \leq \theta \geq 30.57$	$2.34 \leq \theta \geq 30.50$	$1.92 \leq \theta \geq 30.69$
hkl range indices	$-13 \leq h \geq 13$, $-15 \leq k \geq 15$, $-20 \leq l \geq 15$	$-16 \leq h \geq 16$, $-17 \leq k \geq 17$, $-26 \leq l \geq 26$	$-18 \leq h \geq 18$, $-19 \leq k \geq 19$, $-24 \leq l \geq 24$	$-16 \leq h \geq 16$, $-23 \leq k \geq 23$, $-23 \leq l \geq 23$
Nº independent reflections	8122	14798	15337	17674
Reflections with $I > 2\sigma(I)$	5735	10583	9889	11284
R_{int}	0.0692	0.0743	0.0765	0.0829
Final R_1 values	0.0498	0.0580	0.0680	0.0744
Final $wR(F^2)$ values	0.1146	0.1286	0.1575	0.1587
Final R_1 values (all data)	0.0846	0.0954	0.1193	0.1299
Final $wR(F^2)$ values (all data)	0.1288	0.1524	0.1854	0.1923
GOF	1.034	1.0811	1.052	1.0732
Refined parameters	388	687	693	886
Restraints	0	70	29	66
Largest peak and hole (e Å^{-3})	0.942, -0.779	1.1342, -1.6015	1.102, -1.354	1.6254, -2.0257

Compound	$[(\mathbf{L}^{2.1})_3Cu_3(PO_4BF_3)](BF_4)_3$	$[(\mathbf{L}^{2.1})_2Cu_2(OSe(OCH_3)_2)](trif)_2$	$[(\mathbf{L}^{2.2})_2Cu_2(H_2PO_4)(trif)_2](trif)_2$	$[(\mathbf{L}^{2.2})_2Cu_2(PO_4(BF_3)_2)](BF_4)$
Formula	$C_{114}H_{114}B_5Cu_6F_{18}N_{42}O_{20}P_2S_{12}$	$C_{42}H_{44}Cu_2F_6N_{14}O_{16}S_6Se_2$	$C_{43}H_{42}Cu_2F_9N_{12}O_{13}PS_7$	$C_{40}H_{40}B_4Cu_2F_{14}N_{12}O_4PS_4$
M	3616.55	1592.27	1488.40	1348.45
Crystal system	triclinic	monoclinic	triclinic	tetragonal
Space group	P -1	P2 1/n	P -1	I -4 2 d
a (Å)	12.3871(8)	11.768(4)	14.629(5)	22.4423(11)
b (Å)	24.199(2)	20.392(7)	15.453(6)	22.4423(11)
c (Å)	32.271(4)	12.836(4)	17.397(6)	20.6438(10)
α (˚)	78.661(7)	90	93.102(18)	90
β (˚)	85.813(9)	110.219(11)	103.018(14)	90
γ (˚)	78.326(7)	90	95.287(15)	90
V (Å^3)	9283.1(15)	2890.5(18)	3804(2)	10397.4(9)
Z	2	2	2	8
ρ_{calc} (Mg cm^{-1})	1.2937	1.829	1.2994	1.7227
F(000)	3666.8836	1596	1512.1201	5445.3322
Crystal dimensions (mm)	0.1, 0.1, 0.1	0.15, 0.1, 0.03	0.2, 0.1, 0.1	0.25, 0.2, 0.2
Reflections measured	132190	22174	114289	27338
Range	$2.80 \leq \theta \geq 68.32$	$2.097 \leq \theta \geq 30.582$	$1.85 \leq \theta \geq 30.44$	$2.26 \leq \theta \geq 27.66$
hkl range indices	$-14 \leq h \geq 14$, $-28 \leq k \geq 29$, $0 \leq l \geq 38$	$-16 \leq h \geq 14$, $-24 \leq k \geq 29$, $-18 \leq l \geq 17$	$-20 \leq h \geq 20$, $-21 \leq k \geq 21$, $-24 \leq l \geq 24$	$-22 \leq h \geq 32$, $-25 \leq k \geq 31$, $-21 \leq l \geq 29$
Nº independent reflections	33538	22174	22936	7905
Reflections with $I > 2\sigma(I)$	23849	5847	13386	4757
R_{int}	0.1127		0.0777	0.0675
Final R_1 values	0.0997		0.0762	0.0682
Final $wR(F^2)$ values	0.2929	0.0516	0.1957	0.1805
Final R_1 values (all data)	0.1337	0.0977	0.1334	0.1330
Final $wR(F^2)$ values (all data)	0.3299	0.1040	0.2317	0.2259
GOF	1.2535	1.018	1.1000	1.0471
Refined parameters	2014	399	858	384
Restraints	121	0	87	62
Largest peak and hole (e Å^{-3})	1.8506, -1.6788		2.6065, -2.0660	1.1473, -1.9238

Compound	$[(\mathbf{L}^{2,3})_2Cu_2(trif)_2](trif)_2$	$[(\mathbf{L}^{2,3})_2Cu_2(trif)_2](trif)_2$
Formula	$C_{44}H_{36}Cu_2F_{12}N_{12}O_{12}S_8$	$C_{48}H_{42}Cu_2F_{12}N_{16}O_{20}S_8$
M	1536.45	1774.57
Crystal system	monoclinic	monoclinic
Space group	P2(1)/c	P2(1)/c
a (Å)	15.2352(10)	10.7478(6)
b (Å)	15.9447(11)	16.4590(9)
c (Å)	15.9611(11)	20.156(1)
α (˚)	90	90
β (˚)	104.958(2)	90.9567(19)
γ (˚)	90	90
V (Å^3)	3745.9(4)	3565.1(3)
Z	2	2
ρ_{calc} (Mg cm^{-1})	1.3621	1.6530
F(000)	1552.2483	1796.4518
Crystal dimensions (mm)	0.25, 0.2, 0.05	0.2, 0.1, 0.1
Reflections measured	25925	42285
Range	$2.50 \leq \theta \geq 30.60$	$2.37 \leq \theta \geq 33.17$
hkl range indices	$-21 \leq h \geq 20$, $-22 \leq k \geq 22$, $-22 \leq l \geq 19$	$-15 \leq h \geq 15$, $-20 \leq k \geq 24$, $-24 \leq l \geq 29$
Nº independent reflections	11303	11836
Reflections with $I > 2\sigma(I)$	7086	8835
R_{int}	0.0551	0.0450
Final R_1 values	0.0827	0.0489
Final $wR(F^2)$ values	0.1797	0.1223
Final R_1 values (all data)	0.1269	0.0755
Final $wR(F^2)$ values (all data)	0.2022	0.1363
GOF	1.0313	1.0527
Refined parameters	443	498
Restraints	48	80
Largest peak and hole (e Å^{-3})	1.9170, -2.0427	0.9186, -0.7389

6.2. Crystal Data $L^{3.1}$ and $L^{3.2}$

Crystal for **$[(L^{3.1})Cu](ClO_4)_2$**. The structure contained a rotationally disordered perchlorate counter ion and it was modelled in two positions using the *PART* instruction. For the three disordered atoms *SIMU*, *SADI* and *ISOR* constrains were used in the lest-squares refinement.

Crystal for **$[(L^{3.2})_4Cu_4](trif)_8$.** The structure contained an acetonitrile and a water molecule disordered over two sites and they were modelled in two positions using the *PART* instruction with *SIMU*, *SADI* and *ISOR* constrains used in the lest-squares refinement. Furthermore, the structure contained disorder that could not be satisfactorily modelled and as a result the diffuse electron density was removed using the solvent mask facility in Olex2, resulting in voids in the crystal structure.[A3] The solvent mask removed a total of 133.1 electrons in the unit cell which corresponds to six molecules of acetonitrile in the unit cell.

Compound	$[Cu(\mathbf{L^{3.1}})](ClO_4)_2$	$[Cu_4(\mathbf{L^{3.2}})_4](trif)_8$
Formula	$C_{30}H_{23}Cl_2CuN_7O_8S_2$	$C_{136}H_{104}Cu_4F_{24}N_{32}O_{25}S_{16}$
M	808.14	3809.77
Crystal system	*monoclinic*	Monoclinic
Space group	*P21/c*	C2/c
a (Å)	11.3597 (9)	40.4596 (19)
b (Å)	40.568 (3)	17.1105 (8)
c (Å)	7.2878 (6)	23.5882 (12)
α (˚)	90	90
β (˚)	106.143 (3)	95.1214 (18)
γ (˚)	90	90
V (Å^3)	3226.1 (4)	16264.5 (14)
Z	4	4
ρ_{calc} (Mg cm^{-1})	1.666	1.5557
F(000)	1648.2	7745.6093
Crystal dimensions (mm)	0.21, 0.1, 0.01	0.2, 0.2, 0.08
Reflections measured	29209	80137
Range	$2.121 \leq \theta \geq 30.034$˚	$2.13 \leq \theta \geq 30.59$˚

hkl range indices	$-15 \leq h \geq 13$, $-57 \leq k \geq 56$, $-8 \leq l \geq 10$	$-57 \leq h \geq 57$, $0 \leq k \geq 24$, $0 \leq l \geq 33$
Nº independent reflections	8541	24779
Reflections with $I > 2\sigma(I)$	6328	15281
R_{int}	0.0744	0.0531
Final R_1 values	0.0848	0.0753
Final $wR(F^2)$ values	0.1359	0.1820
Final R_1 values (all data)	0.1537	0.1297
Final $wR(F^2)$ values (all data)	0.1536	0.2180
GOF	1.0838	1.0765
Refined parameters	480	1096
Restraints	30	32
Largest peak and hole (e $Å^{-3}$)	1.280, -0.835	1.5233, -1.6240

6.3. Crystal Data $L^{4.1}$

A variety of disorder in all the crystal structures was observed apart from $[(\mathbf{L^{4.1}})_2Cu_3(CrO_4)](BF_4)_4$. Structures $[(\mathbf{L^{4.1}})_2Cu_3(SiF_6)](BF_4)_4$, $[(\mathbf{L^{4.1}})_2Cu_3(Br)](BF_4)_5$, $[(\mathbf{L^{4.1}})_2Cu_3(PO_4)](ClO_4)_3$, and $[(\mathbf{L^{4.1}})_2Cu_3(I)](ClO_4)_5$ contained disorder with the counter anion and / or solvent molecules. This disorder was modelled over two sites using the *PART* instruction and assigned their own free variable. Disordered atoms/molecules were restrained with *DELU*, and *SIMU* and in some cases *ISOR* in the lest-squares refinement, apart from $[(\mathbf{L^{4.1}})_2Cu_3(PO_4)](ClO_4)_3$ and $[(\mathbf{L^{4.1}})_2Cu_3(VO_4)](ClO_4)_3$ for which restrains were not required. The remaining structures contained disorder which could not be successfully modelled and were treated differently:

$[(\mathbf{L^{4.1}})_2Cu_3(BF_4)](BF_4)_5$. In this molecule the anion guest contained in the cavity was significantly disordered and had to be restrained with *DELU*, *SIMU*, *ISOR* and *SADI* in the lest-squares refinement. Furthermore, significant electron density present within the core suggested that the encapsulated BF_4^- was substitutionally disordered with a chloride anion and this was modelled over two sites using the *PART* instruction and assigned their own free variable. Also present was solvent disorder that despite attempts could not be successfully modelled and as a result the diffuse electron density was removed using the solvent mask facility in Olex2, resulting in voids in the crystal structure.[A3] The solvent mask removed a total of 136 electrons in the unit cell which corresponds to two molecules of nitromethane and one molecule of diethyl ether in the unit cell.

$[(\mathbf{L^{4.1}})_2Cu_3(WO_4)](ClO_4)_4$. This structure contained positional disorder of two perchlorate anions which was modelled over two sites using the *PART* instruction and assigned their own free variable. These anions had to be restrained with *DELU*, *SIMU*, *ISOR* and *SADI* in the lest-squares refinement. Also present was solvent disorder that despite attempts could not be successfully modelled and as a result the diffuse electron density was removed using the solvent mask facility in Olex2, resulting in voids in the crystal structure.[A3] The solvent mask removed a total of 303 electrons in the unit cell which corresponds to fourteen molecules of MeCN in the unit cell (3 ~ 4 per asymmetric unit).

$[(\mathbf{L^{4.1}})_2Cu_3(SO_4)](ClO_4)_4$. In this molecule the sulfate anion was disordered (pointing "up and down" with respect to the "Cu_3" plane). This disorder was modelling over two sites using the *PART* instruction and assigned its own free variable and the need for any other restrains was not required. However, the disorder of the perchlorate anions was more significant and the *PART* instruction along with *DELU*, *SIMU* and *ISOR* restrains was used in the lest-squares refinement.

$[(\mathbf{L^{4.1}})_2Cu_4(IO_6)(H_2O)_2](ClO_4)_4$. In this molecule all the perchlorate anions were either rotationally and positionally disordered and these were modelled over two sites using the *PART* instruction and assigned their own free variable. These anions had to be restrained with *DELU*, *SIMU*, *ISOR* and *SADI* in the lest-squares refinement. Also present was solvent disorder that despite attempts could not be successfully modelled and as a result the diffuse electron density was removed using the solvent mask facility in Olex2, resulting in voids in the crystal structure.[A3] The solvent mask removed a total of 397 electrons in the unit cell which corresponds to twelve molecules of MeCN and H_2O in the unit cell (~ 2 per asymmetric unit).

$[(\mathbf{L^{4.1}})_2Cu_3(CO_3)](ReO_4)(CF_3SO_3)_3$. In this structure one of the triflate anions displayed disorder and these were modelled over two sites using the *PART* instruction and assigned their own free variable. These anions had to be restrained with *DELU*, *SIMU*, *ISOR* and *SADI* in the lest-squares refinement. Also present was solvent disorder that despite attempts could not be successfully modelled and as a result the diffuse electron density was removed using the solvent mask facility in Olex2, resulting in voids in the crystal structure.[A3] The solvent mask removed a total of 92 electrons in the unit cell which corresponds to four molecules of MeCN in the unit cell (1 per asymmetric unit).

$[(\mathbf{L^{4.1}})_2Cu_3(CO_3)](CF_3SO_3)_4$. In this molecule the carbonate anion was disordered (pointing "up and down" with respect to the "Cu_3" plane). This disorder was modelling over two sites using the *PART* instruction and assigned its own free variable and the need for any other restrains was not required. Furthermore, two of the triflate anions displayed disorder and these were modelled over two sites using the *PART* instruction and assigned their own free variable. These anions had to be restrained with *DELU*, *SIMU*, *ISOR* and *SADI*

in the lest-squares refinement. Also present was solvent disorder that despite attempts could not be successfully modelled and as a result the diffuse electron density was removed using the solvent mask facility in Olex2, resulting in voids in the crystal structure.[A3] The solvent mask removed a total of 83 electrons from the unit cell which corresponds to four molecules of MeCN in the unit cell (1 per asymmetric unit).

$[(\mathbf{L^{4.1}})_2Cu_3(PO_4)](NO_3)_3$. In this molecule the four nitrate anions were extensive disordered compounded by the high symmetry of the structure (tetragonal R-3c with the anions lying on special positions) despite attempts, modelling of this disorder was unsuccessful. As a result, the diffuse electron density was removed using the solvent mask facility in Olex2, resulting in voids in the crystal structure.[A3] The solvent mask removed a total of 1369 electrons from the unit cell which corresponds to two nitrate counter ions and four molecules of MeCN in the asymmetric unit.

$[(\mathbf{L^{4.1}})_2Cu_3(AsO_4)](ClO_4)_3$. In this molecule one of the perchlorate anions was disordered over two positions and was modelled over two sites using the *PART* instruction and assigned its own free variable. This and other anions were constrained using *DELU*, *SIMU*, *ISOR* and *SADI* in the lest-squares refinement. It also contained several poorly defined acetone and water molecules which were constrained using the same commands. Also present was solvent disorder that despite attempts could not be successfully modelled and as a result the diffuse electron density was removed using the solvent mask facility in Olex2, resulting in voids in the crystal structure.[A3] The solvent mask removed a total of 174 electrons from the unit cell which corresponds to four molecules of Me_2CO and H_2O in the unit cell.

$[(\mathbf{L^{4.1}})_2Cu_3(SeO_3)](BF_4)_4$. In this molecule some of the anions and acetonitrile molecules showed minor disorder and were constrained with *DELU*, *SIMU*, *ISOR* and *SADI* in the lest-squares refinement. Also present was solvent disorder that despite attempts could not be successfully modelled and as a result the diffuse electron density was removed using the solvent mask facility in Olex2, resulting in voids in the

crystal structure.[A3] The solvent mask removed a total of 173 electrons from the unit cell which corresponds to five molecules of MeCN and H_2O in the unit cell.

$[(\mathbf{L^{4.1}})_4Cu_8(SeO_3)_4](ClO_4)_8$. This molecule showed extensive disordered compounded by the high symmetry of the structure (tetragonal P-4n2 with the anions lying on special positions) despite attempts, modelling of this disorder was unsuccessful. As a result, the diffuse electron density was removed using the solvent mask facility in Olex2, resulting in voids in the crystal structure.[A3] The solvent mask removed a total of 450 electrons from the unit cell which corresponds to four perchlorate counter ions and sixteen molecules of MeCN in the unit cell. Furthermore, *DELU*, *SIMU* and *ISOR* constraints were applied to most of the atoms in an effort to make the thermal ellipsoids acceptable.

In the above molecules the solvent mask was only applied once the gross structure had been determined, refined. made anisotropic and hydrogen atoms added. Despite the removal of diffuse electron density, the gross molecular connectivity can be established and the structures (and their hosts) are also confirmed by ESI-MS.

Compound	$[(\mathbf{L^{4.1}})_2Cu_3(BF_4)](BF_4)_5\cdot 3.5\ MeNO_2$	$[(\mathbf{L^{4.1}})_2Cu_3(Br)](BF_4)_5\cdot 4\ MeNO_2$	$[(\mathbf{L^{4.1}})_2Cu_3(SiF_6)](BF_4)_4\cdot 0.52\ (C_4H_8O_2),\ 1.48(CH_3NO_2)$	$[(\mathbf{L^{4.1}})_2Cu_3(PO_4)](ClO_4)_3\cdot 4\ MeCN$	$[(\mathbf{L^{4.1}})_2Cu_3(VO_4)](ClO_4)_3\cdot 4\ MeCN$
Formula	$C_{63.5}H_{60}B_{5.65}Cl_{0.34}Cu_3F_{22.34}N_{23.5}O_7S_6$	$C_{64}H_{72}B_5BrCu_3F_{19}N_{24}O_8S_6$	$C_{63.56}H_{68.61}B_4Cu_3F_{22}N_{21.47}O_4S_6Si$	$C_{68}H_{60}Cl_3Cu_3N_{24}O_{16}PS_6$	$C_{68}H_{66}Cl_3Cu_3N_{24}O_{16}S_6V$
M	2145.26	2183.47	2069.87	1989.70	2015.77
Crystal system	Triclinic	Monoclinic	Triclinic	Triclinic	Triclinic
Space group	P -1	C2/c	P -1	P -1	P -1
a (Å)	13.156(5)	25.334(8)	14.9489(13)	14.9477(11)	14.953(4)
b (Å)	15.680(6)	22.176(6)	15.1172(13)	16.0425(13)	16.095(5)
c (Å)	24.086(10)	15.524(4)	21.1264(19)	19.8313(15)	19.853(7)
α (˚)	75.379(17)	90	88.987(3)	79.370(3)	79.521(12)
β (˚)	81.832(17)	103.559(15)	89.129(3)	81.053(2)	81.124(16)
γ (˚)	77.762(11)	90	62.359(2)	62.975(2)	63.092(9)
V (Å^3)	4678(3)	8478(4)	4228.6(7)	4149.6(6)	4176(2)
Z	2	4	2	2	2

ρ_{calc} (Mg cm^{-1})	1.5229	1.7104	1.6255	1.592	1.6032
F(000)	2164.3088	4416.2861	2099.5673	2026	2059.7709
Crystal dimensions (mm)	0.18, 0.16, 0.12	0.15, 0.15, 0.1	0.2, 0.15, 0.1	0.21, 0.15, 0.02	0.25, 0.15, 0.05
Reflections measured	111659	54547	125042	130503	107901
Range	$1.96 \leq \theta \geq 28.43^{\circ}$	$2.28 \leq \theta \geq 30.10^{\circ}$	$2.44 \leq \theta \geq 29.13^{\circ}$	$2.362 \leq \theta \geq 33.179^{\circ}$	$2.36 \leq \theta \geq 29.67^{\circ}$
hkl range indices	$-17 \leq h \geq 13$, $-20 \leq k \geq 20$, $-32 \leq l \geq 39$	$-35 \leq h \geq 35$, $-21 \leq k \geq 31$, $-21 \leq l \geq 21$	$-20 \leq h \geq 20$, $-20 \leq k \geq 20$, $-20 \leq l \geq 28$	$-22 \leq h \geq 22$, $-24 \leq k \geq 24$, $-30 \leq l \geq 30$	$-20 \leq h \geq 20$, $-22 \leq k \geq 22$, $-27 \leq l \geq 27$
N^{o} independent reflections	23323	12426	22638	31584	23313
Reflections with $I > 2\sigma(I)$	12498	9547	15471	19141	16126
R_{int}	0.1048	0.0733	0.0711	0.0858	0.0843
Final R_1 values	0.0789	0.0782	0.0768	0.0693	0.0509
Final $wR(F^2)$ values	0.1912	0.2008	0.1987	0.1315	0.1141
Final R_1 values (all data)	0.1635	0.1025	0.1207	0.1362	0.0903
Final $wR(F^2)$ values (all data)	0.2278	0.2160	0.2280	0.1540	0.1328
GOF	1.2094	1.0632	1.0915	1.031	1.0607
Refined parameters	1320	638	1269	1109	1111
Restraints	197	54	160	0	0
Largest peak and hole (e Å^{-3})	3.3750, -2.4807	2.4970, -1.3947	1.7354, -1.2316	1.266, -1.021	1.6442, -1.3546

Compound	$[(\mathbf{L}^{4.1})_2Cu_3(WO_4)](ClO_4)_4$	$[(\mathbf{L}^{4.1})_2Cu_3(CrO_4)](BF_4)_4 \cdot 3$ MeCN	$[(\mathbf{L}^{4.1})_2Cu_3(SO_4)](ClO_4)_4 \cdot 4.5$ MeCN$\cdot 0.85H_2O$	$[(\mathbf{L}^{4.1})_2Cu_4(IO_6)(H_2O)_2](ClO_4)_4$	$[(\mathbf{L}^{4.1})_2Cu_3(I)](ClO_4)_3 \cdot 4$ MeCN
Formula	$C_{60}H_{60}Cl_4Cu_3N_{20}O_{20}S_6W$	$C_{66}H_{66}B_4CrCu_3F_{16}N_{23}O_4S_6$	$C_{69.09}H_{65.25}Cl_4Cu_3N_{24.55}O_{20.85}S_7$	$C_{60}H_{64}Cl_4Cu_4IN_{20}O_{24}S_6$	$C_{68}H_{60}Cl_5Cu_3IN_{24}O_{20}S_6$
M	2089.95	2027.71	2130.01	2139.64	2220.58
Crystal system	Monoclinic	Triclinic	Monoclinic	Monoclinic	Triclinic
Space group	P 21/c	P -1	P 21/n	C 2/c	P -1
a (Å)	25.855(2)	14.921(6)	15.2049(11)	33.708(9)	14.7974(11)
b (Å)	23.7175(17)	15.106(5)	23.4075(18)	14.206(5)	15.4462(11)
c (Å)	15.1389(12)	20.643(7)	25.936(2)	35.38(1)	20.6490(15)
α (˚)	90	87.552(17)	90	90	78.763(2)
β (˚)	104.216(3)	88.69(2)	104.615(3)	97.321(10)	73.428(2)
γ (˚)	90	62.396(14)	90	90	74.487(2)
V (Å^3)	8999.1(12)	4120(3)	8932.2(12)	16804(9)	4322.7(6)
Z	4	2	4	8	2
ρ_{calc} (Mg cm^{-1})	1.5425	1.6345	1.5838	1.7110	1.7059
F(000)	4188.3112	2057.1597	4353.4212	8733.7297	2239.0228
Crystal dimensions (mm)	0.18, 0.15, 0.05	0.21, 0.15, 0.12	0.2, 0.2, 0.08	0.16, 0.12, 0.08	0.15, 0.1, 0.05
Reflections measured	125553	105202	147655	74822	129016
Range	$1.9 \leq \theta \geq 30.03$˚	$1.84 \leq \theta \geq 32.60$˚	$1.77 \leq \theta \geq 30.65$˚	$1.9 \leq \theta \geq 29.16$˚	$1.76 \leq \theta \geq 29.57$˚
hkl range indices	$-36 \leq h \geq 36$, $-33 \leq k \geq 21$, $-21 \leq l \geq 21$	$-22 \leq h \geq 22$, $-22 \leq k \geq 22$, $-31 \leq l \geq 31$	$-21 \leq h \geq 21$, $-33 \leq k \geq 33$, $-37 \leq l \geq 37$	$-46 \leq h \geq 38$, $-19 \leq k \geq 19$, $-47 \leq l \geq 48$	$-20 \leq h \geq 20$, $-21 \leq k \geq 21$, $-28 \leq l \geq 28$
Nº independent reflections	26280	29883	27469	22567	24252
Reflections with $I > 2\sigma(I)$	17123	21846	18054	13664	16099
R_{int}	0.0542	0.0572	0.0747	0.0906	0.0892
Final R_1 values	0.0715	0.0746	0.0890	0.0914	0.0582
Final $wR(F^2)$ values	0.1959	0.1870	0.1727	0.1748	0.1264
Final R_1 values (all data)	0.1116	0.1054	0.1403	0.1561	0.1063
Final $wR(F^2)$ values (all data)	0.2392	0.2053	0.1964	0.2004	0.1502
GOF	1.0959	1.0736	1.0956	1.0778	1.0685

Refined parameters	1110	1110	1341	1186	1163
Restraints	143	116	122	271	109
Largest peak and hole (e Å^{-3})	5.6704, -1.7987	4.4765, -1.5728	1.6572, -2.1582	2.8289, -3.6428	1.4330, -1.8615

Compound	$[(\mathbf{L}^{4.1})_2Cu_3(CO_3)](ReO_4)(CF_3SO_3)_3\cdot MeCN\cdot 1.63H_2O$	$[(\mathbf{L}^{4.1})_2Cu_3(CO_3)](CF_3SO_3)_4\cdot MeCN\cdot 2H_2O$	$[(\mathbf{L}^{4.1})_2Cu_3(PO_4)](NO_3)_3$	$[(\mathbf{L}^{4.1})_2Cu_3(AsO_4)](ClO_4)_3\cdot 2.5\ Me_2CO\cdot 2.5H_2O$	$[(\mathbf{L}^{4.1})_2Cu_3(SeO_3)](BF_4)_4$
Formula	$C_{66}H_{62}Cu_3F_9N_{21}O_{17.63}ReS_9$	$C_{67}H_{67}Cu_3F_{12}N_{21}O_{17}S_{10}$	$C_{60}H_{60}Cu_3N_{20}O_4PS_6$	$C_{67.5}H_{60}AsCl_3Cu_3N_{20}O_{20.4}S_6$	$C_{60}H_{60}Cu_3N_{20}O_3S_6Se$
M	2267.82	2177.69	1539.27	2042.36	1951.19
Crystal system	Monoclinic	Monoclinic	Trigonal	monoclinic	triclinic
Space group	P 21/c	P 21/c	R -3 c	C2/c	P -1
a (Å)	13.839(3)	14.087(4)	20.5142(11)	28.317(7)	15.161(6)
b (Å)	30.189(7)	30.726(8)	20.5142(11)	21.627(5)	16.932(6)
c (Å)	21.106(4)	20.559(6)	76.264(5)	29.605(7)	17.887(7)
α (˚)	90	90	90	90	85.721(16)
β (˚)	100.683(7)	100.050(12)	90	109.323(10)	77.024(18)
γ (˚)	90	90	120	90	80.146(14)
V (Å^3)	8665(3)	8762(4)	27795(3)	17109(7)	4405(3)
Z	4	4	12	8	2
ρ_{calc} (Mg cm^{-1})	1.7382	1.6507	1.1035	1.5857	1.471
F(000)	4539.2631	4439.3135	9504.8186	8304.2087	1969.3
Crystal dimensions (mm)	0.2, 0.18, 0.09	0.2, 0.17, 0.15	0.2, 0.15, 0.05	0.1. 0.1, 0.05	0.1, 0.15, 0.05
Reflections measured	88102	147367	61331	93578	23591
Range	$2.05 \leq \theta \geq 32.54^{\circ}$	$2.10 \leq \theta \geq 31.51^{\circ}$	$2.14 \leq \theta \geq 28.38^{\circ}$	$2.27 \leq \theta \geq 30.58^{\circ}$	$1.86 \leq \theta \geq 29.13^{\circ}$
hkl range indices	-20 ≤ h ≥ 19, -45 ≤ k ≥ 45, -31 ≤ l ≥ 29	-20 ≤ h ≥ 20, -45 ≤ k ≥ 45, -30 ≤ l ≥ 28	-19 ≤ h ≥ 27, -27 ≤ k ≥ 20, -102 ≤ l ≥ 78	-40 ≤ h ≥ 40, -30 ≤ k ≥ 27, -42 ≤ l ≥ 37	-20≤ h ≥20, -23≤ k ≥23, -24≤ l ≥24
N^o independent reflections	31266	29162	7715	26160	23591
Reflections with $I > 2\sigma(I)$	19608	17712	5317	16477	14480
R_{int}	0.0519	0.0786	0.0971	0.0671	0.0823
Final R_1 values	0.0659	0.0715	0.0578	0.0631	0.0785

Final $wR(F^2)$ values	0.1572	0.1522	0.1468	0.1421	0.2040
Final R_1 values (all data)	0.1171	0.1312	0.0863	0.1178	0.1315
Final $wR(F^2)$ values (all data)	0.1835	0.1798	0.1630	0.1683	0.2361
GOF	1.0452	1.0673	1.0353	1.0724	1.0765
Refined parameters	1184	1316	283	1150	1073
Restraints	160	121	0	109	75
Largest peak and hole (e Å^{-3})	3.9184, -2.7441	2.6514, -1.5291	0.8145, -0.8660	1.4184, -1.1571	2.9130, -1.2638

Compound	$[(\mathbf{L}^{4.1})_4Cu_8(SeO_3)_4](ClO_4)_8$	$[(\mathbf{L}^{4.1})_2Cu_3(S_20_3)](ClO_4)_4$	Tris-thiourea (**2**)
Formula	$C_{120}H_{120}Cu_8N_{40}O_{12}S_{12}Se_4$	$C_{68}H_{57}Cl_4Cu_3N_{24}O_{19}S_8$	$C_9H_{21}N_7S_3$
M	4088.25	2103.34	323.51
Crystal system	tetragonal	triclinic	monoclinic
Space group	P -4 n 2	P -1	P 21/c
a (Å)	18.797(6)	14.656(7)	16.8002(10)
b (Å)	18.797(6)	15.429(6)	9.2255(7)
c (Å)	25.951(8)	22.006(8)	9.8307(6)
α (˚)	90	87.120(13)	90
β (˚)	90	75.47(2)	102.387(2)
γ (˚)	90	71.956(16)	90
V (Å^3)	9170(5)	4578(3)	1488.19(17)
Z	2	2	4
ρ_{calc} (Mg cm^{-1})	1.481	1.5257	1.444
F(000)	4119.0	2142.0018	688
Crystal dimensions (mm)	0.15, 0.12, 0.05	0.1, 0.1, 0.05	0.2, 0.2, 0.15
Reflections measured	47003	127949	10664
Range	$2.19 \leq \theta \geq 27.02$	$2.30 \leq \theta \geq 29.12$	$2.53 \leq \theta \geq 30.46$
hkl range indices	-25≤ h ≥24, -22≤ k ≥22, -29≤ l ≥34	-20≤ h ≥20, -21≤ k ≥21, -30≤ l ≥30	-22≤ h ≥22, -10≤ k ≥12, -11≤ l ≥13

Nº independent reflections	11299	24532	3994
Reflections with $I > 2\sigma(I)$	6380	16573	2832
R_{int}	0.0865	0.0664	0.0619
Final R_1 values	0.0757	0.0591	0.0624
Final $wR(F^2)$ values	0.1811	0.0987	0.0951
Final R_1 values (all data)	0.1488	0.1357	0.1809
Final $wR(F^2)$ values (all data)	0.2147	0.1552	0.1605
GOF	1.1714	1.0615	1.077
Refined parameters	506	1163	172
Restraints	327	12	0
Largest peak and hole (e $Å^{-3}$)	-1.0092, 1.3074	-1.3199, 2.4711	-0.759, 0.839

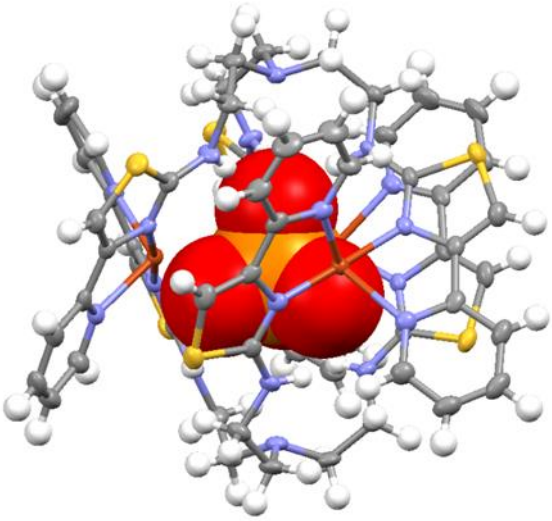

Figure 6.3.1. *X-ray structure of structure of* $[(\mathbf{L}^{4.1})_2Cu_3(PO_4)](NO_3)_3$*. Thermal ellipsoids shown at the 50% probability level. Selected hydrogen atoms and anions omitted for clarity. X-ray structure described but not shown in manuscript.*

A1. SHELXTL Program System, Vers. 5.1, Bruker Analytical X-ray Instruments Inc., Madison, WI, 1998.

A2. G. M. Sheldrick, SADABS: A Program for Absorption Correction with the Siemens SMART System, University of Göttingen (Germany), 1996.

A3. O. V. Dolomanov, L. J. Bourhis, R. J. Gildea, J. A. K. Howard and H. Puschmann, OLEX2: a complete structure solution, refinement and analysis program. *J. Appl. Cryst.* (2009). **42**, 339-341.